New strategies based on nanosystems to facilitate the crossing through biological barriers

Josep Garcia Garcia

Programa de doctorat en Nanociències

New strategies based on nanosystems to facilitate the crossing through biological barriers

Josep Garcia Garcia

Tesi doctoral dirigida per:

Tutor:

Prof. Ernest Giralt Lledó

Universitat de Barcelona

Facultat de Química

Departament de Química Orgànica

Dra. Meritxell Teixidó Turà

IRB Barcelona

Programa de Química i

Farmacologia molecular

Prof. Ernesto Nicolàs Galindo

Universitat de Barcelona

Facultat de Química

Departament de Química Orgànica

Barcelona, 2016

Contents

Abbreviations

ACN	Acetonitrile
Apidra	Insulin glulisine
APS	Ammonium persulfate
a.u.	Arbitrary units
BBB	Blood-brain barrier
BDAC	Benzyldimethylhexadecylammoniumchloride
Boc$_2$O	Di-tert-butyl dicarbonate
bPEI	Branched polyethylenimine
CF	5(6)-carboxyfluorescein
CNS	Central nervous system
cPEG$_{5000}$	Poly(ethylene glycol) 2-mercaptoethyl ether acetic acid (MW: 5000)
CPP	Cell penetrating peptide
CTAB	Hexadecyltrimethylammonium bromide
DCM	Dichloromethane
DIC	Diisopropylcarbodiimide
DIEA	*N,N*-Diisopropylethylamine
DLS	Dynamic light scattering
DMEM	Dulbecco's modified eagle's medium for cell culture
DMF	Dimethylformamide
DMSO	Dimethyl sulfoxide
DTT	Dithiothreitol
ECGS	Endothelial cell growth supplement
ECL	Enhanced chemiluminescence
ECM	Endothelial cells medium
EDC·HCl	1-(3-Dimethylaminopropyl)-3-ethylcarbodiimide hydrochloride
EDTA	Ethylenediaminetetraacetic acid
EE	Encapsulation efficiency
EMA	European medicine agency
EPC	*L*-α-Phosphatidylcholine (Egg, Chicken)
FACS	Fluorescence-activated cell sorting
FBS	Fetal bovine serum
FD4	Fluorescent dextran (MW: 4000 Da)
FDA	Food and drug administration
FRDA	Friedreich's ataxia
FXN	Frataxin
GFP	Green fluorescence protein
h	Hours
HBBS	Hank's balanced salt solution
HOAt	1-Hydroxy-7-azabenzotriazole
LSPR	Longitudinal surface plasmon resonance
MeOH	Methanol
MES	2-(*N*-Morpholino)ethanesulfonic acid
min	Minutes
mPEG$_{5000}$	Mercaptopolyethylene glycol monomethyl ether (MW: 5000)
MUA	11-Mercaptoundecanoic acid
MW	Molecular weight
NHS	*N*-Hydroxysuccinimide
NIR	Near-infrared

NRs	Nanorods
O/N	Overnight
PB	Sodium phosphate buffer
PBS	Phosphate buffered saline
PdI	Polydispersity index
PEI	Polyethylenimine
PEOZ	Poly(2-ethyl-2-oxazoline)
PF68	Pluronic® F-68
PF127	Pluronic® F-127
PLGA	Poly(D,L-lactide-*co*-glycolide acid)
PT	Photothermal therapy
PVA	Poly(vinyl alcohol)
PVDF	Polyvinylidene fluoride
PyBOP	Benzotriazol-1-yl-oxytripyrrolidinophosphonium hexafluorophosphate
RT	Room temperature
sec	Seconds
SDS	Sodium dodecyl sulfate
SDS-PAGE	Sodium dodecyl sulfate polyacrylamide gel electrophoresis
SEC	Size exclusion chromatography
s-NHS	*N*-hydroxysulfosuccinimide
TAE	Tris-acetate-EDTA
TBTU	*O*-(benzotriazole-1-yl)-1,1,3,3-tetramethyluronium tetrafluoroborate
TBE	Tris-borate-EDTA
TBS	Tris-buffered saline
TBST	Tris-buffered saline with Tween 20
TE	Tris-EDTA
TEER	Transepithelial electrical resistance
TEM	Transmission electron microscopy
TEMED	*N,N,N′,N′*-tetramethylethylene diamine
TIS	Triisopropylsilane
TFA	Trifluoroacetic acid
Tris	Tris(hydroxymethyl)aminomethane
w/o/w	Water-in-oil-in-water

General introduction

In 1959, the physicist Richard Feynman (Nobel prize in Physic, 1965) introduced the idea of nanotechnology in his speech "There's Plenty of Room at the Bottom".[1] In his talk, he proposed the possibility to manipulate matter at atomic scale. However, the first time the term *nanotechnology* appeared was in the cover headline of OMNI magazine in 1986.[2] In the article, the writer Fred Hapgood discussed the idea of atomically precise machines building atomically precise products at atomic scale. At present, the term can be referred to the study and control of phenomena and materials, with at least one dimension, ranging from 1 to 100 nanometers. Nevertheless, different perspectives can be acquired depending on the area of nanotechnology, as reflected in the first issue of Nature Nanotechnology in 2006.[3]

When materials are reduced to the nanoscale, they change drastically their properties compared with bulk materials. As the size decrease, some phenomena become pronounced such as the "quantum effect". The properties present in bulk materials are the average of all the quantum forces affecting all the atoms of the material. At nanoscale, this behavior becomes specific to individual atoms or molecules and can be very different to bulk material. Another important aspect affecting nanomaterials is the surface area. By comparing the same volume in bulk form, nanomaterials have a larger surface area. This effect can affect the properties of the nanomaterials such as strength, reactivity or electrical properties.

Manufacturing at nanoscale can be achieved by two methods: *top-down* and *bottom-up*. The first method is based on the modification of bulk materials until reaching refined nanoscale objects. The second approach uses atomic building blocks in order to produce a larger object. Lithography and self-assembly are examples of *top-down* and *bottom-up*, respectively.

Governs have invested high amount of their money on nanotechnology and this trend is increasing year by year as shown in Figure 1. However, these values are low compared to other forms of private funding. The total funding in nanotechnology has been estimated to be 0.25 trillion dollars for 2015.[4]
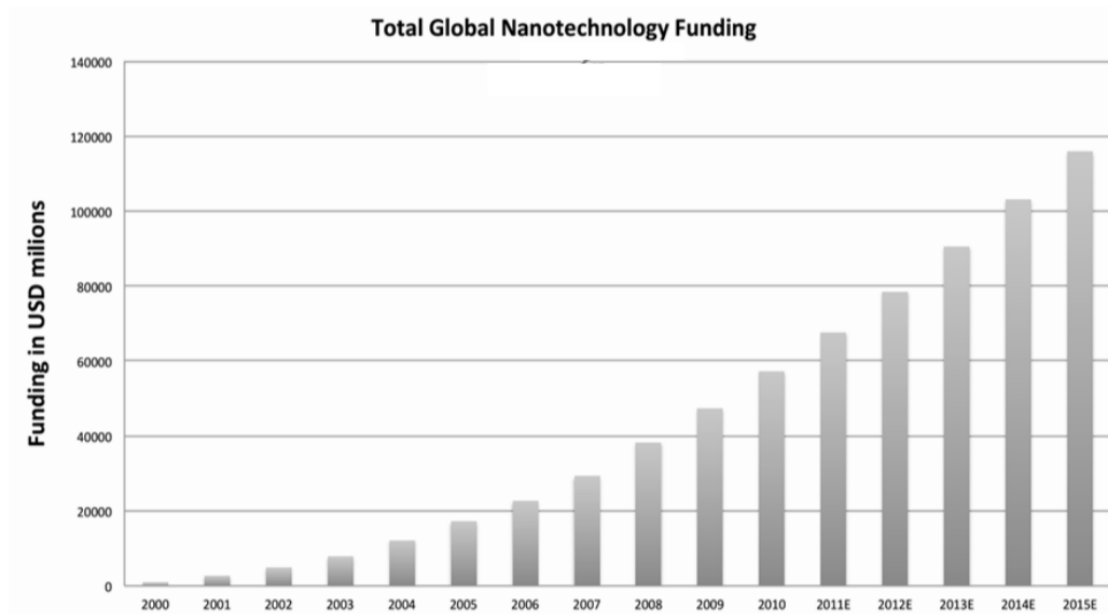
Figure 1. Cumulative global funding of nanotechnologies (source: Cientifica Ltd 2011).

This high investment has also been noticed by the increasing number of scientific publications and patents related to nanotechnology.[5] As shown in Figure 2, patented nanotechnologies were increased year after year both US (USPTO) and Europe (EPO). In the same manner, the indexed scientific publications related to nanotechnology have increased (Figure 2).

A)

B)
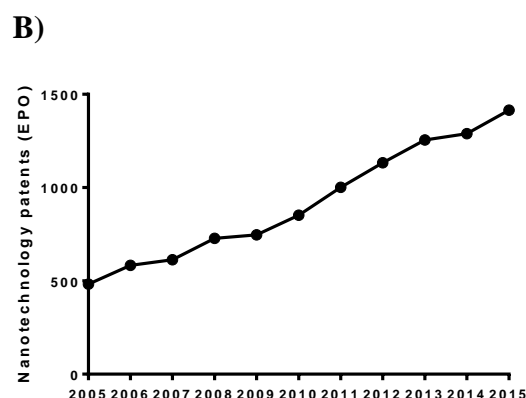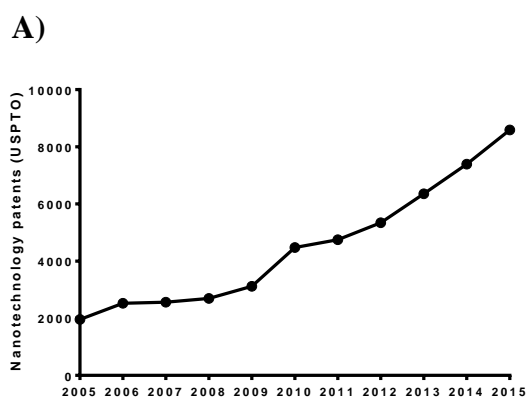
C)
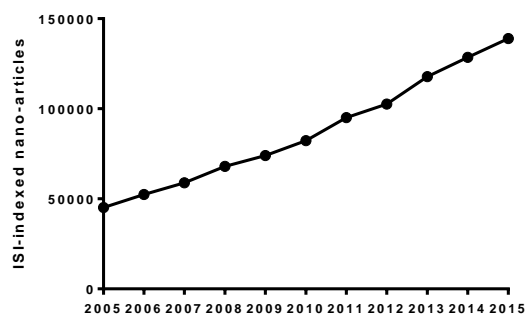
Figure 2. Increasing tendency in nanotechnology patents in A) United States and B) Europe. ISI-indexed scientific articles related to nanotechnology. Source StatNano.com.[6]

Nanotechonolgy has been implemented to an enormous multidisciplinary areas such as food, energy industry and chemistry.[7] But one of the main problems is the cumulative use of these nanomaterials and the potential toxicity.[8] In this regard, new regulations have to be dictated in order to do a proper use of these new nanomaterials. Even though toxicological evaluation has to be taken into consideration, the nanotechnology opens a new door for future improvements in all fields. The question is: are we prepared to use this technology in a proper manner?

In this thesis, three different types of nanoparticles, which correspond to each chapter, are used: gold nanoparticles to achieve endosomal release, polymeric nanoparticles as gene carrier through the blood brain barrier (BBB) and modified peptides (lipopeptides) to increase the transport of insulin through the intestinal barrier.

The link between these three different chapters is the use of nansystems in order to improve the transport through three different biological barriers. In addition, all the compositions contain a peptide part used to increase the internalization of the nanocarrier.

In chapter 1, the selected nanosystem was modified gold nanorods, because of their great optical characteristics and in particular, the capability of emit heat after laser irradiation. These modifications consist in: i) incorporation of a polyethylene glycol (PEG) moiety in order to confer stability to the nanorods; ii) incorporation of a cell penetrating peptide (CPP) to the PEG in order to promote the internalization of the nanoparticle into the cell; iii) incorporation of an electrostatically bound RNA to achieve a biological response after endosomal escape. Therefore, our hypothesis was that these modified gold nanorods were able to internalize into cells by the endocytic route. Once internalized, a specific power from a near infrared laser (wavelength in which the nanorods absorb the light) was applied

in order to heat the endosomes. These locally administered heat hast was then necessary to disrupt the endosome releasing the RNA to the cytosol causing minimal damage to the cell.

The nanosystem employed in chapter 2 was composed by modified poly (D,L-lactide-*co*-glycolide acid) (PLGA) polymer in order to synthesize PLGA nanoparticles for gene therapy to the brain. To accomplish our goal, a peptide BBB-shuttle was coupled to the nanoparticle to improve the transport of encapsulated DNA through the BBB. Friedreich's ataxia is a neurodegenerative disease and therefore we encapsulated a DNA plasmid encoding the frataxin protein, which is deficient in Friedreich ataxia's patients. As a first approximation, nanoparticles were tested in a human BBB cell based model in order to test the ability of nanoparticles crossing and the transfection capacity was tested in a brain derived cell lines.

In chapter 3, modified peptides with aliphatic moieties (lipopeptides) form electrostatically interactions with a model drug (insulin). These interaction were able to induce the formation of nanocomplexes between these lipopeptides and the insulin. We hypothesize that these lipopeptides can protect insulin from gastrointestinal environment and in addition, promote insulin transport to the blood. Therefore, our goal is to achieve the transport of insulin through the intestinal barrier. In this chapter, the complexes were tested in two intestinal models (Caco-2 cell model and rat colon tissue placed in Ussing chambers) in order to find the lipopeptide that promote higher insulin permeation enhancement.

Functionalized gold nanorods as potential endosomal release enhancers

The great applicability of gold nanoparticles (NPs) has been widely studied during this last century. But, it was not since last decades that the researchers could control the anisotropy of these particles.[9] One of the most popular anisotropic nanoparticles are gold nanorods (NRs), not only for they unique optical properties but also for they great applicability in many fields such as imaging,[10] photothermal therapy (PT)[10] or biosensing.[11] These optical properties are strongly related with their size and shape and how the absorbed light can create an electric field around their surface named surface plasmon resonance (SPR). Gold NRs in particular contain two well-differentiated SPR bands corresponding to their width (transversal SPR, TSPR) and length (longitudinal SPR, LSPR). While the first band is usually located in the visible range (just above 500

nm), the LSPR band varies depending on the NRs aspect ratio (length divided by width) and can range between 600 nm and 1800 nm (Figure 3).
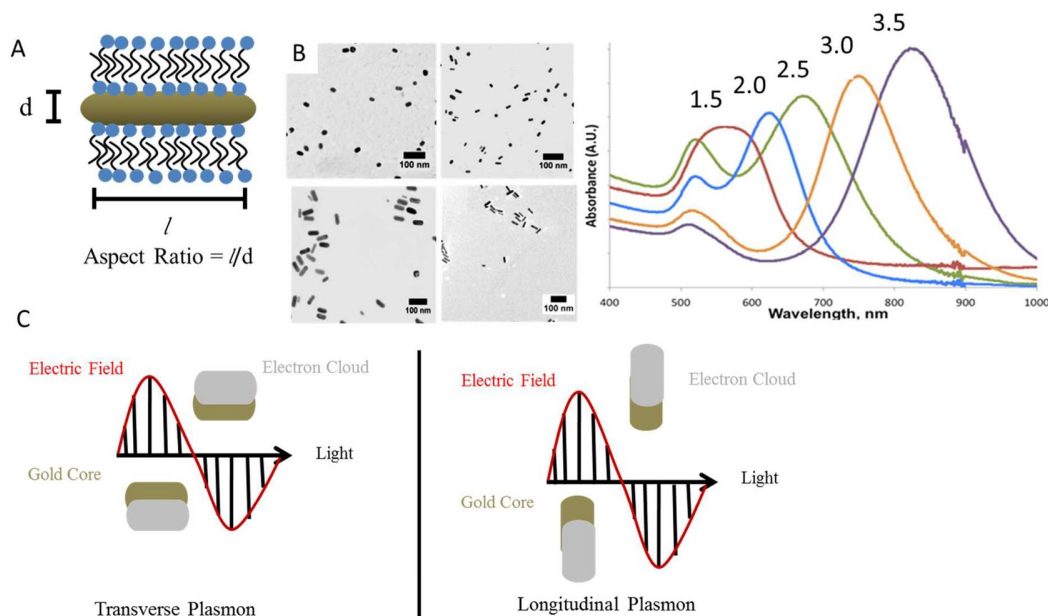
Figure 3. Gold nanrods optical properties depending on their aspect ratio. A) Aspect ratio is the relation between length and width; B) Transmission electron microscopy (TEM) images and UV-Vis-NIR spectra of different NRs varying the aspect ratio (scale bar are 100 nm) and C) Schematic representation of longitudinal and transversal plasmon resonance bands of nanorods. Adapted from reference 12.

Three main methods are employed in order to produce gold nanorods: the template method, electrochemical methods and seed-mediated growth method. Although in the actuality this last method is the most commonly used, in here a summary of each of them is included.

Template method

Firstly introduced by Martin and co-workers, the template method consist on the deposition of gold into nanoporus of polycarbonate or alumina template membranes.[13,14] Briefly, a conductive film (usually Ag or Cu) is placed over the template in which the gold will be electrodeposited within the nanopores. Then, both templates (the film and the membrane) are dissolved in presence of a stabilizer. Finally, rods are dispersed either in water or organic solvent by sonication (Figure 4).
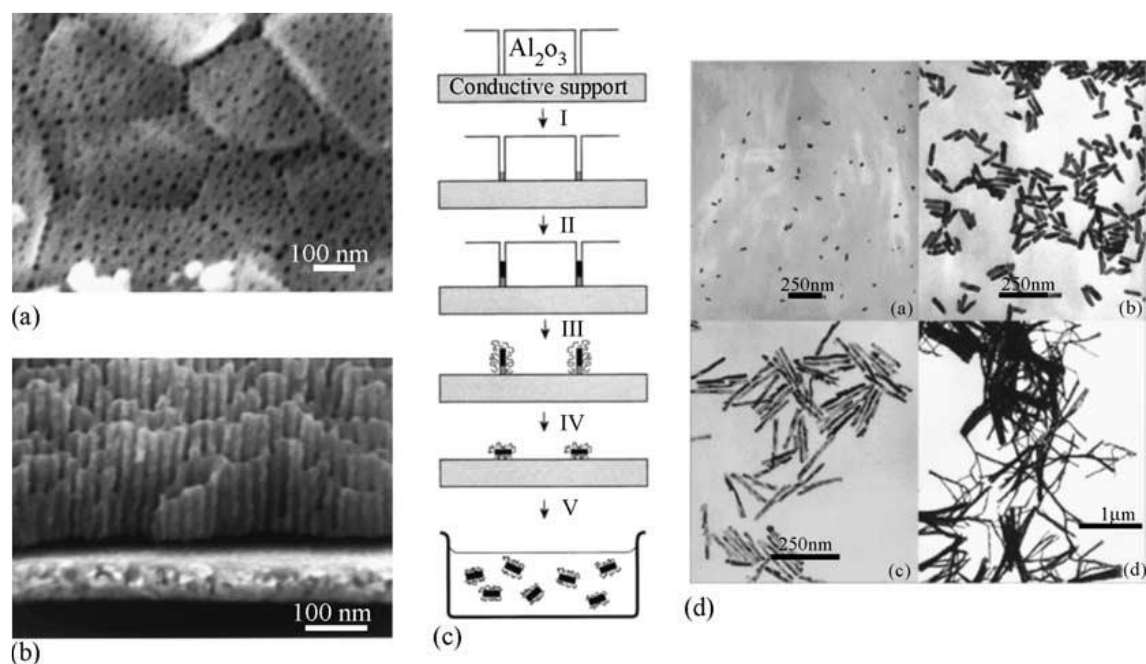
Figure 4. a) and b) Alumina membrane observed by Field Emission Gun Scanning Electron Microscopy (FEG–SEM) images; c) Schematic representation of gold NRs formation via the template method; d) Nanorods obtained by template methods and observed by TEM micrographs. Adapted from reference 15.

This method has the advantage of synthesizing Au NRs with different diameters by controlling the pore diameter from the template. However, the method also present some disadvantages such as control of rods length showing sample polydispersity.[16] Additionally, gold is deposited into the pores which contain some imperfections, thus leading to surface irregularities and therefore broadening the LSPR. This problem can be overcome by controlling the Au deposition time.[17] But undoubtedly, the main limitation is the rod yield obtained by this methodology owing to the fact that only monolayers are prepared at once. Recently, an improved template method for nanorods growth was developed using silica nanotubes as template.[18] In this case, gold rods are deposited into the inner part of silica nanotubes, which can be synthesized at gram scale.

Electrochemical methods

In the late 1990s, Wang and co-workers developed an electrochemical approach to synthesize gold nanorods in a high yield.[19] This method takes place into an electrochemical cell by using two electrodes. A gold plate was used as anode and a platinum plate as cathode as shown in Figure 5. Both electrodes were immersed in a solution containing a mixed surfactant system of hexadecyltrimethylammonium bromide (CTAB) and tetradodecylammonium bromide (TCAB). These surfactants were selected

for their ability to form cylindrical micelles thus directing the gold atoms to a rod shape particle. In addition, CTAB served as stabilizer to prevent further rods aggregation. The presence of a silver plate, producing silver ions in the solution, lead to an increase in rod length and yield.[20] Finally, rods were separated from the cathode by ultrasonication.
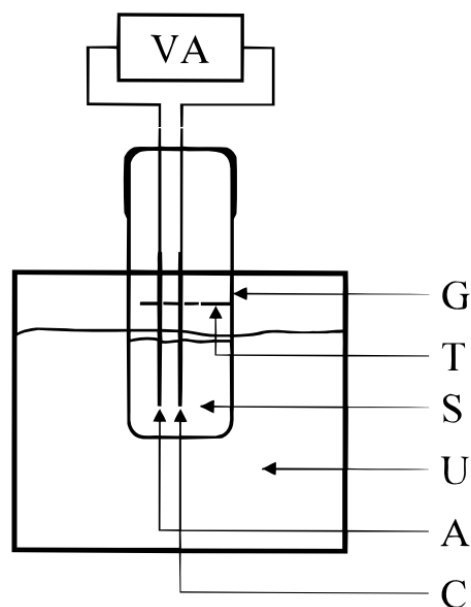
Figure 5. Schematic diagram of the setup for Au nanorods preparation. The electrochemical system contains: VA, power supply; G, glassware electrochemical cell; T, Teflon spacer and the electrode holder; S, electrolytic solution; U, ultrasonic cleaner; A, anode (Au); C, cathode (Pt). Adapted from reference 20.

By this methodology, the rods aspect ratio was ranged from 1 to 7 and the higher longitudinal SPR band was obtained up to 1064 nm. The mechanism of rods formation, as well as the paper of silver ions in the solution, are still unknown. However, it is hypothesized that the gold plate can release ions in the form of $AuBr^-$ which are complexed by the surfactant micelles and migrated to the cathode, where gold ions are reduced to gold atoms and finally form the rod shape.[4]

Seed-mediated growth method

The seed-mediated growth is the most common method and popular technique used due its great advantages over the other techniques, such as simplicity of the procedure, ease of particle size control or high nanorods quality and yield. On 1998, Natan and co-workers synthesized spherical gold particles in solution by using the seed growth method.[21] The approach was based on the reduction of Au^{3+} in solution by a weak reducing agent. Two years later, the same group improved the strategy by using sodium citrate as reductant.[22]

In that case, the monodispersity of the Au nanoparticles was improved obtaining diameters between 20 and 100 nm. Curiously, the authors found a subpopulation of god nanorods which comprised a 5 to10% of the sample.

Based on the same idea, Jana *et al.* studied the effect of various reducing agents on the growth of 12 nm gold nanoparticles stabilized with citrate.[23] These stabilized gold particles were the precursor of a three-step procedure, considered the starting point of the actual seed-mediated growth method, in order to produce gold nanorods (Figure 6).[24]

I. Synthesis of seed
2.5×10^{-4} M HAuCl$_4$ +
2.5×10^{-4} M Na-citrate

0.6 mL 0.1 M
Ice-cold aq NaBH$_4$

Gold nanoparticle seeds
(~ 4nm diameter)

II. Stock solution

Stock solution
2.5×10^{-4} M HAuCl$_4$
+ 0.1 M CTAB

Addition of
Ascorbic acid

Reduction
of Au^{3+} to
Au^{1+} results
in disappearance
of color

II. Three step protocol for nanorod synthesis

Step A
Add 1mL
of A

Step B

Step C

1 mL seed +
9 mL of stock
solution

1 mL A +
9 mL of stock
solution

10 mL B +
90 mL stock

Figure 6. Gold nanorods synthesized by the three-step seed-mediated growth method. The specific conditions shown here, lead to high-aspect ratio gold nanorods. Bottom right: TEM micrograph of gold nanorods (average of 500 nm long). Adapted from reference 25.

This three-step method provided high aspect ratio gold nanorods. However, the main drawback was the Au nanorods yield obtained after the synthesis (5% approximately, compared with other shapes). The long rods could be separated from the spheres and excess surfactant and concentrated by consecutive centrifugation cycles. A few years later, the same group reported an improved method to produce ~90% yield gold nanorods of high aspect ratio, just controlling the pH.[26]

Silver ions were crucial to control shape and length in electrochemical method, thus Murphy and co-workers introduced a small amount of silver nitrate in the three-step synthesis.[27] Shorter rods could be synthesized up to 50% yield. This last method was significantly improved by El-Sayed and co-workers who introduced CTAB-capped seed

rather than citrate-capped.[28] In addition, this seeds were relatively smaller (1.5 nm) than in the previous method. This two-step method produced high yield gold nanorods (up to 99%) with aspect ratios ranging from 1.5 to 4.5. The use of a second surfactant, benzyldimethylhexadecylammonium chloride (BDAC), allowed the synthesis of higher aspect ratio (up to 10) gold NRs. However, the level of byproducts was slightly higher than in the synthesis when the only surfactant was CTAB. In all the cases, the size, shape, monodispersity and yield are affected by several factors, such as temperature, pH, surfactant concentration or seed concentration.[25,29] Additionally, CTAB can contain some impurities which varies from batch to batch and suppliers. These impurities can considerably affect the NRs monodispersity, aspect ratio and yield.[30]

In 2005, Jana presented a one-step silver assisted seed-mediated method in which the seeds were prepared *in situ* directly on the growth solution by adding a small amount of sodium borohydride.[31] This new *seedless* method provided NRs with aspect ratio from 2 to 5 by controlling the amount of sodium borohydride added. In addition, rods had smaller dimensions (20 x 6 nm) compared to the previous two-step synthesis (60 x 12 nm) and they could be synthesized up to a gram scale. Later, El-Sayed and co-workers improved rods monodispersity of the seedless method by adjusting the pH.[32] The plasmon absorbance from these small nanorods was similar to the larger Au NRs but the main difference was that the scattered light was lower. This effect increases the light absorbed making them more effective for PT.

Nowadays, the seed-mediated method has been constantly modified in order to synthesize gold nanorods with high yield, different aspect ratios and low polydispersity.[33,34] However, the mechanism of Au NRs growth is still unclear. Recently, thanks to the new monitoring techniques, such as small angle X-ray scattering (SAXS) and liquid cell TEM a better idea on how the nanorods are formed is obtained.[35-37] As previously mentioned, many factor can affect the formation of rods but the most studied have been the effect of CTAB surfactant, the influence of bromide ions and the role of silver.[12,29] Three different mechanism to control the rods aspect ratio have been proposed: i) the capping effect of a complex formed by CTA^+-Br^--Ar^+; ii) the action of silver and bromide ions to alter the shape of CTAB micelles forming rod-like shapes, and iii) the deposition of a silver layer on the longitudinal surfaces of the Au NR (Figure 7).
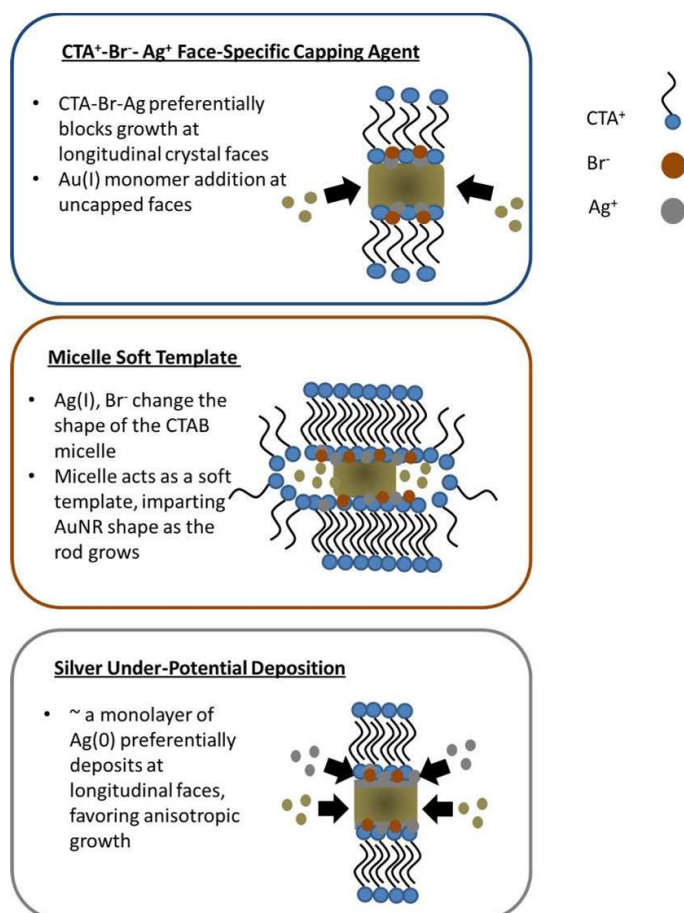
Figure 7. Three proposed mechanism affecting rod growth. Adaped from reference 12.

Many researchers have investigated the effect of silver on the rods growth and supported some of these three mechanism. In the first mechanism, CTA-silver-bromide complexes act as face-specific capping agents, thus forcing the rod-like growth. Niidome *et al.* suggested that CTA^+-Br^--Ar^+ complex was prepared in solution and showed that nanorods synthesis would proceed when this preformed complex was present.[38] In the second mechanism, some researchers have proposed that CTAB micelles can be altered, by the effect of silver and bromide ion, to adopt rod-like shape and consequently, the micelles act as soft templates to direct AuNR growth.[31] In the last mechanism, it is proposed that silver can be partially reduced forming submonolayers at specific rods faces. This effect is energetically favorable on longitudinal faces forcing the particles to an anisotropic growth.[39]

As previously mentioned, rods are densely capped by CTAB molecules after the synthesis. Many researchers have demonstrated the high cell cytotoxicity provided by CTAB-capped gold NRs.[40] In 2009, Alkilany *et al.* demonstrated that the toxicity was produced by the free CTAB which is desorbed from NRs surface.[41] This free CTAB is in constant equilibrium with the one adsorbed on the rods surface, therefore various strategies have been proposed in order to decrease this cytotoxicity.[42] The two common methods employed are the layer-by-layer assembly onto the rods surface and the direct replacement of CTAB. The first methodology alternate layers of polyelectrolytes which are adsorbed onto the positively charged CTAB bilayer.[43] Although this method can efficiently mask the CTAB molecules and is easy to prepare, the main risk can be particle aggregation or polyelectrolyte leaching. Therefore, researchers have focused on developing strategies for completely remove CTAB by direct replacement. Special attention have been paid on thiolated molecules because of their ability to form a semi-covalent bond with the Au surface. The most popular approach employed in this case is the one-step ligand exchange developed by Hostetler *et al.* for gold nanospheres.[44] Recently, Vigderman *et al.* employed this methodology in order to completely replace CTAB from rods surface.[45] A thiolated CTAB ((16-mercaptohexadecyl) trimethylammonium bromide, MTAB) was effectively incorporated on the rods surface by incubation 48 h. These MTAB-rods resulted to be non-toxic and were readily internalized into mammalian cancer cells. A novel advance in the ligand exchange method was recently developed by Kinnear *et al.* where a two-step approach is used to facilitate the incorporation of a thiolated PEG moiety.[46] The use of PEG ligand confer biocompatibility and stability to the rods nanoparticles. In this experiment, the first step is the addition of PEG-SH in order to partially replace CTAB from rods surface. Then, complete incorporation of PEG-SH is achieved by a second step where an ethanolic solution of PEG-SH is added to the nanorods solution and incubated 24 h (Figure 8). In this study, residual CTAB was detected by ^{1}H-NMR, however, rods cytotoxicity was reduced compared to one-step ligand exchange strategy.
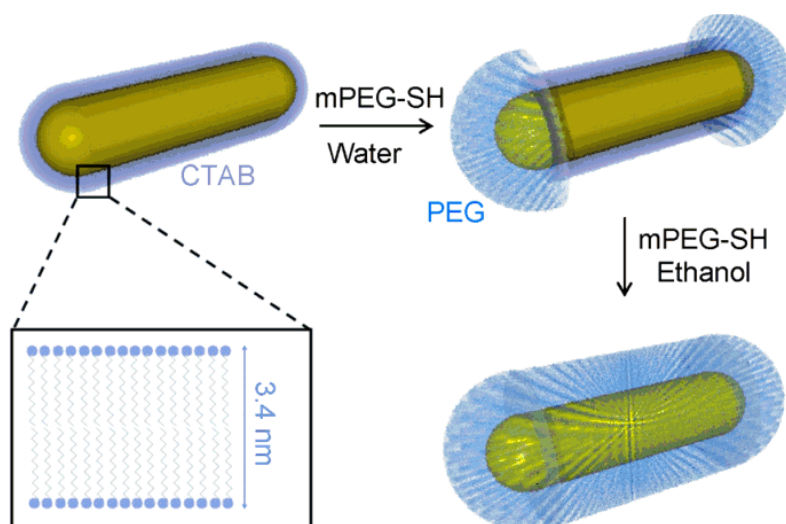
Figure 8. Schematic representation of CTAB replacement by PEG-SH in two-step ligand Exchange approach. Adapted from reference 46.

Many applications have been explored when using gold nanorods due to their great optical properties. Sensing methods, biological imaging and PT are three of the most studied areas.[47,48]

The sensing methods are mainly focused on variations of longitudinal SPR due to an external stimuli which can be employed as detector method. Gold NRs surface can be functionalized in order to capture biological molecules. This binding affects to LSPR reflecting a wavelength shift which can be detected.[49]

Gold nanorods have been widely studied as contrast agents for imaging due to their exceptional optical properties.[10,50] Dark field microscopy,[51] two-photon luminescence[52] or surface enhanced Raman scattering (SERS) spectroscopy[53] are some of the technique employed to detect Au NRs into living organisms.

PT is a well-studied non-invasive treatment in which specific light source, near infra-red in the case of gold nanorods, is administered and NRs can convert to heat increasing the temperature of the surrounding area. The particular shape of gold nanorods confer them an absorption and scattering coefficients that are higher than those for nanoshells and nanospheres.[54] El-Sayed and coworkers were the first in demonstrate the great potential of PT.[10] In that study, functionalized NRs were able to completely destroy cancer cells after NIR light irradiation. In addition, in order to improve NRs targeting and cell uptake, they can be further functionalized with peptides, proteins or even DNA and RNA.[55-58]

In this context, our main goal was focused on the synthesis, optimization and further surface modification of Au NRs in order to achieve a controlled endosomal release after laser irradiation. One of the bottlenecks after drug cell internalization is the endosomal release. In many cases, the efficacy of a drug is decreased because of the impossibility to escape from the endosome. Numerous drugs are degraded into the endosome/lysosome vesicles as a result of the low pH or the attack of lysosomal enzymes. In the last decade, many researchers have investigated different strategies such as pH-responsive polymers,[59,60] in order to overcome this problem. In the field of gold nanoparticles, recent advances have been performed in this direction.[61] For example, Song *et al.* have delivered siRNA into the cytosol by using gold nanoparticles capped with polyethylenimine (PEI) polymer.[62] In this case, gold nanoparticles are used as a vehicle to transport the RNA and the endosomal escape is achieved thanks to the PEI polymer. Tkachenko *et al.* were able to target the nucleus of HepG2 cells by the incorporation of various peptides on the gold nanoparticles surface.[63] More recently, Morales *et al.* have been able to transport the green fluorescent protein (GFP) into the cytosol by applying a femtosecond pulsed-laser to hollow gold nanoshells.[64]

Focusing in this last strategy, our efforts will be directed on application of specific laser intensities in order to achieve the desired endosomal release. Gold nanorods with a longitudinal SPR absorbance at 1000 nm were synthesized and characterized. This relatively high LSPR was selected taking into account the advantage of deeper tissue penetration achieved by the laser compared to lower wavelengths.[65] In addition, the absorbance of biological chromophores such as hemoglobin and melanin is lower at this wavelength. A minor problem can be the absorbance of water molecule which increases from 700 nm, but it has not a strong effect until 1100-1200 nm. Next step, was to replace CTAB molecule by PEG moieties and finally, a cell penetrating peptide (CPP) was attached to the PEG end creating the final NRs-PEG-CPP construct. In our case, the CPP selected was the D-form of octaarginine (r_8) (Figure 9).
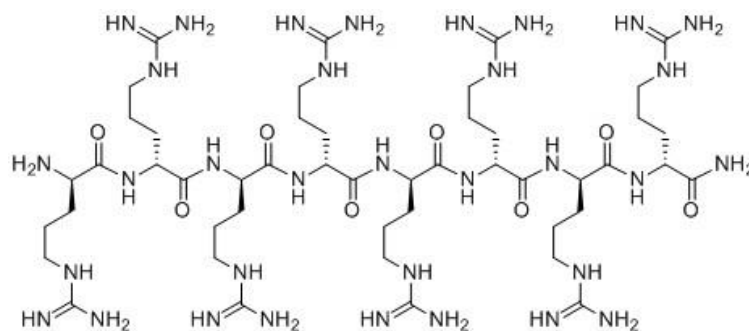
Figure 9. Chemical sequence of r_8 cell penetrating peptide.

  In order to visualize the rods internalization, a fluorescence dye was incorporated at the *N*-terminal of the CPP. Then, the toxicity of our final NR construct was assayed in different cell lines. After CTAB replacement, almost no signs of toxicity were observed, therefore internalization assays were performed. Finally and as preliminary results, RNA was electrostatically attached to the rods surface and served to us as an endosomal release reporter. We hypothesize that when NIR light is applied, the heat provided by Au NRs can disrupt the endosome, thus liberating the RNA. If RNA is able to cross the endosomal membrane, will affect the transduction of the protein selected and therefore we will observe this effect by western blot (WB). In here, we selected human PARP1 siRNA because of its potential related to cancer therapy.[66] PAR1 has a role of DNA repair and, by inhibiting its function, it is possible to prevent DNA repair from cancer cells being of special interest after application of other chemotherapy DNA-damaging agents. A schematic illustration of our main objective is represented in Figure 10.

NIR light
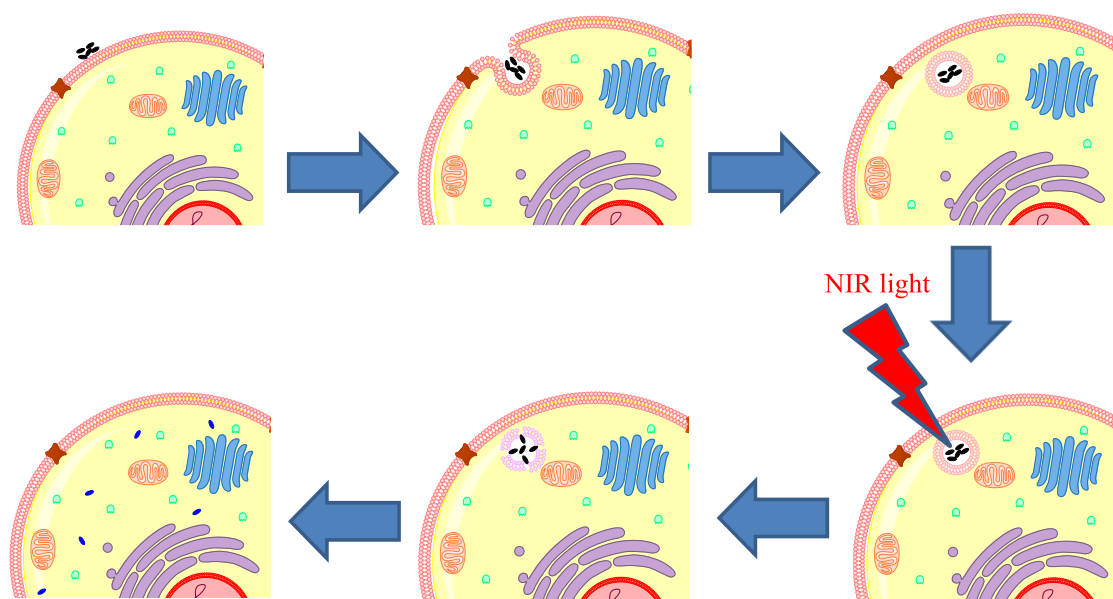
Figure 10. Schematic representation of gold nanorods as potential endosomal release enhancers.

The use of PLGA nanoparticles in gene therapy through the blood-brain barrier

Friedreich's ataxia (FRDA) is an autosomal recessive neurodegenerative disease[67] caused by mutations in the *X25* gene located on chromosome 9q13.[68] However, multiple tissues can be affected in the disease such as heart and pancreas.[69,70] The 98% of the mutations involves the expansion of guanine–adenine–adenine (GAA) trinucleotide situated in the first *X25* intron. This gene encodes a protein, frataxin (FXN), and this trinucleotide expansion causes a decrease in FXN levels in different cell types.[71] Not fully understood, these diminished levels only affect specific cell types, comprising selected neurons, cardiomyocytes and pancreatic islets. The main function of FXN is still under discussion but it has been observed a primary role on activation of iron-sulfur (Fe-S) cluster in mitochondria.[72] At this moment, many strategies are focused on the upregulation of FXN levels at the central nervous system (CNS) in which progressive degeneration leads to disease. These strategies are very versatile and include the use of small molecules, such as nicotinamide[73] and histone deacetylase inhibitor;[74] and large molecules such as transcription activator-like effectors.[75,76] Other strategies have also been explored such as direct protein replacement,[77] viral gene therapy[78,79] and RNA transcript therapy.[80]

In this thesis, the strategy selected in order to achieve higher expression of FXN protein was gene therapy using NPs as non-viral vectors. One of the most important factors to keep in mind is the development of a proper gene delivery system. With this aim, several viral and non-viral systems have been developed.[81,82] Although the viral systems are still preferred because of their long term expression, integrity, and stability; they are difficult to treat due to their toxicity and can cause possible immunogenic reactions. To overcome these problems, non-viral vectors, in special polymer-based carriers, have been developed. One of the polymers which has shown immense potential as delivery system is PLGA.[83] PLGA is one of the most popular biodegradable polymers because of its long clinical experience, the use of the polymer is approved by the US Food and Drug Administration (FDA) and European Medicine Agency (EMA). In addition, the polymer has favorable degradation characteristics (depending on the ratio of lactide to glycolide) and possibilities for sustained drug delivery. The polymer is commercially available with

different molecular weights and copolymer compositions because of its degradation depends on the molecular weight and copolymer ratio varying from weeks to years.[84]
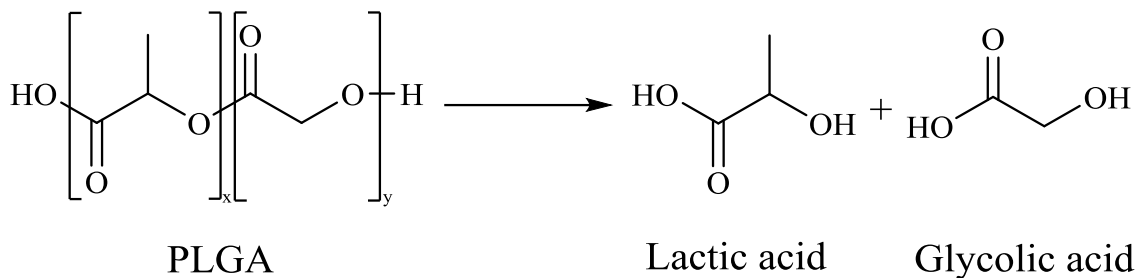
Figure 11. Hydrolysis of PLGA to its monomeric forms.

All these advantages make PLGA suitable to synthesize polymeric nanoparticles used as nanocarriers.[85] Despite of the great potential, there are some pitfalls related to PLGA-based nanoparticles such as poor drug loading (usually around 1%), high burst drug release and particle aggregation. The manufacturing cost and the scaling up are other limitation factors affecting the use of PLGA nanoparticles.

DNA can be either encapsulated into the polymeric matrix[86] or adsorbed on the nanoparticle surface by electrostatic interactions.[87] These nanoparticles are usually synthesized by the double emulsion (water-in-oil-in-water, W/O/W) technique.[88] In a typical procedure, PLGA is dissolved in organic solvent and emulsified with an aqueous phase containing a surfactant (typically polyvinyl alcohol, PVA) to obtain a primary water-in-oil emulsion. This primary emulsion is then added to an aqueous phase containing the same surfactant to finally obtain the W/O/W double emulsion. The main problem of this method is that employs sonication which can lead to nucleic acids degradation. Therefore, a milder formulation process is required. In this sense, modified nanoprecipitation method is used.[89] In brief, the nucleic acid and PLGA are dissolved in the organic phase and the mixture is then added dropwise to the aqueous solution containing the surfactant. Usually, the encapsulation efficiency of hydrophilic DNA into hydrophobic PLGA is low. However, it can be improved by using cationic polymers such as chitosan[90] or PEI[91] in order to complex the DNA. In addition, the cationic moieties can also promote cell internalization and endosomal escape. Even though the encapsulation efficiency can be higher than 80%, the DNA loading remains reasonably low, in the range of 0.1-1 % of the nanoparticle formulation.

In here, we focused our efforts on the encapsulation of FXN plasmid into different PLGA NPs formulations in order to promote DNA transport through the BBB. First, PLGA 50:50 (lactide:glycolide 50:50) and MW around 30000 Da was selected for particle formation because of its rapid degradation[92,93] time compared with other PGA/PLA ratios and MW. Then, the polymer was functionalized with either a CPP (r_8) for promoting nanoparticle internalization or a BBB-shuttle (THR retro-enantio, THRre), well studied by our group (Figure 12)[94] for increasing the transport of NPs through the BBB.
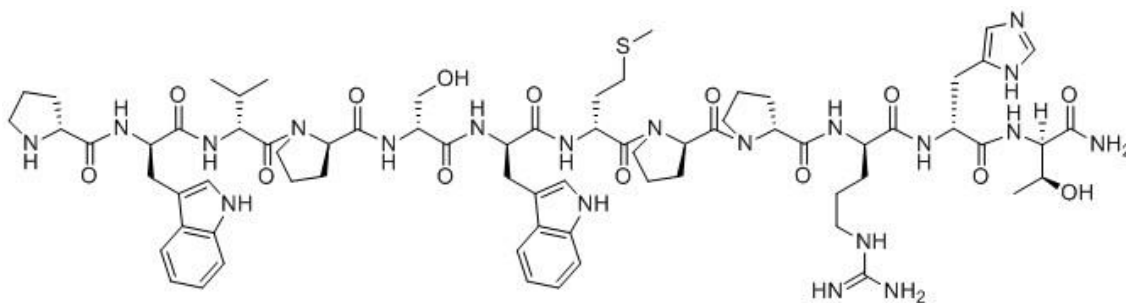
Figure 12. Chemical structure of THRre.

Modified nanoprecipitation method was used in order to synthesize modified PLGA NPs (Figure 13). Before the addition of the organic phase to the aqueous phase, DNA was complexed with a positively charged molecule (chitosan or PEI). In this regard, DNA encapsulation was enhanced. Transfectivity of various formulations was tested obtaining the best results with NPs containing branched PEI (bPEI). Finally, some preliminary formulations were assayed in a human cell based BBB model developed by Prof. Cecchelli.[95]
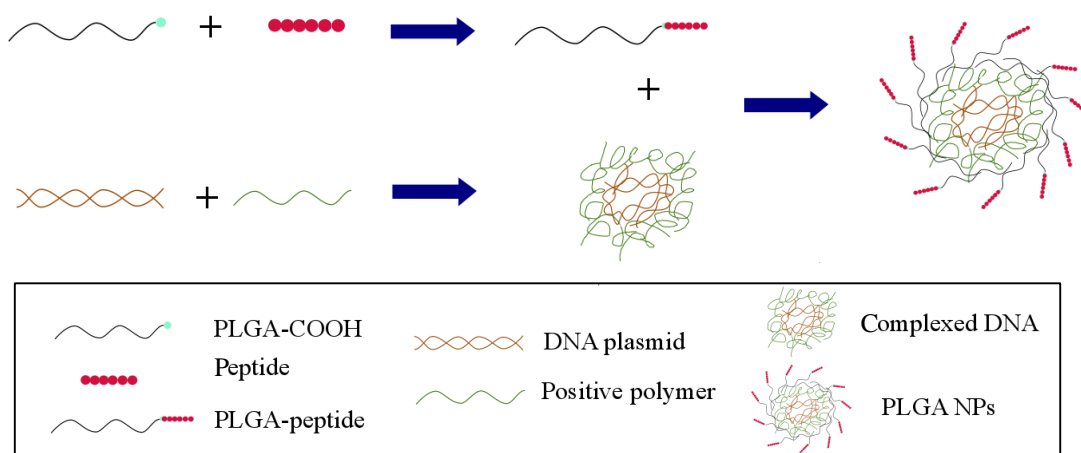
Figure 13. Schematic process of PLGA NPs encapsulating DNA/positive polymer complexes

The use of lipopeptides as intestinal permeation enhancers

During the last decades, the oral administration of proteins and peptides has been the aim of study of many research groups.[96,97] However, due to their instability on the GI tract and their poor bioavailability only a few formulations reached the market.[98] Nowadays, many strategies have been applied to overcome these drawbacks. Among them, the use of protease inhibitors,[99,100] specialized micro/nano formulations[101,102] or the use of intestinal permeation enhancers[103,104] intend to improve the delivery of various peptides and proteins through the intestinal barrier. Focusing in this last strategy, recently, the use of peptides acting as permeation enhancer has attracted much attention to facilitate the transport of biotherapeutics through the intestinal barrier.[105] High specificity towards their targets, low immunogenic response, ease of preparation, affordable price and scalability are some of the great advantages of using peptides as permeation enhancers. However, one of the main remaining limitations is the poor stability on the GI tract. Nowadays, this limitation is being solved by employing non-natural amino acids, cyclization or *N*-methylation methods.[106]

Peptides used as permeation enhancers can be divided into three main groups, namely transcellular absorption enhancers, paracellular enhancers via modulation of tight junctions (TJ) and targeted-mediated intestinal enhancers (Figure 14). The first group comprises peptides able to alter the plasma membrane, mainly CPPs, promoting the transport of the drug. The second group of peptides can transiently open the TJs, responsible for cell-cell adhesion, in a concerted manner. The last group includes all targeting peptides which recognize specific cell types or tissues and can modulate the transport of the compounds of interest.
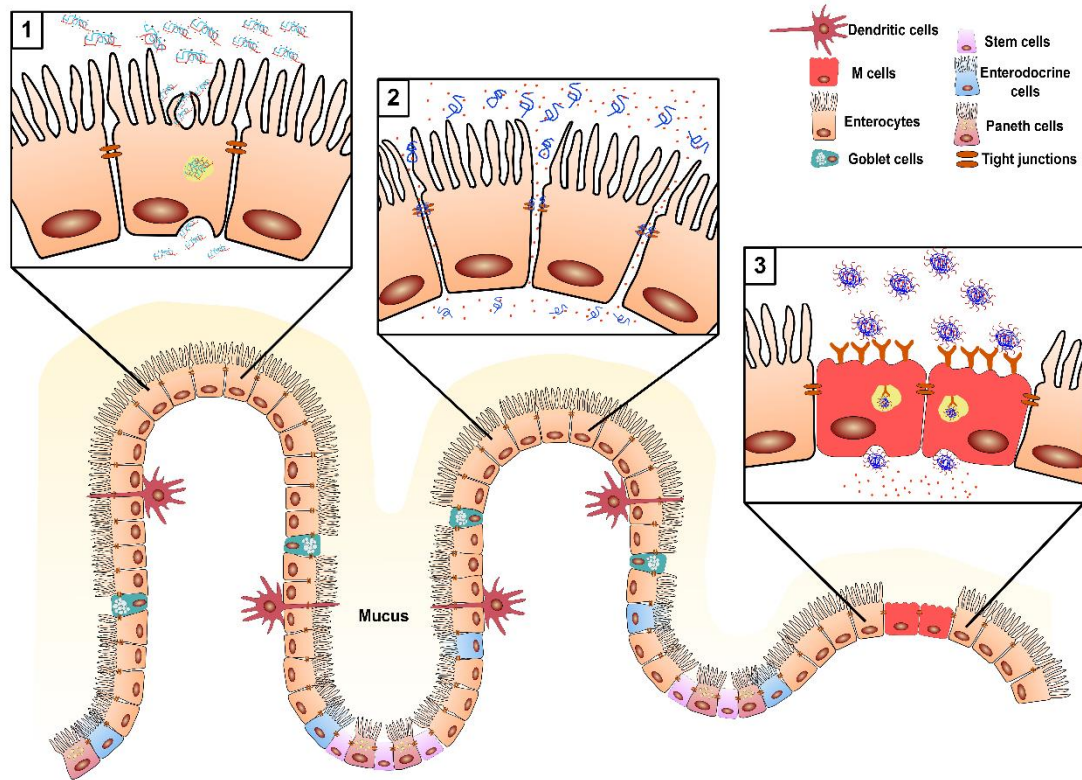
Figure 14. Schematic representation of the intestinal membrane and the different transport mechanisms displayed by: 1. Transcellular peptide enhancers; 2. Paracellular enhancers (TJs modulators); 3. Targeting peptides.

Based on their origin, CPPs have been described from various sources such as venoms,[107] virus[108] or rationally designed synthetic peptides.[109] After discovering the great potential of TAT peptide for delivering β-galactosidase to several tissues, including brain,[110] the use of CPPs in drug delivery systems has enormously increased.

CPPs can be formulated in various forms in order to promote transport of substances of interest. These formulations include covalent linkage to the biotherapeutics,[111] electrostatic interactions[112] or combination with nanoformulations.[113]

One of the first strategies used was a covalent construct of TAT peptide and insulin.[111] Trials on human epithelial colorectal adenocarcinoma cells (Caco-2) cellular model, the gold standard model to simulate the intestinal barrier, demonstrated that this formulation increased 6-8 fold the transport of insulin compared with insulin alone. Inspired on the translocation efficiency of TAT peptide, Futaki *et al.* designed a series of oligoarginine (R_n) peptides to prove their potential as CPPs.[109] In a later study, Kamei *et al.* covalently conjugated one of these polyarginine peptides (R_6) to leuprolide.[114] However, there was

not an improvement on leuprolide transport after *in situ* ileal administration. Finally, they concluded that in some cases covalent bound between the drug and R_n may hamper the ability of R_n to enhance intestinal permeation of therapeutic peptides and proteins.

The same authors used another strategy in order to evaluated 10 different CPPs. The aim of the study was to obtain the best candidate to increase the bioavailability of insulin and reducing the dose of CPP applied.[112] Peptides were either arginine-rich (*L*-R_8, *L*-R_{12}, HIV-1 TAT_{48-60}, HIV-1 Rev_{34-50}) or amphipathic (*L*-penetratin, *L*-pVEC, *L*-Erns, *L*-RRL helix, *L*-PRL4). In that case, the CPP were co-administered with insulin forming physical mixtures. Only *L*-penetratin, *L*-pVEC, and *L*-RRL helix had an enhancement effect of insulin after ileal loop administration in rats. Therefore, the *D*-form of these peptides were tested in order to compare stereoisomeric differences. In all three cases, the *L*-forms of the peptides had a greater enhancing effect than their *D*-counterparts. In addition, the *D*-form of R_8 (r_8) was also evaluated and was found to be more active than its *L*-form. The strongest enhancing effect was achieved by *L*-penetratin despite of its poor stability. The results suggested that fragments of penetratin increased the permeability of insulin across the ileal region of the intestine. In order to improve the enhancement effect of penetratin, rational peptide design led to *Penetramax* peptide.[115] This new peptide improved the intestinal absorption of insulin compared with the parent peptide.

In another study from the same group, r_8 was co-administered as physical mixtures with 16 different peptide drugs.[116] They found that the drugs with higher transport through *in situ* ileum loop were those containing negative charges. Drugs with neutral charge or positively charged were not able to cross the ileum membrane. The results demonstrated that binding affinity (electrostatic) between drugs and CPPs are crucial for intestinal drug absorption. Moreover, the binding ratio between insulin and r_8 was an important factor and by increasing the CPP bound ratio, they enhanced the intestinal insulin transport.

More sophisticated formulations have recently been developed to transport biotherapeutics through the intestinal tract.[117] Some of them use targeting peptides in order to direct their formulations to the specific cells, such as goblet cells, expressed along the intestinal tract.[113,118]

High specificity towards their targets, low toxicity or easy to prepare are some of the advantages peptides present as an alternative to small molecules in the field of penetration intestinal enhancers. In this chapter, the use of peptides as penetration enhancers, and

CPPs in particular, will be studied. These CPPs were modified with fatty acids which are reported as penetration enhancers.[119] Fatty acid based compounds are a great source of absorption enhancers. Despite of their potential, there are some limitations mainly related to their toxicity.[120] Sodium caprate (C_{10}) in particular, has been extensively studied for *in vitro* and *in vivo* studies.[121] This medium chain fatty acid (MCFA), as well as all their homologous (C_8, C_{12}, C_{14}, C_{16}, etc) produce cytotoxicity in a concentration and time dependent manner. Even so, C_{10} has been used in clinical trials.[122] Therefore, an adequate dose of these MCFAs can enhance the intestinal absorption of biotherapeutics by causing low cytotoxicity. Additionally, combined effect between TJ modulator peptides and MCFAs had higher effect on paracellular transport in which covalently bound C_{14} protected the TJ modulator peptide from degradation and aggregation.[123]

In here, we propose that the covalent union between CPPs and MCFAs can be used as new permeation enhancers. With this aim and during my 10 weeks stage in Prof. Brayden's group (University College of Dublin), Ussing chambers were used as a model to test the potential of new permeation enhancers (Figure 15).[124] This technique can be considered a step forward after *in vitro* cell models and it is a good model to study compounds before moving them to *in vivo* experiments. Compounds are tested in different intestinal regions from rats[125] and even human tissue can be adapted on the chamber for a more realistic assay.[126]
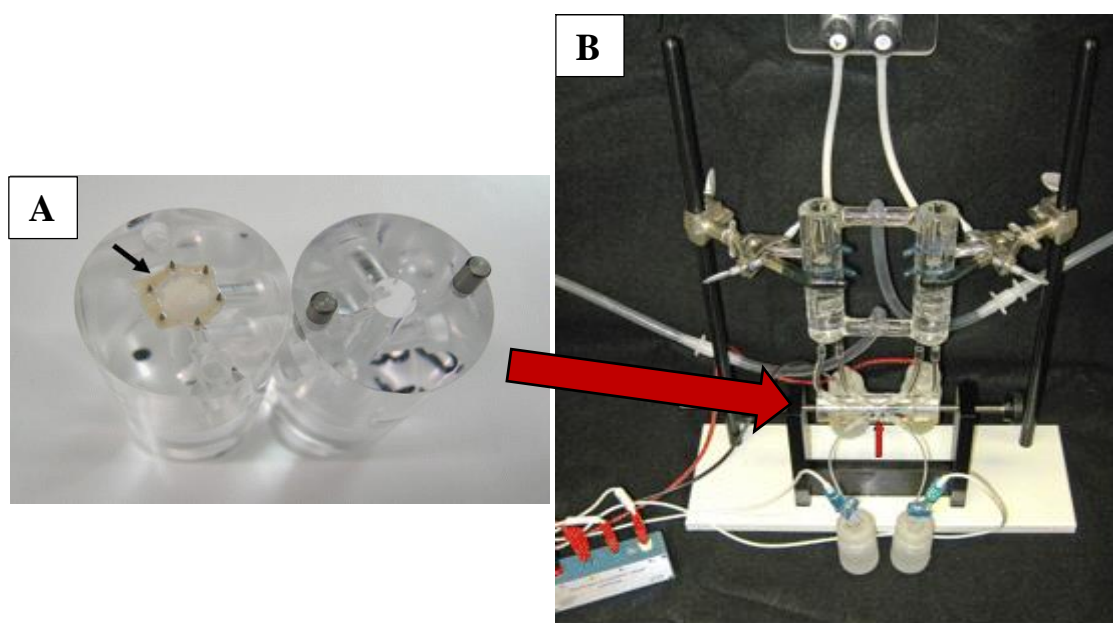
Figure 15. Ussing chambers design: A) tissue preparation (black arrow) mounted on half of an acrylic Ussing chamber. B) assembled apparatus with water-jacketed reservoirs, Ussing chamber (intestinal

preparation is mounted vertically; red arrow) and electrodes attached to voltage clamp head stage. Adapted from reference 124.

Less complexity is exhibited in the cellular model based on Caco-2 intestinal cells (Figure 16).[127] Cells are grown in an insert during at least 21 days and they are able to differentiate creating a monolayer and expressing similar morphological and functional characteristics of mature enterocytes. This cell differentiation has made the Caco-2 model one of the most widely used *in vitro* models used. In addition, cells are able to create tight junctions which its integrity can be controlled by measuring the transepithelial electrical resistance (TEER). More sophisticated cellular based models are used nowadays including HT29-MTX cells[128] which simulate goblet cells and are able to form a mucus layer. However, we selected Caco-2 model for its simplicity and similarity with the intestinal membrane.
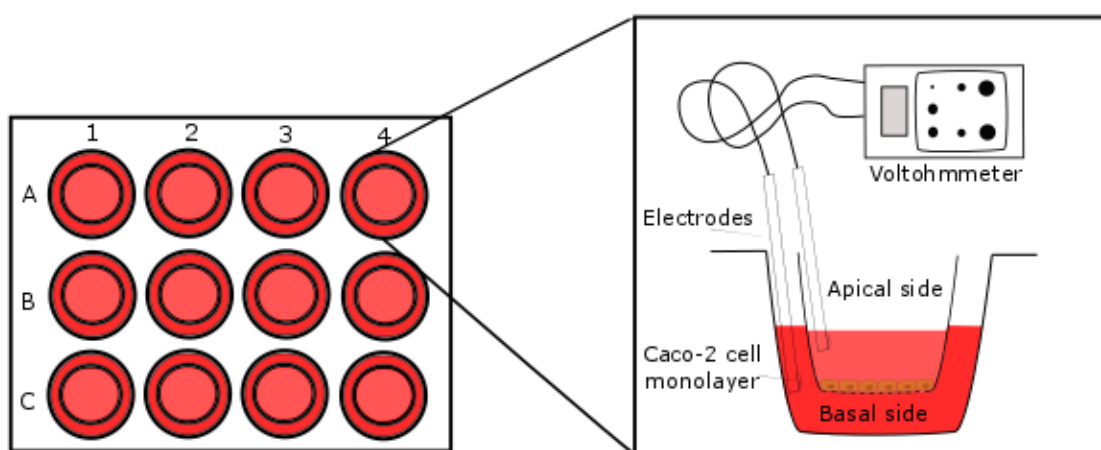
Figure 16. Schematic representation of Caco-2 cell assay. Inserts are placed into a 12 well-plate where Caco-2 cell monolayer is grown. Voltohmmeter is used to measure the membrane resistance.

For synthesizing our lipopeptides, the selected CPP (r_8) was manually synthesized by standard SPPS. Modifications on the *N*-terminal allowed us the introduction of lipophilic moieties on the CPP sequence obtaining two analogs (Figure 17): in the first analog, lauric acid was coupled to the CPP obtaining C_{12}-r_8. The second analog contained a cholesteryl moiety forming the Cho-r_8 peptide.
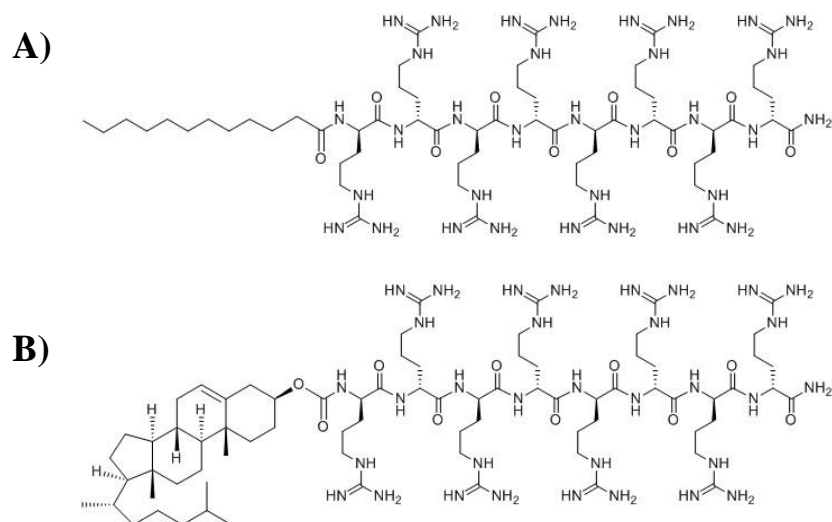
Figure 17. CPP analogs chemical structure: A) C_{12}-r_8 and B) Cho-r_8.

These CPP analogs were then assayed in Caco-2 and Ussing chambers to test their potential as permeation enhancers, compared with the parent peptide r_8. Then, physical mixtures were created by combining the CPP analogs with a fast acting insulin (provided by Sanofi). Insulin glulisine was selected as a drug model in order to increase its poor oral bioavailability. By comparing human insulin and this fast acting insulin, the difference remains on amino acids 3 and 29 from β-chain. In position 3, asparagine is substituted by lysine and in position 29, lysine is substituted by glutamic acid. These modifications confer to it a fast acting assimilation, therefore it can be directly used on the mealtime.

In addition, a new library of 9 lipopeptides analogs derived from C_{12}-r_8 and Cho-r_8 were synthesized and characterized (Figure 18).

D)

E)

F)

G)

H)

I)
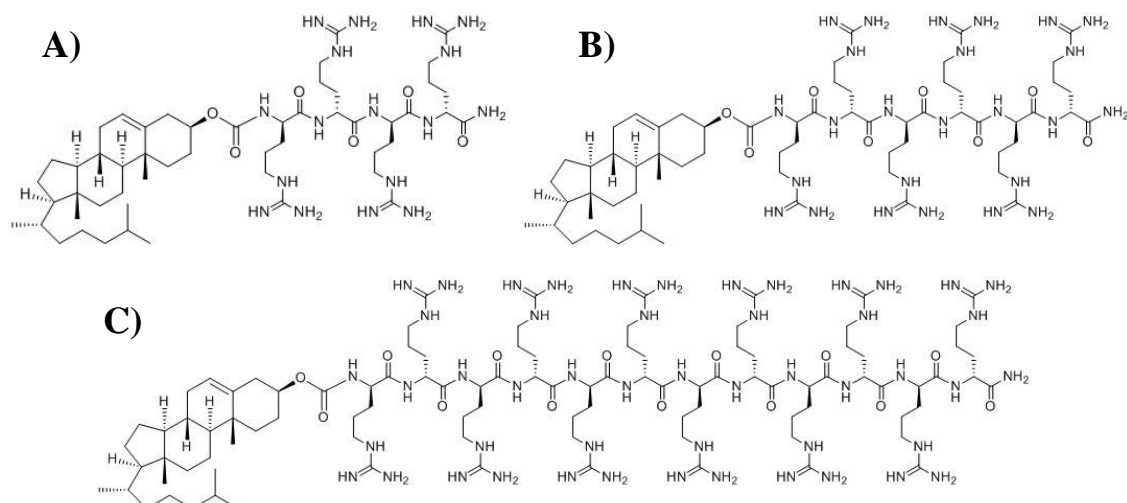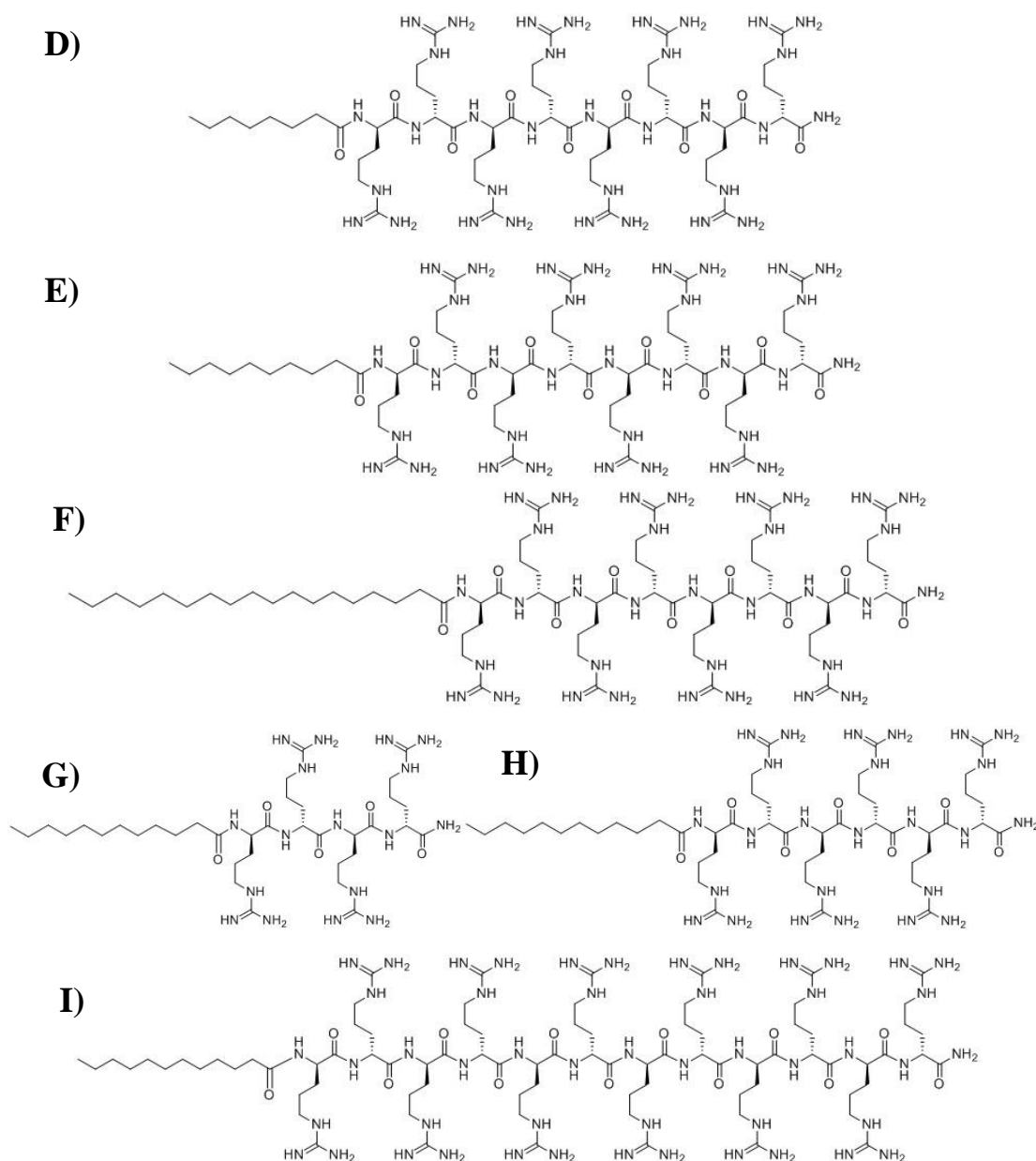
Figure 18. Modified lipopeptides library: A) Cho-r$_4$, B) Cho-r$_6$, C) Cho-r$_{12}$, D) C$_8$-r$_8$, E) C$_{10}$-r$_8$, F) C$_{18}$-r$_8$, G) C$_{12}$-r$_4$, H) C$_{12}$-r$_6$ and I) C$_{12}$-r$_{12}$.

The library was designed taking into consideration the length of both parts, the lipidic and the peptide. In the first case, the length of the MCFA was modified maintaining r$_8$ to obtain C$_8$-r$_8$, C$_{10}$-r$_8$, and C$_{18}$-r$_8$. In the second case, the fatty acid was maintained and the polyarginine length was modified obtaining C$_{12}$-r$_4$, C$_{12}$-r$_6$, and C$_{12}$-r$_{12}$. In the last case, cholesterol moiety was maintained and the polyarginine length was modified to finally obtain Cho-r$_4$, Cho-r$_6$, and Cho-r$_{12}$. As previously mentioned, the chain length of R$_n$ and C$_n$ is directly related to their ability as penetration enhancers. Therefore, these 9 compounds were synthesized and tested as physical mixtures with insulin on Caco-2 cell monolayer to improve the enhancement effect compared with the parent peptides.

26

Objectives

The objectives of this thesis are depicted below:

1) To synthesize and characterize gold nanorods in order to obtain a solution with high yield, homogeneity and reproducibility.

2) To functionalize gold nanorods surface to increase stability and confer to them the capacity to internalize into cells.

3) To assess modified nanorods cytotoxicity compared to CTAB-capped nanorods.

4) To evaluate the ability of cell internalization by using various rod formulations.

5) To detect endosomal release after specific laser irradiation over the cells containing internalized gold nanorods.

6) To successfully encapsulate DNA plasmid into PLGA nanoparticles with high encapsulation efficiency and low particles polydispersity.

7) To study the capability of PLGA nanoparticles to transfect various cell lines.

8) To modify the nanoparticles surfaces with a CPP and/or BBB-shuttle in order to improve transfection efficiency and BBB overpass in a BBB cell model.

9) To study the effect of the peptides as permeation enhancers on Caco-2 cell monolayers.

10) To study the effect of the peptides as permeation enhancers on Ussing chambers.

11) To evaluate the capability of the permeation enhancer peptides to increase transport of insulin, after physical mixtures formation, through Caco-2 cell monolayers and through colonic rat tissue placed on Ussing chambers.

Chapter 1

Functionalized gold nanorods as potential endosomal release enhancers

1.1. Results and Discussion

1.1.1. Gold nanorods synthesis and characterization

Gold NRs synthesis has been optimized in order to prepare them in a large windows of the spectra, ranging from 600 to 1100 nm obtaining a good yield and reproducibility. Since 2003, when El-Sayed's[28] and Murphy's[26] groups first synthesized true gold NRs by growth mediated method, many modifications on the synthesis have been performed.[29] In this chapter, several procedures were applied in order to optimize NRs synthesis. All the synthesis had the same basis but minor modifications were introduced in the growth solution in order to improve rods yield. These modifications affect the rods morphology leading to different length or width, as well as NRs yield and byproducts. The methods will be divided depending on the surfactants used in each synthesis.

1.1.1.1. Method 1 (LSPR peak near 800 nm, CTAB)

The first synthesis of gold nanorods was performed in collaboration with Dr. Marcelo Kogan from Universidad de Chile, who had optimized the synthesis obtaining high NRs yield and centering the LSPR peak near to 800 nm.[129] The synthesis contains minor modifications from the well-reported seed-mediated method.[26,28] For synthesis details see materials and methods. Characterization of these rods solutions was performed by UV-Vis-NIR spectroscopy and TEM. Figure 1.1 shows the characteristic double peak obtained from the rods synthesis. The transversal peak appears approximately at 520 nm and, in this case, the LSPR peak usually appears between 740 and 800 nm.

Figure 1.1. Characterization of gold nanorods synthesized by method 1: A) UV-Vis-IR spectrum. LSPR band maximum at 740 nm. B) Transmission electron micrograph. Scale bar 200 nm.

Deeper characterization was performed by TEM, where the rods can be clearly visualized (Figure 1.1 B). More than 200 particles were measured to obtain an average of 50.2 ± 6.8 nm in length and 13.2 ± 2.5 nm in width. The aspect ratio obtained in this method was 3.8. Around 1000 particles were counted and the yield of gold nanorods compared to byproducts was established as high as 85%.

Despite of the high yield obtained and the homogeneity of the sample, we decided to substitute this synthesis in order to get gold rods absorbing at higher wavelength. As explained before, the optimal NIR windows range from 700 to 1100 nm and one of the main advantages of irradiating at higher wavelengths is the possibility of deeper tissue penetration. Therefore, we decided to synthesize rods with a LSPR absorbing near 1000 nm.

1.1.1.2. Method 2 (LSPR peak higher than 850 nm, BDAC)

Based on the same seed solution, rods can grow until 1200 nm by introducing a second surfactant in the growth solution.[28] BDAC has a structure similar to CTAB and combined with it can lead to rod elongation. Figure 1.2 shows the characterization of this BDAC assisted synthesis.
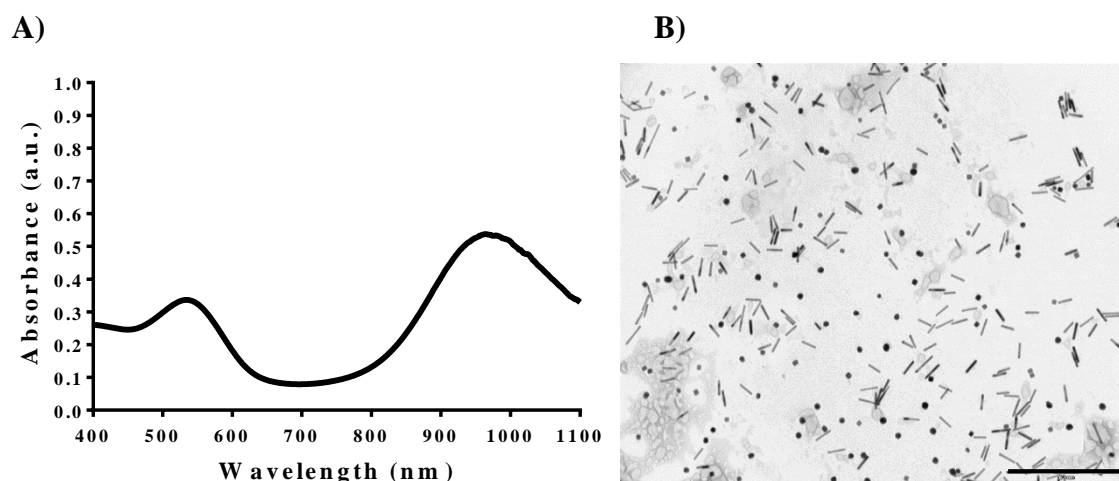
Figure 1.2. Characterization of gold nanorods synthesized by method 2: A) UV-Vis-IR spectrum. LSPR band maximum at 964 nm. B) Transmission electron micrograph. Scale bar 200 nm.

Comparing the spectrum of these NRs (Figure 1.2 A) with the previous one, the difference on the LSPR is clearly observed. Broadening of the peak was also observed meaning a more heterogeneous sample. This fact was corroborated by the TEM (Figure 1.2 B), where, additionally, the NRs yield was quantified giving a 66% in rods compared with byproducts. In this case, the dimension obtained from TEM were 57.1 ± 9.7 nm in length and 10.3 ± 1.4 nm in width reaching an aspect ratio of 5.5.

The high amount of byproducts forced us to take two different approaches: i) enrichment of NRs samples or ii) synthesis optimization. The first approach will be explained in section 1.2.3. Referring to the second approach, different surfactants were introduced on the growth solution.

1.1.1.3. Method 3 (LSPR peak near1000 nm, sodium oleate)

Sodium oleate has similar effect than CTAB and it is described that by combining both surfactants, homogeneous rods absorbing near 1000 nm can be synthesized.[34] When sodium oleate (combined with CTAB) was added to the growth solution, rods with high aspect ratio were obtained (Figure 1.3).

A)

B)
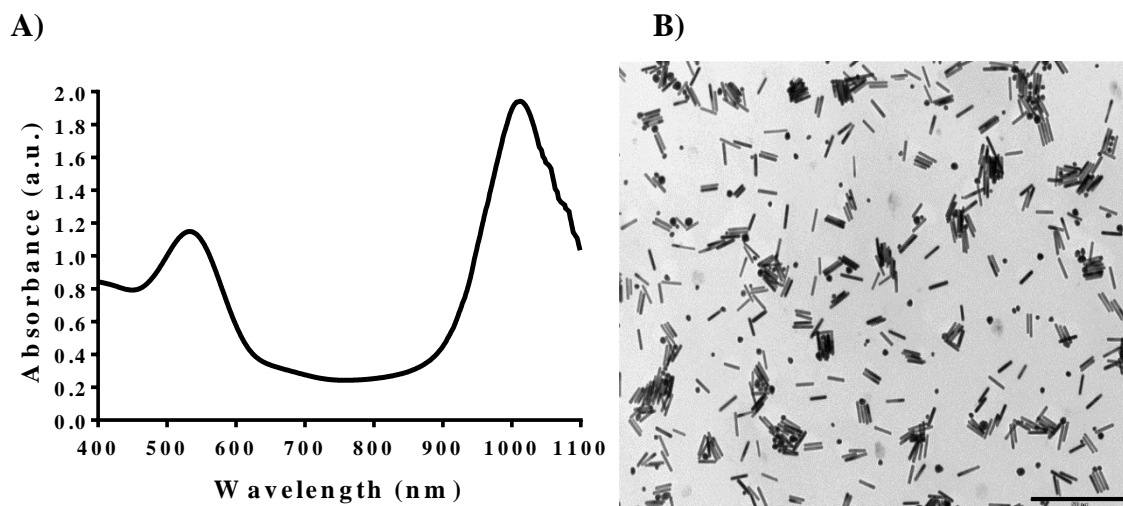
Figure 1.3. Characterization of gold nanorods synthesized by method 3: A) UV-Vis-IR spectrum. LSPR band maximum at 1011 nm. B) Transmission electron micrograph. Scale bar 500 nm.

The first difference observed in this synthesis was the narrowing of the peak (Figure 1.3 A). This higher homogeneity of the rods was further confirmed by TEM (Figure 1.3 B). In this synthesis, the yield was increased, from around 60% to 75% only by changing BDAC to sodium oleate. Larger rods were formed with this method obtaining a length of 95.73 ± 12.77 nm and width of 14.26 ± 2.43 nm. As the length was larger, the aspect ratio also increased, obtaining a value of 6.7.

Despite of higher homogeneity and rod yield, we considered these rod yield values still low for further experiments. Therefore, one last modification was introduced in the synthesis in order to optimize it.

1.1.1.4. Method 4 (LSPR peak near 1000nm, hydroquinone)

Hydroquinone was used instead of ascorbic acid as reducing agent in the growth solution.[33] CTAB was used as unique surfactant (there were no mixture of surfactants for obtaining rods with high aspect ratios) and NaOH was also added to the seed solution. These changes lead to an optimized formulation with high rod yield and homogeneity.
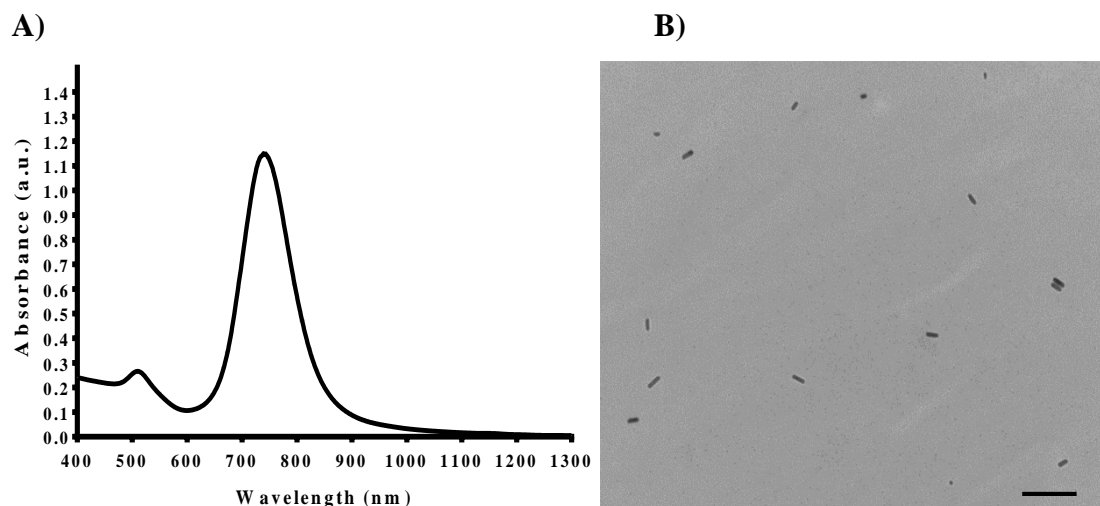
A)

B)
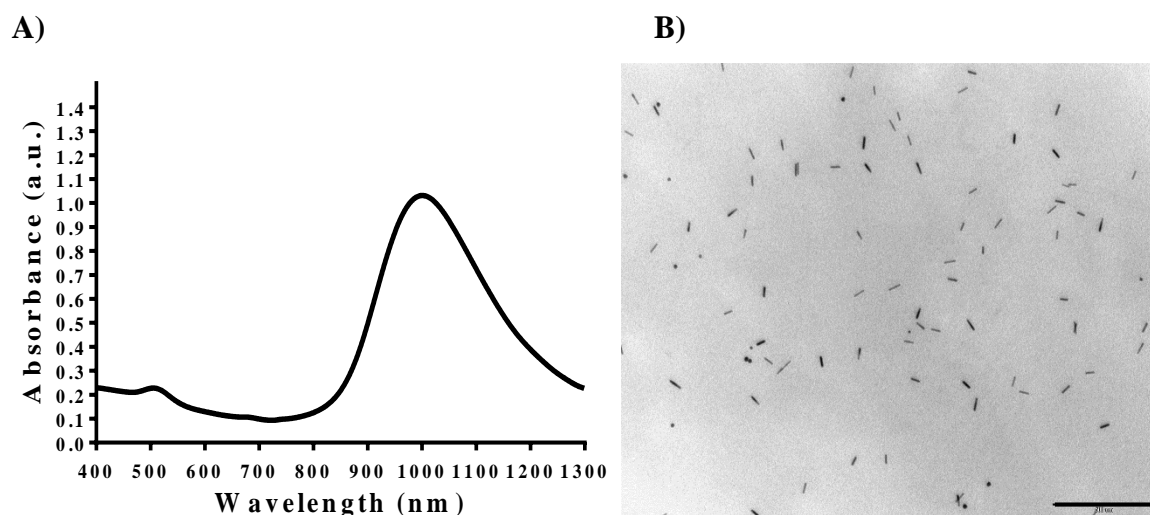
Figure 1.4. Characterization of gold nanorods synthesized by method 4: A) UV-Vis-IR Spectrum. LSPR band maximum at 1001 nm. B) Transmission electron micrograph. Scale bar 500 nm.

In the UV-Vis-NIR spectrum (Figure 1.4 A) we can observe the difference between the LSPR peak and the TSPR peak. This difference reach a ratio higher than 4 meaning a low amount of impurities in the synthesis. TEM micrograph (Figure 1.4 B) corroborated this assumption: the yield achieved values higher than 90% of rods compared to other byproducts. Similar to previous synthesis, the aspect ratio was 5.6 comprising a length value of 50.7 ± 7.7 nm and width of 9.0 ± 0.7 nm.

Table 1.1 summarizes the data obtained from the four different methods of rods synthesis. Details of all methods are described in the materials and methods section.

Table 1.1. Summary of rods characteristics after the synthesis. Absorbance value is attributed to LSPR peak. Length and width were the average measure of more than 200 particles. Yield was obtained after analyzing more than 500 nanoparticles.

Method	*length (nm)*	*width (nm)*	*aspect ratio*	*LSPR band (nm)*	*rods (%)*	*byproducts (%)*
M1	50.2 ± 6.8	13.2 ± 2.5	3.8	740	85	15
M2	57.1 ± 9.7	10.3 ± 1.4	5.5	964	66	34
M3	95.7 ± 12.8	14.3 ± 2.4	6.7	1011	75	25
M4	50.7 ± 7.7	9.0 ± 0.7	5.6	1001	93	7

Finally, after optimization, hydroquinone was crucial for obtaining rods with high aspect ratio in a high yield and homogeneous. This last method (M4) was selected for further cell experiments.

1.1.2. Theoretical rods concentration

Calculation of rods concentration can be challenging and more difficult when the synthesis is not optimized. A usual procedure to obtain gold NRs concentration comprises two steps:[130] first, rods dimensions are obtained by TEM micrographs. Then, the gold concentration is obtained by inductively coupled plasma mass spectrometry (ICP-MS) and finally the rods concentration can be calculated by applying the equation 1.

$$C_{NRs} = \frac{4 \cdot C_{Au}}{\rho_{Au} \cdot \pi \cdot W^2 \cdot L} \qquad \textbf{Equation 1.1}$$

where C_{Au} is the gold measured by ICP-MS, ρ_{Au} is the bulk gold atom density (59 atoms/nm^3), W is the NRs average width and L the NRs average length.

In here, we will explain an approximation taking into account that all the gold reacts in the synthesis (adapted from reference 131 and referred to M4 which was optimized).

First, nanoparticles were visualized by TEM and an average of their dimensions was calculated as (Figure 1.5):

D = 9.04±0.67 nm (r = 4.52 nm)

h = 4.04±0.61 nm

r = 4.52±0.34 nm

H = 42.62±6.54 nm

AuNR

H = 42.62±6.54 nm

h = 4.04±0.61 nm
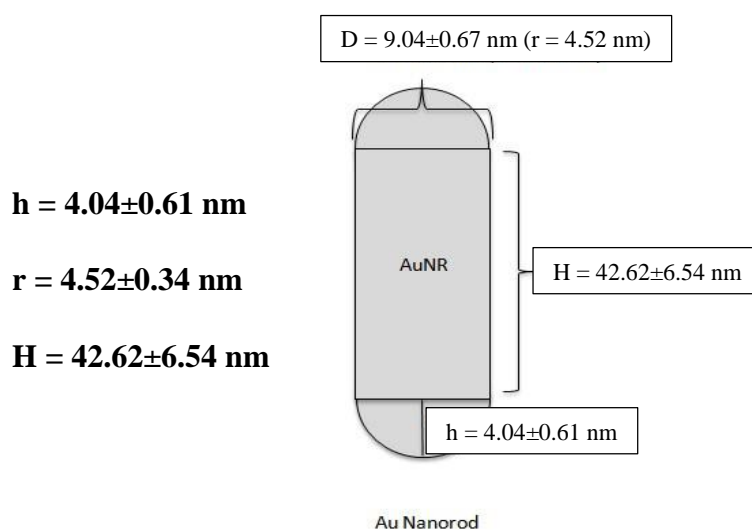
Au Nanorod

Figure 1.5. Gold nanorod dimensions obtained as an average of more than 200 nanoparticles visualized by TEM.

The molecular weight of $HAuCl_4$ is 339.79 g/mol. and the percentage of Au can be calculated as 0.5797. Then, the volume of one single rod was:

$$V_{cap} = \frac{\pi \cdot h \, (3 \cdot r^2 + h^2)}{6}$$

$$V_{cap} = \frac{\pi \cdot 4.04 \, (3 \cdot 4.52^2 + 4.04^2)}{6} = 164.18 \; nm^3$$

$$V_{cyl} = \pi \cdot r^2 \cdot H = 2.735 \cdot 10^3 \; nm^3$$

$$V_{NR} = 2V_{cap} + V_{cyl} = 3.064 \cdot 10^3 \; nm^3$$

The weight of Au in growth solution (Au added to the growth solution) was:

$$W_{Au} = 5.0765 \cdot 10^{-6} mol \cdot 339.97 \cdot 0.5797 = 1.0 \cdot 10^{-3} \; g$$

As the percentage of Au NRs in the samples obtained by M4 was 93.2% (average obtained from TEM micrographs), the final gold nanorods weight was:

$$W_{Au} = 9.32 \cdot 10^{-4} \; g$$

By knowing the volume of a single rods and the gold density (prefixed number), the weight of one single Au NR was calculated as:

$$W_{NR} = V_{NR} \cdot Density = 3.064x10^3 \cdot 19.32x10^{-21} \; g \cdot nm^{-3} = 5.92x10^{-17} g$$

The total number of rods in the final solution was calculated as:

$$N_{NR} = \frac{W_{Au}}{W_{NR}} = \frac{9.32x10^{-4}}{5.92x10^{-17}} = 1.58x10^{13}$$

As the solution contained 10.66 mL, 1 mL contains $1.48x10^{12}$ NRs. Finally, the NRs concentration was obtained as:

$$\boldsymbol{C_{NR}} = \frac{N_{NR \; per \; mL}}{N_A} x10^3 = \frac{1.48x10^{12}}{6.022x10^{23}} x \; 10^3 = 2.45x10^{-9} M = \boldsymbol{2.45 \; nM}$$

1.1.3. Separation of rods from impurities

As previously mentioned, before arriving to the optimized synthesis using hydroquinone (M4), different protocols to enrich the sample in rods content were attempted in M2 (CTAB/BDAC) and M3 (sodium oleate) synthesis.

The fastest and easiest way for separating rods from byproducts is simply centrifugation at specific speed.[132] NRs from M2 were centrifuged 30 min at 7700 rpm and two different pellets appeared. The main problem emerged when collecting both samples: the speed applied was not enough for maintaining the two pellets separated for long time. For this reason, when they were extracted from the tube, a small part of them was mixed and the perfect separation could not be achieved. Although the percentage of rods increased in the rods solution after separation, still a high amount of byproducts were present in the solution. Nanorods from M3 were also subjected to centrifugation process but this methodology did not succeed and still some spheres were also observed by TEM images (Figure 1.6). The centrifugation process was repeated in order to obtain a higher percentage of rods but rod concentration decreased in every centrifugation step. Therefore, this method was abandoned and other methods were tested.
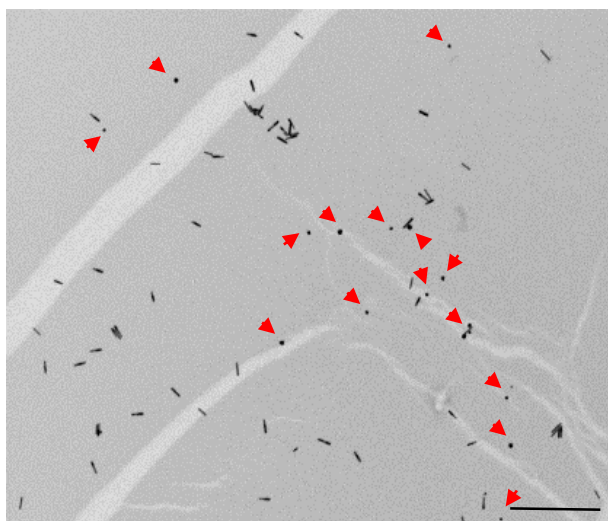
Figure 1.6. Transmission electron micrograph of rods synthesized by M3 after 30 min centrifugation at 7700 rpm. Byproducts are marked in red. Scale bar: 500nm.

Density gradients are used for separation by different sizes and shapes. In this context, two different gradient methods were tested. As a first trial, sucrose solutions at different concentrations were placed in a 2 mL Eppendorf tube.[133] From bottom to top 60%, 50%,

40%, 30% and 20% w/v of sucrose in water were added into the tube. 100 µL rods from M2 were placed on the top and centrifuged at 6000 rpm for 20 min (Figure 1.7 A). After centrifugation, a precipitate appeared attached to the tube walls. Centrifugation time was found to be crucial for rod aggregation at these conditions, so it was reduced until no signs of aggregation were observed. Longer times than 10 min resulted in the appearance of precipitates, therefore 10 min was set as maximum centrifugation time (Figure 1.7 B). Another important factor was the volume of each phase. The volumes ranged from 100 µL to 400 µL obtaining better separation at 200 µL. Finally, sucrose concentration was also varied and adjusted to our solution conditions. Rods were retained on the top phases so we eliminated the 60%, 50% and 40% w/v phases and increased the intervals between 30% and 20%. For that reason, the best conditions for separation of our rod solutions (this methodology was checked using M2 and M3 batches) were from bottom to top 30%, 27.5%, 25%, 22.5% and 20% w/v and 200 µL of each phase. Centrifugation speed was set at 4000 rpm during 10 min (Figure 1.7 C).

A)   **B)**   **C)**
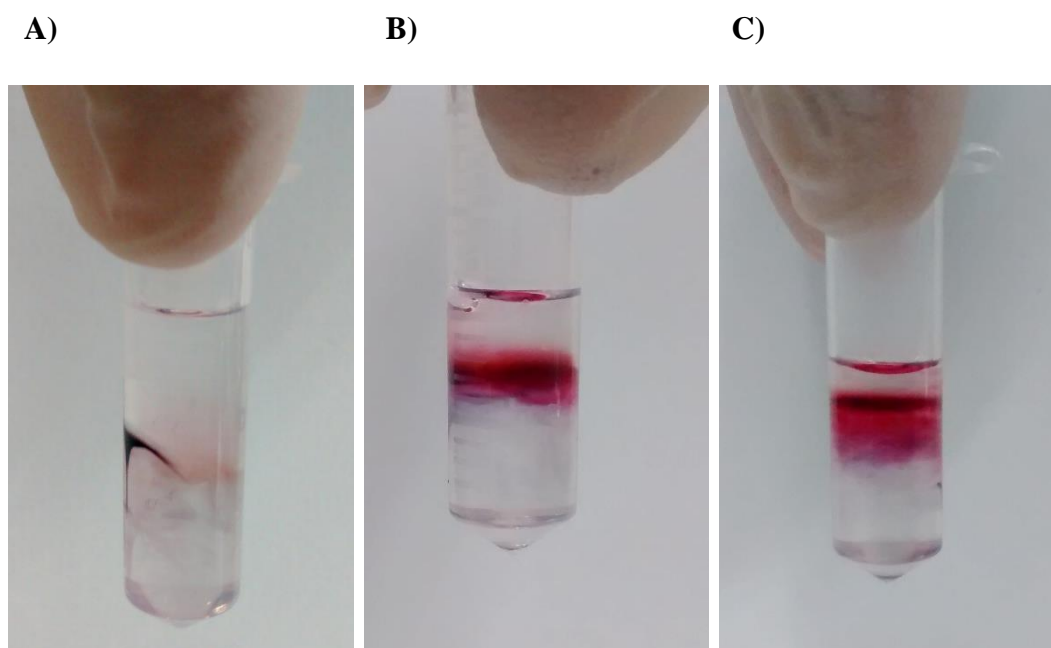
Figure 1.7. Separation of rods solution with sucrose gradient at different conditions: A) 60% (bottom), 50%, 40%, 30% and 20% w/v (top) centrifuged at 6000 rpm for 20 min; B) 60% (bottom), 50%, 40%, 30% and 20% w/v (top) centrifuged at 6000 rpm for 10 min and C) 30% (bottom), 27.5%, 25%, 22.5% and 20% w/v (top) centrifuged at 4000 rpm for 10 min.

Even though the conditions were improved, separation and recovery were complicated to achieve. After dilution of recovered samples on water or CTAB solution, some of the

rods solution precipitated. Consequently, this method was also discarded and other methods were tried.

Following the same strategy, ethylene glycol was used to obtain the different density gradients.[134] As previously mentioned, many parameters have to be optimized in every condition. In our case, volume of each phase, concentration, centrifugation time and speed were optimized. But also temperature had an effect in the distribution of the particles. When temperature control was applied to the centrifuge, a better separation was obtained. So, the best conditions we could obtain were: from bottom to top 80%, 70%, 60%, and 50% w/v and 300 µL of each phase. Centrifugation speed was set at 4000 rpm during 9 min at 20 ℃.

A)   **B)**
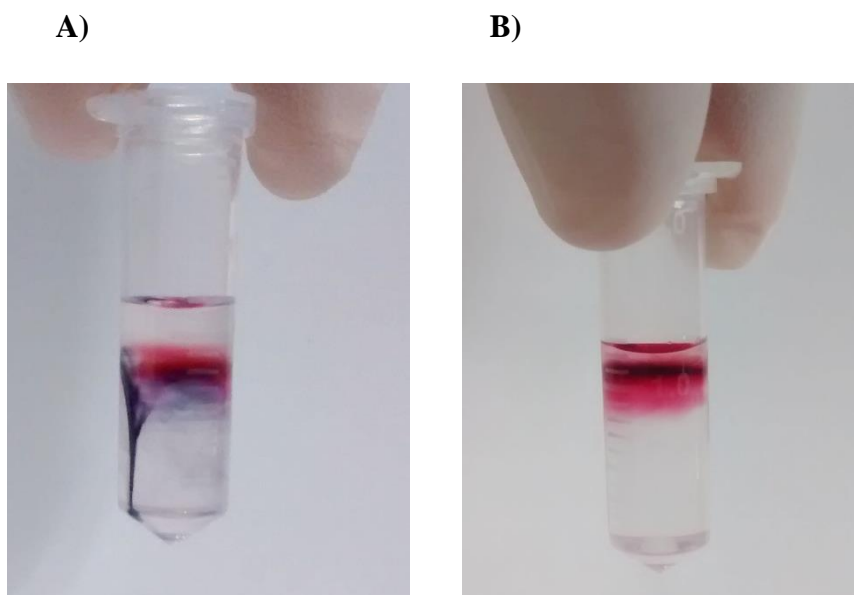
Figure 1.8. Separation of rods solution with ethylene glycol gradient at different conditions: A) 80% (bottom), 70%, 60% and 50% w/v (top) centrifuged at 10000 rpm for 20 min and B) 80% (bottom), 70%, 60% and 50% w/v (top) centrifuged at 4000 rpm for 9 min.

As shown in Figure 1.8, different bands were obtained. Again, the recovery process was complicated. In some cases, aggregation appeared when particles were resuspended. In addition, after recovery the nanorods phase, TEM images still showed some spheres in the solution. Accordingly, this method was also discarded.

Other technique for separating particles by shape is an aqueous three phase system composed by three compounds: Brij® 35 (26% w/v) (top), poly(2-ethyl-2-oxazoline) (PEOZ, 30% w/v) (middle) and Ficoll (35% w/v) (bottom).[135] In this method, rods were

maintained at the top, spheres were migrated to the middle phase and bigger shapes and aggregates were collected at the bottom. Again, centrifugation speed and time were adjusted to a better separation of our system. After optimization, separation could be observed using the following protocol: first, the three phases were added to an Eppendorf tube and stirred during 20 sec (400 µL Ficoll, 400 µL PEOZ and 200 µL Brij 35). Then, it was stirred at 4600 rpm during 5 min at 20ºC in order to settle every phase. Finally, rods were added and centrifuged 8 min at 13000 rpm and 20ºC (Figure 1.9 A). Recovered particles could be observed by TEM images in Figure 1.9. Although the enrichment in rods can be observed, TEM images revealed that there are still many spheres on the nanorods phase (Figure 1.9 B). Middle phase was also analyzed by TEM (Figure 1.9 C) and a huge amount of nanospheres could be observed. After this result, it was clear that the separation occurred. Therefore, we decided to repeat the process two times in order to enrich the rods content. Once more, the concentration of gold NRs in every recovery step decreased a lot. Consequently, this technique did not suit our needs and was abandoned.

A)   **B)**   **C)**
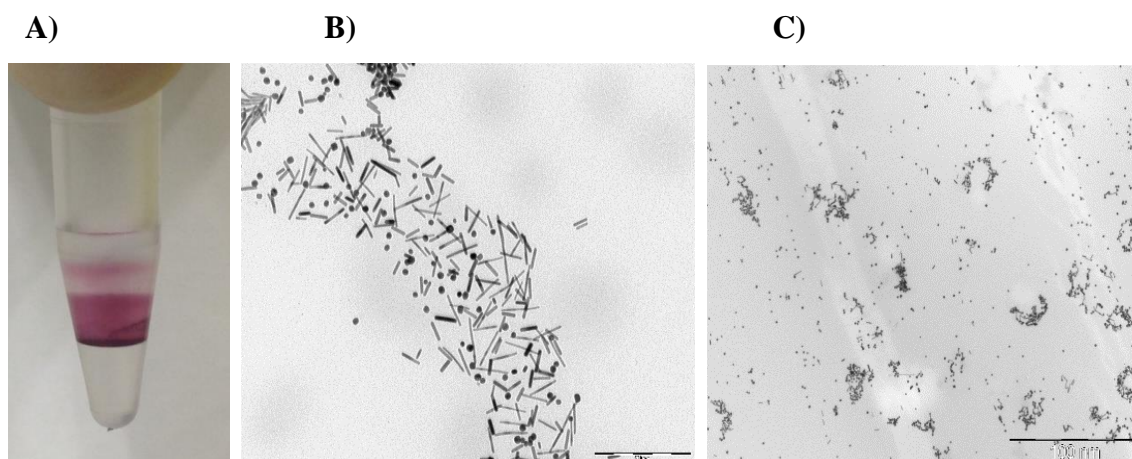
Figure 1.9. A) Separation of S2 rods solution by multiphase system after 8 min centrifugation at 13000 rpm; TEM images of particles recovered from B) the Brij 35 fraction and C) PEOZ fraction. Scale bar: B) 200 nm, C) 100 nm.

Agarose gel electrophoresis is other method used for rod separation.[136,137] Particles run through the gel depending on their superficial charges, therefore rod surface has to be modified. CTAB confers positive charges to rods surface but it is not covalently attached so, when a voltage is applied, the positive CTAB migrates to the negative electrode resulting in rods aggregation. In our case, two different linkers were attached to the rod surface via thiol group: 11-mercaptoundecanoic acid (MUA) and poly(ethylene glycol)

2-mercaptoethyl ether acetic acid (MW: 5000) (cPEG$_{5000}$). These linkers confer negative charges to the rods and theoretical stability when voltage is applied. After modification, rods were applied to 1% agarose gel in tris-acetate-EDTA (TAE) buffer. We could observe in Figure 1.10 that in both cases, rods got stuck and in the case of MUA modification (Figure 1.10A) the color changed; meaning rods precipitation.

A)   **B)**

Figure 1.10. Agarose gel electrophoresis of modified rods: A) rods modified with MUA and B) rods modified with cPEG$_{5000}$.

When conditions were optimized, faster separation in MUA than in cPEG$_{5000}$ modified rods was observed. For example, in a 0.7% agarose gel using tris-borate-EDTA (TBE) buffer, MUA rods could be distinguished from other shapes by applying 150 V during 30 min. Using the same set up, cPEG$_{5000}$ modified rods needed 60 min for separation. In both cases, rods were collected from gel as a unique band but agarose could not be dissolved and rods were not redispersed as a solution. Consequently, because of its tedious recovery, this technique was also discarded.

Finally, by putting effort in optimizing the synthetic methods seemed to be more fruitful than trying to improve the percentage of rods in the samples by purification. Therefore, the implementation of M4 method was perfect to obtain a high yield of gold NRs with high percentage of rods compared with other shapes. This synthesis was used in all the following experiments and no further purification process was required.

1.1.4. Gold nanorods surface functionalization

As a first approximation, rods with the LSPR peak at 800 nm (M1) were used. Lately, we moved to a higher wavelengths because of the advantages on the introduction. Therefore, some of the data presented corresponds to rods of λ_{max} near 800 nm.

Direct incorporation of CPPs to the rods surface was the first option to replace CTAB from NRs solution. Thiol groups from cysteine side chain allowed us to couple the peptide to the rod, so cysteine was incorporated into the peptide sequence (Figure 1.11). The main drawback is rods stability after CTAB replacement. Not all peptides confer stability to the gold nanorods so, when CTAB is partially removed from rods surface, they can aggregate and precipitate.

To check the versatility in front of different CPPs, sap(e) (a negative CPP well studied by our group)[138] was selected to be the first peptide used for rod functionalization. In addition, two well-known positive peptides (TAT and r$_8$) were also employed. Cysteine was incorporated at *N*-terminal of all three peptides as shown in Figure 1.11.

A)
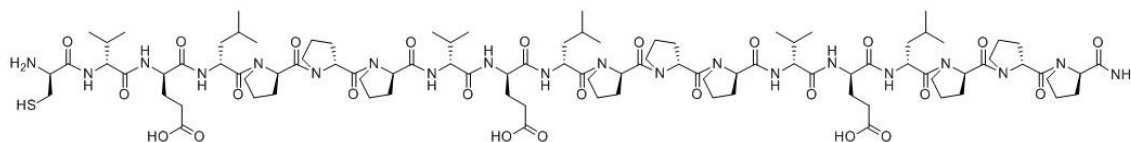
B)
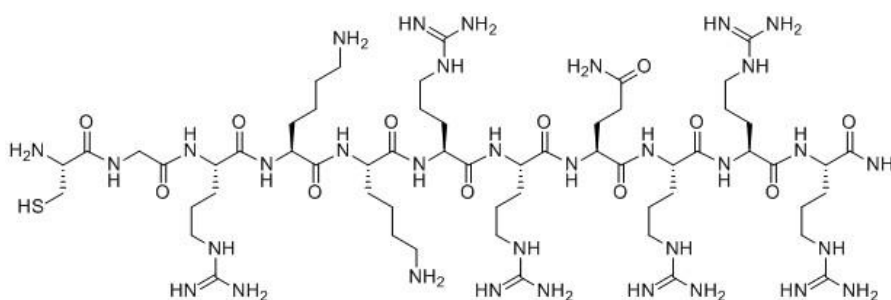
C)
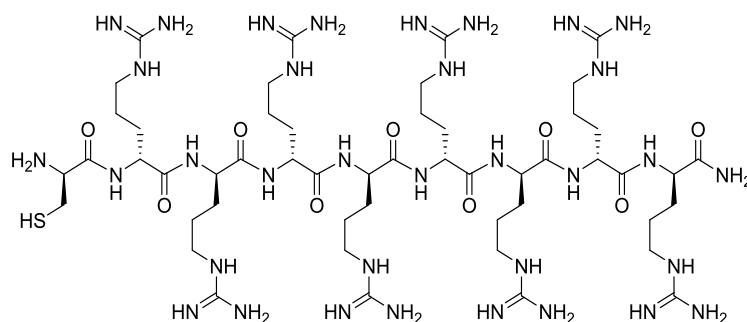
Figure 1.11. Chemical structure of A) csap(e), B) CTAT and C) cr$_8$. *L*-amino acids in capital letters and *D*-amino acids in small letters.

After addition of rod pellet to an aqueous solution containing csap(e), the color of the final solution changed from reddish to purplish. Purple is the typical color of aggregated rods so, after CTAB replacement from rods surface, the NRs seemed to aggregate. This process was further confirmed by spectrophotometry (Figure 1.12 A) presenting a flattered LSPR peak.

A)   **B)**
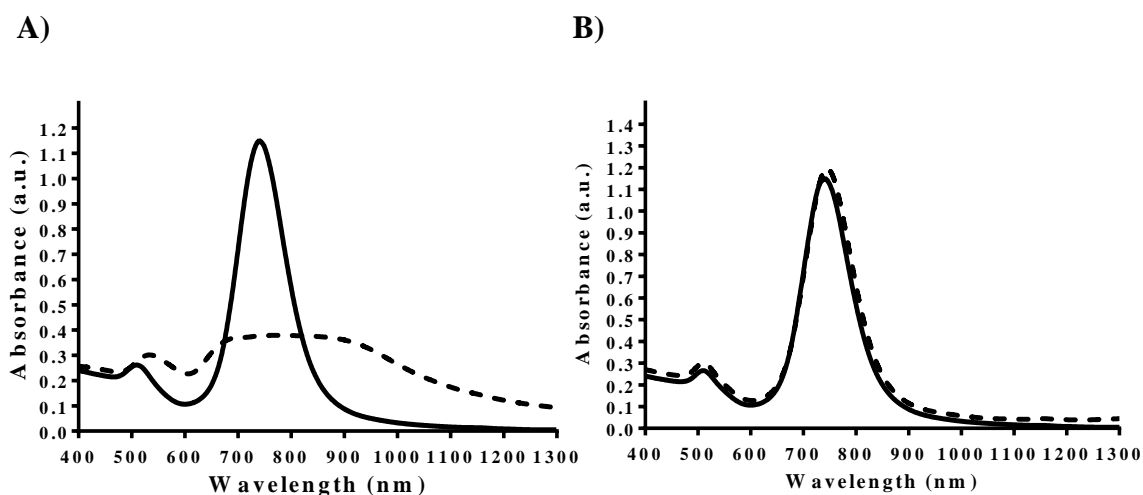
Figure 1.12. UV-Vis-IR spectrum of M1 gold nanorods freshly prepared (continuous line) and after A) csap(e) and B) cr$_8$ modification (dashed line).

Different csap(e) concentrations were added to the rods solution but in all of them, rods aggregation appeared. Either the partially removal of CTAB or the tendency of sap(e) to aggregate were hypothesized as responsible of rod aggregation. When CTAT was incorporated to the rods surface, the same effect as in csap(e) was observed. However, cr$_8$

could be attached to the rods surface and, as can be observed in Figure 1.12 B, minor shift on the spectrum was observed.

Although the incorporation of cr$_8$ to the rods surfaces resulted in a stable formulation, the incorporation of a linker between the rods and the peptides was proposed. Most of the times, thiolated molecules could not completely remove all CTAB from rods surface and only the ends are functionalized.[139] This fact can be responsible of rods aggregation as seen when csap(e) and CTAT were used. Therefore, a bifunctional linker was suggested to completely remove CTAB from rods surface and stabilize them in solution.

11-mercaptoundecanoic acid (MUA) was firstly proposed as a spacer for its simplicity and because it is well studied in bibliography.[11,140] The thiolated fatty acid chain can replace CTAB and the peptide can be more exposed from rods surface. In the first strategy,[11] MUA was successfully incorporated. Then, the carboxyl groups from MUA were activated with 1-(3-Dimethylaminopropyl)-3-ethylcarbodiimide (EDC) and *N*-Hydroxysuccinimide (NHS). But when the modified CPP (Figure 1.13) was coupled to the activated carboxyl groups, some aggregates appeared. After 3 washes for completely removal of the unreacted peptide, rods could not be resuspended since were aggregated.
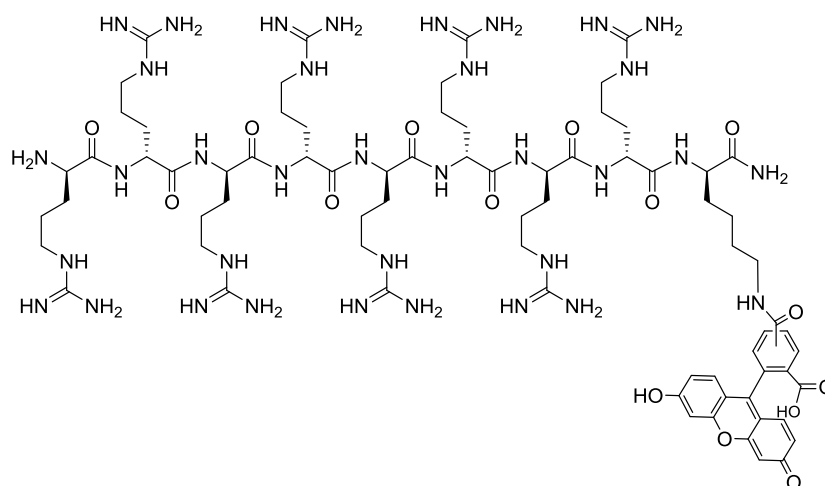
Figure 1.13. Chemical structure of r$_8$k(CF). The CPP contains a lysine at *C*-terminal to incorporate the fluorophore. Carboxyfluorescein (CF) is needed for *in vitro* cell experiments.

The second strategy used mercaptopolyethylene glycol monomethyl ether (MW: 5000) (mPEG$_{5000}$) in combination with MUA.[140] Same as in the previous strategy, when the

peptide was incorporated, aggregation was observed by naked eye. The incomplete elimination of CTAB from rods surface and the poor stability conferred by MUA are the possible causes of rod aggregation. The incorporation of mPEG$_{5000}$ was not enough to stabilize rods in solution, therefore the incorporation of MUA was abandoned.

The use of PEG improved significantly rods stability and dispersibility. In Figure 1.14 the same UV-Vis-NIR profile of freshly M1 rod solution and after mPEG$_{5000}$ modification can be observed. In this case, the synthesis used was M1. The slightly blue shift means mPEG$_{5000}$ incorporation to the rods surface.
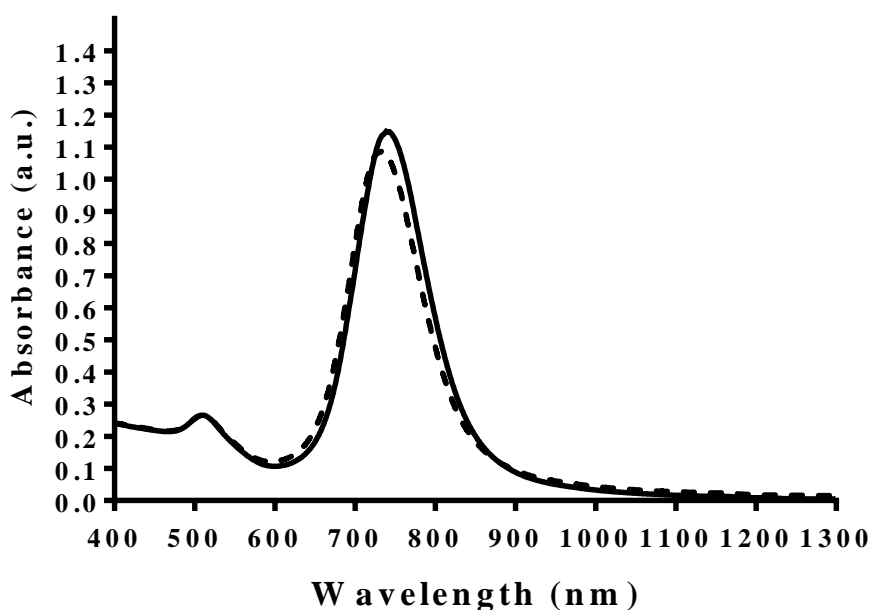
Figure 1.14. UV-Vis-IR spectrum of M1 gold nanorods freshly prepared (continuous line) and after mPEG$_{5000}$ modification (dashed line).

Once mPEG$_{5000}$ was attached, long term stability was tested at different conditions: 4ºC, room temperature (RT) and 37ºC. Then, rods were left at the temperatures previously mentioned during days and weeks. At least after 4 weeks, no significant differences on their spectra were observed from any of the samples.

NR-mPEG$_{5000}$ from M1 were only used for the preliminary laser irradiation assay which will be explained in section 1.2.4, but for further peptide incorporation, M4 rods with LSPR band near 1000 nm were used. Also, the methoxy group did not allow the

incorporation of any molecule. PEG was only conferring stability by replacing the CTAB from the surface.

As previously mentioned, heterobifunctional PEG was coupled to M4 rods surface for peptide incorporation. Thiol group is needed for PEG anchoring to rod surface and the second group used was a carboxyl group for further reaction with the amino *N*-terminal group of the peptide.

The incorporation of cPEG$_{5000}$ directly to the rod surface,[141,142] in our hands, resulted in rod aggregation, the same as MUA. The negative charges from carboxyl groups interacts with the positive charges from CTAB leading to rods precipitation. There were cases where the aggregates were not visible by naked eye but when the solutions were left undisturbed in an Eppendorf tube during 2 days, the aggregates were visible at the bottom of the tube.

A double step cPEG$_{5000}$ modification process was also tested with better results.[46] The use of ethanol in the second step is reported to solubilize better the CTAB and the number of cPEG$_{5000}$ incorporated was higher than in a single step. Then, the carboxyl groups were activated and r$_8$k(CF) peptide was incorporated following the same strategy than in MUA modification. In Figure 1.15 A, the shift after every incorporation step can be observed. In this case, rods could maintain the stability and further cell assays were performed with this formulation.

A)   B)
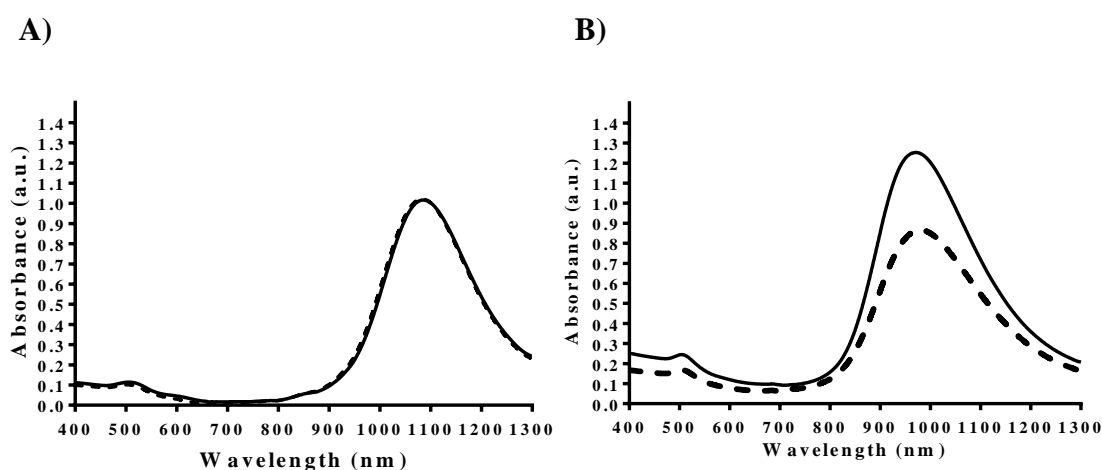
Figure 1.15. UV-Vis-IR spectrum of M4 gold nanorods freshly prepared (continuous line) and after A) double cPEG$_{5000}$/CPP and B) mPEG$_{5000}$-cPEG$_{5000}$/CPP modifications (dashed line).

Combination of mPEG$_{5000}$ with cPEG$_{5000}$ was also tried. The methoxy group confers stability to the rods and the carboxyl group allows peptide incorporation. Again, two steps were used in this methodology: first, mPEG$_{5000}$ was added and then, cPEG$_{5000}$. As in the previous method, carboxyl groups were activated and the fluorescent CPP incorporated. Shift on rods spectra are shown in Figure 1.15 B. Observing the spectra from both methods, the two characteristics bands can be perfectly identified. The shift observed after PEGylation is negligible meaning minor or no aggregation after modifications. Both formulations (double cPEG$_{5000}$ incorporation or mPEG$_{5000}$/cPEG$_{5000}$ incorporation) were selected for further cellular experiments.

1.1.5. Liposomes simulating endosomal release

Liposomes were used as a proof-of-concept for simulating endosomes. In this case, the pegylated rods obtained from M1 were employed. These NRs were modified only with mPEG$_{5000}$ and encapsulated into liposome, in combination with CF, emulating the case where rods are internalized by endocytosis. After formation, the excess of unencapsulated CF was separated from liposome by size exclusion chromatography (SEC) using a Sephadex G-75 column (for further details see materials and methods). Liposomes where collected and characterized by DLS obtaining 200±29 nm in size and 0.3 in polydispersity. They were further characterized by TEM (Figure 1.16). As shown in the images, only few rods are encapsulated into liposomes but still there are many unencapsulated. This is due to the purification process. Liposomes were separated from free CF by SEC, but rods were eluted almost at the same time. In our case, it is not an issue because we want to observe the effect when rods are irradiated and, in that case, the important point is rods proximity to liposomes. Also, from the images, we can observe liposomes with an irregular shape probably caused by the staining process. In all the cases, NRs were observe into or outside lipososome meaning that our samples contained both particles (NRs and liposomes). The detection of both particles was enough for further laser irradiation experiments.

Having the encapsulated rods in hand, stability assays were performed in order to check the release profile of the fluorophore from liposomes. When different CTAB solutions were added to liposomes containing CF, the dye was released proportional to the

concentration. Therefore, CTAB has to be completely removed from rods solutions in order to detect the effect from irradiated rods and not as side effect of CTAB. In this sense, mPEG$_{5000}$ was used for CTAB displacement.

A)   **B)**
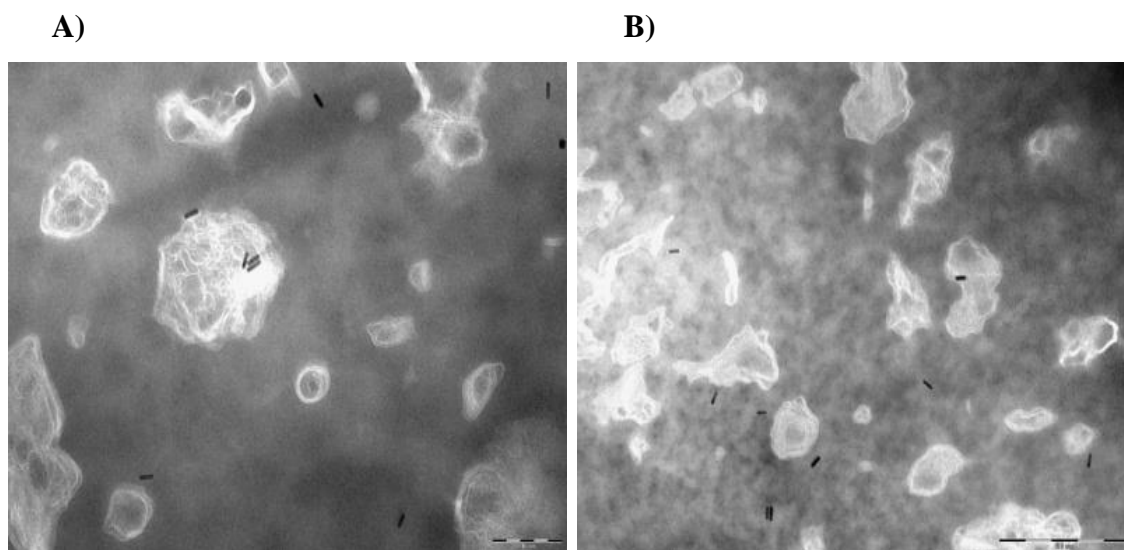
Figure 1.16. TEM images obtained with uranyl acetate staining of CF and rods encapsulated liposomes. Scale bar: 200nm (A) and 500nm (B).

Liposomes containing CF where stable for 5 days with minor release of the dye (Figure 1.17), at least. Three different scenarios in which CF was encapsulated where tested: liposomes alone, rods addition after liposomes formation and rods encapsulated into liposomes.
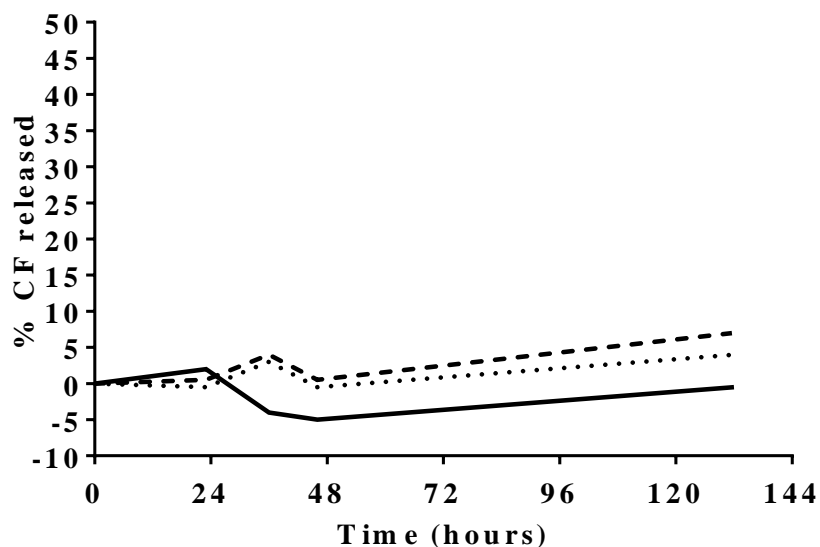
Figure 1.17. Release profile of CF from liposomes in: liposomes containing CF (continuous line), rods added to liposomes containing CF (dashed line) and rods and CF encapsulated into liposomes (dotted line).

The results show good stability in all the cases with no or minor release of CF during 5 days. From this data, we can assure the release when irradiation will be from NRs effect and not because liposomes instability caused by CTAB.

Then the effect of laser irradiation on liposome disruption was tested. After liposomes collection from the column, one droplet was placed in a microscope slide and a cover slide was placed on it to reduce the volume. Femtosecond pulsed laser was set at two photon mode and liposomes were irradiated. Two photons of λ=776 nm (after pegylation, M1 LPSR peak was 776 nm) were used as an excitation source with an output power intensity of approximately 1 W.

As previously mentioned, this experiment was performed as a proof-of-concept. The laser conditions were not the optimal, meaning that the spot size of the laser beam was in the range of μm. Consequently, the laser beam could not irradiate all the sample. A quick way to solve this problem was to set up the laser in scanning mode in order to irradiate a higher sample area.

Different laser intensities were used and fluorescence intensity (released from liposomes) increased when the power intensity increased (Figure 1.18). Then, all samples arrive to an intensity which remains constant during time. It can be probably due to spreading of CF to the surrounding areas. When higher intensity is applied, higher amount of CF is released at the beginning but then, the fluorescence is maintained. In the case of

100% laser intensity, a decrease in fluorescence intensity was observed, meaning that the fluorescence could be quenched by the laser power intensity.

With this work, the potential of NRs as endosomal scape enhancers have been proved. Nevertheless, these were only preliminary results and further *in vitro* experiments need to be performed in order to confirm the interest of this system.
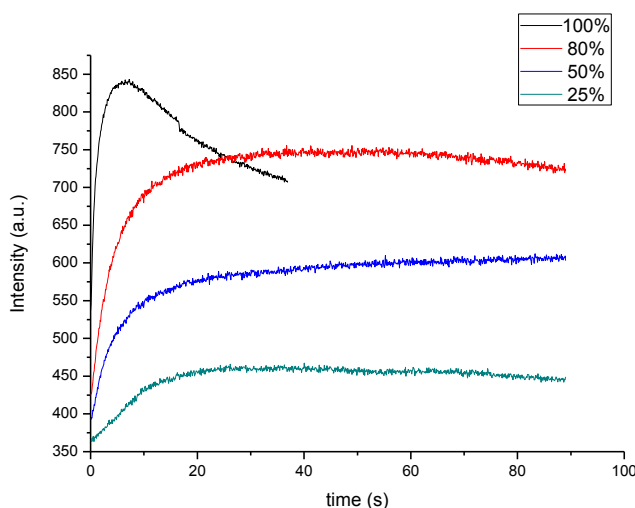
Figure 1.18. Fluorescence released from liposome after laser irradiation at different power intensities: 100% (black line), 80% (red line), 50% (blue line) and 25% (cyan line) of total power intensity from the laser (1 W).

1.1.6. Cytotoxicity assays

The first information we need to know about our complex system before working with biological systems is cytotoxicity. Different assays can be employed to determine the cell viability after rods addition such as MTT or XTT.[143] In this assays, living cells are able to convert MTT or XTT to formazan which absorbance is then measured. This value can give an estimation of living cells compared to dead cells. Formazan formed by cells on MTT assay is not a soluble product, so the cells must be lysed to solubilize it before absorbance can be measured. However, formazan formed by cells on XTT are water soluble, allowing kinetic monitoring of the same samples at different timepoints. Therefore, taking the advantage of XTT assay, it was used in this chapter. Gold nanorods formulations were assayed in two of the most commonly used cell lines: HeLa (cervical cancer human cell line) and fibroblasts 3T3 (mouse embryo tissue). Different concentrations of Au NRs were added to the cells seeded in a 96 well plate: 0.1 nM, 0.2 nM, 0.5 nM and 1 nM.
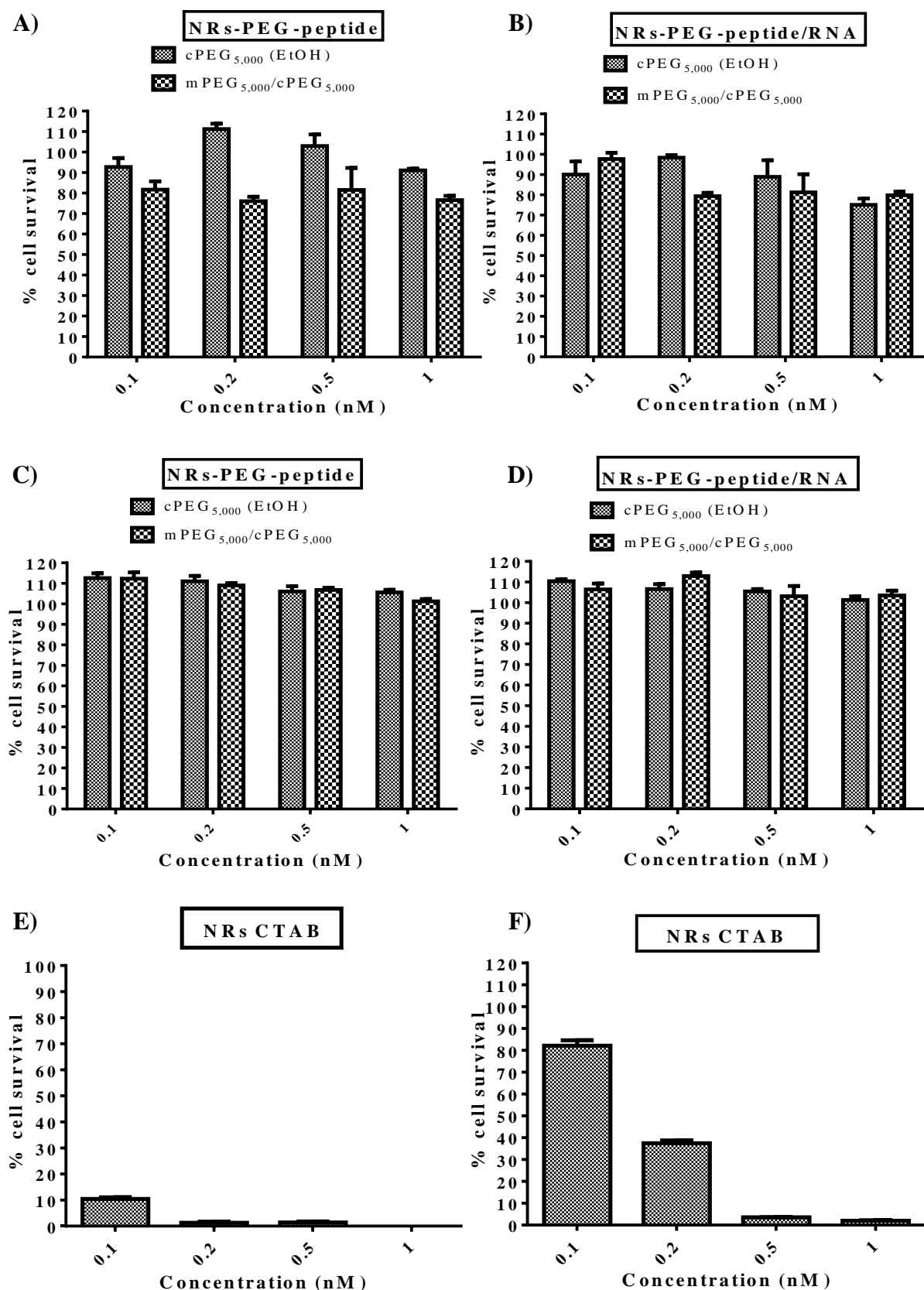
Figure 1.19. Cell viability after 24 h incubation with different concentration of functionalized rods in: Fibroblasts 3T3 cells (A, B); HeLa cells (C D) and unmodified rods in Fibroblasts 3T3 cells (E) and HeLa cells (F).

56

From Figure 1.19, the cytotoxicity of NRs solutions were compared in both cellular lines. It is clear that in HeLa cells, rods were not toxic at any of the concentrations tested (Figure 1.19 C and D). However, in fibroblasts a minor toxicity can be observed when concentration of rods was increased in both modification methods (Figure 1.19 A and B). Interestingly, when rods were modified with mPEG$_{5000}$/cPEG$_{5000}$ slightly higher toxicity was observed compared with those modified twice with cPEG$_{5000}$. This fact can be explained by observing the method employed for pegylation process. The double cPEG$_{5000}$ modification uses two cycles of, at least 12 h; whereas the mPEG$_{5000}$/cPEG$_{5000}$ uses only 75 min for both conjugations. As previously mentioned, Murphy and co-workers demonstrated that the rod ends are preferred when functionalizing the surface, thus CTAB can still remain attached to it. [69] Higher functionalization times or other strategies such as the use of ethanol (employed in the double cPEG$_{5000}$ modification) are needed for complete CTAB removal. This minor amount of remaining CTAB can cause the slightly increase in cytotoxicity which is not appreciated in the double cPEG$_{5000}$ modification.

Other minor differences can be appreciated when RNA is incorporated. Toxicity was decreased in rods solution containing RNA. This effect is observed in the mPEG$_{5000}$/cPEG$_{5000}$ modified rods. We hypothesize that the negatively charged RNA can be attached to the positively charged CTAB, thus this masking effect can decrease the toxicity of the system. However, further characterization assays are needed to confirm it.

Finally, Figure 1.19 E and F perfectly show the effect of CTAB on cell toxicity. When rods are not functionalized, they exhibit toxicity in a dose dependent manner. These last graphs show the clear evidence that the surface must be modified for complete CTAB elimination. Once the rods surface was modified with PEG and fluorescent CPP, internalization assays were performed.

1.1.7. Fluorescent detection of peptide internalization

A quick and easy way of detecting if our system has been internalized into the cells is fluorescence-activated cell sorting (FACS). A fluorescent molecule has to be attached to the system in order to detect and quantify the amount of fluorescence into the cells, therefore, the amount of our system. The peptide attached to the rod surface contains CF and can be detected by this technique.

For internalization experiments, HeLa and fibroblast 3T3 cells were seeded in a 12 well-plate and incubated until 60% confluency. Confluency must not exceed 70% because in the larger incubation times, cells can reach their maximum confluency; thus alterating their morphology and consequently the internalization results. Then, different rod formulations and concentrations were added to the cells and incubated at 2 h and 24 h. After incubation, cells were washed twice with PBS for complete rods removal. Cells were then trypsinized and placed in sorting tubes for finally analyzing by FACS.
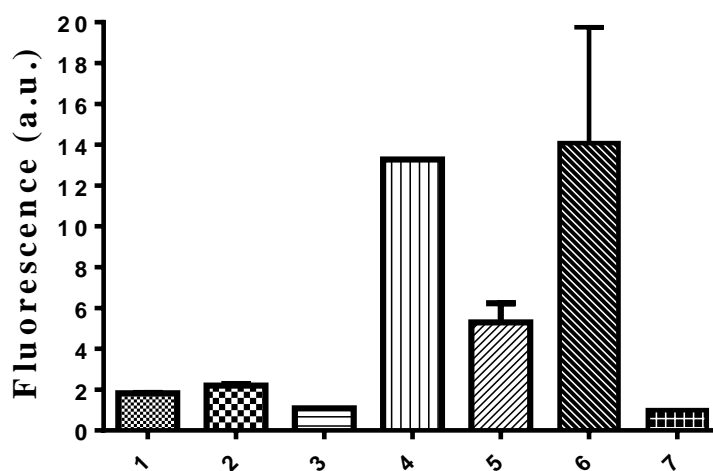
Figure 1.20. Normalized fluorescence obtained by FACS when different NRs formulations were incubated on HeLa cells at different times: 1) 1 nM mPEG$_{5000}$/cPEG$_{5000}$ NRs solution incubated 2 h; 2) 1 nM double cPEG$_{5000}$ NRs solution incubated 2 h; 3) 0.2 nM mPEG$_{5000}$/cPEG$_{5000}$ NRs solution incubated 24 h; 4) 0.2 nM double cPEG$_{5000}$ NRs solution incubated 24 h; 5) 1 nM mPEG$_{5000}$/cPEG$_{5000}$ NRs solution incubated 24 h; 6) 1 nM double cPEG$_{5000}$ NRs solution incubated 24. h and 7) Control cells.

From Figure 1.20 some preliminary conclusions were obtained. When incubating gold NRs at high concentration of 1 nM during 2 h, a minor increase in fluorescence was

appreciated in both formulations compared with control cells (Figure 1.20, column 1 and 2). As the increase was very low, incubation time was changed to 24 h. When 0.2 nM mPEG$_{5000}$/cPEG$_{5000}$ NRs solution was incubated during 24h in HeLa cells, almost no signal was found (Figure 1.20, column 3). Nevertheless, when 0.2 nM double cPEG$_{5000}$ NRs solution was incubated 24 h (Figure 1.20, column 4), a clear increase in fluorescence was appreciated. Comparing both formulations at 24h and 1 nM NRs concentration, an increase in fluorescence was detected being higher for those rods modified with double cPEG$_{5000}$ (Figure 1.20, column 5 and 6).

Finally, fluorescence from both formulations was observed after 24h and, it is worth to mention that, at that time the rods modified with double cPEG$_{5000}$ containing the CPP were internalized also at 0.2 nM.

For a better observation of the fluorescence, spinning disk confocal microscopy was used. This technique is able to scan the fluorescence of different planes in the Z axis, allowing to visualize better if the fluorescence comes from the cytoplasm of the cell. The spinning disk has the advantage, compared to conventional confocal microscope, of using less excitation energy, thus reducing photo-toxicity and photo-bleaching. In addition, the use of the spinning disk decrease the time needed to obtain each scan. In this assay, cells were seeded in glass bottom MatTek dishes. As the laser beam comes from downwards, the plastic dishes cannot be used because of light absorption. Therefore, bottom glass dishes were used. As the glass is not the best surface for cell growth, it was coated by collagen for better cell adhesion and growth (for more details see materials and methods).

For these experiments, fibroblast cells were seeded 24 h before the addition of gold NRs. Then, both rods formulations were added to the cells and incubated during 2 h and 24 h. All formulations contained the fluorescent CPP (r$_8$k(CF)). After 2h incubation and 0.2 nM different scenarios were observed: a few or none modified mPEG$_{5000}$/cPEG$_{5000}$ NRs were visualized meaning poor internalization by this formulation after 2 h incubation time. However, NRs from double cPEG$_{5000}$ formulation were distinguished and, interestingly, in many cells they were attached to the cell membrane (Figure 1.21 A and B). This results suggested that NRs functionalized by double cPEG$_{5000}$ have higher ability to be internalized. Although the rods started to internalize at 2 h in the double cPEG$_{5000}$ NRs formulation, 24 h incubation time was studied in order to visualize better the internalization of both Au NRs formulations.

59

Now, when rods were incubated 24 h, the two rods formulations were visualized into the cells. The fluorescence obtained from 0.2 nM mPEG$_{5000}$/cPEG$_{5000}$ NRs was quite lower compared with the double cPEG$_{5000}$ NRs formulation. Even so, both formulations were internalized.

As 0.2 nM was barely detected in one of the formulations, higher concentration was assayed at 24 h. In this occasion, the fluorescence of 1 nM mPEG$_{5000}$/cPEG$_{5000}$ NRs was clearly identified (Figure 1.21 E and F) and surprisingly, at this concentration, the other formulation (double cPEG$_{5000}$) was remarkably internalized (Figure 1.21 C and D). The huge amount of rods was even observed by bright field images and identified as black dots, also observed at 0.2 nM.

E) **F)**
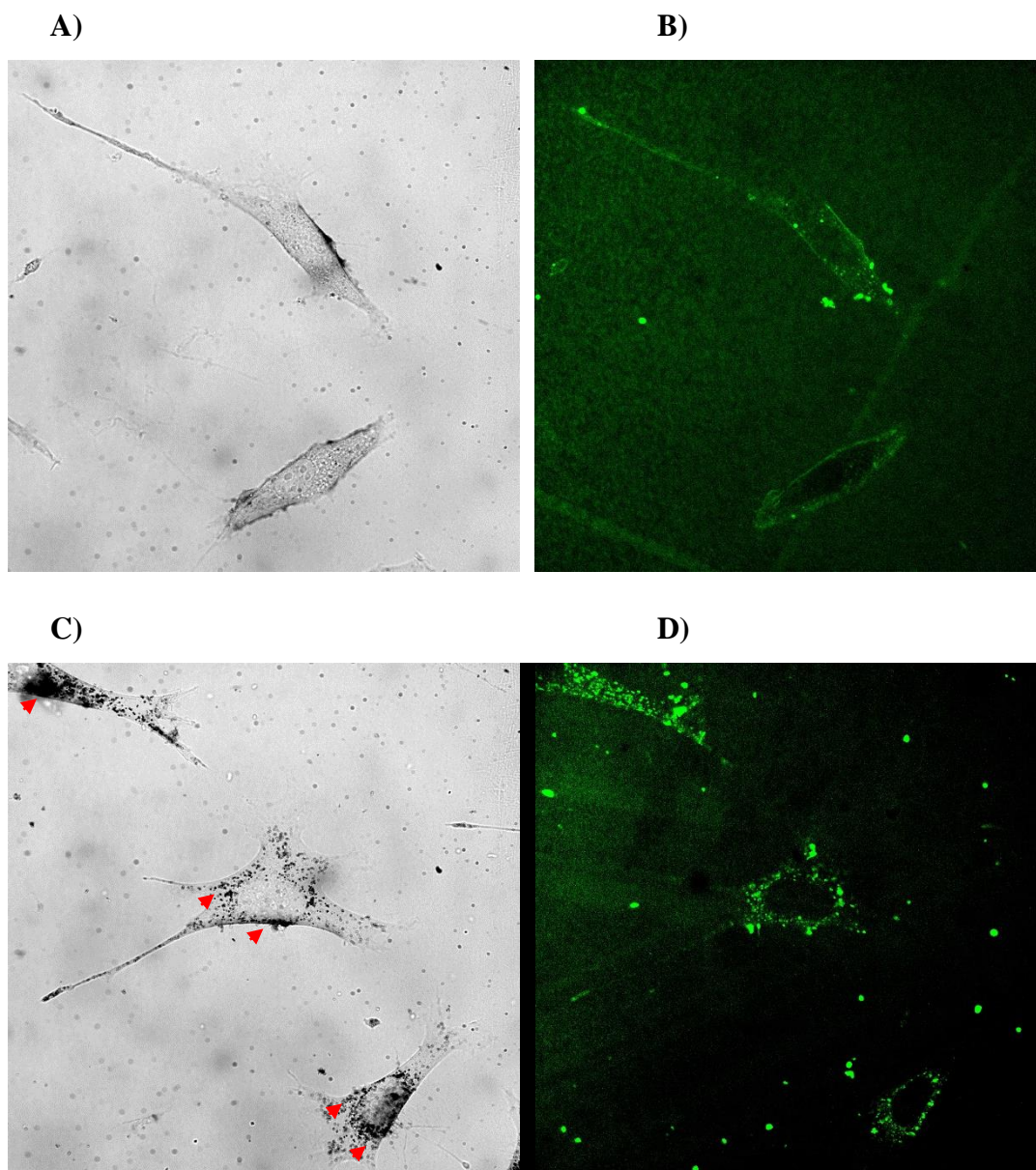
Figure 1.21. Representative spinning disk confocal microscopy images of different rods formulations and concentrations internalized into fibroblasts 3T3 cells at different incubation times. A) and B) 0.2 nM of NRs-cPEG$_{5000}$ –CPP incubated 2 h; C) and D) 1 nM of NRs-cPEG$_{5000}$ –CPP incubated 24 h; E) and F) 1 nM of NRs-mPEG$_{5000}$ /cPEG$_{5000}$ –CPP incubated 24 h. Nanorods accumulation is marked in red. Bright field images on the first column and fluorescence images (irradiated at 488nm) on the second column.

The images revealed the internalization of both formulations into fibroblast cells. The same internalization tendency observed by FACS was also observed by confocal microscopy.

As conclusion, NRs-PEG-CPP system internalization and accumulation into the cell was confirmed. Probably and observing the size of these black dots, the vesicles containing the rods observed by confocal microscopy can be late endosomes or lysosome. As the incubation time was 24 h, rods could be firstly internalized by early endosomes and finally accumulate into larger vesicles.

1.1.8. Detection of rods internalization by electron microscopy

Confirmation of rods internalization was achieved by TEM. Rods were incubated on HeLa and fibroblasts cells at 0.1 nM and 0.2 nM concentrations. After 24 h incubation, rods solution was removed and cells were washed twice with PBS. Then, cells were fixed using glutaraldehyde and stained with OsO_4. After staining, cells were treated with an embedding process and cut in thick sheets. Finally, sheets were placed on a grid and cells were observed by TEM (Figure 1.22).

A)   **B)**
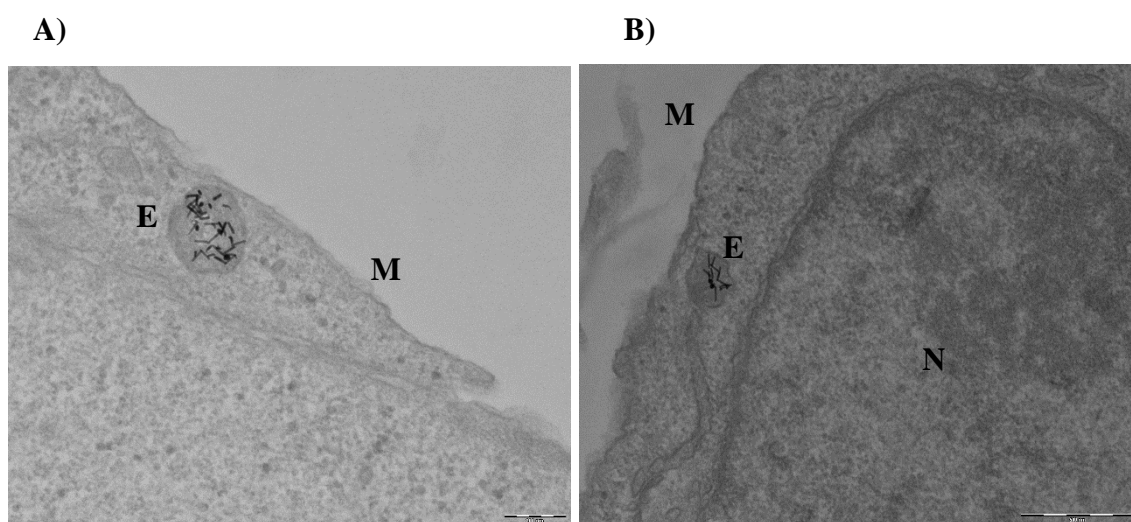
Figure 1.22. Transmission electron micrographs of 0.2 nM gold nanorods on HeLa cells. M: cell membrane, E: mature endosome and N: nucleus. Scale bar: A) 200 nm and B) 500 nm.

Rods could be observed into many cells, two representative images are shown in Figure 1.22. After 24h incubation, we can visualize rods into vesicles. Some of the vesicles are in the range of 200-300 nm. Ganley *et al.* described that fully mature endosomes can be as big as 750 nm in Hela cells.[144] Therefore, we hypothesize that after 24 h incubation, rods are entrapped into mature endosomes.

This result corroborates the entrance of gold NRs into the cells, as we previously observed by confocal microscopy. At this point, the next experiment was the use of NIR light for vesicle disruption.

1.1.9. siRNA incorporation

Visualization of vesicle disruption can be laborious. The equipment or technique for directly measuring/observing endosomal release is still not reached; therefore, indirect methods can be employed for this purpose. The idea of observing a diffusion, of the punctuated green dots, over the cytosol after laser irradiation by confocal microscopy was considered. After some trials, it was impossible to differentiate between irradiated or non-irradiated samples. The diffusion could not be observed or if so, it could be misinterpreted with the background.

In this regard, a biological response from the cells, when the rods were released, was proposed. Negatively charged RNA can be attached to the positively charged CPP (Figure 1.23). Therefore, when RNA is released from the vesicle, cells will response and this effect will be quantified.
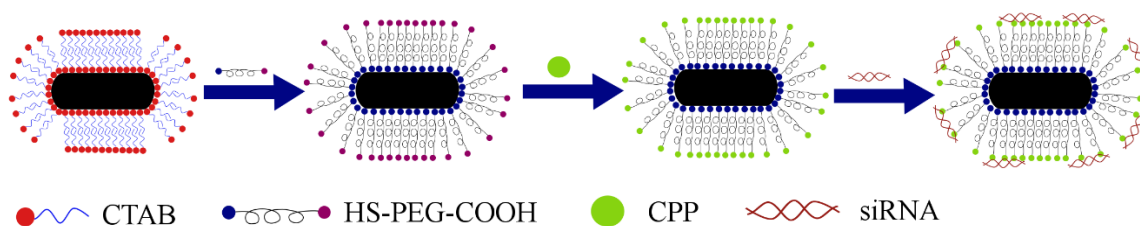
Figure 1.23. Schematic representation of gold nanorods surface functionalization.

In our study, siRNA was incorporated to the rod surface in order to be delivered into cytosol after NIR laser irradiation. Supposing that RNA was incorporated to the rods surface, the LSPR may differ from that obtained without RNA (Figure 1.24).

A)

B)
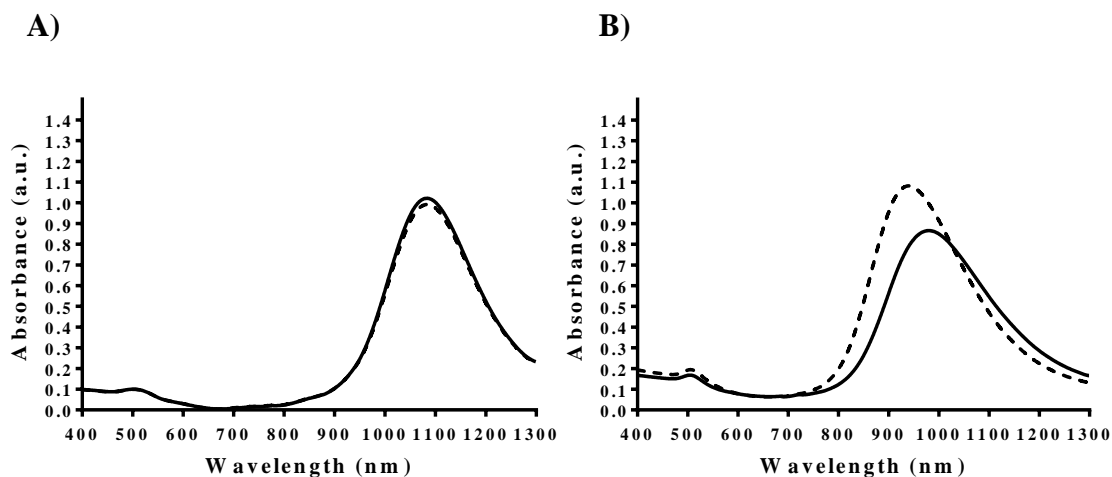
Figure 1.24. UV-Vis-IR spectrum of two different batches of M4 gold nanorods: A) after double $cPEG_{5000}$ /CPP modification (continuous line) and after $cPEG_{5000}$ /CPP/siRNA modification (dashed line); B) after $mPEG_{5000}$-$cPEG_{5000}$ /CPP modification (continuous line) and after $mPEG_{5000}$-$cPEG_{5000}$ /CPP/siRNA modification (dashed line).

A blue shift was observed in both modified NRs formulations after siRNA incorporation. However, this shift was slightly identified on NRs-$cPEG_{5000}$ -CPP-siRNA formulation (from 1085 to 1081 nm). On the contrary, the shift observed when RNA was incorporated to NRs-$mPEG_{5000}$-$cPEG_{5000}$ -CPP was bigger (from 979 to 940 nm). We hypothesize that in the case of NRs-$mPEG_{5000}$-$cPEG_{5000}$ –CPP, as explained before, still some CTAB molecules can be adsorbed on the rods surface. Therefore, when the negative siRNA is attached to the positive CTAB, rods can be destabilized, thus varying the LSPR. On the other hand, CTAB is completely removed when double $cPEG_{5000}$ is conjugated to the rods, so minor destabilization is observed.

After RNA incorporation, rods internalization properties were studied. Perhaps, RNA can mask the CPP when complexed and penetration properties from rods can be lost. Taking this into consideration, the final rods formulation was incubated again in fibroblast cells for spinning disk confocal microscopy visualization (Figure 1.25).

G)

H)

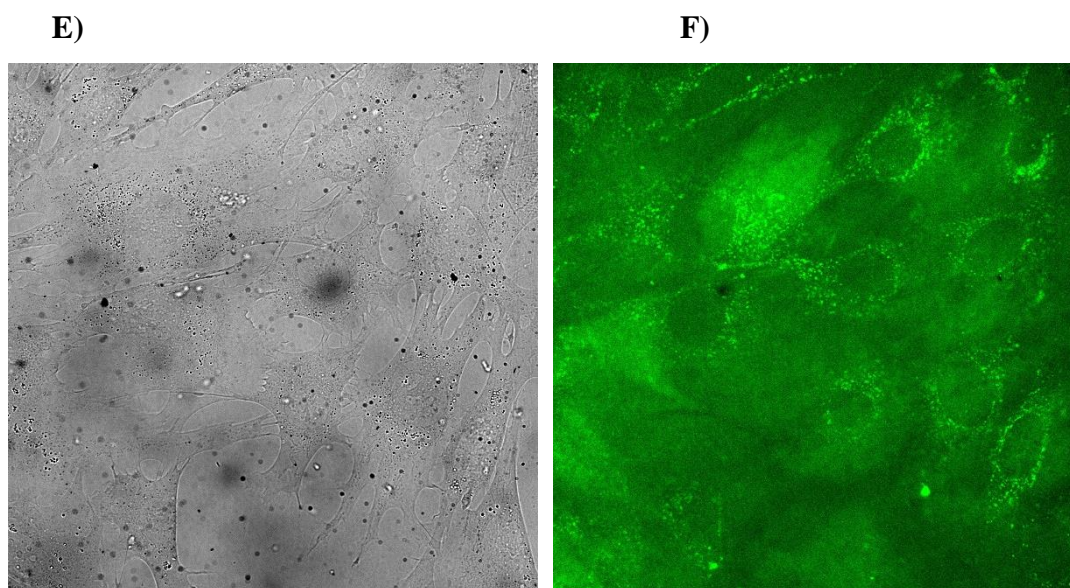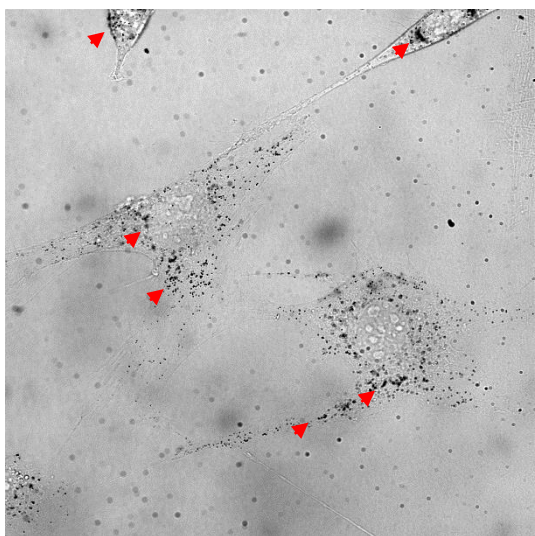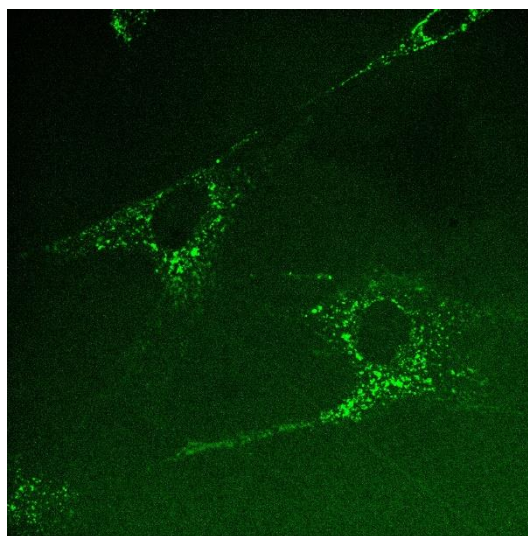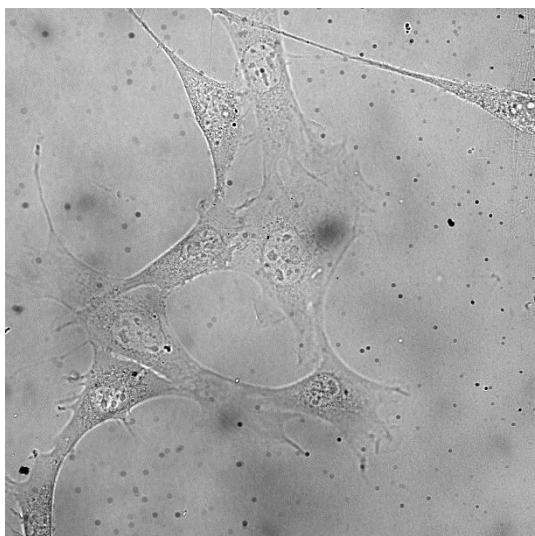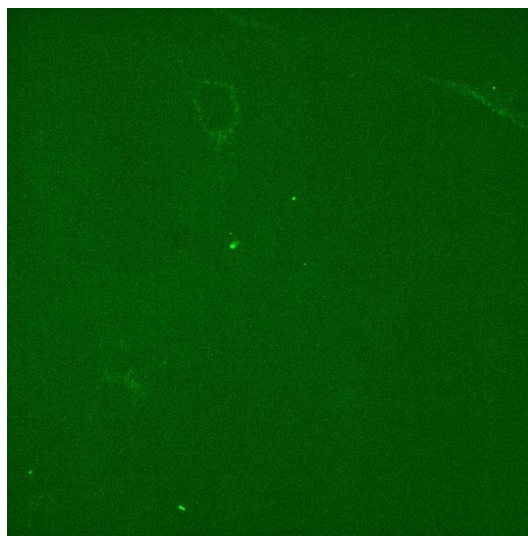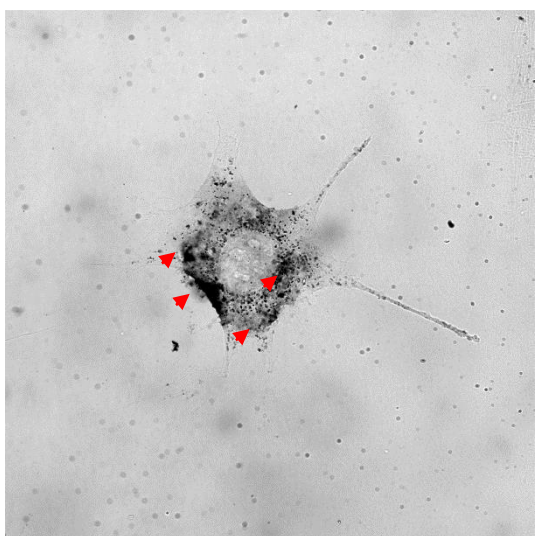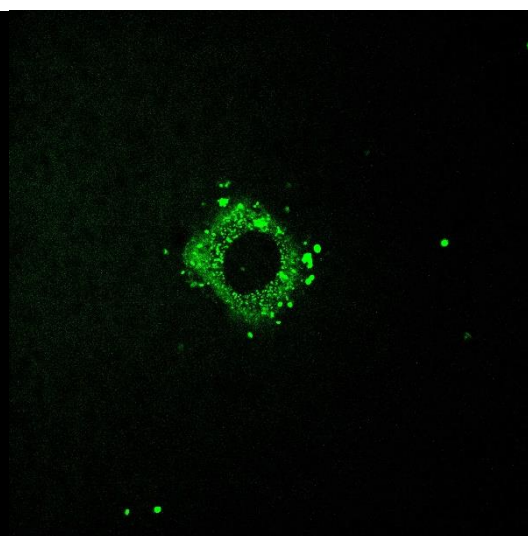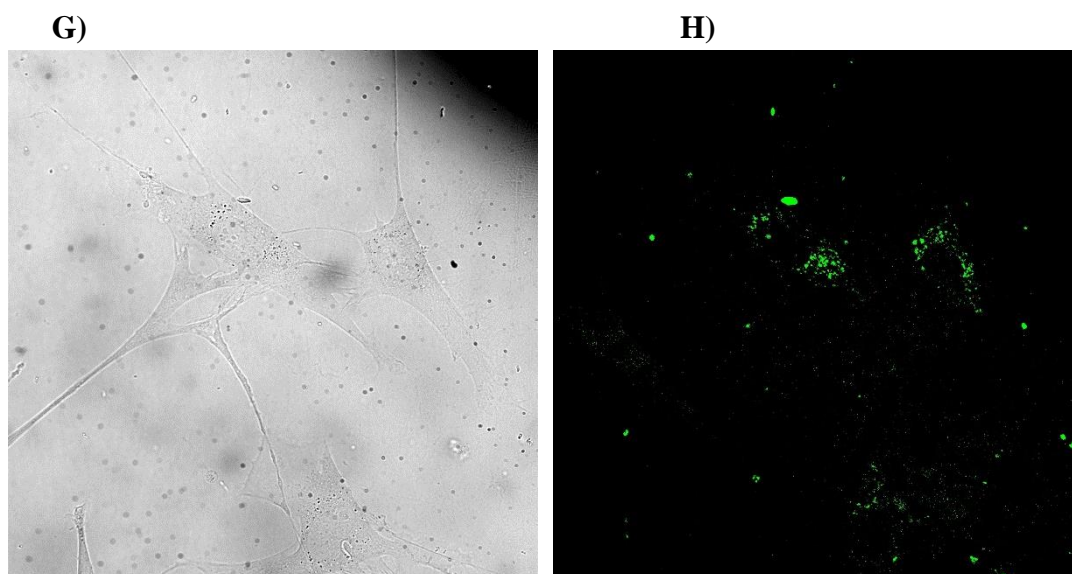**Figure 1.25.** Spinning disk confocal microscopy images of different rods formulations and concentrations internalized into fibroblasts 3T3 cells at different incubation times. A) and B) 0.2 nM of NRs-cPEG$_{5000}$ – CPP-RNA incubated 24 h; C) and D) 0.2 nM of NRs- mPEG$_{5000}$/cPEG$_{5000}$ –CPP-RNA incubated 24 h; E) and F) 1 nM of NRs-cPEG$_{5000}$ –CPP-RNA incubated 24 h; G) and H) 1 nM of NRs- mPEG$_{5000}$/cPEG$_{5000}$ – CPP-RNA incubated 24 h. Nanorods accumulation is marked in red. Bright field images on the first column and fluorescence images (irradiated at 488nm) on the second column.

Same as in previous experiments, rods could be observed into the cells. Again, double cPEG$_{5000}$ formulation entered in a higher extent compared with the formulation containing mPEG$_{5000}$. Already checked the rods internalization properties, irradiation assays were performed.

1.1.10. Endosomal escape attempt

1.1.10.1. Laser irradiation assay

Homemade set up laser was used to irradiate the cells (details explained in materials and methods). The focusing objective was removed to increase the spot size. When the objective is applied, the laser is used as scanning mode and the spot size is reduced to micrometer scale. In this mode, the power is concentrated and the two photon effect can occur. In our case, all the area containing the cells needs to be irradiated, therefore the objective was removed. This set up used less concentrated power but more distributed around the dish. At the beginning of the experiment, the light power arriving to the dish was measured as 55-60 mW/cm^2. Table1.2 summarizes time, concentration and formulations irradiated.

Table1.2. Summary of irradiation times of both formulations at different concentrations. Laser power arriving to the sample was 55-60 mW/cm^2 in our case.

formulations	*10 min irradiation*	*30 min irradiation*	*60 min irradiation*
NRs-mPEG$_{5000}$-cPEG$_{5000}$/CPP/siRNA	0.2 and 1 nM	0.2 and 1 nM	0.2 nM
NRs-double cPEG$_{5000}$/ CPP/siRNA	0.2 and 1 nM	0.2 and 1 nM	0.2 nM

After irradiation, samples were observed again by spinning disk confocal microscopy in order to visualize any difference compared with the non-irradiated samples. Almost no differences were observed in all samples tested as can be appreciated in Figure 1.26.

A)   **B)**
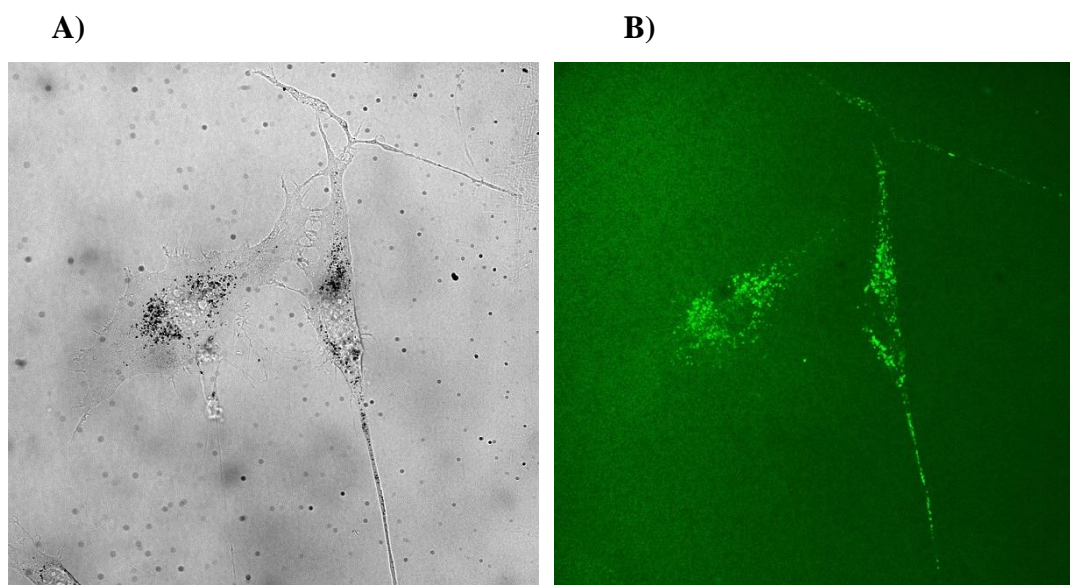
Figure 1.26. Spinning disk confocal microscopy images of 0.2 nM of NRs-cPEG$_{5000}$−CPP-RNA incubated 24 h after 30 min irradiation at 55-60 mW/cm^2. A) Bright field image and B) fluorescence images (irradiated at 488nm).

All irradiated samples were then incubated during 48 to 96 h. This time was needed for silencing effect of siRNA and degradation of the already synthesized protein.

1.1.10.2. Western blotting

48 to 96 h after irradiation, cells were washed and lysed. Protein amount from the lysates was quantified by BCA (Pierce™) assay and 20 µg of protein were loaded into polyacrylamide gel. After sodium dodecyl sulfate polyacrylamide gel electrophoresis

(SDS-PAGE), the proteins were transferred to a nitrocellulose membrane. Then, anti-PARP-1 primary antibody (rabbit) was applied over the membrane during 90 min. As a control anti-β-actin primary antibody (mouse) was used. Once primary antibodies were conjugated, HRP-secondary antibodies (anti-rabbit or anti-mouse) were incubated with the membrane. Finally the membrane was developed using ECL chemiluminescent substrate (Figure 1.27).
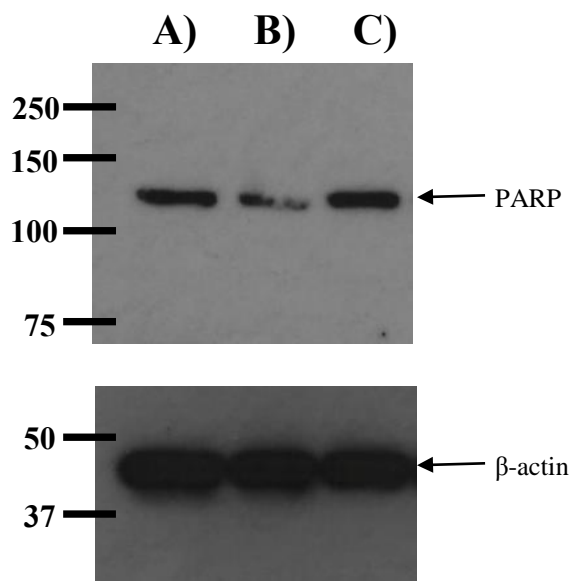
Figure 1.27. Western blot of PARP protein (118 kDa) and β-actin (40 kDa) as a control protein. A) Non irradiated control cells, B) 0.5 nM double cPEG$_{5000}$/CPP/siRNA after 10 min irradiation and C) 0.2 nM double cPEG$_{5000}$/CPP/siRNA after 10 min irradiation.

Preliminary results showed a decrease in PARP expression (Figure 1.27, lane B) compared with control cells. The formulation used was 0.5 nM of rods modified with double cPEG$_{5000}$/CPP/siRNA after 10 min irradiation at 55-60 mW/cm^2. It is also observed that when 0.2 nM was irradiated the same time, no effect was observed. These results encouraged us to keep following in this direction. Further experiments will be performed increasing irradiation times and concentration.

In this chapter, the synthesis of Au NRs was optimized obtaining more than 93 % rods yield. After surface functionalization, we demonstrated low cytotoxicity of our formulations composed by NRs, different PEG moieties, CPP and siRNA. These formulations were able to internalize to HeLa and fibroblasts cells by the endocytic route. Preliminary results of laser irradiation have shown siRNA scape from endosome and protein silencing demonstrating the potential of Au NRs as endosomal scape enhancers.

1.2. Materials and Methods

1.2.1. Materials

In the following table, the reagents, solvents and materials used in this chapter are listed. The supplier of every material is also indicated:

Supplier	Materials
Albatros Chem Inc	TBTU
AMRESCO®	40% Acrylamide solution
Applied GL Biochem	HOAt
Avanti Polar Lipids	EPC and cholesterol
BD Discardit II BD Plastipak	Syringes (1,2, 5, 10 and 20 mL)
Biochrom A.G.	Trypsin-EDTA
Cell signaling	PARP (46D11) rabbit mAb and β-Actin (8H10D10) mouse mAb
Corning Costar	12 well-plates, 24 well-plates, 48 well-plates and 96 well-plates, culture flasks and petri dishes
Dharmacon GE lifesciences	ON-TARGETplus Human PARP1 siRNA: SMARTpool
Deltalab	Falcon tubes
EMD Millipore	Filtres 0.45 µM (PVDF) and Collagen type I, rat tail
Eppendorfs	Eppendorf tubes
Iris Biotech	Fmoc-*D*-Arg(Pbf)-OH, Fmoc-*D*-Lys(Alloc)-OH, Fmoc-*D*-Cys(Trt)-OH and EDC·HCl
Jenkem Technology USA	mPEG$_{5000}$ and cPEG$_{5000}$
KaliChemie	TFA
MatTek corporation	35 mm glass bottom dishes (20 mm glass inside)
Novabiochem	PyBOP and NHS
Panreac	DMF and DMSO
PCAS BioMatrix Inc.	H-Rink amide ChemMatrix® resin
PIERCE	s-NHS
Pyrex	Pyrex® culture tubes (14 x 100 mm)
Roche	Agarose MP
Scharlab	Syringes (2, 5, 10 and 20 mL) fitted with polyethylene

	porous disk for peptide synthesis
Scharlau	HCl and methyl *tert*-butyl ether
SDS	Acetone, DCM, ACN, MeOH and piperidine
Sigma-Aldrich	5(6)-carboxyfluorescein, DIEA, DIC, ninhydrin, triisopropylsilane, sucrose, ethylene glycol, Brij 35, PEOZ, ficoll, MUA, DMEM, gold (III) chloride ($HAuCl_4$), silver nitrate ($AgNO_3$), ascorbic acid, CTAB, BDAC, hydroquinone, Sephadex-G75, NaOH, $NaBH_4$, MES, hyperfilm ECL, *L*-DTT, cell Proliferation Kit II (XTT), APS, TEMED and cOmplete™, EDTA-free
TCI Europe	Sodium oleate
ThermoFisher Scientific	LysoTracker® Red DND-99, Hoechst 33342, Pierce™ BCA Protein Assay Kit, RIPA Lysis and Extraction Buffer and Pierce™ ECL Western Blotting Substrate

1.2.2. Peptide synthesis

In this chapter, $r_8k(CF)$ was selected for promoting the nanorods internalization into the cell. The CPP was synthesized by solid-phase peptide synthesis (SPPS) following Fmoc/*t*Bu strategy. H-Rink amide ChemMatrix® resin was used for obtaining an amide group in the *C*-terminal of both peptides. Peptide elongation was performed manually in 50 mL polypropylene syringes containing a polyethylene porous disk. Solvents and excess of soluble reagents were removed by suction. Resin was washed every synthetic step with DMF (3 x 30 s) and DCM (3 x 30 s) using 10 mL of solvent/g resin each time. During couplings, the mixture was allowed to react with intermittent manual stirring.

1.2.3. Resin conditioning

Resin has to be conditioned before the first amino acid incorporation. H-Rink amide ChemMatrix®, with a substitution of 0.45 mmol/g, was treated as follows:

Reagent	Treatment
MeOH	Wash (3 x 30s)
DMF	Wash (3 x 30s)
DCM	Wash (3 x 30s)
1% TFA in DCM	Wash (2 x 5min)
DCM	Wash (3 x 30s)
5% DIEA in DCM	Wash (2 x 5min)
DCM	Wash (3 x 30s)
DMF	Wash (3 x 30s)
DCM	Wash (3 x 30s)

1.2.4. Ninhydrin test

Colorimetric tests are used in solid-phase peptide synthesis (SPPS) for controlling the deprotection and coupling steps. In this case, ninhydrin or Kaiser test,[145] allows the detection of primary amines. Into a small glass tube, 6 drops of solution A and 2 drops of solution B were added. Then, a small amount of dried resin is transferred into the tube

and heated at 110ºC for 3 min. A dark blue or purple solution indicates the presence of free amines meaning an incomplete coupling. On the contrary, a yellowish solution means the absence of free amines meaning the coupling worked at least at 99%.

Solution A: 400 g of phenol were dissolved in 100 mL of absolute ethanol and heated until phenol is dissolved completely. 20 mL of KCN 0.65 mg/ml aqueous solution were added to 1 L of freshly distilled pyridine over ninhydrin. Both solutions were stirred for 45 min with 40 g of Amberlite MB-3 resin, filtered, and combined.

Solution B: 2.5 g of ninhydrin were dissolved in 50 mL of absolute ethanol. The resulting solution has to be kept in a flask protected from light.

1.2.5. Fmoc group removal and quantification of resin loading capacity

Fmoc was removed from protected amino acids by addition of 20% piperidine in DMF (5mL/g resin, 1 x 1 min and 2 x 10 min). After the first amino acid incorporation, piperidine washes were collected and the absorbance of Fmoc group was measured for obtaining the loading capacity:

$$Z = \frac{A \cdot x}{\varepsilon \cdot Y \cdot l}$$

Where Z is the loading capacity (mmol/g), A is the Fmoc absorbance measured at 290 nm, x is the solvent volume (mL), ε is the molar extinction coefficient at 290 nm (5800 L/(mol·cm)), Y is the resin weight (g) and the l is the path length (cm).

1.2.6. Peptide chain elongation

Due to the bulky structure of pentamethyl dihydrobenzofurane (Pbf) side chain protecting group for arginine, the complete incorporation of the Fmoc-Arg(Pbf)-OH peptide is not always achieved. The method A is used as a default for coupling the amino acid, but if the first coupling is not complete, method B is applied. In rare cases, method C was used after 2 incomplete recouplings:

Method A

Reagent	Treatment
DCM	Wash (3 x 30s)
DMF	Wash (3 x 30s)
3 eq Fmoc-Aa-OH	Coupling (60-90min)
3 eq TBTU	in DMF
6 eq DIEA	
DMF	Wash (3 x 30s)
DCM	Wash (3 x 30s)
DMF	Wash (3 x 30s)
20% piperidine in DMF	Deprotection (1 x 1min, 2 x 10min)
DMF	Wash (3 x 30s)

Method B

Reagent	Treatment
DCM	Wash (3 x 30s)
DMF	Wash (3 x 30s)
3 eq Fmoc-Aa-OH	Coupling (60-90min)
3 eq PyAOP	in DMF
9 eq DIEA	
DMF	Wash (3 x 30s)
DCM	Wash (3 x 30s)
DMF	Wash (3 x 30s)
20% piperidine in DMF	Deprotection (1 x 1min, 2 x 10min)
DMF	Wash (3 x 30s)

Method C

Reagent	Treatment
DCM	Wash (3 x 30s)
DMF	Wash (3 x 30s)
3 eq Fmoc-Aa-OH	Coupling (60-90min)
3 eq HOAt	in DMF
3 eq DIC	
DMF	Wash (3 x 30s)
DCM	Wash (3 x 30s)
DMF	Wash (3 x 30s)
20% piperidine in DMF	Deprotection (1 x 1min, 2 x 10min)
DMF	Wash (3 x 30s)

1.2.7. Coupling of 5(6)-carboxyfluorescein

The amino *N*-terminal of the peptide was used for conjugating it to the gold nanorods surface. Therefore, the CF was coupled to the side chain of a *D*-lysine, orthogonally protected, placed at the *C*-terminal. First, the *N*-amino-terminal was temporary protected, in our case we incorporated a Boc protecting group using Boc_2O. Then, the Alloc protecting group from the *D*-lysine side chain was selectively removed and finally, CF was coupled to the lysine side chain. The treatment was performed as follows:

Reagent	Treatment
DCM	Wash (3 x 30s)
DMF	Wash (3 x 30s)
10 eq Boc_2O	Protection (60-90min)
30 eq DIEA	in DMF
DMF	Wash (3 x 30s)
DCM	Wash (3 x 30s)

DMF	Wash (3 x 30s)
0.1 eq tetrakis (triphenylphosphine) palladium (0) 10 eq phenylsilane	Alloc removal (3 x 15 min) in DMF
DMF	Wash (3 x 30s)
DCM	Wash (3 x 30s)
DMF	Wash (3 x 30s)
3 eq CF 3 eq PyAOP 9eq DIEA	Coupling (120-180min) in DMF
20% piperidine in DMF	Wash (3 x 30s)
DMF	Wash (3 x 30s)
DCM	Wash (3 x 30s)

In the case that the Boc group is not completely incorporated to the *N*-terminal, a second treatment using the same amount of reagents is needed. For the final coupling of CF, the same equivalents are added again in case of incomplete incorporation. This process needs to be protected from the light because of CF can be quenched.

1.2.8. Cleavage and side chain deprotection

The peptide was completely deprotected and cleaved from the resin by using the following cleavage cocktail: TFA:TIS:H_2O (95:2.5:2.5) during 4-5h. Then, TFA was evaporated under N_2 stream and the peptide was precipitated in cold *tert*-butyl methyl ether. Protecting groups were soluble in the organic phase and the precipitated peptide was collected by centrifugation. After three washes with *tert*-butyl methyl ether, the peptide was dissolved in a mixture 1:1 of ACN:H_2O and lyophilized.

1.2.9. Peptide purification

Peptide was solubilized in H_2O with a few microliters of ACN. Previously to injection to semi-preparative HPLC system, the sample was filtered through a 0.45 μm PVDF filter.

Purification was performed in a 25 min linear gradient from 10% to 60% ACN in H_2O using a Sunfire C_{18} column (150 x 10 mm x 5 μm, 100 Å, Waters). Both solvents (ACN and H_2O) contained 0.1% TFA. Flow rate was adjusted to 6.6 mL/min and the peaks detections was observed at 220 nm. Peaks of interest were collected, combined and lyophilized.

1.2.10. Peptide characterization

Characterization of the peptide was performed by HPLC/UPLC, MALDI-TOF mass spectroscopy and amino acids analysis. For more details see Annex II.

HPLC

Chromatogram was obtained on a Waters Alliance 2695 coupled to a photodiode array detector 2998 Waters using a Sunfire C_{18} column (100 x 4.6 mm x 3.5 μm, 100 Å, Waters). The flow rate was 1 mL/min using ACN (0.036% TFA) and H_2O (0.045% TFA). 8 min linear gradients were used.

UPLC

Chromatogram was obtained on an Acquity UPLC H class using an Acquity UPLC$^{®}$ BEH C_{18} column (50 x 2.1 mm x 1.7 μm, Waters). The flow rate was 0.6 mL/min using ACN (0.036% TFA) and H_2O (0.045% TFA). 2 min linear gradients were used.

MALDI-TOF MS

Molecular weight was determined using a MALDI-TOF/TOF Applied Biosystem 4700. Sample was prepared by mixing 1 μL of peptide solution with 1 μL of α-cyano-4-hydroxycinnamic acid (ACH) matrix on the MALDI plate. The matrix (10 mg/mL) was prepared in ACN/H_2O 1:1 (v/v) containing 0.1% TFA.

Amino acids analysis

A known amount of dissolved peptide was transferred to a Pyrex tube. The complete peptide hydrolysis was accomplished by adding HCl 6M at 110ºC for 16 h. Then, the solution was evaporated under vacuum and resuspended in HCl 20 mM aqueous solution. The final solution was derivatized using AccQ-Tag™ protocol (Waters) and analyzed by ion exchange HPLC.

1.2.11. Gold nanorods synthesis

Gold NRs synthesis has been optimized in order to prepare them in a large window of the spectra, ranging from 600 to 1100 nm obtaining a good yield and reproducibility. In our case, various methods were tested until the optimal rod yield and shape was achieved. In this section, they will be explained following the chronological order they were synthesized.

Method 1 (LSPR peak near 800nm)

The synthesis begins with the formation of a seed solution by adding 300 µL of fresh NaBH$_4$ 10 mM to a 5 mL of 100 mM CTAB solution containing HAuCl$_4$ 0.25 mM. The solution turned brownish and was stirred 30 min before used. Second, the growth solution was prepared by adding 75 µL of AgNO$_3$ 10 mM to a 10 mL of 100 mM CTAB solution containing HAuCl$_4$ 0.5 mM. Gold (III) was reduced to gold (I) when 55 µL of ascorbic acid 100 mM was added and we could notice the solution went from yellow to colorless. The pH of the solution was adjusted by the addition of 250 µL HCl 100 mM. Finally, 12 µL of seed solution were added, stirred 30 s vigorously and the final formulation was left undisturbed 10 min. After this period, the rods solution was centrifuged 8600 rpm during 15 min, supernatant was discarded and the pellet was resuspended in 5 mL ultra-pure water. CTAB solution crystallize at RT; therefore, the synthesis was performed at 30-35°C. As the final rod solution contains CTAB, it was kept at the same temperature.

Method 2 (LSPR peak higher than 850nm, BDAC)

The seed solution was prepared following the same strategy explained in method 1 but the growth solution contained minor modifications. CTAB (0.1 g) was added to a 5 mL of 150 mM BDAC solution and stirred 20 min at 30-35 °C. Then, 200 µL of $AgNO_3$ 4 mM and 5 mL of $HAuCl_4$ 1 mM were added to the solution. Same as previous, growth solution turned yellowish when gold (III) was added. The synthesis continued with the addition of 70 µL ascorbic acid 77.8 mM, solution turned colorless and was acidified by the addition of 200 µL HCl 100 mM. Again, the rod formation finished after the addition of 12 µL seed solution. The final formulation was stirred during 4h and then centrifuged at 12000 rpm during 15 min. NRs were resuspended in 1 mL ultra-pure water and the supernatant was removed.

Method 3 (LSPR peak near 1000nm, sodium oleate)

Briefly, 900 mg CTAB and 123.4 mg sodium oleate were dissolved in 25 mL ultra-pure water. 3.6 mL of $AgNO_3$ 4 mM were added and the solution was left undisturbed. After 15 min, 25 mL of $HAuCl_4$ 1 mM were added and the solution was stirred 90 min. Then, pH was adjusted by the addition of 300 µL HCl 12 N under stirring. Fifteen minutes later, 125 µL ascorbic acid 64 mM were added and finally, 80 µL seed solution were added. The final solution was left undisturbed overnight. Excess of surfactants was removed by centrifugation and resuspension in 1 mL ultra-pure water.

Method 4 (LSPR peak near 1000nm, hydroquinone)

The synthesis begins as the previous, with formation of a seed solution; but in here we can find the first modification. NaOH is introduced in the seed formation in a mixture with $NaBH_4$. Briefly, 230 µL of $NaOH/NaBH_4$ 10 mM were added to 5 mL CTAB solution 100 mM containing $HAuCl_4$ 0.5 mM. The solution was stirred 30 min before used. The growth solution also included some modifications: 700 µL $AgNO_3$ 10 mM were added to a solution containing CTAB (364 mg) and $HAuCl_4$ 0.5 mM to a final volume of 10 mL. Then, 500 µL hydroquinone 100 mM were added and gold (III) was reduced to gold (I). It could be observed when the solution turned from yellowish to colorless after

30 sec of agitation. Finally, 160 µL seed solution were added and the solution was left undisturbed overnight. CTAB was reduced from rods solution by centrifuging it at 12000 rpm during 15 min. Supernatant was discarded and rods were redispersed in 1 mL ultra-pure water.

1.2.12. Gold nanorods characterization

Gold nanorods were characterized by measuring their spectra. For rods with LSPR peak at 800 nm, the absorbance was measured on a Shimadzu UV-2501PC spectrophotometer from 400 nm to 900 nm. For LSPR at higher wavelengths, UV-Vis-NIR Shimadzu 3600 was used ranging from 400 nm to 1300 nm. Samples were diluted in water, placed in a quartz cuvette and analyzed.

NRs shape was confirmed by TEM. Briefly, 20 µL rod solution were placed on carbon film supported by copper grids and dried at RT. Images were recorded in a FEI Tecnai Spirit electron microscope equipped with an Olympus Mega View III (soft imaging system).

1.2.13. Assessment of gold nanorods homogeneity

Before achieving a NRs solution with high yield and homogeneity, different techniques were employed in order to increase the percentage of rods, in the NRs solutions synthesized by the methods 2 and 3, respect to other byproducts.

Centrifugation

Rods suspension was placed in an Eppendorf tube and centrifuged at 7700 rpm for 30 min. NRs formed a pellet on the wall of the Eppendorf which was separate from the other shapes, concentrated on the bottom of the tube. Different fractions were then analyzed by TEM.

Density gradient centrifugation

Two different gradient solutions were used for rods separation: the first gradient solution contained increasing percentages of sucrose. The more concentrated sucrose solution was placed on the bottom. Different ranges were tested from 60% w/v (bottom) to 20% (top). NRs sample was added to the top of the tube and centrifuged at different speeds. The different phases, containing rods, were collected and analyzed by TEM.

The second gradient solution was formed by ethylene glycol. In this case, the gradient ranged from 80% v/v (bottom) to 5/0% v/v (top). The NRs samples were placed on the top and the Eppendorf was centrifuged at different speeds. Same as previous, the different phases were collected and analyzed by TEM.

Multiphase systems

Three different compounds were placed in a tube for creating the multiphase system: Brij 35 (26% w/v), PEOZ (30% w/v) and Ficoll (35% w/v). The density, ρ, and viscosity, η of this system were: Brij 35 $\rho_{top} = 1.031$ g/cm^3, $\eta_{top} = 31$ cP; PEOZ $\rho_{middle} = 1.045$ g/cm^3, $\eta_{middle} = 542$ cP; and Ficoll $\rho_{bottom} = 1.112$ g/cm^3, $\eta_{bottom} = 139$ cP. Different volumes of three compounds were used for rods separation. Before adding the rods solution, the multiphase system was stirred 20 sec and centrifuged 5 min at 4600 rpm for better disposition of the phases. Then, rods are added and the system was centrifuged. Many different times and speeds were analyzed, as discussed in section 1.2.3.

Agarose gel electrophoresis

NRs were modified with either HS-PEG$_{5000}$-COOH or 11-mercaptoundecanoic acid for negatively charge the rods surface (modification is explained in the following section), therefore modified NRs will migrate to the positive electrode. 20 µL of functionalized NRs, substituted with both linkers, were applied to a 1% agarose gel in 50 mL TAE or TBE buffer. Gel was run 30 min at 120 V. Different bands were collected and dissolved in hot water. Collected NRs were centrifuged at 10000 rpm for 10 min and resuspended in ultra-pure water.

1.2.14. Nanorods surface modification

After gold NRs synthesis, CTAB had to be removed from the surface to avoid cytotoxicity problems. The different strategies employed are listed below.

Cysteine-peptide conjugation

From NRs synthesis, rods are centrifuged and the supernatant is discarded. The pellet was added to a 5 mL solution containing different amounts of Cys-peptide (cysteine was incorporated to *N*-terminal following the strategy explained in section 1.4.6). The final solution was stirred overnight (O/N). Excess of peptide was removed by 5 cycles of centrifugation (15 min at 10000 rpm) and resuspended in PBS buffer.

11-mercaptoundecanoic acid

Two different methods were used for attaching MUA to the rods: In the first one, 0.5 mL of 20 mM ethanolic solution of MUA was added into 5 mL of the gold nanorods solution and stirred for 24 h at RT.

In the second method, MUA was added drop wise to 5 mL NRs solution under stirring (2.5 µL of 2 mM ethanolic MUA for each 1 mL solution of NR-CTAB). After 1 h of mixing at RT, mPEG$_{5000}$-SH was added to the previous solution (2.5 µL of 8 mM mPEG$_{5000}$ for each 1 mL solution of GNR). The final solution was stirred O/N.

Next day, 20 µL of s-NHS 10 mM and 20 µL of EDC·HCl 10 mM were added to the gold nanorods solution (1 mL) and stirred for 1 h in both cases. Finally, excess of CPP was added and the solutions were stirred O/N again. Unreacted reagents were removed from the rods solutions by 3 cycles of centrifugation at 10000 rpm for 15 min and further resuspension in PBS buffer.

PEGylation

Many PEGylation strategies are currently employed for CTAB removal. In the following lines the five strategies used in this chapter are summarized.

In the first strategy, two rounds of mPEG$_{5000}$ were used. Briefly, 50 µL of mPEG$_{5000}$ 1 mM were added to 5 mL rods synthesis and stirred during 1 h. Then, rods were centrifuged 15 min at 10000 rpm. The supernatant was discarded and the pellet was resuspended to a final volume of 5 mL with ultra-pure water. Finally, 50 µL of mPEG$_{5000}$ 1 mM were added again to the rods solution and stirred O/N. After rods functionalization, the solution was centrifuged three times in order to remove the excess of unreacted reagents and resuspended in a desired buffer. These, capped NRs won't be further functionalized with a peptide and will be used only for encapsulation into liposome (explained in the following section).

In the second strategy, cPEG$_{5000}$ was introduced in the second step. After NRs synthesis, the solution was centrifuged and the pellet was resuspended in 10 mL ultra-pure water. To this solution, 50 µL of mPEG$_{5000}$ 1 mM were added and the solution mixture was stirred for 10 min. PEGylated rods were centrifuged 10 min at 14000 rpm and redispersed again in 10 mL ultra-pure water. Then, 300 µL of cPEG$_{5000}$ 1mM were added and solution was stirred 1h. The final functionalized rods were centrifuged 10 min at 14,000 rpm and redispersed in the desired buffer.

In the third strategy, cPEG$_{5000}$ was directly coupled to the nanorods surface for higher carboxyl group incorporation. Au NRs were centrifuged and resuspended in 4.5 mL of a solution containing 200 µM K$_2$CO$_3$ and 10 µM HOOC-PEG$_{5000}$-SH. The final solution was stirred O/N. After functionalization, rods were centrifuged and redispersed in the desired buffer.

The fourth strategy was similar than the previous. Nanorods solution was concentrated to a final volume of 1 mL. To this solution, 10 mg of HOOC-PEG$_{5000}$-SH were added and stirred 24 h. Again, the functionalized rods were centrifuged and redispersed in the desired buffer.

In the fifth strategy, two rounds of cPEG$_{5000}$ were employed. In brief, nanorods solution was concentrated to a final volume of 1 mL, 10 mg cPEG$_{5000}$ were added to this solution and stirred O/N. Then, the rods were centrifuged and resuspended in 1 mL 90% ethanol.

The second step began with the addition of 1 mg HOOC-PEG$_{5000}$-SH and the solutions was stirred O/N again. Finally, rods were centrifuged and resuspended in buffer.

In all cases where cPEG$_{5000}$ was incorporated, the carboxyl groups were further activated and r$_8$k(CF) peptide was attached. The activation was performed by the addition of 50 µL EDC·Cl (2 mg/mL) and s-NHS (2 mg/mL) and stirred for 15 min in 0.1 MES buffer. Then, an excess of peptide was added and the reaction was left O/N under stirring. Finally, nanorods were washed five time by centrifugation in order to remove the excess of unreacted peptide and they were resuspended in PBS.

1.2.15. Endosomal release simulation

Liposome formation

The method used for liposomes formation was the freeze-thawed multilamellar vesicles (MLVs).[146] As indicated, the first step was the formation of MLVs. Lipids (EPC:cholesterol to a molar ratio of 5:1 and final weight of 5 mg) were dissolved in a mixture of MeOH:CHCl$_3$ (1:3 to a final volume of 1 mL). Then, solvent was evaporated under N$_2$ flow and lipids formed a thin film all around the Eppendorf wall. It is reported that the addition of an aqueous phase form the MLVs. In or case, 1 mL buffer solution containing 20 mM NaCl, 10 mM Tris, CF 40 mM and mPEG$_{5000}$ modified rods (1mL modified mPEG$_{5000}$ rods were centrifuged and resuspended in the buffer) was added to the lipids and MLVs were formed spontaneously. Vesicles were freeze-thawed 4 times and liposomes were formed. For obtaining a more homogeneous sample, liposomes were extruded through a polycarbonate 400 nm pore size membrane. Finally, unencapsulated CF was removed from liposome solution by SEC using a homemade packed Sephadex-75 column (2.8 x 50 cm). Particles were eluted from column by gravity using PBS.

Laser irradiation: preliminary results

Liposomes solution were seeded in a glass slide and covered with a cover slip forming a thin layer liposomes solution. A pulsed femtosecond Ti:Saphire laser (Leica SP5 Spectral Confocal) was used in this experiment as a laser source. This equipment was not

the most adequate to perform the experiment, but it was used as a proof-of-concept and the data obtained was considered as preliminary result. Irradiation was performed at different power intensities during a short period of time in scanning mode and using two photon mode.

1.2.16. Cell culture

The HeLa and fibroblasts 3T3 cells were incubated in Dulbecco's minimum essential medium (DMEM) supplemented with 10% fetal bovine serum (FBS), 2 mM *L*-glutamine, 100 U/mL penicillin and 100 mg/mL streptomycin in a humidified atmosphere of 5% CO_2 at 37 ºC. When a different condition was used, it was clearly specified.

1.2.17. Cytotoxicity assays

Gold NRs cytotoxicity was evaluated on HeLa and fibroblasts 3T3 cells using XTT assay. In brief, Cells were seeded in a 96-well plate at 5000 cells/well and incubated 24 h. Different rods solutions and concentration were added to the wells complemented with complete DMEM to a final volume of 150 µL and cells were further incubated for 24 h. After that, 50 µL of XTT and electron coupling reagent were added to each well (XTT/electron coupling reagent 1:50) and incubated during 4 h. Mitochondria from living cells are able to convert XTT to a soluble formazan in a few hours which can be quantified using a spectrophotometer at λ=475 nm. Finally, the plate was read at λ=475 nm in ELx800 BioTEK UV-Vis plate reader. Absorbance values were compared with the negative control (untreated cells). XTT solution was incubated with different rods concentration and its absorbance subtracted to the corresponding sample tested.

1.2.18. Flow cytometry

FACS was used to observe rods internalization as a first approximation. HeLa and fibroblasts 3T3 cells were seeded on a 24-well plate (30000 cells per well) and cultured for 24 h. The medium was removed and cells were incubated at different times with fresh

medium containing different rods concentrations. Then, cells were rinsed with PBS and trypsinized. After centrifugation, cells were resuspended in fresh cold DMEM medium and analyzed on a Gallios Beckman Coulter flow cytometer.

1.2.19. Spinning disk confocal microscopy

For spinning disk visualization experiments, fibroblasts 3T3 cells were seeded on MatTek glass-bottom dishes (10000 cells per dish) and incubated during 24 h. Then, different rods concentrations were added and incubated during different times (specified in section 1.2.7). Finally, cells were washed with fresh DMEM medium and analyzed in an Andor Tech. spinning disk microscope. All images were recorded in CO_2 and temperature-controlled conditions.

In some cases, collagen coating was used for better cell adherence and growth. Briefly, glass dishes were incubated O/N with a 10 µL/mL collagen type I solution from rat tail. Then, collagen was removed and cell were seeded.

For a better visualization of lysosomes and nuclei, Lysotracker® Red and Hoechst 33342 were used respectively. Lysotracker® was diluted to a concentration of 50-75 nM and 5 µL were added to each MatTek dish at the same time as NRs solution. Hoechst 33342 was diluted to 1 mg/mL and 1 µL was added 30 min before observing the images.

1.2.20. Cell fixation in electron microscopy

For cell fixation, HeLa cells were seeded in a 90 x 15 mm petri dishes and incubated at 37 ºC under 5% CO_2 to a minimum confluence of 70%. After 24 h internalization of rod solutions (0.1 nM to 0.5 nM final concentration), fresh medium replaced NRs solution. Then, a fixative containing 2.5% glutaraldehyde in 0.1 M PB buffer was added to the media (1:1) and let it sit for 10 min. Medium was removed and replaced by pure fixative for 30 min. The process was repeated and the fixative was left 60 more minutes. Cells were scrapped and placed in an Eppendorf tube with fresh fixative. Cell pellets were then fixed overnight in a refrigerator. After this, pellets were postfixed with 1% OsO_4 in PB for 90 min, dehydrated in a graded series of acetone and embedded in Epon.

Approximately 80 nm thick sections were cut, placed on carbon film supported by copper grids, stained with uranyl acetate and lead citrate and observed on a FEI Tecnai Spirit electron microscopy.

1.2.21. Cell irradiation

All laser experiments were performed with the collaboration and supervision of Dra. Dobryna Zalvidea, who created a specific laser set-up for our experiments. The homemade set up comprises a fiber laser (Fianium Femtopower 1W) generating 180 femtoseconds pulses at 1064 central wavelength, with repetition rate of 20 MHz. A 1/2 lambda plate and a polarizer were used to control the power reaching the sample plane. The beam was directed to a microscope (Nikon) using a galvoscanner system (Thorlabs) that allowed fine positioning of the IR beam. The diameter of the beam was increased using a telescope to fulfil the area occupied by cells on the dish. A collimated beam was sent to the sample controlling the exposure time with an external shutter (Thorlabs). A schematic representation of the set-up is shown in Figure 1.28.
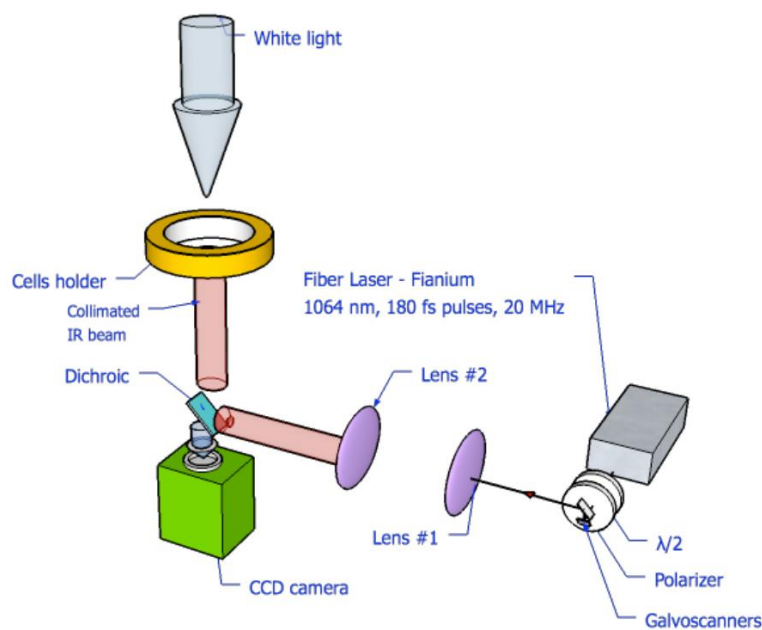
Figure 1.28. Schematic representation of the homemade setup laser used for cell irradiation.

Fibroblast were imaged using a spinning disk microscope (Andor Tech.) immediately before and after the irradiation experiment. They were exposed to the IR beam for $\Delta t =$ 10 min, 30 min and 1 h keeping the flux at 55-60 mW/cm$_2$.

1.2.22. siRNA attachment

As the rod surface contains positive charge from the CPP, negative PARP1 siRNA was incubated with the modified rods at RT. 0.33 µg RNA were incubated with 100 µL concentrated rod solution (usually 10 nM rod concentration) and stirred during 10 min. Then, rods were washed twice by centrifuging them at 10,000 rpm during 10 min. Supernatant was discarded and rods were resuspended in PBS buffer.

1.2.23. Western blot

Western blot technique was employed for the detection of PARP1 protein after laser irradiation. The procedure was the following:

Preparation of cell lysates

After irradiation, cells were incubated during 3-4 days allowing siRNA to silence PARP1 protein and completely degradation of the previous synthesized protein. Fibroblast were then trypsinized and resuspended in 1 mL complete DMEM medium. Cells were centrifuged 5 min at 1500 rpm, medium discarded and pellet resuspended in PBS buffer. Again, cells were centrifuged and PBS discarded. RIPA buffer containing 1 mM DTT and a protease inhibitor cocktail (cOmplete™, EDTA-free) was added to the pellet (50-80 µL) and agitated 20 sec. The Eppendorf tubes were incubated on ice during 15 min and then centrifuged 10 min at maximum speed. Supernatant was kept at -80 ℃ for protein quantification and posterior addition into acrylamide gel.

Protein quantification (BCA assay)

BCA assay was used following manufacturer specifications. Briefly, 200 µL working reagent (WR) was placed on a 96 well plate. Then, 10 µL of each sample and controls (BSA standards) were mixed with WR on a plate shaker during 30 sec. The plate was covered and incubated 30 min at 37 ºC. Finally, the plate was read at 562 nm in a UV-Vis plate reader.

Sample preparation for SDS-PAGE

Usually, 20 µg protein are loaded into acrylamide gel. First, lysates were mixed with an equal volume of 2x Laemmli sample buffer. Then, the lysates were boiled at 95 ºC during 5 min and the tubes were spun down for collection all the sample. When higher amount of lysates are needed, Laemmli 4x or 8x can be used.

Polyacrylamide gel preparation

Depending on the size of the protein studied, the percentage of acrylamide in the gel can vary. In our case, PARP1 protein appears at 118 kDa approximately, therefore 8% acrylamide gel was selected. The gel was 1.5 mm thick and prepared in two phases: first (at the bottom) the resolving gel was added and let it undisturbed during 30 min aprox for acrylamide polymerization. Then (on the top) the stacking gel was placed and 30 more min were needed for gel polymerization.

Recipe for 10 mL of 8% resolving gel:

Reagent	Amount
Distilled water	5.3 mL
40% Acrylamide solution	2 mL
1.5 M Tris buffer pH 8.8	2.5 mL
10% SDS solution	100 µL
10% APS solution	100 µL
TEMED	10 µL

Recipe for 5 mL of 6% stacking gel:

Reagent	Amount
Distilled water	2.9 mL
40% Acrylamide solution	0.75 mL
0.5 M Tris buffer pH 6.8	1.25 mL
10% SDS solution	50 µL
10% APS solution	50 µL
TEMED	5 µL

SDS-PAGE

Samples and molecular weight marker were loaded into acrylamide gel and it was run at 80 V during 15 min. Then, the voltage was increased at 120-150 V during 1 h. 1x Tris-glycine buffer was used as running buffer.

Nitrocellulose membrane protein transfer

The membrane was sandwiched as follows: sponge / 2x Whatman paper / gel / membrane / 2x Whatman paper / sponge. After ensuring no air bubbles were remaining between the gel and the membrane, the sandwich was submerged into transfer buffer and transferred to the tank. Usually, an ice bock is placed into the tank. The tank was place at 4 ºC and a current of 30 V was applied overnight for transferring the proteins to the membrane.

Blocking the membrane

5% skim milk in TBS solution was added over the membrane for avoiding unspecific interactions of primary and secondary antibodies. The solution was incubated with the membrane during 1 h at RT under agitation. Then, the membrane was washed three times with TBST buffer for 10 min.

Primary antibody incubation

PARP (46D11) rabbit mAb was diluted 1:1000 in TBST buffer and incubated with the membrane for 90 min at RT under agitation. Then, the membrane was again washed with TBST buffer 3 x 10 min.

β-actin mouse antibody was added to the membrane diluted 1:5000 in TBST buffer in order to detect β-actin protein, used as a control. Same as previous, the primary antibody was incubated 90 min at RT under agitation. Finally, the membrane was washed with TBST buffer 3 x 10 min.

Secondary antibody incubation

Similar to the previous step, the HRP-secondary antibodies (anti-rabbit or anti-mouse) was diluted 1:10000 in TBST buffer. Then, the membrane was incubated 90 to 120 min at RT under agitation. Again, the membrane was washed 3 x 10 min with TBST.

Membrane development

For developing the membrane, ECL Chemiluminescent kit from ThermoFisher Scientific was applied over the membrane following the manufacturer manual. Briefly, $500\,\mu L$ of reagent A were mixed with the same amount of reagent B and the final solution applied over the membrane during 1 minute. Then, the membrane was placed into the cassette and developed using ECL hyperfilms. Different exposure times were used depending on the intensity of the bands.

Chapter 2

The use of PLGA nanoparticles in gene therapy through the blood-brain barrier

2.1. Results and Discussion

2.1.1. PLGA nanoparticles synthesis and characterization

Several methods are employed for PLGA synthesis depending on the molecule to be encapsulated. In this chapter, two of the most used methods for DNA encapsulation are described. DNA plasmid encoding green fluorescent protein (GFP) was used as a model for its similitude with FXN plasmid (both of them contains 4.7 kpb approximately). In this chapter, the use of 'DNA' will be referred to plasmid DNA expressing the GFP unless otherwise stated.

2.1.1.1. Double emulsion method

A number of conditions were tested in order to achieve a stable PLGA formulation. In our hands, all the attempts lead to particle aggregation when the double emulsion technique was used to synthesize the NPs.

In some cases, aggregation appeared after sonication. In others, the formulations were not stable after centrifugation for buffer replacement or organic phase elimination. Sonication was applied in order to resuspend PLGA NPs after centrifugation, however, NPs loosed their integrity or aggregation persisted. An example of size and polydispersity index (PdI) obtained from PLGA NPs synthesis using the w/o/w double emulsion technique is summarized in Table 2.1.

Table 2.1. Mean size and PdI from PLGA NPs obtained by w/o/w double emulsion technique using DLS.

formulation	Mean size (nm)	PdI
w/o/w double emulsion 1	659.5	1.00
w/o/w double emulsion 2	323.3	0.971
w/o/w double emulsion 3	851.9	0.828

The variability on the mean size measurements of the same sample was indicative of particle aggregation. This fact was further confirmed by the PdI indicating a high heterogeneity of particles in the formulation. In the major part of the synthesis, DLS measurement could not be performed due to the presence of visible (by naked eye) aggregates. Evaluation of the NP prepared by this synthetic methodology gave similar results to those shown in Table 2.1. Therefore, due to low NPs homogeneity and high

particle size, we decided to discard this methodology and try to formulate PLGA NPs by the modified nanoprecipitation method.

2.1.1.2. Modified nanoprecipitation method

First of all, DNA encapsulation was attempt without complexation. As two different approaches were used for the synthesis of PLGA NPs, we decided to abbreviate the nomenclature based on the organic phase used. Thus, the organic solvents used were acetone and DMSO and we will refer to A and D, respectively. In A, PLGA polymer was dissolved in the organic phase and DNA in the aqueous phase containing the surfactant Pluronic® F68 (PF 68). In D, PLGA polymer and DNA were dissolved in the organic phase and the aqueous phase contained the surfactant Pluronic® F127 (PF 127). When the organic phase was added over the aqueous phase under stirring, NPs formed spontaneously. Table 2.2 summarize the mean size and polydispersity index (PdI) obtained from both synthesis (A and D) using the nanoprecipitation method.

Table 2.2. Mean size and polydispersity from PLGA NPs obtained by nanoprecipitation technique using DLS.

formulation	Mean size (nm)	PdI
Nanoprecipitation D	118.8	0.119
Nanoprecipitation A	121.2	0.502

From these results, almost no difference in the mean size can be observed. However, moderate polydispersity was observed on PLGA NPs by nanoprecipitation A. This fact can be attributed to various populations present in the sample.

For nanoprecipitation D method, the encapsulation efficiency (EE) was obtained by measuring the amount of non-encapsulated DNA after particles centrifugation. In this sense, the amount of encapsulated DNA was calculated as the difference between the total amount of DNA used and the non-encapsulated DNA detected by spectrophotometry. In any case, the EE was higher than 50-60%. These results were further confirmed by agarose gel electrophoresis (Figure 2.1). A band corresponding to GFP plasmid was obtained in the supernatant. This band had almost the same intensity than that obtained

after DNA extraction with $CHCl_3$ (see materials and methods for extraction details), meaning that there was still a high amount of non-encapsulated DNA.
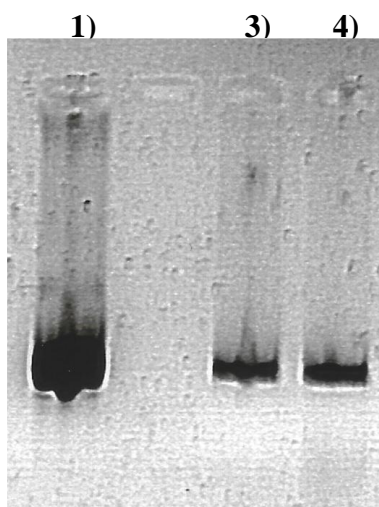
Figure 2.1. DNA detection by 0.8% agarose gel. Lane 1) naked DNA, lane 3) supernatant from PLGA NPs synthesized by nanoprecipitation D and lane 4) DNA extracted with chloroform from PLGA NPs synthesized by nanoprecipitation D.

For nanoprecipitation A method, the EE was even lower. A possible explanation for this poor encapsulation when using acetone could be the phase where the DNA was dissolved. In this case, DNA was dissolved in the aqueous phase. Consequently, the possibilities of DNA being encapsulated by the PLGA polymer were lower than in the case where the DNA was dissolved in the organic phase.

Higher EE can be obtained by introducing a positive polymer in the synthesis.[147] Positive charges can form complexes with the DNA negative charges. Thus, DNA can be condensed for a later surrounding of the slightly negative PLGA polymer. In this sense, the encapsulation efficiency can be increased up to 90%.

For this project, chitosan and bPEI were selected as positively charged polymers. In adition, r_8 (positive CPP used in chapter 1), C_{12}-CPP and Cho-CPP (lipopetides used in chapter 3 for complexing insulin) were used for DNA complexation.

Chitosan is a well-studied polymer used for its highly positive charge. One of its great properties is the ability of complexing DNA to form nanosized complexes. In this study, low molecular weight chitosan (Sigma) was used for that purpose. Nanoprecipitation A and D methods including minor modifications were used for PLGA:chitosan NPs synthesis. Different conditions are summarized in Table 2.3.

Table 2.3. Reagents used for PLGA:chitosan:DNA nanoparticles synthesized by nanoprecipitation A and D methods.

Method	*Solvent (mL)*	*PLGA (mg)*	*DNA (µg)*	*Chitosan (µg)*	*Surfactant (%w/v)*	*H₂O (mL)*
Nanoprecipitation D'	DMSO (0.5)	10	100	100	PF127 (0.5)	10
Nanoprecipitation A'	Acetone (2)	6	100	100	PF68 (1.5)	5

The methodology was similar to the previously used but including a previous step of DNA complexation. First, DNA was dissolved in the aqueous phase containing the respective surfactant (Table 2.3). Then, a solution of acidified chitosan (2 mg/mL acidified with 0.5% v/v acetic acid) was added to the aqueous phase and agitated 15 min for complex formation. Finally, the organic phase was added dropwise over the aqueous phase and stirred 3h. NPs were centrifuged and resuspended in PBS. Supernatant was used for quantifying DNA EE.

DLS was used to measure the mean size and PdI of both formulations obtaining values of 118.8±1.4 nm and 0.1 in PdI for the nanoprecipitation D' and 228.6±33.0 nm and 0.3 in PdI for the nanoprecipitation A'. In the case of nanoprecipitation D', the NPs mean size and PdI were similar to those particles without chitosan. On the contrary, in the case of nanoprecipitation A' there was an increase in mean size and PdI compared with the same particles without chitosan. These results are a clear example of how the organic phase can affect to the NPs properties. Nevertheless, both solvents were employed on the next NPs synthesis for comparing the characteristics of PLGA NPs obtained when using acetone or DMSO.

Again, quantification of non-encapsulated DNA was performed by measuring the absorbance at 260 nm. Calibration curve was made by adding different DNA/chitosan concentrations to the supernatant from blank NPs. In this case, the use of chitosan improved greatly the EE of both formulations obtaining values of more than 90% for PLGA NPs synthesized by nanoprecipitation D' method and around 90% for PLGA NPs synthesized by nanoprecipitation A' method.

These results were further confirmed by applying the supernatant and DNA extracted from PLGA NPs to a 0.8% agarose gel (Figure 2.2).
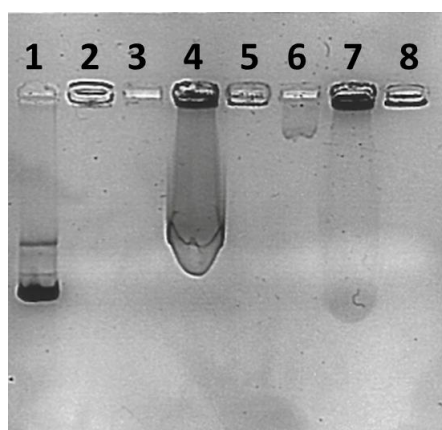
Figure 2.2. DNA detection by 0.8% agarose gel. Lane 1) naked DNA, lane 2) DNA:chitosan complex, lane 3) supernatant from PLGA NPs synthesized by nanoprecipitation D', lane 4) DNA extraction with 0.4% SDS solution from PLGA NPs synthesized by nanoprecipitation D', lane 5) DNA extraction with chloroform from PLGA NPs synthesized by nanoprecipitation D', lane 6) supernatant from PLGA NPs synthesized by nanoprecipitation A', lane 7) DNA extraction with 0.4% SDS solution from PLGA NPs synthesized by nanoprecipitation A', lane 8)) DNA extraction with chloroform from PLGA NPs synthesized by nanoprecipitation A'.

As shown in lanes 3 and 6 from Figure 2.2, DNA from supernatant of both formulations was detected by agarose gel electrophoresis. These result confirmed the previous ones obtained by spectrophotometry which indicated that DNA was encapsulated over 90% in both cases. The complex formed by DNA and chitosan was observed as a control in lane 2. As the negative charges from DNA were counteracted by the positively charged chitosan, the band did not move from the initial position and remained into the sample well.

When extracting the DNA from PLGA:chitosan NPs, two reported methodologies were used.[89,148] The first one,[148] used a 0.4% w/v sodium dodecyl sulfate (SDS) in order to disrupt PLGA:chitosan NPs after centrifugation. In the second strategy,[89] chloroform was added to the PLGA aqueous solution. Thus, PLGAwas solubilized in the chloroform releasing the DNA in the aqueous phase. In lanes 4 and 7 are shown DNA extracted by adding 0.4% SDS solution. As can be seen, an enormous band was detected, indicating a high percentage of DNA encapsulated. In lanes 5 and 8 are shown DNA extracted by adding chloroform and agitating the sample during 1 h. Again, a clear band appeared indicating DNA encapsulation but the intensity was lower than when extracted by SDS solution. A possible explanation could be the time employed for extracting the PLGA from NPs. In the next experiments, higher agitation times were used to ensure the pass of PLGA from aqueous phase to the chloroform organic phase. In this case, all DNA would

be released from NPs. These data led us to conclude that DNA was successfully encapsulated into PLGA NPs by using chitosan.

bPEI is a positive polymer used as a control for DNA transfection. Even its known toxicity at high concentrations, bPEI is still used in combination with other polymers presenting minor or no cytotoxicity.[149]

In this thesis, bPEI was used for complexing the DNA as a first step and then, PLGA was incorporated by two different strategies. In the first strategy (Figure 2.3 panel 1), bPEI was added over the surface of previously created blank PLGA NPs. Then, DNA was added forming the final formulation. In the second (Figure 2.3 panel 2), bPEI:DNA were complexed in the aqueous phase and PLGA (dissolved in the organic phase) was added dropwise in order to form the PLGA NPs.
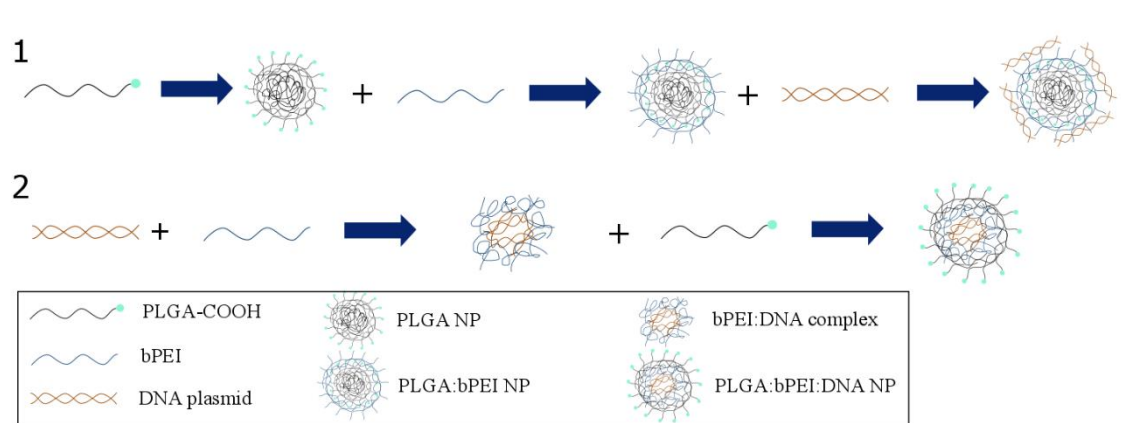
Figure 2.3. Shematic representation of two different strategies incorporating DNA and bPEI to PLGA NPs.

Similar to chitosan loaded NPs, the mean size of these formulations were between 150 nm to 200 nm. DMSO and acetone were also used as organic solvent obtaining similar results. Polydispersity values were low, 0.1-0.2, in all cases. Further characterization was performed when r_8 and THRre were incorporated into PLGA:bPEI:DNA formulations which are explained in section 2.3.4.

2.1.2. Peptide incorporation on the PLGA NPs

In order to promote the delivery of PLGA NPs through the BBB, r_8, and THRre were incorporated to the PLGA polymer. A glycine was incorporated at the *N*-terminal of THRre in order to introduce a primary amine (Figure 2.4). This primary amine was then coupled to the PLGA carboxyl group.
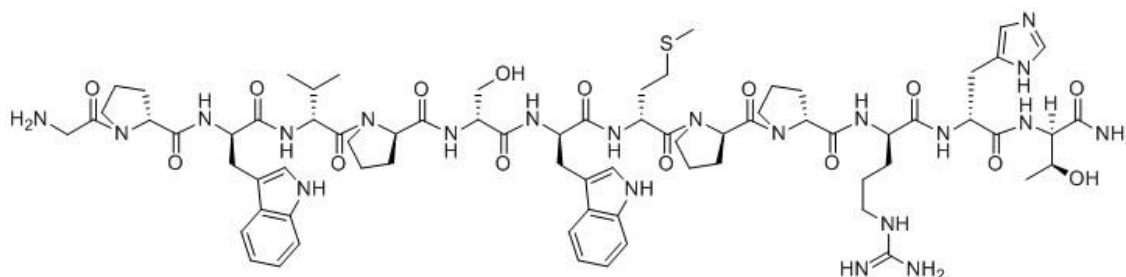
Figure 2.4. Schematic representation of glycine-THRre (GTHRre).

Two strategies were used to incorporate the peptides: in the first one, peptides were conjugated to the PLGA NPs surface after being synthesized. In the second strategy, peptides were conjugated to the PLGA polymer before the NPs synthesis. Then, the PLGA-peptide co-polymer was used for synthesizing the NPs.

The manipulation of PLGA nanoparticles in the first strategy is higher than in the second strategy. Once the nanoparticles were formed, carboxyl groups were activated with a soluble carbodiimide and then, both peptide (r_8 and THRre) were conjugated. Finally, the excess of coupling reagents and peptides had to be removed, usually by a few rounds of centrifugation. All these processes can alter the integrity of the nanoparticles and even the DNA encapsulated into it. Future transfection efficiency can be affected by this nanoparticle manipulation. Another problem can be the amount of peptide incorporated. By this strategy, the quantification of incorporated peptide could be tedious and can vary batch to batch, making the reproducibility of the assay even more difficult.

On the other hand, the conjugation of the peptide before creating the nanoparticles can be an alternative. The major problem of this strategy is the orientation of the peptides when the particles are formed. In the hypothetical case where the peptides are entrapped into the inner part of the particles, their effect would be highly reduced. However, the particles are not further manipulated after their preparation.

Both formulations were tested for transfection assays (section 2.2.3). The characterization of these formulations was not completely performed and screening of different conditions were tested in a cellular assay. In the future, deeper characterization of the formulations (DLS, TEM images, etc) and the number of peptides per particle need to be known.

2.1.3. PLGA nanoparticles transfection efficiency

As a proof-of-concept, DNA encoding the GFP was encapsulated into PLGA NPs. Various formulations were tested in different cell lines obtaining the best results in HeLa cells. In this section, different parameters of PLGA NPs synthesis were tested in order to achieve the higher transfection efficiency. This section is divided in three parts, depending on the positive polymer used in the synthesis.

2.1.3.1. PLGA NPs containing chitosan polymer

Chitosan was the first positive polymer selected for complexing the DNA. Chitosan:DNA complexes in combination with PLGA polymer.[150] In this section, four chitosan compositions were used for complexing the DNA (Table 2.4). Other parameters were also varied in order to obtain the best conditions for DNA transfection.

Table 2.4. Chitosan types and characteristics.

Chitosan type	Molecular weight (Da)	Deacetylation (%)
Oligosaccharide lactate	4,000-6,000	> 90
Low molecular weight	50,000-190,000	75-85
Protasan UP CL 113	50,000-150,000	75-90
From shrimp shells (low-viscosity)	-	-

The first chitosan type tested was low molecular weight chitosan, which was combined with DNA for creating the complex. Then, PLGA polymer was added dropwise and the particles were formed. The characterization of these particles was explained in section 1.2.1.2. In here, the transfection efficiency was tested.

In here, the same amount of DNA and chitosan (w/w) were used for creating the complexes. Nanoparticles were synthesized by both methods previously mentioned (nanoprecipitation A' and nanoprecipitation D'). Once characterized, the particles were incubated 2 h in HeLa cells, fibroblast cells and bEnd.3 cells. After this time, NPs solution was removed and replaced by fresh complete DMEM medium. After 24-48 h, fluorescence from the cells was measured, only the controls being positive (Figure 2.5).

A)   B)   C)
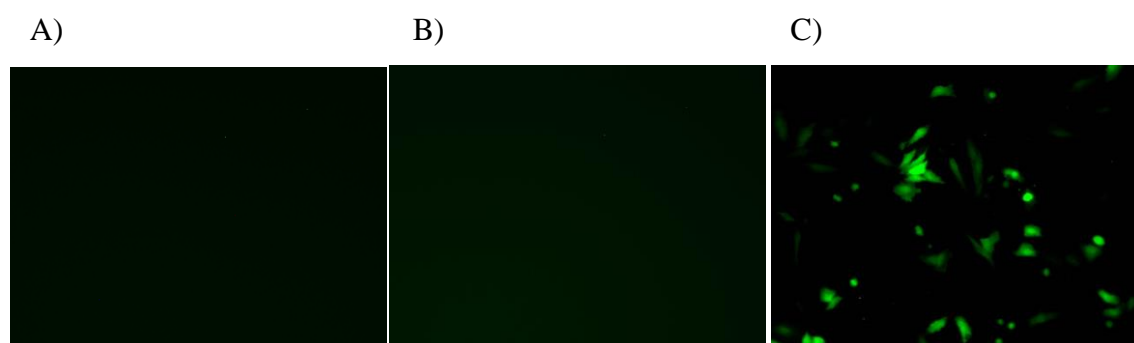
Figure 2.5. Fluorescent microscopy images (excitation at green range) obtained in HeLa cells from DNA transfection of: A) PLGA:chitosan:DNA NPs synthesized by nanoprecipitation D' method, B) PLGA:chitosan:DNA NPs synthesized by nanoprecipitation A' method and C) Superfect:DNA complex as a transfection control.

After these negative results, optimization of PLGA formulation was proposed; thus different parameters from the synthesis were modified. Various surfactants were used (PVA, PF68 and PF127), the amount of surfactant used was varied from 0.5% to 1.5% w/v, various ratios between chitosan and DNA were tested, the amount of PLGA added on the synthesis and even the NPs incubation time were also studied. In our hands, any DNA transfection was achieved after all these modifications.

Poor particle internalization was the first hypothesis we decided to prove, therefore, the use of a peptide for better particle was proposed. As a CPP vector, r_8 was attached to the particles surface in order to achieve better transfection efficiency. The peptide was incorporated by two strategies: physical mixtures forming electrostatic complexes with the negative charges of PLGA and covalently bound to the carboxyl groups from PLGA. In this sense, GTHRre was also covalently incorporated to test more variables.

These variations did not improve the DNA transfection in any of the cases. Therefore, chitosan polymer was varied by the commercially available chitosan oligosaccharide lactate, Protasan UP CL 113 and chitosan low viscous. All the previous formulations were tested with these chitosan types. Once again, fluorescence was not detected after NPs

incubation indicating that DNA transfection was not achieved. In all of these last formulations, no further characterization was performed. As none of the formulations was successful in transfection, only a screening of the compositions and trials for transfection assay were performed.

Another important factor affecting the transfection of PLGA NPs was the centrifugation process after particle formation. This process was needed for completely elimination of the organic solvent and the excess of unreacted reagents. After centrifugation of many formulations, difficulties in nanoparticle resuspension were observed and, in a few cases, sonication was needed for disaggregating the pellet formed. This nanoparticle aggregation could affect to the internalization of the particles into the cells, therefore, other strategies were tested for overcoming this problem.

The use of Micron centrifugal filter devices was thought as a possibility for exchanging the buffer without forming aggregates. The formulations were also tested without any modification, directly from the synthesis. Although great efforts were performed in order to optimize the formulations, no fluorescence was observed in any of the cases when incubated with HeLa or fibroblast cells.

Finally, more simplified formulations (only the complexes between DNA and chitosan) were tested. It is described that chitosan particles containing DNA are able to internalize into the cells and transfect them.[151] In Table 2.5 summarizes all the conditions tested. As previously explained, the complexes were formed by adding the chitosan over an aqueous solution containing DNA and agitating during 15 min.

Table 2.5. Conditions used for creating chitosan:DNA complexes. Incubation in HeLa cells.

Chitosan type	*Amount (μg)*	*DNA (μg)*	*Surfactant (%w/v)*	*Aqueous phase*	*Incubation time (h)*
Low molecular weight	10/50/100	1/5/10	PF68/ PF127 (0.5)	H_2O/PBS	2/3/24
Oligosaccharide lactate	10/50/100	1/5/10	PF68/ PF127 (0.5)	H_2O/PBS	2/3/24
Protasan UP CL 113	10/50/100	1/5/10	PF68/ PF127 (0.5)	H_2O/PBS	2/3/24
Low viscous	10/50/100	1/5/10	PF68/ PF127 (0.5)	H_2O/PBS	2/3/24

In our hands and after testing all the conditions summarized in Table 2.5, the conclusion was that chitosan:DNA complexes were not able to transfect HeLa cells. Therefore, the use of PLGA over these formulations had no effect for transfecting the cells. Analysis of various chitosan formulation have been reported as high transfection efficiency but those chitosan were modified in each research group.[152] Searching into the chitosan characteristics, the most effective were those containing a degree of deacetylation, molecular weight and amine-to-phosphate ratio of 92–10–5 and 80–10–10, respectively. The modification of chitosan supposed to us another variable to optimize; consequently, this approximation was not considered and other polymers or peptides were tested.

2.1.3.2. PLGA NPs containing r_8 and analogs

Poly (*L*-lysine) is a positive polymers that has been widely investigated as a non-viral gene delivery vector.[153] Similar to poly (*L*-lysine) in chapter 1, oligoarginine (r_8) was presented as CPP and it was used to promote rods internalization into cells. As a highly positive peptide, r_8 complexed DNA. In addition, two analogs which will be explained in detail in chapter 3 (C_{12}-CPP and Cho-CPP), were used for DNA complexation. It is described that the modification of CPPs with fatty acids can encapsulate DNA or RNA in the form of nanomicelles, thus achieving higher transfection.[154]

As in the case of chitosan, only the complex between DNA and the peptides were tested for transfection assays. A screening of various formulations were assayed in HeLa, fibroblasts and bEnd.3 cells. In Table 2.6, there is a summary of the modifications used for DNA complexation.

Table 2.6. Conditions used for creating CPP analogs/DNA complexes. Incubation was performed in HeLa, fibroblasts and bEnd.3 cells.

CPP analog	Amount (μg)	DNA (μg)	Aqueous phase	Incubation time (h)
r_8	25/50/250	5	H_2O/PBS/HEPES buffer	2/3
C_{12}-CPP	25/50/250	5	H_2O/PBS/HEPES buffer	2/3
Cho-CPP	25/50/250	5	H_2O/PBS/HEPES buffer	2/3

Once again, any of the formulations was able to transfect the cells lines used. A possibility is that the complex was internalized by the effect of the CPP; but DNA was not able to arrive to the nucleus. The effect of pH in the endosomal or lysosomal compartments can disrupt the complex, therefore DNA remained entrapped. In order to overcome this possible drawback, recently, a new class of CPPs capable to transport siRNA into cytosol has been described.[155]

2.1.3.3. PLGA NPs containing bPEI polymer

bPEI polymer is well described as an efficient gene delivery agent.[156] In here, bPEI was proposed for improving the transfection efficiency of our formulations. First of all, bPEI:DNA complexes (3:1 w/w) were synthesized and tested in HeLa, fibroblasts 3T3 and bEnd.3 cells (Figure 2.6).

A)   B)   C)
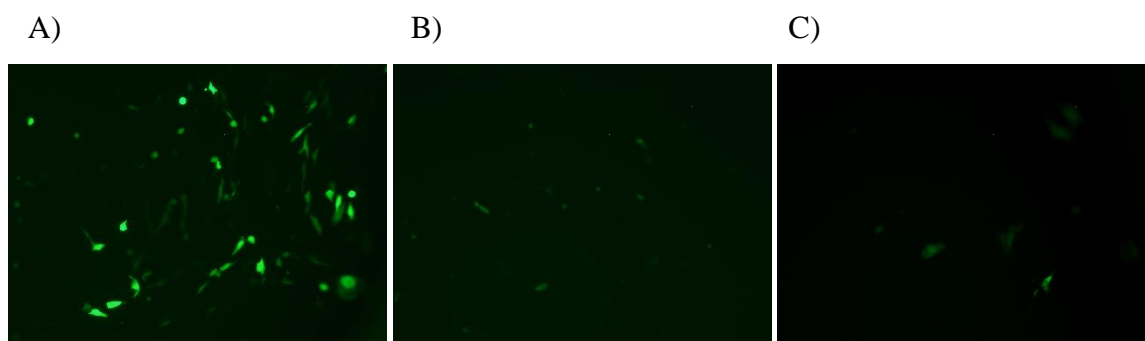
Figure 2.6. Fluorescent microscopy images (excitation at green range) obtained from bPEI:DNA (3:1 w/w) complexes in A) HeLa cells, B) fibroblasts 3T3 cells and C) bEnd.3 cells. Incubation time was 2 h.

As can be observed in Figure 2.6, the transfection efficiency of bPEI:DNA complexes was higher in HeLa cells compared to the other cell lines. Transfection was also achieved on fibroblasts cells but bEnd.3 cells were almost no transfected. This was a clear evidence that the transfection efficiency depends on the cell line used. Therefore, for further transfection assays with GFP encoding DNA plasmid, HeLa cells were preferentially used. Although HeLa cells were selected by its robustness, the optimized formulations will be tested in a more specific brain-related cell line such as glioblastoma (see section 2.3.4).

At this point and taking into account that the use of bPEI enhanced the DNA transfection, PLGA was incorporated into the synthesis. Following the methodology from

reference Seo *et al.*,[157] blank PLGA nanoparticles were synthesized and then, the complex bPEI:DNA was added on the particles surface. These final NPs were then incubated 3h in HeLa cells and the fluorescence was measured at 24-48 h after transfection (Figure 2.7).
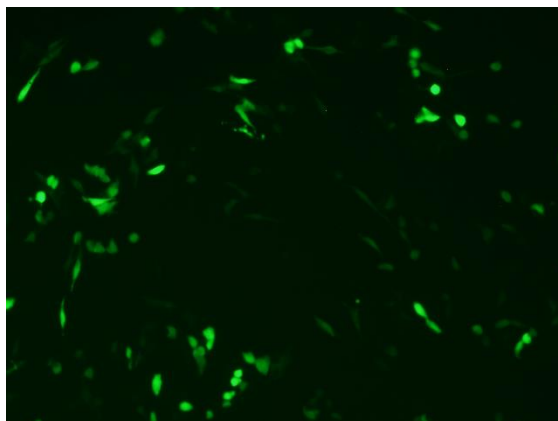
Figure 2.7. Fluorescent microscopy images (excitation at green range) obtained from bPEI:DNA (3:1 w/w) complexes added on blank PLGA NPs surface. Incubation time was 3 h in HeLa cells.

In the same ways as in bPEI:DNA complexes, the PLGA NPs containing bPEI:DNA transfected perfectly HeLa cells. The problem of this formulation is that the carboxyl groups from PLGA cannot be further modified. Therefore, the incorporation of the CPP or BBB-shuttle to promote the transport through the BBB was not possible. To overcome this problem, bPEI:DNA complexes were formed and PLGA was added in the same way as in chitosan formulations. A screening of various compositions was done in HeLa cells (Table 2.7).

Table 2.7. Conditions used for creating PLGA:bPEI:DNA nanoparticles. Incubation time was 2 h in HeLa cells.

PLGA type	*Amount (mg)*	*DNA (µg)*	*bPEI (µg)*	*Organic phase*	*Aqueous phase*	*Surfactant*
PLGA	1.5/3/6	50	150	DMSO/Acetone	H_2O	PF68/ PF127
PLGA-r₈	1.5/3/6	50	150	DMSO/Acetone	H_2O	PF68/ PF127
PLGA-GTHRre	1.5/3/6	50	150	DMSO/Acetone	H_2O	PF68/ PF127
PLGA-r₈/ PLGA-GTHRre	1.5 (0.75+0.75) 3 (1.5+1.5) 6 (3+3)	50	150	DMSO/Acetone	H_2O	PF68/ PF127

The conditions summarized in Table 2.7 were employed to synthesize 48 PLGA formulations. Nanoprecipitation A' (24 formulations) and D' (24 formulations) methods were used in this case. Minor modifications were introduced in both methods. For nanoprecipitation D' method, the aqueous phase final volume was 10 mL and the surfactant was added at 0.5% w/v. When nanoprecipitation A' methods was used, the aqueous phase final volume was 5 mL and the surfactant was added at 1.5% w/v.

In almost every condition tested, fluorescence was observed 24-48 h post-transfection. Analyzing the results, PLGA NPs formulated by both methods had similar transfection efficiency. The introduction of PLGA-peptide co-polymer to form NPs increased transfection efficiency compared to particles synthesized only with PLGA. The first trend detected was that particles containing PF127 had higher transfection efficiency than those containing PF68. Another tendency observed was that when decreasing the amount of PLGA used, the transfection efficiency increase. Almost no differences in transfection were observed between formulations when using 3 mg and 1.5 mg PLGA-peptide. However, when 6 mg PLGA-peptide was used, the transfection efficiency decreased. In these formulations, PLGA served to protect DNA from degradation and also for peptide incorporation. When decreasing PLGA amount, the BBB-shuttle or the CPP incorporated to the NPs surface is lower; so the possibilities to cross the BBB by the effect of peptides will be reduced. However, by increasing PLGA amount, the transfectivity obtained was lower. An optimal ratio of PLGA:DNA is crucial to synthesize PLGA NPs with the best transfection and transport characteristics. Consequently, a ratio around 50-60:1 (PLGA:DNA, w/w) was selected for further assays. After these results, most representative formulations, synthesized by nanoprecipitation method containing PF 127, were characterized by DLS and Z-potential (Table 2.8).

Table 2.8. Mean size and Z-potential of various PLGA:bPEI:DNA NPs synthesized by nanoprecipitation method were characterized by DLS. PF 127 was added as a stabilizer surfactant.

PLGA NPs formulation	*Mean size (nm)*	*PdI*	*Z-potential (mV)*	*Z deviation*	*Solvent*
PLGA-r_8:bPEI:DNA (60:3:1)	107.6±2.7	0.2	6.8±1.1	10.2	
PLGA-GTHRre:bPEI:DNA (60:3:1)	146.3±4.4	0.1	3.3±0.3	12.8	DMSO
PLGA-r_8/PLGA-GTHRre:bPEI:DNA (30/30:3:1)	194.9±3.2	0.3	3.5±0.6	9.9	
PLGA-r_8:bPEI:DNA (60:3:1)	200.3±6.6	0.4	19.4±1.3	13.4	
PLGA-GTHRre:bPEI:DNA (60:3:1)	234±46	0.4	20.9±3.4	9.4	Acetone
PLGA-r_8/PLGA-GTHRre:bPEI:DNA (30/30:3:1)	214.4±5.2	0.3	13.7±1.2	7.0	

When DMSO was used, particles size were different depending on the PLGA-peptide. The polydispersity obtained was low, meaning a homogeneous sample. In the other hand, when acetone was used, the particle mean size was around 200 nm in all cases. In this case, the PdI was a bit higher indicating that the sample was more heterogeneous. In all cases, Z-potential was positive. This value was higher when acetone was used. Notably, the deviation was high meaning a heterogeneous distribution of positive charges around PLGA NPs surface.

By comparing the formulations when using different PLGA-peptide, the use of r_8 increased the transfection efficiency in most of the cases. In Figure 2.8 is shown the fluorescence obtained by fluorescence microscopy from representative formulations assayed in HeLa cells.
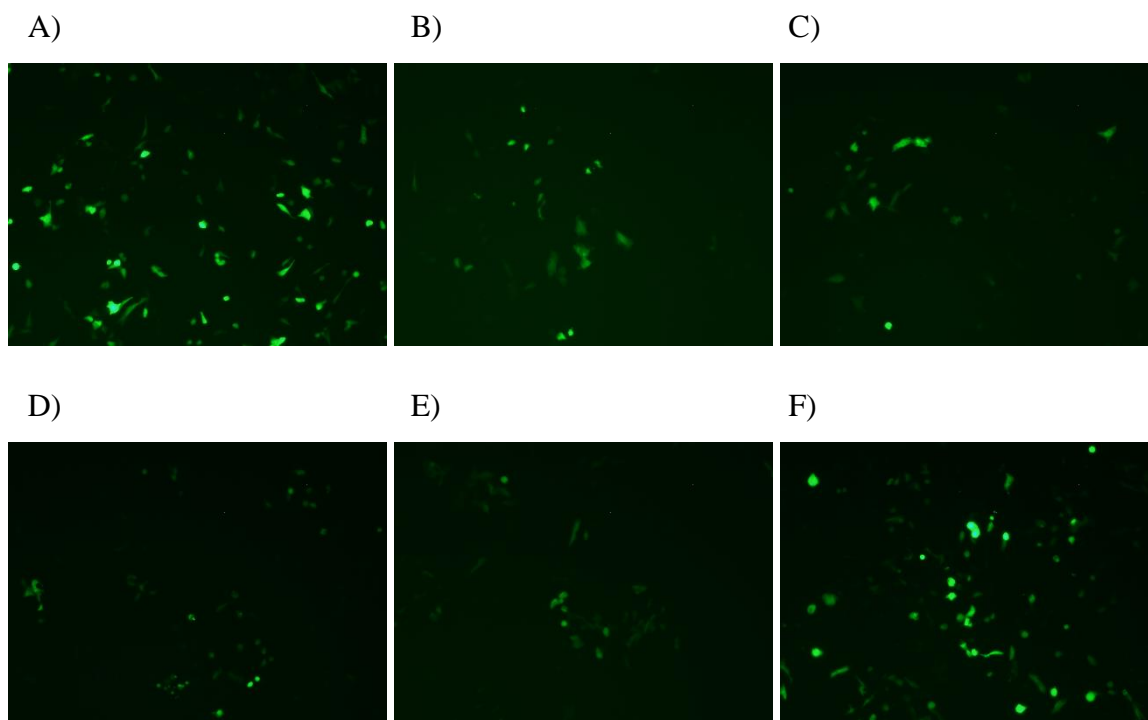
Figure 2.8. Fluorescent microscopy images (excitation at green range) obtained from various PLGA:bPEI:DNA nanoparticles in HeLa cells. Incubation time was 2-3 h. A) PLGA-r_8:bPEI:DNA (60:3:1) NPs synthesized by nanoprecipitation D' method, B) PLGA-GTHRre:bPEI:DNA (60:3:1) NPs synthesized by nanoprecipitation D' method, C) PLGA-r_8/PLGA-GTHRre:bPEI:DNA (30/30:3:1) NPs synthesized by nanoprecipitation D' method, D) PLGA-r_8:bPEI:DNA (60:3:1) NPs synthesized by nanoprecipitation A' method, E) PLGA-GTHRre:bPEI:DNA (60:3:1) synthesized by nanoprecipitation A' method, F) PLGA-r_8/PLGA-GTHRre:bPEI:DNA (30/30:3:1) NPs synthesized by nanoprecipitation A' method.

As shown in Figure 2.8, transfection of most representative samples worked perfectly in HeLa cells. DNA transfection was finally achieved by incorporating bPEI into the nanoparticles. At this point and encouraged by the great preliminary results, the formulations were sent to Madrid in order to assay the transfection potential in brain-derived cell lines (section 2.3.4).

2.1.4. Transfection assay in brain-derived cell lines

In collaboration with Prof. Javier Díaz-Nido from Centro de Biología Molecular Severo Ochoa (UAM-CSIC) in Madrid (Spain), we are trying to develop a system in order to transport frataxin DNA plasmid through the BBB. In their group, they have developed the technology to test the formulations in cell lines related Friedreich's ataxia. But first and as a proof-of-concept, some of our PLGA:bPEI:DNA NPs were tested in glioblastoma G16-9 (Figure 2.9).

This time, frataxin DNA plasmid was complexed with bPEI and surrounded by modified PLGA. Similar formulations, which were positive transfecting GFP, were synthesized. The same transfection procedure as in HeLa cells was employed for the NPs containing frataxin DNA plasmid. After 48h transfection, cells were trypsinized and lysed. Then, proteins from lysates were detected by western blot for frataxin protein identification (Figure 2.9).
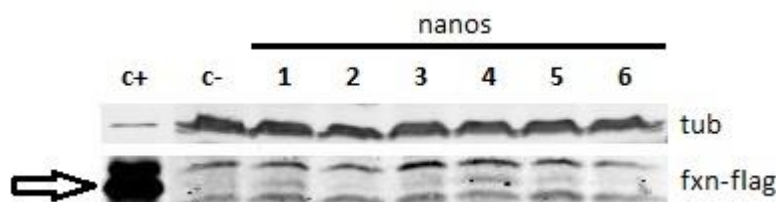
Figure 2.9. Transfection assay of various PLGA:bPEI:DNA formulations encapsulating frataxin plasmid synthesized by nanoprecipitation A' method. 1) PLGA-r_8:bPEI:DNA at 120:3:1 (w/w/w), 2) PLGA-r_8:bPEI:DNA at 30:3:1 (w/w/w), 3) PLGA-GTHRre:bPEI:DNA at 120:3:1 (w/w/w), 4) PLGA-GTHRre:bPEI:DNA at 30:3:1 (w/w/w), 5) PLGA-r_8/PLGA-GTHRre:bPEI:DNA at 60/60:3:1 (w/w/w), 6) PLGA-r_8/PLGA-GTHRre:bPEI:DNA at 15/15:3:1 (w/w/w). Untreated cells were used as negative control (c-) and cells transfected with Superfect reagent as positive control (c+).

As shown in Figure 2.9, for the formulation 1, 3, 4 and 5 appeared a positive band, the 4 being the most intense. The two bands obtained in all samples were unspecific antibody recognition. Only the band in the middle indicated frataxin expression. These were preliminary results and need to be repeated and improved but the detection of frataxin indicated to us to keep working in this direction. Further NPs characterization and optimization is still needed and will be our focal point in the future experiments.

2.1.5. BBB cellular model

Taking all these results together, next step was to test our formulations in a BBB *in vitro* cell based human model.[95] Perycites and human endothelial cells derived from pluripotent stem cells were seeded in 12-well plate and on the inserts respectively. After 7-8 days, NPs and lucifer yellow (LY), as a control of paracellular permeability, were added to the donor sides and incubated during 2 h. Then, the acceptor solutions were collected and LY Papp was calculated to check membrane integrity (Equation 2.1 in section 2.4.11). Papp from all formulations ranged between $10 \cdot 10^{-6}$ to $20 \cdot 10^{-6}$ cm/s. When LY Papp is higher than $15 \cdot 10^{-6}$ cm/s it is considered a sign of membrane disruption. In our case, only in a few cases it was above this limit. Therefore, and taking into account this was a preliminary result, all the values were considered. Finally, the acceptor wells were lyophilized and DNA was extracted from NPs with chloroform during 12 h. Samples were then loaded onto a 0.8% agarose gel to detect DNA bands (Figure 2.10).
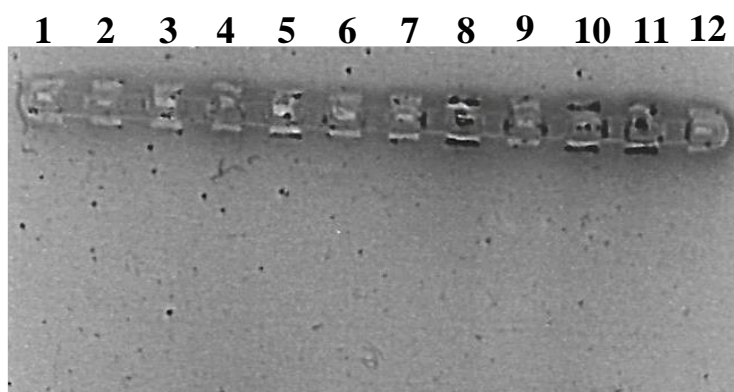
Figure 2.10. DNA bands detection in a 0.8% agarose gel. 1) PLGA-r$_8$:bPEI:DNA at 60:3:1 (w/w/w) by using nanoprecipitation A' method, 2) PLGA:bPEI:DNA at 60:3:1 (w/w/w) by using nanoprecipitation A' method, 3) PLGA-r$_8$/ PLGA-GTHRre:bPEI:DNA at 30/30:3:1 (w/w/w) by using nanoprecipitation A' method, 4) PLGA-r$_8$:bPEI:DNA at 60:3: (w/w/w) by using nanoprecipitation D' method, 5) PLGA-GTHRre:bPEI:DNA at 60:3:1 (w/w/w) by using nanoprecipitation D' method, 6) PLGA-r$_8$/ PLGA-GTHRre:bPEI:DNA at 30/30:3:1 (w/w/w) by using nanoprecipitation D' method, 7) Double concentrated PLGA-r$_8$:bPEI:DNA at 60:3:1 (w/w/w) by using nanoprecipitation A' method, 8) Double concentrated PLGA-GTHRre:bPEI:DNA at 60:3:1 (w/w/w) by using nanoprecipitation A' method, 9) Double concentrated PLGA-r$_8$/ PLGA-GTHRre:bPEI:DNA at 30/30:3:1 (w/w/w) by using nanoprecipitation A' method, 10) Double concentrated PLGA-r$_8$:bPEI:DNA at 60:3:1 (w/w/w) by using nanoprecipitation D' method, 11) Double concentrated PLGA-GTHRre:bPEI:DNA at 60:3:1 (w/w/w) by using nanoprecipitation D' method, 12) Double concentrated PLGA-r$_8$/ PLGA-GTHRre:bPEI:DNA at 30/30:3:1 (w/w/w) by using nanoprecipitation D' method.

Samples from column 7 to 12 were two times more concentrated to test NPs concentration effect. As explained before, when bPEI is electrostatically conjugated to the DNA, the complex cannot run into the agarose gel, therefore we will find the bands at the top of the gel.

As it is shown in Figure 2.10, bands from lanes 5, 8, 10 and 11 can be easily identified indicating the detection of DNA. Curiously, the bands were detected in all cases when the NPs contained only PLGA-GTHRre co-polymer in both conditions (DMSO or acetone as organic solvent). Additionally, when the NPs concentration was doubled, DNA from NPs containing r_8 was also identified.

It should be also mentioned that the most concentrated samples were those which LY Papp was higher. Therefore, some signs of toxicity were detected. We hypothesize that toxicity is originated from an incomplete organic solvent elimination. In order to overcome this problem, the buffer from the NPs formulations will be exchanged by using prepacked desalting columns. Another possible explanation could be that the toxicity is derived by the use of bPEI polymer as it is well reported.[158] This problem can be also overcome by the use of desalting columns which can eliminate the free PEI mainly responsible of cytotoxicity.[159]

These promising results guide us to continue in this direction. Further NPs characterization is still needed. Toxicity assays, transfection in different brain-derived cell lines and even some *in vivo* experiments are also planned.

2.2. Materials and Methods

2.2.1. Materials

Reagents, solvents and materials used in PLGA nanoparticles chapter are listed below. Plasmids (GFP and frataxin plasmid) were obtained from the Protein Expression Core Facility at IRB.

Supplier	Materials
Albatros Chem Inc	TBTU
AMRESCO®	40% acrylamide solution
Applied GL Biochem	HOAt
BD Discardit II BD Plastipak	Syringes (1,2, 5, 10 and 20 mL)
Biochrom A.G.	Gentamycin 10 mg/mL and trypsin-EDTA
Biotium	GelRed® nucleic acid stain
Corning Costar	12 well-plates and 96 well-plates, culture flasks, petri dish and BD matrigel growth factor reduced matrix
Deltalab	Falcon tubes
EMD Millipore	Filters 0.45 µM (PVDF) and micron centrifugal filter devices (MWC: 100000)
Eppendorfs	Eppendorf tubes
Fluka	Chitosan low-viscous
Gibco™	Fetal bovine serum (FBS)
Innoprot	Endothelial cells medium (ECM)
Iris Biotech	All amino acid derivatives needed for the synthesis of r_8 and GTHRre and EDC·HCl
KaliChemie	TFA
Life technologies	Quant-iT™ PicoGreen® dsDNA assay kit and DNA gel loading dye (6X)
Malvern	Disposable folded capillary cells
Novabiochem	PyBOP and NHS
NovaMatrix	Protasan Ultrapure CL 113
Panreac	DMF and DMSO
PCAS BioMatrix Inc.	H-Rink amide ChemMatrix® resin

PIERCE	s-NHS
Qiagen	Superfect transfection reagent
Roche	Agarose MP
Sciencell™	Endothelial cell growth supplement
Scharlab	Syringes (2, 5, 10 and 20 mL) fitted with polyethylene porous disk for peptide synthesis
Scharlau	HCl and methyl *tert*-butyl ether
SDS	Acetone, DCM, ACN, MeOH and piperidine
Sigma-Aldrich	PLGA (50:50, MW: 24000-38000), DIEA, DIC, ninhydrin, triisopropylsilane, Pluronic®-F68, Pluronic®-F127, PVA (MW 31000-50000, 98-99% hydrolyzed), chitosan oligosaccharide lactate (MW: 5000 Da), chitosan low molecular weight, DMEM, NaOH, MES, hyperfilm ECL, *L*-DTT, APS, TEMED and gelatin from porcine skin
ThermoFisher Scientific	BCA protein assay kit, RIPA lysis and extraction buffer and Pierce™ ECL western blotting substrate

2.2.2. Peptide synthesis and characterization

Synthesis and characterization of the peptides used in this chapter were performed following the same methodology explained in the chapter 1. In this case, apart of the CPP r_8, we used a BBB-shuttle (GTHRre: Gpwvpswmpprht) to incorporate them to the nanoparticles surface. Annex II can be consulted for characterization details of each peptide.

2.2.3. PLGA NPs synthesis

Double emulsion technique

In the first method used,[89] 100 µL Tris–EDTA buffer (pH 8.0) was emulsified into 1 mL ethyl acetate containing 20 mg PLGA by sonication (Branson 1510 Ultrasonic cleaner) for 1 minute. The resulting primary emulsion was added to 5 mL of 1.0% (w/v) Pluronic®-F127 (50 mg) aqueous solution and sonicated for 1 minute to form a double emulsion (water-in-oil-in-water). The resultant emulsion was then poured into 15 mL magnetically stirring 0.5% (w/v) Pluronic®-F127 (75 mg) aqueous solution and agitated O/N. Ethyl acetate was removed under evaporation. The final solution was centrifuged at $16000 \times g$, 4°C for 30 min and resuspended in PBS followed by filtering through 0.45-µm PVDF filter. DNA was incorporated to the NPs surface by adding 100 µg GFP dropwise to the NPs solution and stirred 1h.

In the second method, DNA was also incorporated at the NPs.[160] Briefly, 5% w/v PLGA (50 mg) was dissolved in 1 mL DCM/acetone (1:1) and stirred 30 min. For preparing the aqueous phase, 0.2% w/v chitosan (400 µg) were dissolved in 1 mL sodium acetate buffer (3 M, pH 5.2). Separately, a 5% PVA (50 mg) was dissolved in 1 mL water. Then, 1 mL from both aqueous solutions were mixed. The organic phase was added to the aqueous solution and the sample was sonicated 4 min at 30% intensity in a Sonics Vibracell VCX 750 (3 mm Microtip). Finally, the organic solvent was evaporated under vacuum and the NPs were centrifuged twice at 16000 g during 30 min (twice) and resuspend in water. For DNA incorporation, 100 µg GFP was added dropwise to the NPs solution and stirred 1h.

In the last case, DNA was firstly complexed with $CaCl_2$ and then the NPs were formed.[161] In short, 8 mg PLGA were dissolved in 0.75 mL DCM:ethyl acetate (1:1). 100 µg DNA was dissolved in 125 µL $CaCl_2$ 2.5 M and agitated 5 min. Then, 125 µL of a pH 7 buffered solution (0.28 M NaCl, 10 mM KCl, 10 mM Na_2HPO_4, 40 mM HEPES) were added to the aqueous phase. The organic phase was poured into the aqueous phase and emulsified 50 s at 30% in the sonicator. This primary emulsion was added dropwise to 3 mL 1% (w/v) PVA solution and the mixture was sonicated 50 s followed by evaporation of organic solvents. NPs were centrifuged 16000 g at 4ºC for 90min. Supernatant was kept for DNA quantification and NPs resuspended in water.

Modified nanoprecipitation method

The basis of the method used was the same in all cases, but different methods were used depending on the polymer used for DNA condensation, the organic solvent used for solubilizing the PLGA or surfactant used for particle stabilization:

<u>Chitosan for DNA complexation</u>

In this method defined as nanoprecipitation D,[89] different amounts of PLGA (50:50, MW: 24000-38000), ranging from 1 mg to 10 mg, were solubilized in 0.5 mL DMSO and added drop by drop into a continuous stirring 10 mL aqueous solution containing 0.5% w/v Pluronic® F127. After 3h stirring, NPs were centrifuged 30 min at 16000 g. The supernatant was removed and NPs were resuspended in PBS buffer to a final volume of 1 mL. For DNA encapsulation, different amounts of DNA were solubilized in the DMSO phase. In this case, the supernatant was kept for DNA quantification. When chitosan was used in this synthesis, DNA and chitosan, at different ratios, were added to the aqueous phase and stirred 10 min for complete complexation. This last method was defined as nanoprecipitation D'.

The second method (defined as nanprecipitation A) uses acetone for polymer solubilization.[148] In short, PLGA was solubilized in 2 mL acetone and added dropwise to an acidified (0.25% v/v acetic acid) aqueous solution containing 1.5% w/v Pluronic®-F68. Same as previous, nanoparticles were centrifuged 30 min at 16000 g. The supernatant was removed and NPs were resuspended in PBS buffer to a final volume of 1 mL. For DNA encapsulation, different amounts of chitosan and DNA were added into

the aqueous solution. The previous method was defined as nanoprecipitation A'. Again, encapsulated DNA was quantified by measuring the DNA in the supernatant.

<u>bPEI for DNA complexation</u>

Similar to chitosan, bPEI was used for DNA complexation. Minor modifications of nanoprecipitation A' and D' were employed for NPs formulation.

In nanoprecipitation D' and A', PLGA was dissolved on DMSO and acetone, respectively. The aqueous phase was composed by PF 68 or PF F127 at 0.5, 1 or 1.5% w/v aqueous solution. First, DNA was complexed by bPEI at 1:3 w/w ratio and the solution was stirred 5 min. Then, the organic phase containing PLGA (ranging from 1 to 10 mg) was added to the aqueous phase by two different methods: 1) dropwise and under stirring at 1000 rpm; 2) homogenizing the sample at 13000 rpm with an Ultra Turrax T-25 basic (IKA) during 1 min. The NPs were formed spontaneously and the solutions were filtered through a 0.45 µm filter.

In another strategy blank PLGA NPs were synthesized by the nanoprecipitatin method. Different amounts of bPEI were added to the NPs.[157] In brief, PLGA solutions were diluted in HEPES-NaOH (pH 7) to a final PLGA concentration of 0.1 mg/mL. Then, different amounts were selected depending the well plate used:

Culture vessel	Amount of PLGA/bPEI (µg/µg)	Amount of DNA (µg)	Total volume (mL)
24 well	12/6	2	500 µl
12 well	18/9	3	1 ml

For example, for a 12 well plate, we conjugated 180 µL PLGA NPs 0.1 mg/mL with 9 µL bPEI 1 mg/ml (bPEI was dissolved in HEPES). The mixture was stirred 5 min and then 3 µg of DNA were added. The final construct was agitated 20 min at 4ºC. Finally, serum free DMEM medium was added to a total volume of 1 mL and added to each well. Formulations were incubated during 3 h and then, the medium was replaced for complete DMEM medium.

2.2.4. Peptide incorporation

Peptide incorporation to the PLGA polymer

The carboxyl group of PLGA polymer was used to couple r_8 and GTHRre peptides. Firstly, PLGA was dissolved in ACN (usually 40-50 mg/mL) and the carboxyl groups were activated by adding 3 equivalents of EDC and s-NHS. After 15 min activation, both peptides were added and agitated O/N (only 1 equivalent of the peptide was used). Once the peptide were conjugated, the modified polymer was precipitated with Et_2O and recovered by centrifugation. In another strategy, the coupling reagent used was PyAOP (3 eq). The rest of the methodology was the same as explained above.

Peptide incorporation on the PLGA NPs surface

Excess of r_8 was added to 500 µL of PLGA NPs solution and agitated 30 min. Then, NPs were centrifuged 30 min at 16000 g and resuspended in desired buffer.

The second strategy bound covalently the peptide to the PLGA nanoparticles. In this case, 50 µL of s-NHS (2 mg/mL) and 50 µL of EDC·HCl (2 mg/mL) were added to the PLGA NPs solution (1 mL) and stirred for 1 h. Finally, excess r_8 was added and the solution was stirred O/N again. Unreacted reagents were removed from the solution by centrifugation at 1000 rpm for 30 min and further resuspension in desired buffer.

GTHRre peptide was also incorporated to the surface using the covalent strategy. Furthermore, both peptides were added together for simultaneously incorporation following the strategy previously explained.

2.2.5. PLGA NPs characterization

All PLGA formulations were characterized by DLS. PLGA formulations were placed in a disposable folded capillary cell. Zetasizer Nano S (Malvern) upgraded with zeta potential capability was used to measure the mean size and Z-potential. The equipment was adjusted to 3 measures of 3 runs (10 sec each run) for size measurement and 3 measures of 20 runs for Z-potential. If needed, PLGA formulations were diluted.

2.2.6. DNA precipitation

DNA was complexed with 1/10 volumes of sodium acetate buffer (3 M, pH 5.2). After 20 s agitation, 2.5-3.0 volumes (calculated after addition of sodium acetate) of at least 95% ethanol were added to the previous solution and the mixture was incubated on ice for 15 min. Then, the sample was centrifuged at 14000 g for 30 min at 4°C. Supernatant was discarded and the pellet was resuspended in 70% ethanol. DNA was washed twice by centrifuging again at 14000 g for 15 min and resuspending in 70% ethanol. Finally, ethanolic supernatant was removed and DNA resuspended in the desired buffer.

2.2.7. Agarose gel

Samples (20 µL) were mixed with 4 µL DNA Gel Loading Dye (6x) and loaded onto a 0.8% agarose gel in 50 mL TAE buffer containing 5 µL GelRed® nucleic acid stain. Gel was run 30 min at 120 V. Bands were observed under UV light.

2.2.8. DNA extraction

For acetone NPs, formulations were centrifuged and resuspended in a 0.4% (w/v) SDS solution. The particles were stirred during, at least, 60 min. For DMSO NPs, an equal amount of $CHCl_3$ and PLGA NPs were mixed and stirred 60 min. Finally, 20 µL of each solution is applied into agarose gel. Time used for DNA extraction was varied for a higher DNA extraction. In some cases, 12 h extraction was used.

2.2.9. DNA quantification

Absorbance at 260 nm was used as the standard procedure for DNA quantification. Then, a calibration curve was performed by dissolving different amounts of DNA with supernatant from blank nanoparticles. After nanoparticle synthesis and centrifugation, the supernatant was used for DNA quantification. In the case of acetone NPs, all the acetone had to be evaporated in order to quantify the DNA. Non-encapsulated DNA was measured by spectrophotometry; therefore, the DNA encapsulated was calculated by the difference between the total amount added to the formulation and the non-encapsulated DNA.

For the detection of lower amounts of DNA, Quant-iT™ PicoGreen® dsDNA Assay Kit was used. In short, 20 mL TE 1x solution was prepared by diluting TE 20x in ultra-pure water from the kit. 2 mL PicoGreen reagent was prepared by diluting 200 fold PicoGreen solution from the kit with TE 1x. 2 µg/mL DNA standard solution was prepared by diluting 50 fold 100 µg/mL Standard DNA solution from the kit with TE 1x.

Calibration curves and samples where reacted by mixing, in a 96 well plate, 100 µL of each solution with 100 µL PicoGreen solution previously prepared. The reaction was left undisturbed 5 min and fluorescence was read in a FL600 BIO-Tek fluorescence plate reader. Sensitivity of the equipment was adjusted for a better measure of the sample.

2.2.10. Transfection assay

For *in vitro* transfection assays, GFP DNA plasmid was encapsulated. First, different cell lines were seeded on a 24 well plate. When the confluence reached 50% approximately, PLGA nanoparticles at different DNA concentrations were added and incubated during 2, 3 or 24 h. For the shorter incubation periods (2 h and 3 h), NPs solution was varied: PBS buffer, non-supplemented DMEM medium or complete DMEM medium were used. For 24 h incubation, only complete DMEM medium could be used because of the survival of the cells. After this incubation period, PLGA solutions were removed from the wells and cells were supplemented with complete DMEM medium. After 24 h to 48 h transfection, fluorescence was detected on an inverted Nikon TE200 microscope equipped with an Olympus DP72 camera in order to check the transfection efficiency of the formulations.

Positive control was performed by using Superfect transfection reagent. For each well of a 24 well plate the following procedure was used: 75 µL non-supplemented DMEM medium were added to an Eppendorf tube. 1µg DNA /well was used as positive control and added to the previous Eppendorf, followed by the addition of 7.5 µL Superfect solution. The Eppendorf was stirred 20 sec and incubated 20 min. at RT. After this time, 400 µL complete DMEM medium was added into the tube and the final solution added to each well. The positive control was incubated during 2-3 h and then, the medium was replaced by complete DMEM medium. Florescence was observed 24 h to 48 h after transfection.

Transfection assays in brain-derived cell lines were performed as previously explained. The difference was that in this case, FXN DNA plasmid was encapsulated into PLGA NPs. FXN protein expression was determined by western blot (explained in chapter 1 materials and methods) in order to compare the PLGA NPs transfection efficiency.

2.2.11. BBB cellular model

Thawing human endothelial cells (CD34+) and pericytes

Two petri dishes (Corning) were coated with 10 mL gelatin from porcine skin (type A) solution (2 mg/mL) and incubated at 37 °C during 15 min. Then, the gelatin solution was removed and the petri dishes filled with 20 mL of pericytes medium and sECM. Both cell lines were thawed and immediately placed into the petri dishes containing their appropriate medium. After 3 h, the medium was replaced by fresh medium. The cell were grown until 90% confluence was achieved (approximately 48 h)

Pericytes seeding

12 well plates were coated with 1 mL gelatin solution at 37 °C during 15 min. Then, gelatin solution was removed and 1.5 mL perycites medium was added to each well. Perycites were trypsinized and resuspended in perycites medium. Perycites were counted and 50000 cells were added per well.

Endothelial cells seeding

Inserts were coated with 0.5 mL BD matrigel growth factor reduced matrix diluted with BBB model DMEM (20 µL/mL) at least 1 h. Then, matrigel solution was removed and inserts were washed with BBB model DMEM. After that, DMEM was replaced by sECM and the inserts were placed into the wells containing perycites. Endothelial cells were trypsinized and resuspended in sECM medium supplemented with 20% FBS. Cells were counted and seeded on the inserts at 80000 cells per insert. After 3 h perycites seeding, medium was replaced by sECM. Finally, inserts containing endothelial cells were placed over perycite wells. Medium from both sides (basal and apical) was replaced by fresh sECM every two days. 24 h before the assay, the medium has to be replaced.

BBB transport assay

Transport assay was performed 7-8 days after cells seeding. Medium was removed from apical and basal sides and cells were washed twice with Ringer-HEPES buffer. Then, 0.5 mL were added to apical side and 1.5 mL to the basal side and left to equilibrate for 10 min at 37 °C. New 12 well plates were also equilibrated with exact 1.5 mL Ringer-HEPES buffer in each well. After equilibration, inserts were placed into the new plates (without perycites) and the NPs formulations were added into apical side. Lucifer yellow (50 µM) was added in each insert as a membrane integrity control. Formulations were incubated during 2 h. After this period, apical and basal compartments were kept for studying the NPs transport. Fluorescence of lucifer yellow from basal compartment was read in a fluorescent plate reader. Apparent permeability (Papp) higher than $15 \cdot 10^{-6}$ cm/s was considered as membrane disruption and if so, these inserts were not considered. Papp was obtained by equation 2.1:

$$Papp = \frac{d\,Q_A(t)}{d\,t} \cdot \frac{1}{A} \cdot \frac{V_D}{Q_D(t_0)} \qquad \textbf{Equation 2.1}$$

where Papp is obtained in cm/s, t is the duration of the assay (s), A is the area of the insert (cm), V_D is the volume in the apical well (cm^3), QA(t) is the amount of compound at time t in the basal well, $QD(t_0)$ is the amount of compound at the beginning of the experiment in the apical well.

Qualitatively DNA detection

As a first approximation for DNA detection, agarose gel was employed. PicoGreen method could not be used because of complexation between DNA and bPEI. Therefore, the reagent do not have access to the DNA.

First, the 1.5 mL from basal compartment was lyophilized and resuspended in 50 µL mili q water for concentrating 30 fold. Then, DNA was extracted by adding 200 µL chloroform and agitated overnight. Finally, 20 µL from the extracted aqueous phase were loaded to a 0.8% agarose gel for DNA detection.

Chapter 3

The use of lipopeptides as intestinal permeation enhancers

3.1. Results and Discussion

3.1.1. Ussing chambers

First of all, the three parent compounds (r_8, C_{12}-r_8 and Cho-r_8) were assayed in Ussing chambers to observe their effect on isolated rat colon. TEER was controlled during all experiment and a decrease of this value provided to us an estimation of temporary tight junction opening or membrane disruption (Figure 3.1). As a positive control for tight junction opening, C_{10} was used. Krebs-Heinsleit (KH) buffer was used as negative control.
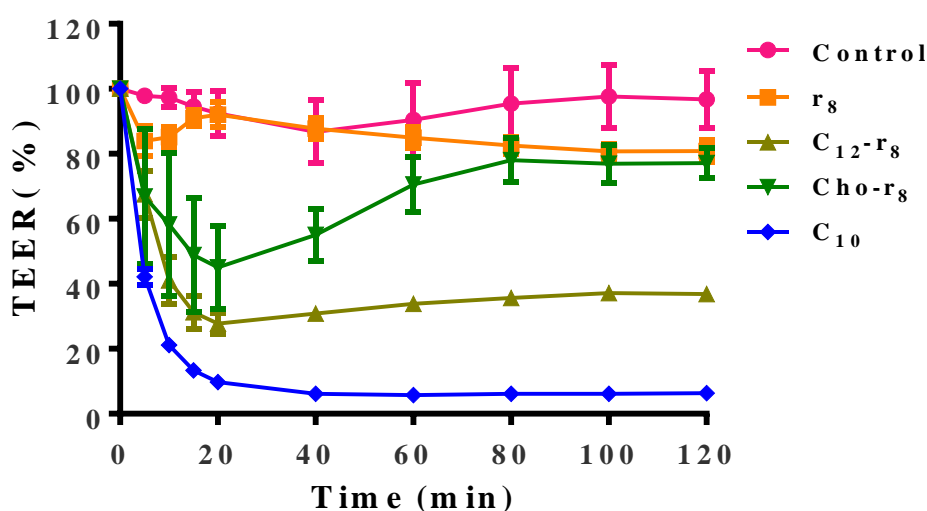
Figure 3.1. . Effect of CPP analogs on the TEER, expressed as a percentage related to control, in isolated rat colonic mucosae. Number of experiments (n) was 3-4. Data represent mean values ± SEM.

  In Figure 3.1, the different profiles from CPP analogs are compared. The profile obtained for r_8 peptide was similar to the negative control maintaining the TEER values during all the experiment. However, CPP analogs had different effects on the colon tissue. C_{12}-r_8 decreased the TEER values similar to the standard positive control, C_{10}. Cho-r_8 decreased the values to a 50% of their initial TEER and after 20 min, the TEER recovered. This last compound could be a potential penetration enhancer because of its ability to temporary open tight junctions.

  After observing the TEER profiles, the CPP analogs were assayed with a dextran labelled with fluorescein isothiocyanate (FITC), MW: 4000 Da, (FD4). In this sense, FD4 can be detected and quantified, obtaining the apparent permeability (Papp) (Equation 3.1).

$$P_{app} = \frac{dQ_B(t)}{dt} \cdot \frac{1}{A} \cdot \frac{V_A}{Q_A(t_0)}$$ **Equation 3.1**

where Papp is obtained in cm/s, $Q_B(t)$ is the amount of compound at time t in the basal compartment, t is the duration of the assay in seconds, A is the area of the insert in cm^2, V_A is the volume of the apical compartment, $Q_A(t_0)$ is the amount of compound at the beginning of the experiment of the apical compartment.

After 2 h, FD4 was excited at 495 nm and its emission was measured at 520 nm. Results are presented in Figure 3.2.
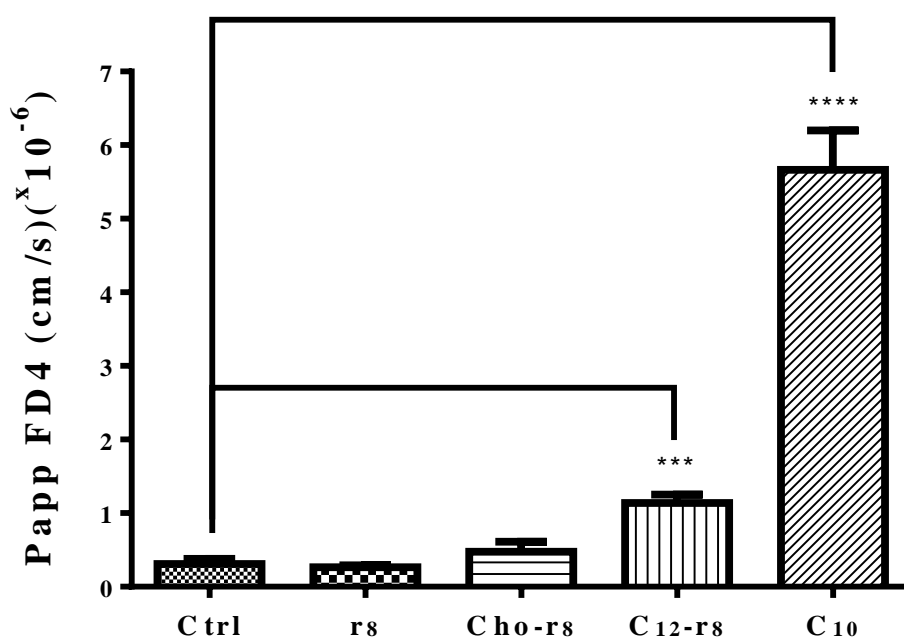
Figure 3.2. Papp of FD4 in isolated rat colonic mucosae after addition of CPPs analogs. Data represent mean values ± SEM (n=3-4). ***P = 0.0001; ****P < 0.0001 (t-test).

For r_8 and Cho-r_8 peptides, no statistical increase in Papp was observed, compared to the negative control. Although a minor increase in Papp was observed when Cho-r_8 was added, no statistical difference compared with the control (only FD4) was registered. Nevertheless, C_{12}-r_8 caused a statistical increase in FD4 apparent permeability. These results are in concordance with the TEER values obtained. These results suggest that C_{12}-r_8 peptide may act by opening tight junctions. As a control, FD4 Papp was determined when C_{10} was co-administered with FD4. The values from CPP analogs were far from those obtained for C_{10} but it is worth mentioning that the concentration used for C_{10} was around 20 fold higher than those used for the CPP analogs (Table 3.1).

Table 3.1. Conditions used and Papp of FD4 in isolated colonic mucosae after addition of CPPs analogs. (n= 3-4). ***P = 0.0001; ****P < 0.0001 (t-test).

Treatment	Concentration (mg/ml)	Concentration (mM)	Papp (x10^{-6}cm/s)	Statistical significance
Control	0	0	0.309±0.190	ns
r_8	0.8	0.63	0.265±0.049	ns
Cho-r_8	0.8	0.48	0.478±0.266	ns
C_{12}-r_8	0.8	0.55	1.139±0.230	***
C_{10}	1.94	10	5.667±0.920	****

Time was a limiting factor for repeating the experiments with C_{10} at lower concentration. In the near future, the experiments will be repeated by the Dublin team in order to obtain more comparative Papp values. The amount of peptide analogs needed to perform the experiment was another crucial factor. At that time, the amount of the peptides synthesized was limited and only a few and preliminary experiments could be performed. As previously mentioned, a higher amount of CPP analogs will be sent to Dublin in order to perform more experiments for obtaining clearer conclusions.

Once the effect of the CPP analogs in intestinal mucosae was observed, insulin was assayed in combination with the CPP compounds. Electrostatic interactions between the negatively charged insulin glulisine and the positively charged CPP analogs were formed by adding the same volume of each compound. Mixtures were clear at the concentrations they were formed. The insulin concentrations used ranged between 100 and 180 µM and the CPP analogs were between 400 and 700 µM. In all the cases, the ratio between CPP:insulin was 4:1 and the final volume used was 1 mL. Mixtures were agitated during 5 min and then added to the apical chamber. Finally, 1mL KH solution was removed from each apical side and compounds were added to Ussing chambers.

The first problem observed was the foam coming out from the apical chamber of samples containing C_{12}-r_8 and Cho-r_8. In the previous assays, foam also appeared in the same compounds due to the O_2 bubbling, but in this case seemed to be higher. This problem was partially solved by destroying foam before spilling over the chamber. However, after a few minutes, a second problem appeared on the same samples. Visible (by naked eye) small aggregates appeared on the chamber and over time, these aggregates

were attached to the mucus segregated by the tissue. This fact probably decreased the transport of insulin through the membrane. Anyway, TEER was monitored on the chambers containing the mixtures and the results obtained were similar to the CPP analogs alone (Figure 3.3).
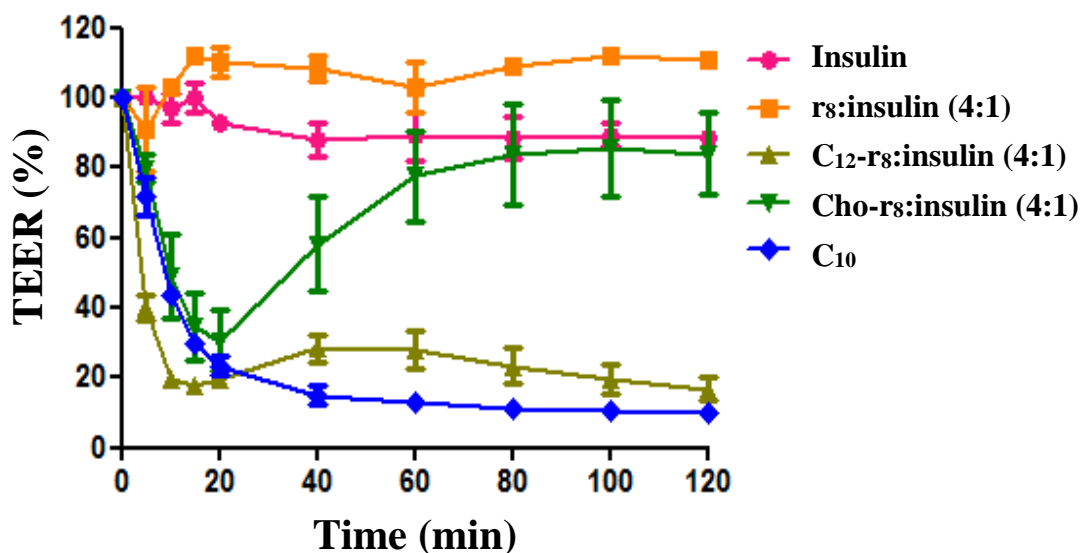
Figure 3.3. Effect of physical mixture on the TEER, expressed as a percentage related to control, in isolated colonic mucosae. Data represent mean values ± SEM (n=3-4).

After 2 h, basal samples were collected and analyzed by HPLC in order to detect insulin. It could not be detected by HPLC, therefore the basal samples were lyophilized and resuspended in a lower amount of water. In this way, samples were concentrated 10 fold, but still insulin was not detected by HPLC.

MALDI-TOF was also used to detect the insulin in the basal samples, but again, it was not detected. In some samples, byproducts in the range of 3000 - 5000 Da which could not be assigned to any insulin degradation products were observed. Curiously, the mass corresponding to r_8 could be observed by MALDI-TOF in some samples. Interestingly, the mass of r_8 was not only observed in the samples when it was added; but in the Cho-r_8 samples. These curious results, could explain the TEER profile obtained by Cho-r_8. A hypothesis could be that the compound decreased the TEER during a limited period of time after which it was dissociated in cholesterol and r_8. This dissociation increased the TEER values obtaining values similar to r_8 alone. Further experiments need to be performed in order to validate this hypothesis.

An option that was not completely explored because of time limitations was the use of an ELISA iso-insulin kit to detect low insulin concentrations in basal samples. This technique requires optimization of several parameters such as buffer adjustment or sample concentration. Therefore, dilutions have to be performed in order to achieve the optimal sample concentration to quantify insulin.

In order to compare the toxicity from our compounds, carbachol was added to the basal chambers. Then, the short-circuit current (I_{sc}), which is the equivalent to the algebraic sum of electrogenic ion movement by active transport and indicative of electrogenic chloride secretion, was measured (Figure 3.4). In all cases there was an increase of I_{sc} meaning that tissue functionality was retained in the presence of each CPP analog.
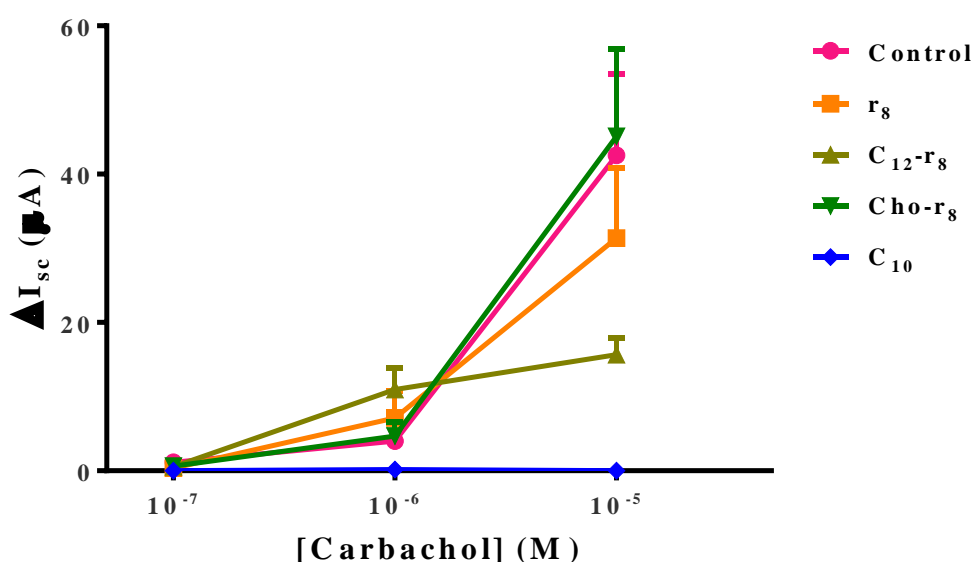
Figure 3.4. I_{sc} response in rat colon after 120 min. Data represent mean values ± SEM (n=3-4).

Moreover, after the experiment the tissue was preserved in 10% formalin and stained with haematoxylin and eosin (H&E) which is one of the gold standard stains for histology and stains nuclei in blue and eosinophilic structures (generally intracellular or extracellular proteins) in various shades of red. Also, neutral red and alcian blue (stain mucopolysaccharides) were used to observe possible tissue damage.

Tissue from control samples remained unaffected (Figure 3.5 A and B) and those containing r_8 and Cho-r_8 showed similar minimal damage (Figure 3.5 C, D, E and F) as can be observed in the morphology of the cells. In addition, almost no mucus (in blue) was observed, meaning minimal tissue suffering. However, C_{12}-r_8 showed cell sloughing

and an increase in the amount of mucus secreted by goblet cells (Figure 3.5 G and H). This result suggests that due to the attachment of C_{12}-r_8:insulin complex to the tissue, it segregated higher amount of mucus, indicating tissue damage. However, in all cases the damage was lower than that induced by C_{10} (Figure 3.5 I and J).

A)

B)

C)

D)

E)

F)

G)

H)

I)

J)
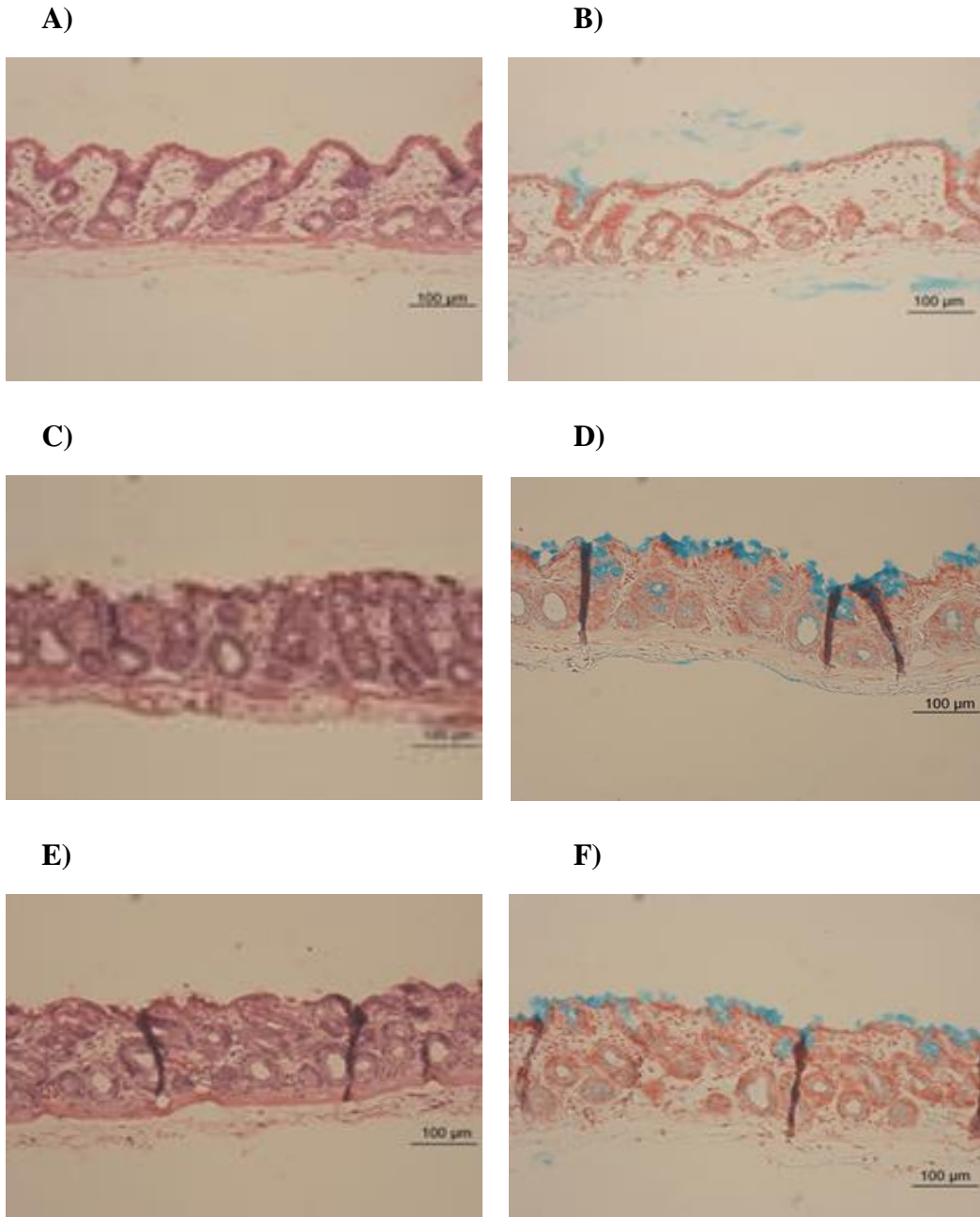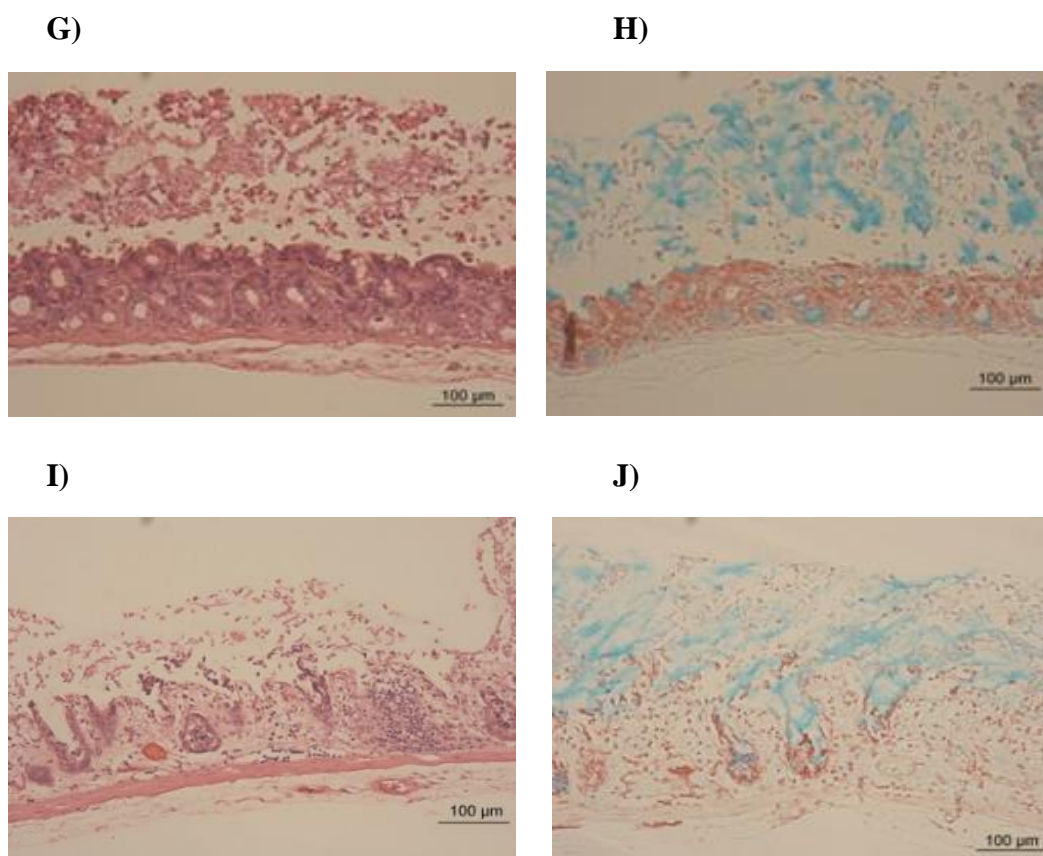
Figure 3.5. Staining of colonic tissue after 120 min. H&E (A, C, E, F and I) and neutral red and alcian blue (B, D, F, H and J). Scale bar 100 µm. Mucus was stained in blue.

At the end, an *in vitro* cell based model was thought to be more practical, for its simplicity, to optimize the conditions between CPP analogs and insulin. As previously explained, Caco-2 cell monolayer was selected to test the complexes. This cellular model is a simplified version of intestinal barrier and do not contain mucus which was one of our major problems when compounds were assayed on Ussing chambers. The absence of mucus could improve insulin transport considering that the complexes will not be stuck on it. For this reason and after my stage in Dublin, the Caco-2 cell model was set up in Barcelona in order to test more sample conditions and the effect of other lipopeptide analogs.

3.1.2. Caco-2 cell monolayer

As explained in the introduction, Caco-2 cells have been widely used as a model of the intestinal barrier.[127] These cells have the ability to differentiate and form tight junctions between them forming a characteristic monolayer.

In this section, CPP analogs (r_8, C_{12}-r_8 and Cho-r_8), which were tested in Ussing chambers, were also assayed in Caco-2 cell monolayer in order to compare the results between both models. In addition, an amphiphilic lipopeptide library composed by 9 modified versions of the CPP analogs was tested. Characterization of these compounds are depicted in annex II.

First, the cells were cultured on 12-well plate inserts during 21-29 days for completely monolayer differentiation. TEER values were used as a parameter of monolayer formation and, in all cases assayed, it was higher than 500 $\Omega \cdot cm^2$. Lower TEER values are not accepted for performing the experiment. Then, by mixing the same volume of CPP analogs and insulin, the complexes were formed to a final volume of 0.5 mL in HBSS buffer. Methylcellulose (0.001%) was added in all samples to prevent the compounds attachment to the Eppendorf and insert walls.[114] Complexes were added to the basal side and the transport experiment lasted 2 h. After this period, TEER was measured to check membrane integrity and both sides (apical and basal) were collected for further analysis. After 24 h TEER was checked in order to see recovery on membrane integrity. Complexes were assayed at CPP analog:insulin molar ratio of 10:1 (Figure 3.6).
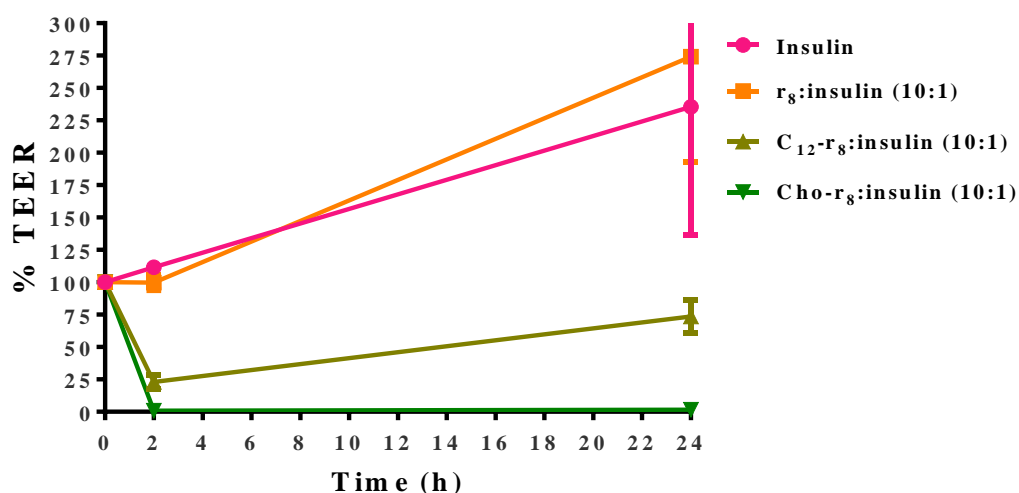
Figure 3.6. Effect of physical mixture on the % control TEER in Caco-2 cell monolayer. Data represent mean values $\pm$ SEM (n=3).

Similar results as in Ussing chambers were obtained in Caco-2 cell model after 2 h. The complex formed by r_8 and insulin had no effect in TEER compared with the control (insulin alone). The C_{12}-r_8:insulin complex decreased the TEER values to around 20% of its initial TEER. However, the TEER measured for Cho-r_8:insulin complex was much lower in Caco-2 cell monolayer than that obtained from the same complex in Ussing chambers. This TEER value was maintained after 24 h for this last complex meaning a clear disruption of the cell monolayer. For C_{12}-r_8:insulin complex the TEER values were recovered until obtaining values around 70% of its initial TEER. In the case of r_8, same values as the control were maintained.

Similar results were obtained when the complexes were formed at CPP analog:insulin molar ratio of 4:1 and 33:1. Molar ratio of 4:1 was studied to compare the results between Ussing chambers and Caco-2 cell monolayer. Higher molar ratios were selected based on a previously reported article where Kamei *et al.* demonstrated that at higher CPP concentrations (in their case r_8) the transport of insulin was higher.[116]

The same problem observed when working with Ussing chambers appeared after 2 h in Caco-2 cellular model. The complexes formed by C_{12}-r_8:insulin and Cho-r_8:insulin aggregated and appeared precipitated all over the insert. This problem was detected in all the molar ratios tested. Therefore, the presence of rat tissue or mucus did not cause complexes aggregation since the problem also appeared in Caco-2 cell model. This phenomenon needs further investigation. Stability studies of the complexes are planned to be performed.

Despite the fact that the aggregation could affect the transport of the complexes through the cell monolayer, the basal sides were analyzed both by HPLC and UPLC in order to detect insulin. It could not be detected by any of the techniques. Basal samples were then concentrated by lyophilization and reanalyzed on UPLC, which is approximately one order of magnitude more sensible than HPLC. Again, insulin could not be detected. Possibly, the aggregation observed during the experiment affected the transport of insulin through the cell monolayer and therefore decreasing the amount of protein in the basal side.

The library of 9 new compounds derived from CPP analogs was synthesized in an attempt to improve the transport of insulin. These modifications were either on the lipophilic chain or in the polyarginine length chain: C_8, C_{10} and C_{18} were incorporated to

the *N*-terminal of r_8 peptide, the length of C_{12}-r_8 was varied to r_4, r_6 and r_{12} and finally the same modifications were applied to Cho-r_8 analog.

Insulin was complexed with these compounds at molar ratio of 33:1 and the complexes were tested in Caco-2 cell monolayer (Figure 3.7).
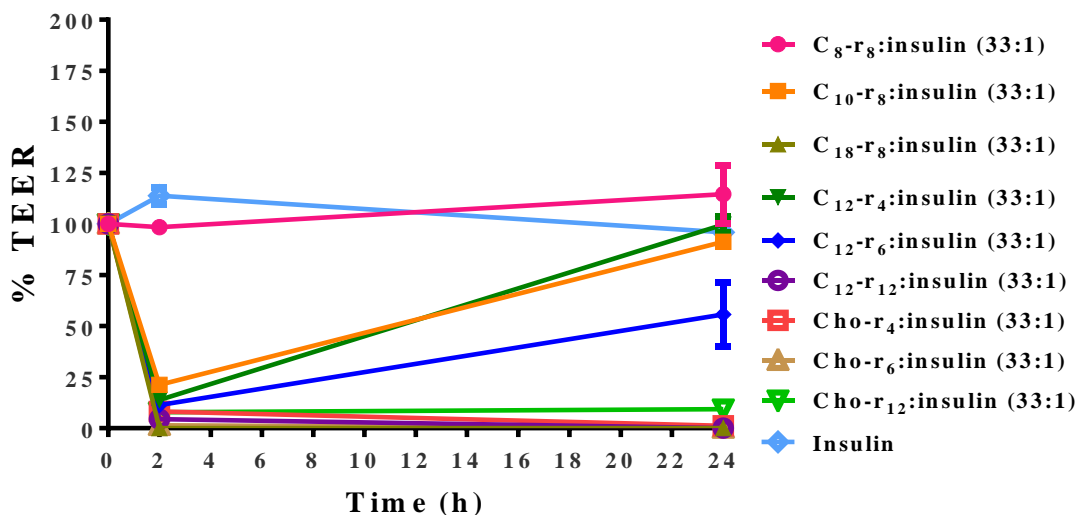
Figure 3.7. Effect of the new CPP derivatives/insulin complexes on the % control TEER in Caco-2 cell monolayer. Data represent mean values ± SEM (n=3).

From Figure 3.7 better idea on how the modification of the lipophilic or hydrophilic part of the CPP analogs can affect Caco-2 cell monolayer was obtained. All the derivatives decreased the TEER to values below 25% from their initial TEER except C_8-r_8. This last compound had no effect on the TEER values compared with insulin (as a control) even after 24 h. This result confirmed that the fatty acid chain length affects the tight junction integrity, thus varying the number of -CH_2 is a crucial factor for tight junctions opening.[163] When the fatty acid chain length is increased, all the compounds decreased the TEER values after 2 h, but different profiles were found after 24 h. TEER values from C_{10}-r_8 were similar to control. However, C_{12}-r_8 only recovered its TEER values up to 70%. Additionally, when the fatty chain length was increased to C_{18}, TEER values were not recovered indicating permanent Caco-2 cell monolayer damage.

Similar results were obtained when comparing the results from different polyarginine lengths by maintaining the fatty acid (C_{12}). All three compounds decreased the TEER to values below 20% of their initial TEER after 2 h. After 24 h, monolayers assayed with complexes composed by C_{12}-r_4 recovered TEER values similar to control. Additionally,

cell monolayers assayed with C_{12}-r_6 complexes also recovered TEER values but only up to 55%. When C_{12}-r_{12} was used, TEER values did not recover. Therefore, by increasing the number of arginines on the CPP peptide, TEER values decreased until reaching membrane disruption when this number was 12.

Cholesterol derivatives had always the same profile in which TEER values decreased to their minima after 2 h and they were not recovered after 24 h meaning cell damage and monolayer disruption.

Once again, all new complexes aggregated after 2 h at the concentrations the assays were performed. The CPP:insulin molar ratio was decreased to 10:1 and 4:1 but aggregation appeared in all cases. The buffer was also changed and HBSS buffered with MES (pH 6) and HEPES (pH 7.4) were used for transport assays using molar ratios of 33:1, 20:1 and 10:1. The first buffer was used to simulate the more acidic environment on the GI tract and the second in an attempt to improve complex stability. Almost in all the cases the complexes aggregated and visible precipitates were observed by naked eye after 2 h incubation on Caco-2 cells. A possible explanation for this complex instability is the ionic strength from the buffer.[164] The high amount of salts contained in the buffer can affect to the stability of the complex which is formed by electrostatic interactions. Other possible explanations of complex aggregation can be the effect of pH or their amphipathicity which can be related to the ability to form micelles and therefore compound aggregation. Higher complex characterization needs to be performed in order to solve this issue. Future experiments will be focused in this direction and complexes will be formed at different pH and different lipopetide concentrations in order to improve their stability.

At this moment, the amount of insulin on the basal chambers is being analyzed by UPLC and UPLC-MS (recently acquired by our laboratory). Also, preliminary ELISA iso-insulin test has been performed in order to detect lower amount of insulin. This last method still needs optimization and results are not available yet. Some of the studied compounds have the ability to be potential peptide penetration enhancers as they can decrease TEER transiently. The complexation between insulin and these compounds need to be reformulated in order to optimize the formulations and test their capability to improve transport of insulin through the GI tract.

3.2. Materials and Methods

3.2.1. Materials

In the following table, the reagents, solvents and materials used in this chapter are listed. Ussing chambers were performed in the lab of Prof. David Brayden, therefore male Wistar rats were obtained from University College of Dublin (UCD), Caco-2 cells were supplied by Veneto Nanotech (passage 32) and fast insulin was provided by Sanofi.

Supplier	Materials
Albatros Chem Inc	TBTU
Applied GL Biochem	HOAt
BD Discardit II BD Plastipak	Syringes (1,2, 5, 10 and 20 mL)
Biochrom A.G.	Trypsin-EDTA
Corning Costar	12 well-plates, 24 well-plates, 48 well-plates and 96 well-plates, culture flasks and petri dishes and Corning® Matrigel® matrix phenol red-free
Deltalab	Falcon tubes
EMD Millipore	Filters 0.45 µM (PVDF)
Eppendorfs	Eppendorf tubes
Iris Biotech	Fmoc-D-Arg(Pbf)-OH and EDC·HCl
KaliChemie	TFA
Mercodia	Mercodia iso-insulin ELISA
Novabiochem	PyBOP and NHS
Panreac	DMF and DMSO
PCAS BioMatrix Inc.	H-Rink amide ChemMatrix® resin
PIERCE	s-NHS
Pyrex	Pyrex® culture tubes (14 x 100 mm)
Roche	Agarose MP
Scharlab	Syringes (2, 5, 10 and 20 mL) fitted with polyethylene porous disk for peptide synthesis
Scharlau	HCl and methyl *tert*-butyl ether
SDS	DCM, ACN, MeOH and piperidine
Sigma-Aldrich	DIEA, DIC, ninhydrin, triisopropylsilane, DMEM, NaOH, $CaCl_2$, $MgCl_2 \cdot 6\ H_2O$, $MgSO_4 \cdot 7\ H_2O$, KCl,

	KH$_2$PO$_4$, NaHCO$_3$, NaCl, Na$_2$HPO$_4$ anhydrous, *D*-glucose, agar, lauric acid, cholesteryl chloroformate caprilic acid, capric acid, stearic acid and methyl cellulose
TCI Europe	Sodium oleate
ThermoFisher Scientific	LysoTracker® Red DND-99, Hoechst 33342, Pierce™ BCA protein assay kit, RIPA lysis and extraction buffer and Pierce™ ECL western blotting substrate

3.2.2. Peptide synthesis and characterization

CPP peptide was synthesized as described in chapter 1 and then the *N*-terminal was modified with either lauric acid or cholesteryl moieties. lauric acid was incorporated by adding:

Reagent	Treatment
DCM	Wash (3 x 30s)
DMF	Wash (3 x 30s)
3 eq lauric acid	
3 eq PyAOP	Coupling (90min) in DMF
9 eq DIEA	
DMF	Wash (3 x 30s)
DCM	Wash (3 x 30s)

Cholesteryl chloroformate was coupled by adding:

Reagent	Treatment
DCM	Wash (3 x 30s)
DMF	Wash (3 x 30s)
3 eq Cholesteryl chloroformate	Coupling (90min) in DMF
9 eq DIEA	
DMF	Wash (3 x 30s)
DCM	Wash (3 x 30s)

Peptides were characterized by HPLC and MALDI-TOF (Annex II). For more details on sample preparation and specific equipment used, materials and methods from chapter 1 can be consulted.

The 9 lipopeptide analogs were synthesized following the strategy explained before.

3.2.3. Ussing chambers protocol

Agar solution (3% in KCl 3M) preparation

  Three grams of agar were added to a 100 mL of KCl solution (3 M). KCl solution with agar were stirred slowly and heated for 80 sec in microwave. If agar is not completely dissolved, the solution was heated 15-20 more seconds.

Electrodes preparation

  The electrodes were rinsed for old KCl-agar with distilled H_2O using a syringe. Then, they were dried and filled with the prepared gel with a 20 mL syringe. It is crucial to ensure that there are no air bubbles in the KCl-agar electrodes because it could affect to the final lecture. The electrodes were paired using a voltmeter/multimeter. The multimeter was set to resistance (Ω): when black and red leads were together the resistance was 0 when apart it was infinite. The resistance of the electrodes was measured with the red lead on the KCl-agar and the black lead on the contact of the electrodes. The resistance should ideally be around 0 if it is above 10 the electrode is not working. Electrodes were paired with the same measured resistance. Electrodes should be kept in 3M KCl and paired with parafilm when stored.

Starting Ussing chambers

  The heat bath (37°C) and O_2/CO_2 (95%/5%) from the gas cylinder were turned on for the chambers. Red electrodes measured the current and the blue ones the voltage. 5 mL KH buffer were added to each chamber with a 5 mL syringe with special catheter. The oxygen was turned on for each chamber. The bubbling have to be the same in the control chamber as well as the other chambers. Meaning, if the bubbling in the apical chambers with enhancer is low (due to foam) the control chamber should be the same. Too high bubbling is not recommended as it might tear the tissue. Furthermore, make sure that the tissue is not oscillating due to the bubbling, it can damage the tissue. The chambers were equilibrated for 30 min and the voltage and 'Fluid res' measurement were adjusted to 0.0 (if needed).

Gastrointestinal dissection

Male Wistar rats (250-300 g) were euthanized by approved method of stunning and cervical dislocation. We adhered to the UCD AREC policy, 'Regarding the use of post mortem animal tissue in research and research (2007)' (see: http://www.ucd. ie/researchethics/pdf/arec_post_mortem_tissue_policy.pdf). Rat colons were removed, opened along the mesenteric border and rinsed with warm oxygenated KH buffer (37 ºC). Then, the colon was placed on a tissue draped and wetted on a dissection mat. A pin was inserted at the end of the section and the intestinal tissue was cut open along the mesenteric border. Fecal matter was removed and the tissue washed with KH. Carefully, the colon was turned over (the serosal side faces upwards) and the end was pinned. A small section of the colon was removed with a sharp blade for better differentiation of the different layers. Using sharp forceps, the serosal and muscular layers were gently removed. Finally, the entire muscular layer was removed and the mucosal layer was kept (with some pins).

Ussing chambers assay

Once the mucosal layer was clean, the tissue was mounted in the chambers (the apical, mucosal side, was placed on the left and the basolateral, serosa/blood side, on the right) and 5 mL of KH buffer were added to each chamber. The chambers were equilibrated for 15 min and then started the I/V clamp on the Pro4 device. 30 min clamping was needed before the experiment starts. The TEER values may be calculated during this 30 min. During the experiment the Pro4 settings were programed for I/V clamp clamping to 0 mV during 30 sec and then, the clamp was off for 3 sec. The TEER cut-off value for colon is $70 \, \Omega \cdot cm^2$, when lower TEER values were registered the experiment was not used. Lastly, a small amount of KH buffer was taken out from each apical chamber and replaced by the compounds assayed to a final volume of 5 mL. Experiments were performed for 2 h and the tissue was collected for toxicity assays.

Transport studies

Firstly, the three potential permeation enhancer were assayed in Ussing chambers. Compounds were dissolved in KH buffer at different concentrations to a final volume of 250 µl. Then, 250 µl KH solution were taken out from the apical chamber and the compounds were added. Always maintaining the final volume of both chambers to 5 mL. To prove the permeation enhancement of the different compounds, FD4 was added to the apical side (final concentration into apical chamber was 2.5 mg/mL). Every 20 min, 200 µL from apical chamber were collected in a 96 well plate and replaced for fresh KH buffer. These samples were then analyzed on a plate reader fluorescence microscope for FD4 quantification.

In order to form complexes, insulin was mixed with r_8 and analogs forming physical mixtures. Briefly, insulin was dissolved in 50 µL HCl 0.1 M. Then, KH was added and finally the pH was adjusted by adding 50 µL NaOH 0.1 M. To the previous solution, the peptidic compounds dissolved in KH buffer, were added and the final solution was stirred during 5 min. In all cases, the same volume of both solutions (insulin and lipopeptides) was used and the final complex solution was 1mL. When the complexes were formed, 1mL KH was removed from apical chamber and the compounds were assayed. 10 µL methyl cellulose (5 mg in 1 mL) were added to each Eppendorf to prevent insulin adherence to the plastic walls.

3.2.4. Caco-2 cell based model

Caco-2 cell line was obtained from Veneto Nanotech and the cells were used in the cellular model from passage 32 to 40. Complexes between insulin and CPP analogs were assayed in Caco-2 cell model.

Defrost

10 mL complete DMEM medium were added to a 25 mL cell culture flask. Caco-2 cells were defrost and immediately added to the flask. After 4 h incubation at 37°C and 5% CO_2, old medium was replaced by fresh complete DMEM medium.

Cell maintenance

When 90% cell confluence was reached, cells were trypsinized by adding 1 mL 1x trypsin. The flask was incubated 90 sec at 37°C and then 10 mL complete DMEM medium was added to stop trypsin effect. Caco-2 cells were spun down by centrifuging at 1,000 rpm during 5 min. After that, cells were resuspended in fresh complete DMEM medium and counted on a Neubauer chamber. Approximately 500,000 cells were added to a new 75 mL cell culture flask supplemented with 10 mL complete DMEM medium.

Insert preparation

Matrigel was diluted with non-supplemented DMEM medium to a final ratio of 10 µL matrigel/ 1 mL non-supplemented medium. Then, 300 µL of the above mentioned solution was added to each insert, in sterile conditions, for 1 h. After this time, Matrigel was removed and inserts were washed three times with non-supplemented medium. Caco-2 cells, after trypsinization, were added to each insert (500,000 cells per well) in 500 µL complete DMEM medium. 1.5 mL were added to each well in the basolateral side and cells were grown at 37°C and 5% CO_2 for 19-21 days in order to obtain a monolayer. When TEER values were lower than 500 $\Omega \cdot cm^2$, the experiment was not considered.

Transport studies

Inserts and 12-well plate were washed with HBSS buffer and equilibrated 30 min at 37 °C and 5% CO_2 by adding 0.5 mL HBSS on the apical side and 1.5 mL in the basolateral side. The 12-well plate was also equilibrated with 1.5 mL HBSS during 30 min. After this time, TEER was measured and then, the inserts were placed into the equilibrated 12-well plate. Buffer from inserts was removed and the formulations were added to a final volume of 0.5 mL. Samples were incubated 2 h at 37°C and 5% CO_2. After this period, apical and basolateral solutions were kept for further compounds quantification and the inserts and wells were refilled with complete DMEM medium. TEER was measured again for observing the effect of the different formulations to the cell monolayer. Finally, the plates, including the inserts, were incubated for 24 h and TEER was registered again.

3.2.5. Techniques for compounds detection

Apical and basal sides from all experiments were collected and analysed by different techniques.

HPLC and UPLC

HPLC and UPLC methods were explained in materials and methods from chapter 1. Basal samples were lyophilized and concentrated 10 fold in order to improve insulin detection.

MALDI-TOF MS

Insulin and CPP analogs molecular weight was determined using a MALDI-TOF/TOF Applied Biosystem 4700. For more details in sample preparation see chapter 1 material and methods.

ELISA assay

  ELISA kit was used for detecting insulin glulisine from basal sides of Ussing chambers and Caco-2 assays at low concentrations. Briefly, enzyme conjugate (1x) and wash buffer solution (1x) were firstly prepared. The previous solutions were provided by the supplier's kit. Then, 25 µL of each sample, control and calibrator (also provided) were added into the wells. 50 µL enzyme conjugate (1x) solution were added to each well and the plate was agitated during 1 h at RT. Next step was washing each well 5 times for completely elimination of the solvents. After that, 200 µL of substrate TMB (provided) were added into each well and incubated again 15min at RT. Finally, 50 µL stop solution were added to each well, plate was agitated and the absorbance was read at 450 nm.

Conclusions

The conclusions obtained for this thesis are the following:

1) Gold nanorods were successfully synthesized by modified seed mediated growth method. The incorporation into the synthesis of hydroquinone as a reducing agent was crucial to obtain high yield (more than 90% tods compared to byproducts), homogeneity and reproducibility. Nanoparticles were characterized by UV-Vis-NIR spectroscopy and transmission electron microscopy.

2) The incorporation of a bifunctional PEG provided almost completely CTAB removal, conferring stability to the gold nanorods and allowing further CPP incorporation.

3) Negligible cytotoxicity was obtained from modified nanorods on HeLa and fibroblasts 3T3 cells compared to CTAB-capped nanorods, which toxicity was higher than 90% at the same concentrations tested.

4) Fluorescence from the modified CPP was measured by FACS and confocal microscopy indicating rods internalization. TEM images of fixated cells corroborated that the internalization was by the endocytic route and after 24 h rods were localized into late-endosmes.

5) Preliminary results showed protein silencing after irradiation with NIR of cell containing siRNA complexed nanorods; demonstrating the potential of gold nanorods as endosomal release enhancers.

6) DNA plasmid was effectively encapsulated into PLGA nanoparticles by using a modified nanoprecipitation method. When positive polymers (chitosan and bPEI) were used to complex DNA, the encapsulation efficiency was higher than 90%. For these formulations, average size was lower than 200 nm obtaining low polydispersity.

7) The introduction of bPEI highly increased the transfection of PLGA NPs compared to those synthesized with chitosan. Particles showed different transfection efficiency depending on the cell line (transfection in HeLa or fibroblasts cells was much higher compared to brain endothelial cells).

8) The use of peptides (r_8 as CPP and THRre as BBB-shuttle) attached to the PLGA nanoparticles clearly increased the DNA transfection efficiency. Preliminary results showed DNA transfection in a brain-derived cell line (glioblastoma). Additionally,

some of these formulations (in special those containing THRre) were able to cross an *in vitro* cell based BBB model.

9) Different profiles in TEER values were obtained in Caco-2 cellular model from the peptide moieties studied. When the peptide contained a cholesterol moiety, TEER values decreased after 2 h and did not recover after 24 h indicating membrane disruption. In the case of medium chain fatty acids conjugated to the peptides, their effect on TEER values relied on the fatty acid length. Whereas, C_8-r_8 did not alter TEER values even at 24 h, C_{18}-r_8 decreased TEER values which were not recovered after 24 h. The same effect was observed when increasing the number of arginines maintaining the fatty acid. C_{10}-r_8 and C_{12}-r_8 compounds were considered as potential intestinal enhancers because of their capability to decrease TEER values temporally.

10) The compounds r_8, C_{12}-r_8 and Cho-r_8 were assayed in Ussing chambers obtaining three different TEER profiles. Whereas, r_8 did not affect TEER values during all the experiments, C_{12}-r_8 and Cho-r_8 decreased TEER. The most promising effect was achieved when FD4 was added, where C_{12}-r_8 increased FD4 Papp significantly. Tissue histology revealed minor or no damage from peptidic moieties compared to the positive control (C_{10}).

11) Physical mixtures between lipopeptides and insulin resulted in aggregation in almost all combinations tested. Further experiments will be done in order to increase the stability of these physical mixtures.

References

1. Plenty of room at the bottom. (**last accessed 01/03/2016**), (http://www.pa.msu.edu/~yang/RFeynman_plentySpace.pdf)

2. Hapgood, F. Tinytech. *OMNI*, **1986**, (9) 56-63.

3. Nan'o·tech·nol'o·gy n. *Nat Nano*, **2006**, (1) 8-10.

4. Harper, T. Global funding of nanotechnologies & its impact. (**last accessed 01/03/2016**),(http://cientifica.com/wp-content/uploads/downloads/2011/07/Global-Nanotechnology-Funding-Report-2011.pdf)

5. Chen, H., Roco, M.C., Son, J., Jiang, S., Larson, C.A. & Gao, Q. Global nanotechnology development from 1991 to 2012: Patents, scientific publications, and effect of nsf funding. *Journal of nanoparticle research*, **2013**, (15) 1-21.

6. Statnano. (**last accessed 01/03/2016**), (http://statnano.com/)

7. Porter, A.L. & Youtie, J. How interdisciplinary is nanotechnology? *Journal of Nanoparticle Research*, **2009**, (11) 1023-1041.

8. Oberdorster, G., Oberdorster, E. & Oberdorster, J. Nanotoxicology: An emerging discipline evolving from studies of ultrafine particles. *Environmental health perspectives*, **2005**, (113) 823-839.

9. Dreaden, E.C., Alkilany, A.M., Huang, X., Murphy, C.J. & El-Sayed, M.A. The golden age: gold nanoparticles for biomedicine. *Chemical Society Reviews*, **2012**, (41) 2740-2779.

10. Huang, X., El-Sayed, I.H., Qian, W. & El-Sayed, M.A. Cancer cell imaging and photothermal therapy in the near-infrared region by using gold nanorods. *Journal of the American Chemical Society*, **2006**, (128) 2115-2120.

11. Yu, C. & Irudayaraj, J. Multiplex biosensor using gold nanorods. *Analytical Chemistry*, **2007**, (79) 572-579.

12. Lohse, S.E. & Murphy, C.J. The quest for shape control: a history of gold nanorod synthesis. *Chemistry of Materials*, **2013**, (25) 1250-1261.

13. Foss, C.A., Hornyak, G.L., Stockert, J.A. & Martin, C.R. Optical properties of composite membranes containing arrays of nanoscopic gold cylinders. *The Journal of Physical Chemistry*, **1992**, (96) 7497-7499.

14. Martin, C.R. Membrane-based synthesis of nanomaterials. *Chemistry of Materials*, **1996**, (8) 1739-1746.

15. van der Zande, B.M.I., Böhmer, M.R., Fokkink, L.G.J. & Schönenberger, C. Colloidal dispersions of gold rods: synthesis and optical properties. *Langmuir*, **2000**, (16) 451-458.

16. van der Zande, B.M.I., Böhmer, M.R., Fokkink, L.G.J. & Schönenberger, C. Aqueous gold sols of rod-shaped particles. *The Journal of Physical Chemistry B*, **1997**, (101) 852-854.

17. Wirtz, M. & Martin, C.R. Template-fabricated gold nanowires and nanotubes. *Advanced Materials*, **2003**, (15) 455-458.

18. Gao, C., Zhang, Q., Lu, Z. & Yin, Y. Templated synthesis of metal nanorods in silica nanotubes. *Journal of the American Chemical Society*, **2011**, (133) 19706-19709.

19. Yu, Chang, S.-S., Lee, C.-L. & Wang, C.R.C. Gold nanorods: electrochemical synthesis and optical properties. *The Journal of Physical Chemistry B*, **1997**, (101) 6661-6664.

20. Chang, S.-S., Shih, C.-W., Chen, C.-D., Lai, W.-C. & Wang, C.R.C. The shape transition of gold nanorods. *Langmuir*, **1999**, (15) 701-709.

21. Brown, K.R. & Natan, M.J. Hydroxylamine seeding of colloidal Au nanoparticles in solution and on surfaces. *Langmuir*, **1998**, (14) 726-728.

22. Brown, K.R., Walter, D.G. & Natan, M.J. Seeding of colloidal Au nanoparticle solutions. 2. Improved control of particle size and shape. *Chemistry of Materials*, **2000**, (12) 306-313.

23. Jana, N.R., Gearheart, L. & Murphy, C.J. Evidence for seed-mediated nucleation in the chemical reduction of gold salts to gold nanoparticles. *Chemistry of Materials*, **2001**, (13) 2313-2322.

24. Jana, N.R., Gearheart, L. & Murphy, C.J. Wet chemical synthesis of high aspect ratio cylindrical gold nanorods. *The Journal of Physical Chemistry B*, **2001**, (105) 4065-4067.

25. Murphy, C.J., Sau, T.K., Gole, A.M., Orendorff, C.J., Gao, J., Gou, L., Hunyadi, S.E. & Li, T. Anisotropic metal nanoparticles: synthesis, assembly, and optical applications. *The Journal of Physical Chemistry B*, **2005**, (109) 13857-13870.

26. Busbee, B.D., Obare, S.O. & Murphy, C.J. An improved synthesis of high-aspect-ratio gold nanorods. *Advanced Materials*, **2003**, (15) 414-416.

27. Jana, N.R., Gearheart, L. & Murphy, C.J. Seed-mediated growth approach for shape-controlled synthesis of spheroidal and rod-like gold nanoparticles using a surfactant template. *Advanced Materials*, **2001**, (13) 1389.

28. Nikoobakht, B. & El-Sayed, M.A. Preparation and growth mechanism of gold nanorods (NRs) using seed-mediated growth method. *Chemistry of Materials*, **2003**, (15) 1957-1962.

29. Pérez-Juste, J., Pastoriza-Santos, I., Liz-Marzán, L.M. & Mulvaney, P. Gold nanorods: synthesis, characterization and applications. *Coordination Chemistry Reviews*, **2005**, (249) 1870-1901.

30. Smith, D.K. & Korgel, B.A. The importance of the CTAB surfactant on the colloidal seed-mediated synthesis of gold nanorods. *Langmuir*, **2008**, (24) 644-649.

31. Jana, N.R. Gram-scale synthesis of soluble, near-monodisperse gold nanorods and other anisotropic nanoparticles. *Small*, **2005**, (1) 875-882.

32. Ali, M.R.K., Snyder, B. & El-Sayed, M.A. Synthesis and optical properties of small Au nanorods using a seedless growth technique. *Langmuir*, **2012**, (28) 9807-9815.

33. Vigderman, L. & Zubarev, E.R. High-yield synthesis of gold nanorods with longitudinal SPR peak greater than 1200 nm using hydroquinone as a reducing agent. *Chemistry of Materials*, **2013**, (25) 1450-1457.

34. Ye, X., Zheng, C., Chen, J., Gao, Y. & Murray, C.B. Using binary surfactant mixtures to simultaneously improve the dimensional tunability and monodispersity in the seeded growth of gold nanorods. *Nano Letters*, **2013**, (13) 765-771.

35. McKenzie, L.C., Haben, P.M., Kevan, S.D. & Hutchison, J.E. Determining nanoparticle size in real time by small-angle X-ray scattering in a microscale flow system. *The Journal of Physical Chemistry C*, **2010**, (114) 22055-22063.

36. Zheng, H., Smith, R.K., Jun, Y.-w., Kisielowski, C., Dahmen, U. & Alivisatos, A.P. Observation of single colloidal platinum nanocrystal growth trajectories. *Science*, **2009**, (324) 1309-1312.

37. Gómez-Graña, S., Hubert, F., Testard, F., Guerrero-Martínez, A., Grillo, I., Liz-Marzán, L.M. & Spalla, O. Surfactant (bi)layers on gold nanorods. *Langmuir*, **2012**, (28) 1453-1459.

38. Niidome, Y., Nakamura, Y., Honda, K., Akiyama, Y., Nishioka, K., Kawasaki, H. & Nakashima, N. Characterization of silver ions adsorbed on gold nanorods: surface analysis by using surface-assisted laser desorption/ionization time-of-flight mass spectrometry. *Chemical Communications*, **2009**, 1754-1756.

39. Murphy, C.J., Thompson, L.B., Alkilany, A.M., Sisco, P.N., Boulos, S.P., Sivapalan, S.T., Yang, J.A., Chernak, D.J. & Huang, J. The many faces of gold nanorods. *The Journal of Physical Chemistry Letters*, **2010**, (1) 2867-2875.

40. Alkilany, A.M. & Murphy, C.J. Toxicity and cellular uptake of gold nanoparticles: what we have learned so far? *Journal of Nanoparticle Research*, **2010**, (12) 2313-2333.

41. Alkilany, A.M., Nagaria, P.K., Hexel, C.R., Shaw, T.J., Murphy, C.J. & Wyatt, M.D. Cellular uptake and cytotoxicity of gold nanorods: molecular origin of cytotoxicity and surface effects. *Small*, **2009**, (5) 701-708.

42. Vigderman, L., Khanal, B.P. & Zubarev, E.R. Functional gold nanorods: synthesis, self-assembly, and sensing applications. *Advanced Materials*, **2012**, (24) 4811-4841.

43. Gole, A. & Murphy, C.J. Polyelectrolyte-coated gold nanorods: synthesis, characterization and immobilization. *Chemistry of Materials*, **2005**, (17) 1325-1330.

44. Hostetler, M.J., Templeton, A.C. & Murray, R.W. Dynamics of place-exchange reactions on monolayer-protected gold cluster molecules. *Langmuir*, **1999**, (15) 3782-3789.

45. Vigderman, L., Manna, P. & Zubarev, E.R. Quantitative replacement of cetyl trimethylammonium bromide by cationic thiol ligands on the surface of gold nanorods and their extremely large uptake by cancer cells. *Angewandte Chemie*, **2012**, (124) 660-665.

46. Kinnear, C., Dietsch, H., Clift, M.J., Endes, C., Rothen-Rutishauser, B. & Petri-Fink, A. Gold nanorods: controlling their surface chemistry and complete detoxification by a two-step place exchange. *Angewandte Chemie International Edition*, **2013**, (52) 1934-1938.

47. Indrasekara, A., Wadams, R.C. & Fabris, L. Ligand exchange on gold nanorods: going back to the future. *Particle & Particle Systems Characterization*, **2014**, (31) 819-838.

48. Huang, X., Neretina, S. & El-Sayed, M.A. Gold nanorods: from synthesis and properties to biological and biomedical applications. *Advanced Materials*, **2009**, (21) 4880-4910.

49. Truong, P.L., Cao, C., Park, S., Kim, M. & Sim, S.J. A new method for non-labeling attomolar detection of diseases based on an individual gold nanorod immunosensor. *Lab on a Chip*, **2011**, (11) 2591-2597.

50. Sönnichsen, C., Franzl, T., Wilk, T., von Plessen, G., Feldmann, J., Wilson, O. & Mulvaney, P. Drastic reduction of plasmon damping in gold nanorods. *Physical Review Letters*, **2002**, (88) 077402.

51. Hu, R., Yong, K.-T., Roy, I., Ding, H., He, S. & Prasad, P.N. Metallic nanostructures as localized plasmon resonance enhanced scattering probes for multiplex dark-field targeted imaging of cancer cells. *The Journal of Physical Chemistry C*, **2009**, (113) 2676-2684.

52. Durr, N.J., Larson, T., Smith, D.K., Korgel, B.A., Sokolov, K. & Ben-Yakar, A. Two-photon luminescence imaging of cancer cells using molecularly targeted gold nanorods. *Nano Letters*, **2007**, (7) 941-945.

53. Alvarez-Puebla, R.A., Agarwal, A., Manna, P., Khanal, B.P., Aldeanueva-Potel, P., Carbó-Argibay, E., Pazos-Pérez, N., Vigderman, L., Zubarev, E.R. & Kotov, N.A. Gold nanorods 3D-supercrystals as surface enhanced raman scattering spectroscopy substrates for the rapid detection of scrambled prions. *Proceedings of the National Academy of Sciences*, **2011**, (108) 8157-8161.

54. Jain, P.K., Lee, K.S., El-Sayed, I.H. & El-Sayed, M.A. Calculated absorption and scattering properties of gold nanoparticles of different size, shape, and composition: applications in biological imaging and biomedicine. *The Journal of Physical Chemistry B*, **2006**, (110) 7238-7248.

55. Tong, R., Chiang, H.H. & Kohane, D.S. Photoswitchable nanoparticles for *in vivo* cancer chemotherapy. *Proceedings of the National Academy of Sciences*, **2013**, (110) 19048-19053.

56. Ahn, S., Seo, E., Kim, K. & Lee, S.J. Controlled cellular uptake and drug efficacy of nanotherapeutics. *Scientific Reports*, **2013**, (3)

57. Huff, T.B., Tong, L., Zhao, Y., Hansen, M.N., Cheng, J.-X. & Wei, A. Hyperthermic effects of gold nanorods on tumor cells. *Nanomedicine*, **2007**, (2) 125-132.

58. Takahashi, H., Niidome, Y. & Yamada, S. Controlled release of plasmid DNA from gold nanorods induced by pulsed near-infrared light. *Chemical Communications*, **2005**, 2247-2249.

59. Lackey, C.A., Press, O.W., Hoffman, A.S. & Stayton, P.S. A biomimetic pH-responsive polymer directs endosomal release and intracellular delivery of an endocytosed antibody complex. *Bioconjugate Chemistry*, **2002**, (13) 996-1001.

60. Murthy, N., Robichaud, J.R., Tirrell, D.A., Stayton, P.S. & Hoffman, A.S. The design and synthesis of polymers for eukaryotic membrane disruption. *Journal of Controlled Release*, **1999**, (61) 137-143.

61. Nativo, P., Prior, I.A. & Brust, M. Uptake and intracellular fate of surface-modified gold nanoparticles. *ACS Nano*, **2008**, (2) 1639-1644.

62. Song, W.-J., Du, J.-Z., Sun, T.-M., Zhang, P.-Z. & Wang, J. Gold nanoparticles capped with polyethyleneimine for enhanced siRNA delivery. *Small*, **2010**, (6) 239-246.

63. Tkachenko, A.G., Xie, H., Coleman, D., Glomm, W., Ryan, J., Anderson, M.F., Franzen, S. & Feldheim, D.L. Multifunctional gold nanoparticle−peptide complexes for nuclear targeting. *Journal of the American Chemical Society*, **2003**, (125) 4700-4701.

64. Morales, D.P., Braun, G.B., Pallaoro, A., Chen, R., Huang, X., Zasadzinski, J.A. & Reich, N.O. Targeted intracellular delivery of proteins with spatial and temporal control. *Molecular Pharmaceutics*, **2015**, (12) 600-609.

65. Henderson, T.A. & Morries, L.D. Near-infrared photonic energy penetration: can infrared phototherapy effectively reach the human brain? *Neuropsychiatric Disease and Treatment*, **2015**, (11) 2191-2208.

66. Wiggans, A.J., Cass, G.K., Bryant, A., Lawrie, T.A. & Morrison, J. Poly(ADP-ribose) polymerase (PARP) inhibitors for the treatment of ovarian cancer. *The Cochrane Database of Systematic Reviews*, **2015**, (5) Cd007929.

67. Morral, J.A., Davis, A.N., Qian, J., Gelman, B.B. & Koeppen, A.H. Pathology and pathogenesis of sensory neuropathy in Friedreich's ataxia. *Acta Neuropathologica*, **2010**, (120) 97-108.

68. Campuzano, V., Montermini, L., Molto, M.D., Pianese, L., Cossee, M., Cavalcanti, F., Monros, E., Rodius, F., Duclos, F., Monticelli, A., Zara, F., Canizares, J., Koutnikova, H., Bidichandani, S.I., Gellera, C., Brice, A., Trouillas, P., De Michele, G., Filla, A., De Frutos, R., Palau, F., Patel, P.I., Di Donato, S., Mandel, J.L., Cocozza, S., Koenig, M. & Pandolfo, M. Friedreich's ataxia: autosomal recessive disease caused by an intronic GAA triplet repeat expansion. *Science*, **1996**, (271) 1423-1427.

69. Payne, R.M. & Wagner, G.R. Cardiomyopathy in Friedreich ataxia: clinical findings and research. *Journal of Child Neurology*, **2012**, (27) 1179-1186.

70. Weidemann, F., Störk, S., Liu, D., Hu, K., Herrmann, S., Ertl, G. & Niemann, M. Cardiomyopathy of Friedreich ataxia. *Journal of Neurochemistry*, **2013**, (126) 88-93.

71. Lazaropoulos, M., Dong, Y., Clark, E., Greeley, N.R., Seyer, L.A., Brigatti, K.W., Christie, C., Perlman, S.L., Wilmot, G.R., Gomez, C.M., Mathews, K.D., Yoon, G., Zesiewicz, T., Hoyle, C., Subramony, S.H., Brocht, A.F., Farmer, J.M., Wilson, R.B., Deutsch, E.C. & Lynch, D.R. Frataxin levels in peripheral tissue in Friedreich ataxia. *Annals of Clinical and Translational Neurology*, **2015**, (2) 831-842.

72. Rouault, T.A. Mammalian iron-sulphur proteins: novel insights into biogenesis and function. *Nature Reviews Molecular Cell Biology*, **2015**, (16) 45-55.

73. Libri, V., Yandim, C., Athanasopoulos, S., Loyse, N., Natisvili, T., Law, P.P., Chan, P.K., Mohammad, T., Mauri, M. & Tam, K.T. Epigenetic and neurological effects and safety of high-dose nicotinamide in patients with Friedreich's ataxia: an exploratory, open-label, dose-escalation study. *The Lancet*, **2014**, (384) 504-513.

74. Soragni, E., Miao, W., Iudicello, M., Jacoby, D., De Mercanti, S., Clerico, M., Longo, F., Piga, A., Ku, S., Campau, E., Du, J., Penalver, P., Rai, M., Madara, J.C., Nazor, K., O'Connor, M., Maximov, A., Loring, J.F., Pandolfo, M., Durelli, L., Gottesfeld, J.M. & Rusche, J.R. Epigenetic therapy for Friedreich ataxia. *Annals of Neurology*, **2014**, (76) 489-508.

75. Chapdelaine, P., Coulombe, Z., Chikh, A., Gerard, C. & Tremblay, J.P. A potential new therapeutic approach for Friedreich ataxia: induction of frataxin expression with TALE proteins. *Molecular Theraphy-Nucleic Acids*, **2013**, (2) e119.

76. Tremblay, J.P., Chapdelaine, P., Coulombe, Z. & Rousseau, J. Transcription activator-like effector proteins induce the expression of the frataxin gene. *Human Gene Therapy*, **2012**, (23) 883-890.

77. Vyas, P.M., Tomamichel, W.J., Pride, P.M., Babbey, C.M., Wang, Q., Mercier, J., Martin, E.M. & Payne, R.M. A TAT–frataxin fusion protein increases lifespan and cardiac function in a conditional Friedreich's ataxia mouse model. *Human Molecular Genetics*, **2012**, (21) 1230-1247.

78. Pérez-Luz, S., Gimenez-Cassina, A., Fernández-Frías, I., Wade-Martins, R. & Díaz-Nido, J. Delivery of the 135kb human frataxin genomic DNA locus gives rise to different frataxin isoforms. *Genomics*, **2015**, (106) 76-82.

79. Gérard, C., Xiao, X., Filali, M., Coulombe, Z., Arsenault, M., Couet, J., Li, J., Drolet, M.-C., Chapdelaine, P. & Chikh, A. An AAV9 coding for frataxin clearly improved the symptoms and prolonged the life of Friedreich ataxia mouse models. *Molecular Therapy. Methods & Clinical Development*, **2014**, (1) 14044.

80. Nabhan, J.F., Wood, K.M., Rao, V.P., Morin, J., Bhamidipaty, S., LaBranche, T.P., Gooch, R.L., Bozal, F., Bulawa, C.E. & Guild, B.C. Intrathecal delivery of frataxin mRNA encapsulated in lipid nanoparticles to dorsal root ganglia as a potential therapeutic for Friedreich's ataxia. *Scientific Reports*, **2016**, (6) 20019.

81. Manjila, S.B., Baby, J.N., Bijin, E.N., Constantine, I., Pramod, K. & Valsalakumari, J. Novel gene delivery systems. *International Journal of Pharmaceutical Investigation*, **2013**, (3) 1-7.

82. Nayerossadat, N., Maedeh, T. & Ali, P.A. Viral and nonviral delivery systems for gene delivery. *Advanced Biomedical Research*, **2012**, (1) 27.

83. Makadia, H.K. & Siegel, S.J. Poly lactic-co-glycolic acid (PLGA) as biodegradable controlled drug delivery carrier. *Polymers*, **2011**, (3) 1377-1397.

84. Vert, M., Mauduit, J. & Li, S. Biodegradation of PLA/GA polymers: increasing complexity. *Biomaterials*, **1994**, (15) 1209-1213.

85. Danhier, F., Ansorena, E., Silva, J.M., Coco, R., Le Breton, A. & Préat, V. PLGA-based nanoparticles: an overview of biomedical applications. *Journal of Controlled Release*, **2012**, (161) 505-522.

86. Ribeiro, S., Hussain, N. & Florence, A.T. Release of DNA from dendriplexes encapsulated in PLGA nanoparticles. *International Journal of Pharmaceutics*, **2005**, (298) 354-360.

87. Kim, I.-S., Lee, S.-K., Park, Y.-M., Lee, Y.-B., Shin, S.-C., Lee, K.C. & Oh, I.-J. Physicochemical characterization of poly (L-lactic acid) and poly (D, L-lactide-co-glycolide) nanoparticles with polyethylenimine as gene delivery carrier. *International Journal of Pharmaceutics*, **2005**, (298) 255-262.

88. Davda, J. & Labhasetwar, V. Characterization of nanoparticle uptake by endothelial cells. *International Journal of Pharmaceutics*, **2002**, (233) 51-59.

89. Niu, X., Zou, W., Liu, C., Zhang, N. & Fu, C. Modified nanoprecipitation method to fabricate DNA-loaded PLGA nanoparticles. *Drug Development and Industrial Pharmacy*, **2009**, (35) 1375-1383.

90. Tahara, K., Sakai, T., Yamamoto, H., Takeuchi, H. & Kawashima, Y. Establishing chitosan coated PLGA nanosphere platform loaded with wide variety of nucleic

acid by complexation with cationic compound for gene delivery. *International Journal of Pharmaceutics*, **2008**, (354) 210-216.

91. Patil, Y.B., Swaminathan, S.K., Sadhukha, T., Ma, L. & Panyam, J. The use of nanoparticle-mediated targeted gene silencing and drug delivery to overcome tumor drug resistance. *Biomaterials*, **2010**, (31) 358-365.

92. Samadi, N., Abbadessa, A., Di Stefano, A., van Nostrum, C.F., Vermonden, T., Rahimian, S., Teunissen, E.A., van Steenbergen, M.J., Amidi, M. & Hennink, W.E. The effect of lauryl capping group on protein release and degradation of poly(D,L-lactic-co-glycolic acid) particles. *Journal of Controlled Release*, **2013**, (172) 436-443.

93. Zolnik, B.S. & Burgess, D.J. Effect of acidic pH on PLGA microsphere degradation and release. *Journal of Controlled Release*, **2007**, (122) 338-344.

94. Prades, R., Oller-Salvia, B., Schwarzmaier, S.M., Selva, J., Moros, M., Balbi, M., Grazú, V., de La Fuente, J.M., Egea, G., Plesnila, N., Teixidó, M. & Giralt, E. Applying the retro-enantio approach to obtain a peptide capable of overcoming the blood–brain barrier. *Angewandte Chemie International Edition*, **2015**, (54) 3967-3972.

95. Cecchelli, R., Aday, S., Sevin, E., Almeida, C., Culot, M., Dehouck, L., Coisne, C., Engelhardt, B., Dehouck, M.-P. & Ferreira, L. A stable and reproducible human blood-brain barrier model derived from hematopoietic stem cells. *PloS One*, **2014**, (9) e99733.

96. Hamman, J.H., Enslin, G.M. & Kotze, A.F. Oral delivery of peptide drugs: barriers and developments. *BioDrugs : Clinical Immunotherapeutics, Biopharmaceuticals and Gene Therapy*, **2005**, (19)165-177.

97. Choonara, B.F., Choonara, Y.E., Kumar, P., Bijukumar, D., du Toit, L.C. & Pillay, V. A review of advanced oral drug delivery technologies facilitating the protection and absorption of protein and peptide molecules. *Biotechnology Advances*, **2014**, (32)1269-1282.

98. Fosgerau, K. & Hoffmann, T. Peptide therapeutics: current status and future directions. *Drug Discovery Today*, **2015**, (20)122-128.

99. Copeland, R.A. in *Evaluation of Enzyme Inhibitors in Drug Discovery* (John Wiley & Sons, Inc., **2013**).

100. Lee, V.H.L. Protease inhibitors and penetration enhancers as approaches to modify peptide absorption. *Journal of Controlled Release*, **1990**, (13)213-223.

101. Yin, L., Ding, J., He, C., Cui, L., Tang, C. & Yin, C. Drug permeability and mucoadhesion properties of thiolated trimethyl chitosan nanoparticles in oral insulin delivery. *Biomaterials*, **2009**, (30)5691-5700.

102. Torchilin, V.P. Recent advances with liposomes as pharmaceutical carriers. *Nature reviews. Drug Discovery*, **2005**, (4)145-160.

103. Aungst, B.J. Absorption enhancers: applications and advances. *The American Association of Pharmaceutical Scientists Journal*, **2012**, (14)10-18.

104. Maher, S. & Brayden, D.J. Overcoming poor permeability: translating permeation enhancers for oral peptide delivery. *Drug Discovery Today: Technologies*, **2012**, (9)e113-e119.

105. Sánchez-Navarro, M., Garcia, J., Giralt, E. & Teixidó, M. Using peptides to increase transport across the intestinal barrier. *Advanced Drug Delivery Reviews*, **(accepted)**

106. Gentilucci, L., De Marco, R. & Cerisoli, L. Chemical modifications designed to improve peptide stability: incorporation of non-natural amino acids, pseudo-peptide bonds, and cyclization. *Current Pharmaceutical Design*, **2010**, (16)3185-3203.

107. Habermann, E. Bee and wasp venoms. *Science*, **1972**, (177)314-322.

108. Vives, E., Brodin, P. & Lebleu, B. A truncated HIV-1 TAT protein basic domain rapidly translocates through the plasma membrane and accumulates in the cell nucleus. *The Journal of Biological Chemistry*, **1997**, (272)16010-16017.

109. Futaki, S., Suzuki, T., Ohashi, W., Yagami, T., Tanaka, S., Ueda, K. & Sugiura, Y. Arginine-rich peptides. An abundant source of membrane-permeable peptides having potential as carriers for intracellular protein delivery. *The Journal of Biological Chemistry*, **2001**, (276)5836-5840.

110. Schwarze, S.R., Ho, A., Vocero-Akbani, A. & Dowdy, S.F. In vivo protein transduction: delivery of a biologically active protein into the mouse. *Science*, **1999**, (285)1569-1572.

111. Liang, J.F. & Yang, V.C. Insulin-cell penetrating peptide hybrids with improved intestinal absorption efficiency. *Biochemical and Biophysical Research Communications*, **2005**, (335)734-738.

112. Kamei, N., Morishita, M., Eda, Y., Ida, N., Nishio, R. & Takayama, K. Usefulness of cell-penetrating peptides to improve intestinal insulin absorption. *Journal of Controlled Release*, **2008**, (132)21-25.

113. Jin, Y., Song, Y., Zhu, X., Zhou, D., Chen, C., Zhang, Z. & Huang, Y. Goblet cell-targeting nanoparticles for oral insulin delivery and the influence of mucus on insulin transport. *Biomaterials*, **2012**, (33)1573-1582.

114. Kamei, N., Morishita, M., Ehara, J. & Takayama, K. Permeation characteristics of oligoarginine through intestinal epithelium and its usefulness for intestinal peptide drug delivery. *Journal of Controlled Release*, **2008**, (131)94-99.

115. Kamei, N., Kikuchi, S., Takeda-Morishita, M., Terasawa, Y., Yasuda, A., Yamamoto, S., Ida, N., Nishio, R. & Takayama, K. Determination of the optimal cell-penetrating peptide sequence for intestinal insulin delivery based on molecular orbital analysis with self-organizing maps. *Journal of Pharmaceutical Sciences*, **2013**, (102)469-479.

116. Kamei, N., Morishita, M. & Takayama, K. Importance of intermolecular interaction on the improvement of intestinal therapeutic peptide/protein absorption using cell-penetrating peptides. *Journal of Controlled Release*, **2009**, (136)179-186.

117. Sheng, Y., He, H. & Zou, H. Poly(lactic acid) nanoparticles coated with combined WGA and water-soluble chitosan for mucosal delivery of β-galactosidase. *Drug Delivery*, **2014**, (21)370-378.

118. Li, X., Wang, C., Liang, R., Sun, F., Shi, Y., Wang, A., Liu, W., Sun, K. & Li, Y. The glucose-lowering potential of exenatide delivered orally via goblet cell-targeting nanoparticles. *Pharmaceutical Research*, **2015**, (32)1017-1027.

119. Lindmark, T., Nikkila, T. & Artursson, P. Mechanisms of absorption enhancement by medium chain fatty acids in intestinal epithelial Caco-2 cell monolayers. *The Journal of Pharmacology and Experimental Therapeutics*, **1995**, (275)958-964.

120. Sakai, M., Imai, T., Ohtake, H. & Otagiri, M. Cytotoxicity of absorption enhancers in Caco-2 cell monolayers. *The Journal of Pharmacy and Pharmacology*, **1998**, (50)1101-1108.

121. Maher, S., Leonard, T.W., Jacobsen, J. & Brayden, D.J. Safety and efficacy of sodium caprate in promoting oral drug absorption: from in vitro to the clinic. *Advanced Drug Delivery Reviews*, **2009**, (61)1427-1449.

122. Lindmark, T., Soderholm, J.D., Olaison, G., Alvan, G., Ocklind, G. & Artursson, P. Mechanism of absorption enhancement in humans after rectal administration

of ampicillin in suppositories containing sodium caprate. *Pharmaceutical Research*, **1997**, (14)930-935.

123. Tavelin, S., Hashimoto, K., Malkinson, J., Lazorova, L., Toth, I. & Artursson, P. A new principle for tight junction modulation based on occludin peptides. *Molecular Pharmacology*, **2003**, (64)1530-1540.

124. Clarke, L.L. A guide to ussing chamber studies of mouse intestine. *American Journal of Physiology - Gastrointestinal and Liver Physiology*, **2009**, (296)G1151-G1166.

125. Polentarutti, B.I., Peterson, A.L., Sjoberg, A.K., Anderberg, E.K., Utter, L.M. & Ungell, A.L. Evaluation of viability of excised rat intestinal segments in the ussing chamber: Investigation of morphology, electrical parameters, and permeability characteristics. *Pharmaceutical Research*, **1999**, (16)446-454.

126. Riegler, M., Sedivy, R., Pothoulakis, C., Hamilton, G., Zacherl, J., Bischof, G., Cosentini, E., Feil, W., Schiessel, R., LaMont, J.T. & et al. Clostridium difficile toxin B is more potent than toxin A in damaging human colonic epithelium in vitro. *The Journal of Clinical Investigation*, **1995**, (95)2004-2011.

127. Sambuy, Y., De Angelis, I., Ranaldi, G., Scarino, M.L., Stammati, A. & Zucco, F. The Caco-2 cell line as a model of the intestinal barrier: influence of cell and culture-related factors on Caco-2 cell functional characteristics. *Cell Biology and Toxicology*, **2005**, (21)1-26.

128. Hilgendorf, C., Spahn-Langguth, H., Regardh, C.G., Lipka, E., Amidon, G.L. & Langguth, P. Caco-2 versus Caco-2/HT29-MTX co-cultured cell lines: permeabilities via diffusion, inside- and outside-directed carrier-mediated transport. *Journal of Pharmaceutical Sciences*, **2000**, (89)63-75.

129. Adura, C., Guerrero, S., Salas, E., Medel, L., Riveros, A., Mena, J., Arbiol, J., Albericio, F., Giralt, E. & Kogan, M.J. Stable conjugates of peptides with gold nanorods for biomedical applications with reduced effects on cell viability. *ACS Applied Materials & Interfaces*, **2013**, (5) 4076-4085.

130. Link, S. & El-Sayed, M.A. Spectroscopic determination of the melting energy of a gold nanorod. *The Journal of Chemical Physics*, **2001**, (114) 2362-2368.

131. Chen, T., Du, C., Tan, L.H., Shen, Z. & Chen, H. Site-selective localization of analytes on gold nanorod surface for investigating field enhancement distribution in surface-enhanced raman scattering. *Nanoscale*, **2011**, (3) 1575-1581.

132. Sharma, V., Park, K. & Srinivasarao, M. Shape separation of gold nanorods using centrifugation. *Proceedings of the National Academy of Sciences*, **2009**, (106) 4981-4985.

133. Xiong, B., Cheng, J., Qiao, Y., Zhou, R., He, Y. & Yeung, E.S. Separation of nanorods by density gradient centrifugation. *Journal of Chromatography. A*, **2011**, (1218) 3823-3829.

134. Jia, J.L., Xu, H.H., Zhang, G.R., Hu, Z. & Xu, B.Q. High quality gold nanorods and nanospheres for surface-enhanced raman scattering detection of 2,4-dichlorophenoxyacetic acid. *Nanotechnology*, **2012**, (23) 495710.

135. Akbulut, O., Mace, C.R., Martinez, R.V., Kumar, A.A., Nie, Z., Patton, M.R. & Whitesides, G.M. Separation of nanoparticles in aqueous multiphase systems through centrifugation. *Nano Letters*, **2012**, (12) 4060-4064.

136. Xu, X., Caswell, K.K., Tucker, E., Kabisatpathy, S., Brodhacker, K.L. & Scrivens, W.A. Size and shape separation of gold nanoparticles with preparative gel electrophoresis. *Journal of Chromatography. A*, **2007**, (1167) 35-41.

137. Hanauer, M., Pierrat, S., Zins, I., Lotz, A. & Sonnichsen, C. Separation of nanoparticles by gel electrophoresis according to size and shape. *Nano Letters*, **2007**, (7) 2881-2885.

138. Martin, I., Teixido, M. & Giralt, E. Design, synthesis and characterization of a new anionic cell-penetrating peptide: sap(e). *ChemBioChem*, **2011**, (12) 896-903.

139. Caswell, K., Wilson, J.N., Bunz, U.H. & Murphy, C.J. Preferential end-to-end assembly of gold nanorods by biotin-streptavidin connectors. *Journal of the American Chemical Society*, **2003**, (125) 13914-13915.

140. Liopo, A., Conjusteau, A., Tsyboulski, D., Ermolinsky, B., Kazansky, A. & Oraevsky, A. Biocompatible gold nanorod conjugates for preclinical biomedical research. *Journal of nanomedicine & nanotechnology*, **2012**, (Suppl 2: 001).

141. Rostro-Kohanloo, B.C., Bickford, L.R., Payne, C.M., Day, E.S., Anderson, L.J., Zhong, M., Lee, S., Mayer, K.M., Zal, T. & Adam, L. The stabilization and targeting of surfactant-synthesized gold nanorods. *Nanotechnology*, **2009**, (20) 434005.

142. Choi, J., Yang, J., Bang, D., Park, J., Suh, J.S., Huh, Y.M. & Haam, S. Targetable gold nanorods for epithelial cancer therapy guided by near-IR absorption imaging. *Small*, **2012**, (8) 746-753.

143. Stevens, M.G. & Olsen, S.C. Comparative analysis of using MTT and XTT in colorimetric assays for quantitating bovine neutrophil bactericidal activity. *Journal of Immunological Methods*, **1993**, (157) 225-231.

144. Ganley, I.G., Carroll, K., Bittova, L. & Pfeffer, S. Rab9 GTPase regulates late endosome size and requires effector interaction for its stability. *Molecular Biology of the Cell*, **2004**, (15) 5420-5430.

145. Kaiser, E., Colescott, R., Bossinger, C. & Cook, P. Color test for detection of free terminal amino groups in the solid-phase synthesis of peptides. *Analytical Biochemistry*, **1970**, (34) 595-598.

146. Mayer, L., Hope, M. & Cullis, P. Vesicles of variable sizes produced by a rapid extrusion procedure. *Biochimica et Biophysica Acta (BBA)-Biomembranes*, **1986**, (858) 161-168.

147. Bivas-Benita, M., Romeijn, S., Junginger, H.E. & Borchard, G. PLGA–PEI nanoparticles for gene delivery to pulmonary epithelium. *European Journal of Pharmaceutics and Biopharmaceutics*, **2004**, (58) 1-6.

148. Cosco, D., Federico, C., Maiuolo, J., Bulotta, S., Molinaro, R., Paolino, D., Tassone, P. & Fresta, M. Physicochemical features and transfection properties of chitosan/poloxamer 188/poly (D, L-lactide-co-glycolide) nanoplexes. *International Journal of Nanomedicine*, **2014**, (9) 2359.

149. Son, S. & Kim, W.J. Biodegradable nanoparticles modified by branched polyethylenimine for plasmid DNA delivery. *Biomaterials*, **2010**, (31) 133-143.

150. Buschmann, M.D., Merzouki, A., Lavertu, M., Thibault, M., Jean, M. & Darras, V. Chitosans for delivery of nucleic acids. *Advanced Drug Delivery Reviews*, **2013**, (65) 1234-1270.

151. Mansouri, S., Lavigne, P., Corsi, K., Benderdour, M., Beaumont, E. & Fernandes, J.C. Chitosan-DNA nanoparticles as non-viral vectors in gene therapy: strategies to improve transfection efficacy. *European Journal of Pharmaceutics and Biopharmaceutics*, **2004**, (57) 1-8.

152. Lavertu, M., Methot, S., Tran-Khanh, N. & Buschmann, M.D. High efficiency gene transfer using chitosan/DNA nanoparticles with specific combinations of molecular weight and degree of deacetylation. *Biomaterials*, **2006**, (27) 4815-4824.

153. Wagner, E., Ogris, M. & Zauner, W. Polylysine-based transfection systems utilizing receptor-mediated delivery. *Advanced Drug Delivery Reviews*, **1998**, (30) 97-113.

154. Okada, H., Ogawa, T., Tanaka, K., Kanazawa, T. & Takashima, Y. Cytoplasm-responsive delivery systems for sirna using cell-penetrating peptide nanomicelles. *Journal of Drug Delivery Science and Technology*, **2014**, (24) 3-11.

155. Montrose, K., Yang, Y., Sun, X., Wiles, S. & Krissansen, G.W. Xentry, a new class of cell-penetrating peptide uniquely equipped for delivery of drugs. *Scientific Reports*, **2013**, (3) 1661.

156. Boussif, O., Lezoualc'h, F., Zanta, M.A., Mergny, M.D., Scherman, D., Demeneix, B. & Behr, J.-P. A versatile vector for gene and oligonucleotide transfer into cells in culture and in vivo: polyethylenimine. *Proceedings of the National Academy of Sciences*, **1995**, (92) 7297-7301.

157. Seo, E.J., Jang, I.H., Do, E.K., Cheon, H.C., Heo, S.C., Kwon, Y.W., Jeong, G.O., Kim, B.R. & Kim, J.H. Efficient production of retroviruses using PLGA/bPEI-DNA nanoparticles and application for reprogramming somatic cells. *PloS One*, **2013**, (8) e76875.

158. Moghimi, S.M., Symonds, P., Murray, J.C., Hunter, A.C., Debska, G. & Szewczyk, A. A two-stage poly (ethylenimine)-mediated cytotoxicity: implications for gene transfer/therapy. *Molecular Therapy*, **2005**, (11) 990-995.

159. Boeckle, S., von Gersdorff, K., van der Piepen, S., Culmsee, C., Wagner, E. & Ogris, M. Purification of polyethylenimine polyplexes highlights the role of free polycations in gene transfer. *The Journal of Gene Medicine*, **2004**, (6) 1102-1111.

160. Zeng, P., Xu, Y., Zeng, C., Ren, H. & Peng, M. Chitosan-modified poly (D, L-lactide-co-glycolide) nanospheres for plasmid DNA delivery and HBV gene-silencing. *International Journal of Pharmaceutics*, **2011**, (415) 259-266.

161. Tang, J., Chen, J.-Y., Liu, J., Luo, M., Wang, Y.-J., Wei, X.-w., Gao, X., Wang, B.-l., Liu, Y.-B. & Yi, T. Calcium phosphate embedded PLGA nanoparticles: a promising gene delivery vector with high gene loading and transfection efficiency. *International Journal of Pharmaceutics*, **2012**, (431) 210-221.

162. TRAN INT: understand the barrier, understand the carrier. (**last accessed 01/03/2016**), http://www.trans-int.eu/.

163. Lindmark, T., Kimura, Y. & Artursson, P. Absorption enhancement through intracellular regulation of tight junction permeability by medium chain fatty acids in Caco-2 cells. *The Journal of Pharmacology and Experimental Therapeutics*, **1998**, (284)362-369.

164. Pueyo, M.T., Mutafci, B.A., Soto-Arriaza, M.A., Di Mascio, P. & Carmona-Ribeiro, A.M. The self-assembly of a cyclic lipopeptides mixture secreted by a B. megaterium strain and its implications on activity against a sensitive Bacillus species. *PloS One*, **2014**, (9)e97261.

ANNEX I

Buffers and medium preparation

BBB-model DMEM

Reagent	Amount	Final concentration
DMEM	1,000 mL	25 mM
NaHCO₃	2 g/L	24 mM

The pH was adjusted at 6.8 with HCl 6M.

Complete DMEM medium

Reagent	Amount	Final concentration
DMEM	500 mL	
FBS	50 mL	10%
L-glutamine	5.5 mL (200 mM)	2mM
Penicillin G		100 units/mL
Streptomycin		100 µg/mL

Not recommended to use the medium after 2 months from the date prepared.

HBSS

Reagent	Amount	Final concentration
$CaCl_2$	0.14 g/L	1.26 mM
$MgCl_2 \cdot 6\ H_2O$	0.1 g/L	0.49 mM
$MgSO_4 \cdot 7\ H_2O$	0.1 g/L	0.41 mM
KCl	0.4 g/L	5.33 mM
KH_2PO_4	0.06 g/L	0.44 mM
NaHCO₃	0.35 g/L	4.17 mM
NaCl	8 g/L	137.93 mM
Na_2HPO_4 anhydrous	0.048 g/L	0.34 mM
D-Glucose	1 g/L	5.55 mM

HBSS was buffered with 10 mM HEPES (pH 7.4) and 10 mM MES (pH 6) in any occasion for Caco-2 cell mnolayer. Also, calcium and magnesium free HBSS was prepared ($CaCl_2$ and $MgSO_4$ were not included).

Krebs-Heinsleit buffer solution

Stock solutions:

Reagent	Amount
$MgSO_4$-7·H_2O	29.6 g/L
KH_2PO_4	16.3 g/L
$CaCl_2$	36.76 g/L
KCl	35 g/L

Keep stock solutions in fridge, they will not expire.

Reagent	Amount	Final concentration
NaCl	6.58 g/L	112.5 mM
$NaHCO_3$	8.15 g/L	25 mM
D-glucose	18.38 g/L	12 mM
* mL of each stock solution		
$MgSO_4$-7·H_2O	10 mL/L	1.2 mM
KH_2PO_4	10 mL/L	1.2 mM
$CaCl_2$	10 mL/L	3.3 mM
KCl	10 mL/L	4.7 mM

KH buffer expires after 24 h but if glucose is not added to the solution it can be kept for more than 1 day. $CaCl_2$ is added the last else it can precipitate, if so bubble with oxygen. All solutions were prepared with distilled H_2O.

MES buffer

Reagent	Amount	Final concentration
MES	19.5 g/L	100 mM

The pH was adjusted to 6 with NaOH.

Laemmli 2X buffer

Reagent	Amount	Final concentration
Tris·HCl	19.7 mg/mL	125 mM
Glycerol	0.2 mL/mL	20%
2-mercaptoehtanol	0.1 mL/mL	10%
SDS	40 mg/mL	4%
Bromophenol blue		0.004%

The pH was adjusted to 6.8.

PB 0.1 M buffer

Reagent	Amount	Final concentration
$NaH_2PO_4 \cdot H_2O$	3.1 g/L	22.5 mM
Na_2HPO_4 (anhydrous)	10.9 g/L	76.8 mM

The pH of the final solution will be 7.4. This buffer can be stored for up to 1 month at 4°C.

PBS buffer

Reagent	Amount	Final concentration
NaCl	8 g/L	137 mM
KCl	0.2 g/L	2.7 mM
Na_2HPO_4	1.44 g/L	10 mM
KH_2PO_4	0.24 g/L	1.8 mM

The pH was adjusted at pH 7.4 with HCl.

Perycites medium

Reagent	Amount	Final concentration
NaHCO$_3$ DMEM	200 mL	
FBS	50 mL	25%
L-glutamine	2.5 mL (200 mM)	2mM
Gentamycin	1.25 mL	

FBS was especially tested for BBB assays.

Ringer-HEPES buffer

Reagent	Amount	Final concentration
NaCl	8.77 g /L	150 mM
KCl	0.388 g/L	5.2 mM
CaCl$_2$	0.244 g/L	2.2 mM
MgCl$_2$	0.019 g/L	0.2 mM
NaHCO$_3$	0.504 g/L	6 mM
HEPES	1.19 g/L	5 mM
D-Glucose	0.504 g/L	2.8 mM

RIPA (Radio Immunoprecipitation Assay) buffer

Reagent	Amount	Final concentration
NaCl	8.7 g/L	150 mM
Tris	6.05 g/L	50 mM
Triton X-100	10 mL/L	1%
Sodium deoxycholate	5 g/L	0.5%
SDS	1 g/L	0.1%

Running buffer

Reagent	Amount	Final concentration
Tris	3 g/L	25 mM
Glycine	14.25 g/L	190 mM
SDS	1 g/L	0.1%

The pH was adjusted at pH 8.3.

Supplemented ECM (sECM)

Reagent	Amount	Final concentration
ECM	500 mL	
FBS	25 mL	5%
ECGS	5 mL	ECGS
Gentamycin	2.5 mL	

TAE buffer

Reagent	Amount	Final concentration
Tris	4.84 g/L	40 mM
EDTA	0.3 g/L	1 mM
Glacial Acetic acid	1.15 mL/L	20 mM

EDTA was completely solubilized at pH 8, then pH was adjusted at pH 7.6.

TBE buffer

Reagent	Amount	Final concentration
Tris	10.8 g/L	89 mM
EDTA	0.93 g/L	2 mM
Boric acid	5.5 g/L	89 mM

EDTA was completely solubilized at pH 8, then pH was adjusted at pH 8.3.

TBS buffer

Reagent	Amount	Final concentration
Tris	2.4 g/L	20 mM
NaCl	8.7 g/L	150 mM

TBST buffer

Reagent	Amount	Final concentration
Tris	2.4 g/L	20 mM
NaCl	8.7 g/L	150 mM
Tween 20	1 mL/L	0.1%

TE buffer

Reagent	Amount	Final concentration
Tris-HCl	1.58 g/L	10 mM
EDTA	0.3 g/L	1 mM

EDTA was completely solubilized at pH 8, then pH was adjusted to 7.5.

Transfer buffer

Reagent	Amount	Final concentration
Tris	3 g/L	25 mM
Glycine	14.25 g/L	190 mM
Methanol	200 mL/L	20%

The pH was adjusted at pH 8.3.

ANNEX II

Peptide characterization

Peptide	Theoretical Mass (Da)	Experimental Mass (Da)	Retention time (min)	Sequence
r_8	1266.54	1267.84	0.75	H-rrrrrrrr-NH$_2$
$r_8k(CF)$	1597.3	1598.3	0.94	H-rrrrrrrrk(CF)-NH$_2$
cr_8	1369.68	1670.67	0.78	H-crrrrrrrr-NH$_2$
$csap(e)$	2019.4	2020.15	1.48	H-cvelpppvelpppvelppp-NH$_2$
$GTHRre$	1547.8	1548.08	1.21	H-Gpwvpswmpprht-NH$_2$
C_{12}-r_8	1448.85	1150.08	1.18	CH$_3$-(CH$_2$)$_{10}$-CONH-rrrrrrrr-NH$_2$
Cho-r_8	1679.20	1681.8	1.63	Cho-CONH-rrrrrrrr-NH$_2$
C_8-r_8	1392.74	1393.96	0.96	CH$_3$-(CH$_2$)$_6$-CONH-rrrrrrrr-NH$_2$
C_{10}-r_8	1420.80	1421.41	1.06	CH$_3$-(CH$_2$)$_8$-CONH-rrrrrrrr-NH$_2$
C_{18}-r_8	1533.01	1534.49	1.18	CH$_3$-(CH$_2$)$_{16}$-CONH-rrrrrrrr-NH$_2$
C_{12}-r_4	824.09	825.38	1.29	CH$_3$-(CH$_2$)$_{10}$-CONH-rrrr-NH$_2$
C_{12}-r_6	1136.47	1137.48	1.20	CH$_3$-(CH$_2$)$_{10}$-CONH-rrrrrr-NH$_2$
C_{12}-r_{12}	2073.61	2074.03	1.11	CH$_3$-(CH$_2$)$_{10}$-CONH-rrrrrrrrrrrr-NH$_2$
Cho-r_4	1054.45	1055.46	1.73	Cho-CONH-rrrr-NH$_2$
Cho-r_6	1366.82	1367.48	1.71	Cho-CONH-rrrrrr-NH$_2$
Cho-r_{12}	2303.58	2305.88	1.59	Cho-CONH-rrrrrrrrrrrr-NH$_2$

Retention times were obtained from UPLC chromatograms. The flow rate was 0.6 mL/min using ACN (0.036% TFA) and H$_2$O (0.045% TFA). 2 min linear gradients from 0% to 100% ACN were used.

Experimental mass was obtained from UPLC-MS waters equipment coupled to a PDA Acquity detector and SQ detector 2. The flow rate was 0.6 mL/min using ACN (0.07% formic acid) and H$_2$O (0.1% formic acid). 2 min linear gradients from 0% to 100% ACN were used. A C$_{18}$ Acquity UPLC® BEH (2.5 x 50 mm x 1.7 μm) column was used.

Resum en Català

Introducció general

En les últimes dècades, l'ús de nanomaterials ha augmentat de forma exponencial gràcies a les propietats úniques atribuïdes a les seves dimensions. Al disminuir la mida dels materials, alguns dels fenòmens que afecten aquestes partícules es veuen incrementats com per exemple la seva força, reactivitat o conductivitat. Aquestes noves i superiors propietats de les nanopartícules ha causat un gran interès en la comunitat científica, el qual es observable amb el gran increment de publicacions, patents i finançament relacionat amb la nanotecnologia en els últims anys (Figura 1).[1,2,3]

Total Global Nanotechnology Funding
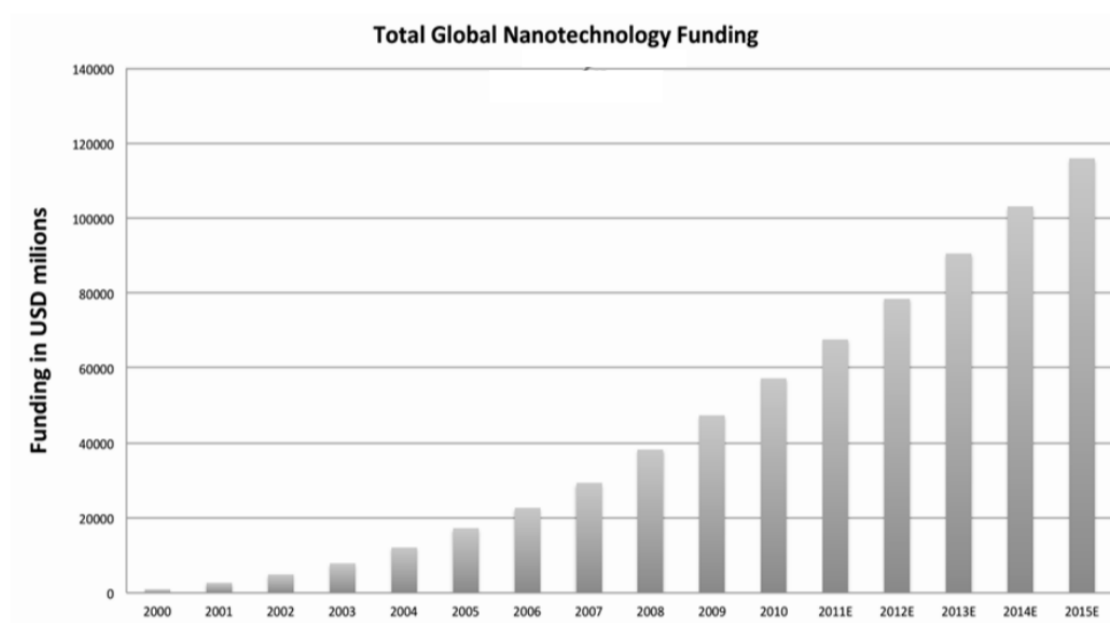
Figura 1. Finançament global acumulatiu relacionat amb les nanotecnologies (font: Cientifica Ltd 2011).

Tot i que està havent-hi un enorme implantació dels nanomaterials en moltes disciplines tal com en la indústria alimentaria o química, la major preocupació es centra en l'ús abusiu i excessiu d'aquest nous materials. Aquest ús incontrolat i perllongat pot causar toxicitat, altrament coneguda com a nanotoxicitat, per bé que a dia d'avui encara no s'ha caracteritzat.[4]

Encara que existeixen riscos molt alts, els científics segueixen utilitzant els nanomaterials per tal de millorar tècniques ja descrites i poder avançar tecnològicament. És pels avantatges que presenten els nanomaterials que aquesta tesis està centrada en l'ús

de nanopartícules per tal d'incrementar el creuament de molècules terapèutiques a través de determinades membranes biològiques.

Aquesta tesi està dividida en tres capítols, els quals tenen com a punt en comú l'ús de pèptids units a nanopartícules o com a membres de complexes de mida nanomètrica. Aquests nanomaterials estan dissenyats per tal de millorar el seu transport a través de les següents barreres biològiques: la membrana cel·lular, la barrera hematoencefàlica (BHE) i la barrera intestinal.

Capítol 1. Ús de nanovaretes d'or per aconseguir l'alliberació endosomal

Introducció

El primer capítol té com a objectiu principal la síntesi, caracterització i optimització de nanovaretes d'or (NR, nanorods) decorades amb pèptids de penetració cel·lular (CPPs, de l'anglès *cell penetrating peptides*) per tal d'aconseguir una alliberació endosomal controlada mitjançant la irradiació amb un làser infraroig (IR). Aquests nanorods presenten dos pics característics en el seu espectre d'absorció. El primer pic absorbeix en el rang del visible, *ca.* 500-520 nm, i ve determinat per l'absorció dels electrons per la part transversal de la nanopartícula. El segon pic ve donat per l'absorció dels electrons per la part longitudinal, el qual pot variar depenent del ràtio entre la seva longitud i diàmetre. El control d'aquesta relació permet doncs obtenir nanorods que absorbeixin a unes longituds determinades (Figura 2).
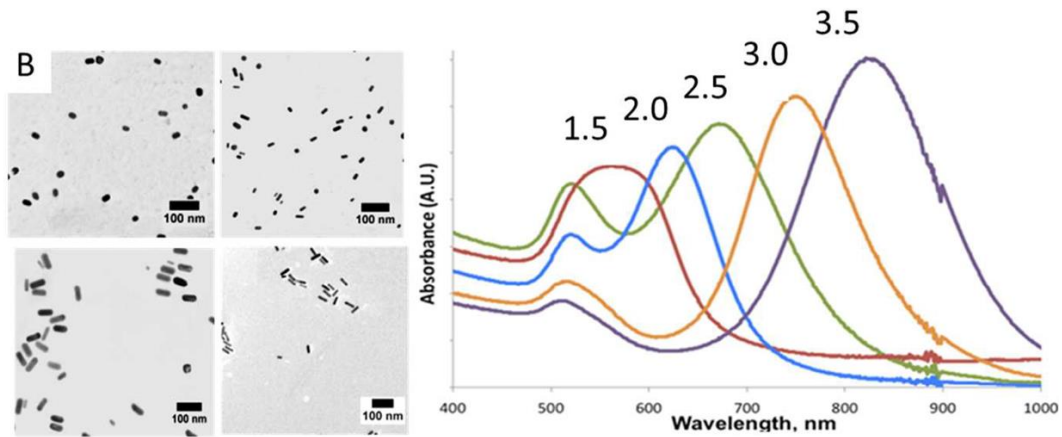
Figura 2. A) Imatges dels diferents nanorods obtingudes amb microscopi de transmissió electrònica (TEM). Escala: 100 nm. B) Espectre d'absorció de les diferents formulacions variant el ràtio entre longitud i diàmetre dels nanorods.

Els nanorods sintetitzats en la present tesi es van caracteritzar per absorbir a 1000 nm. El gran avantatge d'absorbir a aquesta longitud d'ona és que hi ha una major penetració del làser a l'hora d'irradiar els nanorods, en comparació amb aquells que absorbeixen a longituds d'ona inferiors.[5] Un cop caracteritzats els nanorods, les molècules de bromur de hexadeciltrimetilamoni (CTAB, de l'anglès *cetyltrimethylammonium bromide*) adherides a la seva superfície (provinent de la síntesi) van ser substituïdes, ja que està descrit que aquestes molècules són citotòxiques.[6] Per tal de reemplaçar les molècules de CTAB, i addicionalment conferir estabilitat a les nanopartícules, es va escollir polietilé glicol (PEG). Aquest polímer estava compost per dos grups funcionals: un grup tiol, el qual formava un enllaç covalent amb la superfície d'or dels nanorods, i un grup carboxílic, al qual posteriorment vam unir el CPP. Per al nostre propòsit, es va seleccionar la octaarginina composta per D-aminoàcids (r_8) com a CPP (Figura 3).[7]
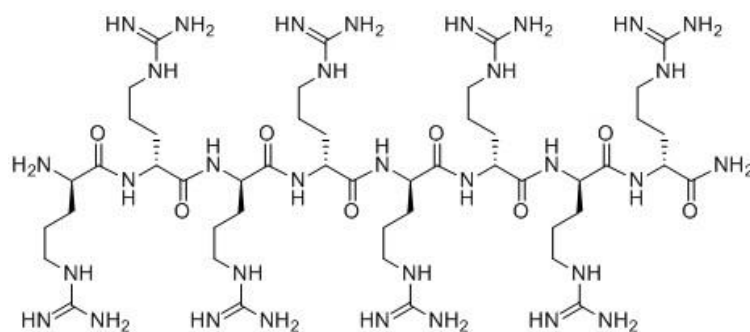

Figura 3. Seqüència química del r_8.

D'altra banda, per tal de poder visualitzar el nostre sistema, vam conjugar una molècula fluorescent al pèptid. Al constructe final, composat per NR-PEG-CPP, es va afegir siARN com a marcador per tal de detectar si els nanorods eren capaços d'arribar al citosol. La conjugació del siARN amb la nanopartícula es donava perquè les seves càrregues negatives interaccionaven electrostàticament amb les càrregues positives del CPP. L'ús del siARN com a marcador era possible perquè la irradiació dels nanorods amb un làser d'infraroig, alliberava el siARN al citosol i que al seu torn silenciava una determinada proteïna. Finalment, mitjançant la tècnica de Western Blot, podíem ser capaços de detectar si aquest siARN conjugat a la nanopartícula havia sigut efectivament capaç d'arribar al citosol. En la Figura 4 es mostra un esquema del l'assaig descrit.
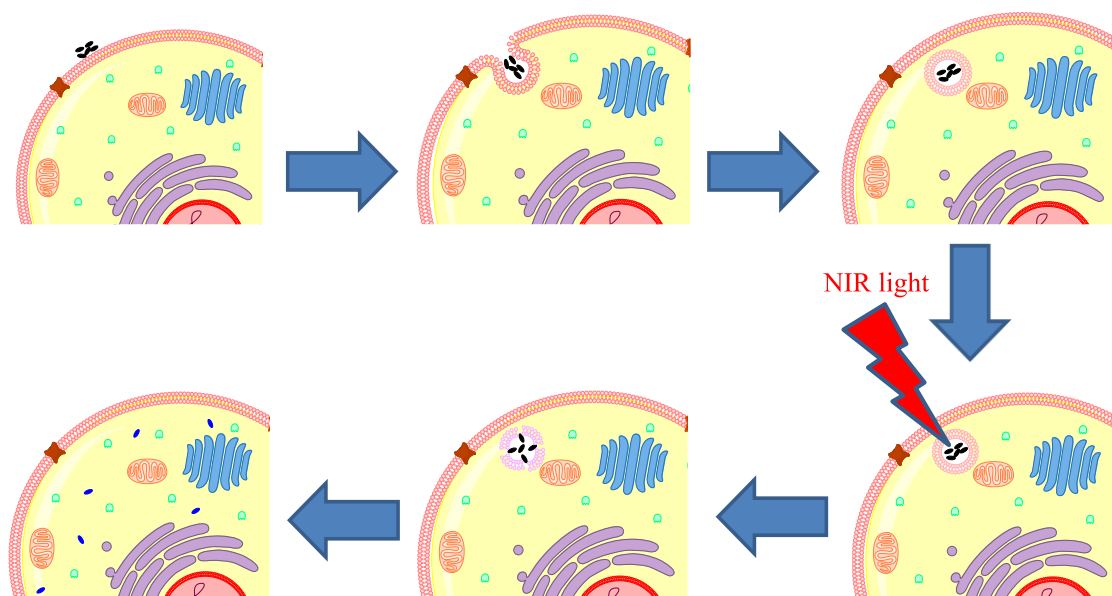

Figura 4. Representació esquemàtica del nostre objectiu final.

Resultats i conclusions

Primerament, vam preparar els nanorods mitjançant el conegut mètode de *seed mediated growth*.[8,9] Petites modificacions van ser necessàries per tal d'aconseguir una dissolució amb un contingut de nanorods de més del 90% comparat amb altres subproductes tal com nanoesferes.[10] La caracterització d'aquestes nanopartícules es va fer mitjançant microscòpia electrònica i espectrofotometria, tal i com es mostra en la Figura 5.
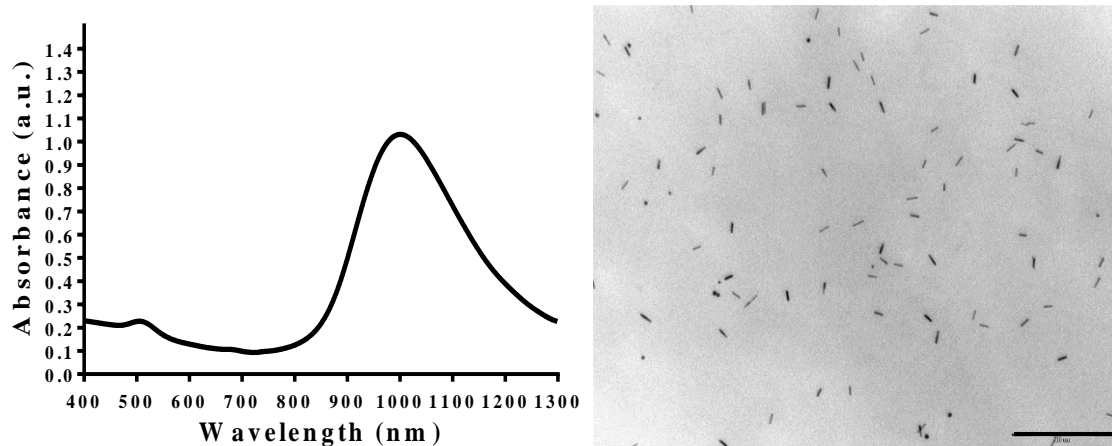
Figura 5. Caracterització dels nanorods d'or mitjançant: A) Espectre de UV-Vis-IR. Absorció longitudinal a 1000 nm. B) Imatge de microscopi de transmissió electrònica. Escala gràfica: 500 nm.

A partir d'aquesta síntesi, es van obtenir nanorods amb una mida mitjana de 50.7 ± 7.7 en longitud i 9.0 ± 0.7. A partir d'aquestes mesures, es va derivar que la concentració de nanorods era de 2.45 nM en cada síntesi de 10 mL.

Posteriorment, tal i com prèviament havíem comentat, la superfície dels nanorods va ser funcionalitzada per tal d'eliminar el CTAB i donar estabilitat a les partícules. En primer lloc, el PEG va ser acoblat a la superfície dels nanorods, eliminant el CTAB. Seguidament, el pèptid r_8 marcat amb una molècula fluorescent, va ser conjugat al PEG mitjançant un enllaç amida. Finalment, el siARN es va adherir electrostàticament al CPP. Aquest procés s'esquematitza en la Figura 6.
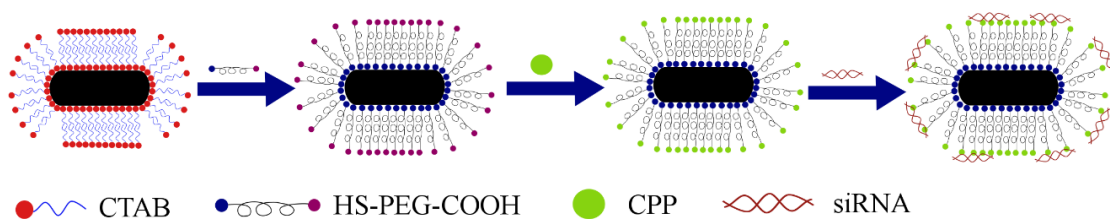

Figura 6. Representació esquemàtica de la funcionalització dels nanorods d'or.

A continuació, la toxicitat d'aquests nanorods modificats va ser provada en un assaig de toxicitat nomenat XTT, que mesura l'activitat metabòlica de les cèl·lules vives. Dos tipus de línies cel·lulars van ser escollides per fer aquest assaig: HeLa i fibroblasts 3T3. En els dos casos, les cèl·lules van tenir una viabilitat superior al 90% fins a una concentració de 1 nM. En canvi, les cèl·lules tractades amb la mateixa concentració però sense modificar, van tenir una viabilitat inferior al 10% en les dos línies cel·lulars. Va quedar demostrat,

per tant, que la funcionalització amb PEG és imprescindible per poder treballar amb cèl·lules.

Un cop demostrada la baixa toxicitat de les nanopartícules modificades, es va prosseguir a confirmar la internalització cel·lular d'aquestes partícules. L'ús de microscòpia confocal i de transmissió electrònica van ser suficients per tal de demostrar que les partícules eren capaces d'internalitzar-se (Figura 7). En aquests experiments, els nanorods modificats (0.2 nM) van ser afegits en el medi de les cèl·lules i incubats durant 24 hores a 37ºC i 5% CO_2.

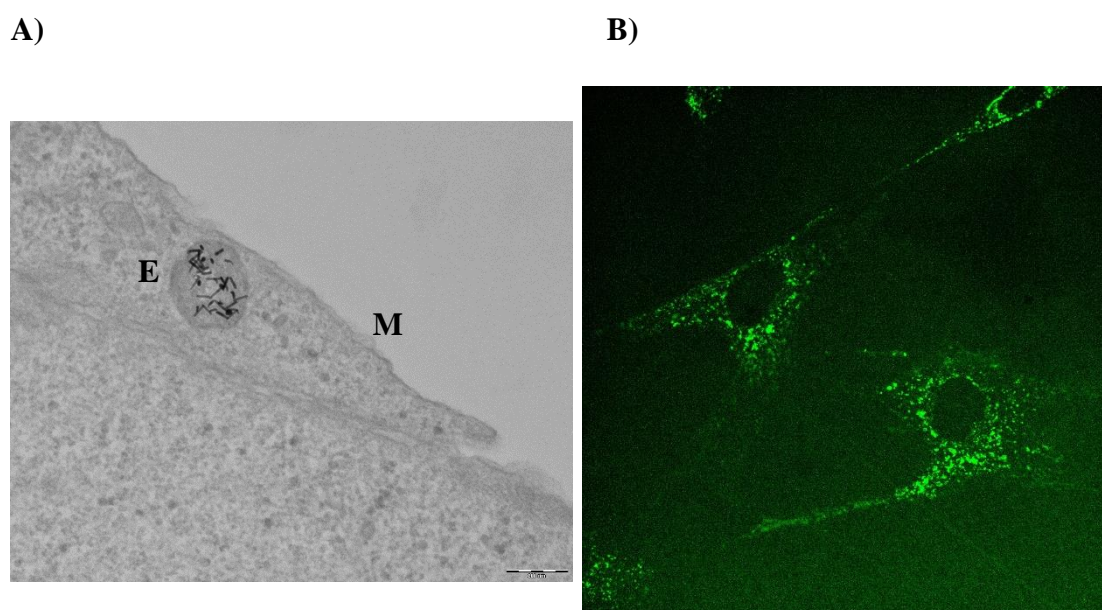A)   B)

Figura 7. Confirmació de la internalització dels nanorods a dintre de fibroblasts. A) Imatge representativa de transmissió electrònica. M: membrana cel·lular, E: endosoma madur. Escala gràfica 200 nm. B) Fluorescència provinent dels nanorods obtinguda amb un microscopi confocal.

Finalment, un cop confirmada la internalització de les nanopartícules en l'endosoma, aquestes van ser irradiades amb un làser d'infraroig proper (longitud d'ona de sortida de 1064 nm). Per als experiments, 0.2 nM de nanords van ser incubats durant 24 h en fibroblasts. Seguidament, les cèl·lules van ser irradiades a diferents temps (10, 30 i 60 minuts) a 60 mW/cm^2. Després, les cèl·lules van ser incubades de nou durant 3 dies per tal de que el siRNA silencies la expressió de la proteïna. Passat aquest temps, les cèl·lules van ser lisades i la proteïna carregada en un gel de poliacrilamida. Les proteïnes van ser transferides a una membrana, la qual va ser tractada amb els anticossos primaris i

secundaris corresponents. Finalment, la membrana va ser revelada obtenint el resultats que es mostra en la Figura 8. La proteïna escollida per ser silenciada va ser la PARP1 i com a control vam utilitzar la β-actina.

Com a resultat preliminar, vam observar un decreixement de la intensitat de la banda B on els nanorods (0.5 nM) van ser irradiats durant 10 minuts. Quan la mostra irradiada tenia una concentració inferior (banda A), no es va detectar cap efecte. Aquest resultats ens van indicar que aquests nanorods poden arribar a tenir un gran potencial com a potenciadors del transport endosomal. Futurs experiments es centraran en augmentar els temps d'irradiació i una millora de la detecció de l'efecte d'alliberament del siARN.
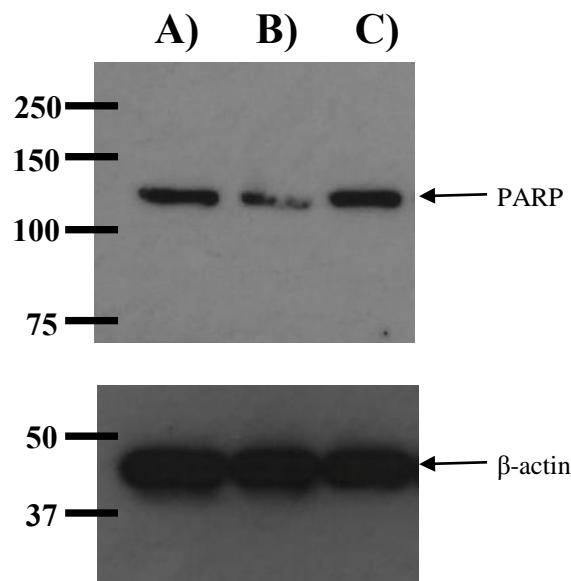

Figura 8. Tècnica de western blot aplicada a la proteïna PARP (118 kDa) i β-actina (40 kDa). A) Cèl·lules no irradiades, B) 0.5 nM nanorods modificats després de 10 min d'irradiació i C) 0.2 nM nanorods modificats després de 10 min d'irradiació.

Capítol 2. Ús de nanopartícules de PLGA per a millorar el transport de ADN a través de la BHE.

Introducció

L'atàxia de Friedreich es una malaltia neurodegenerativa causada per la mutació d'un gen (X25).[11] Aquest fet produeix una expansió en la producció d'un trinucleotid (GAA) el qual es el causant d'una menor quantitat de la proteïna frataxina en diferents tipus cel·lulars.[12] Al tractar-se d'una malaltia neurodegenerativa, la major quantitat de cèl·lules

deficients en frataxina es troba al cervell. Per tant, en aquest capítol el nostre objectiu és transportar ADN encapsulat dins de nanopartícules d'àcid poli làctic-glicòlic (PLGA) per tal de que aquestes creuin la BHE i arriben a transfectar les cèl·lules del cervell. El PLGA va ser escollit pel seu ús extens en fases clíniques, ja que està aprovat per la US Food and Drug Administration (FDA) i la European Medicine Agency (EMA). Aquest polímer té el gran avantatge de ser biodegradable, formant àcid làctic i àcid glicòlic,[13] i addicionalment és comercial.

La nostra aproximació està centrada en la formulació de nanopartícules de PLGA, les quals puguin encapsular el ADN que codifiqui la frataxina. A la superfície d'aquestes, i per tal de millorar el seu transport a través de la BHE, vam acoblar un pèptid llançadora (THRre)[14] i/o un CPP (r_8). A més a més, per tal de millorar la seva transfecció, vam incorporar un polímer positiu (chitosà o bPEI), el qual quedava unit al ADN. L'esquema de la reacció es mostra en la Figura 9.
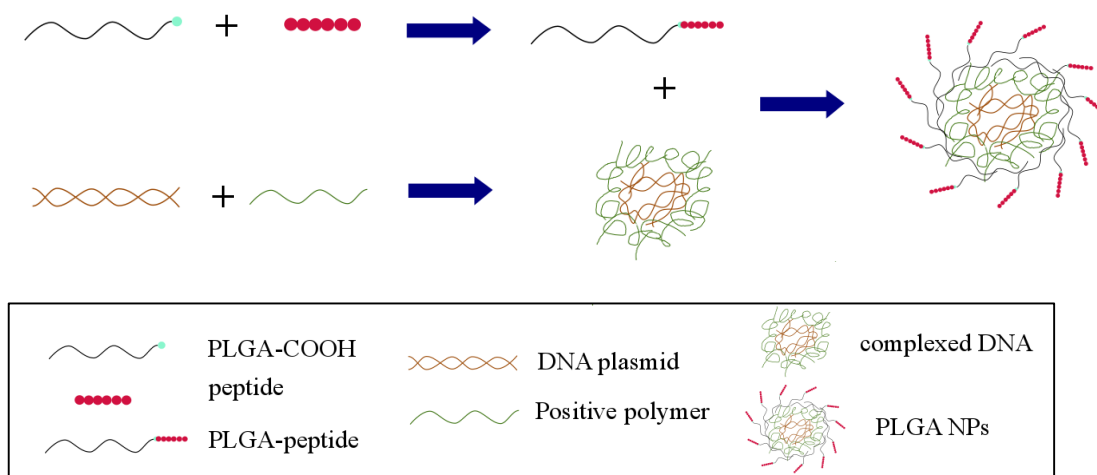

Figura 9. Esquema del procés d'encapsulació del ADN a dintre de les nanopartícules de PLGA.

Primer, el polímer de PLGA es funcionalitzat amb el pèptid d'interès. Seguidament, el ADN queda complexat pel polímer positiu bPEI. Finalment, les nanopartícules es formen envoltant aquest complex ADN:bPEI. Es van utilitzar diferents línies cel·lular per tal de provar la transfectivitat de varies formulacions. Com a prova de concepte, es va posar a punt un model cel·lular imitant la BHE[15] i les nanopartícules van ser assajades per veure si eren capaces de travessar la membrana.

Resultats i conclusions

Inicialment, els dos pèptids (r₈ i THRre) van ser conjugats al polímer de PLGA mitjançant un enllaç amida (el *N*-terminal del pèptid va reaccionar amb l'àcid carboxílic del PLGA). A partir d'aquest co-polímer, es van sintetitzar totes les nanopartícules. El mètode utilitzat per tal de sintetitzar les nanopartícules va ser el de nanoprecipitació, incloent petites modificacions.[16] Els dos polímers utilitzats per tal de complexar el ADN van ser chitosà i bPEI. Amb els dos polímers, es va aconseguir més d'un 90% d'encapsulació del ADN a dintre de les nanopartícules de PLGA. Tot i això, les nanopartícules que contenien chitosà van resultar no transfectives en totes les línies cel·lulars assajades (HeLa, fibroblasts i endotelials de cervell). Pel contrari, les nanopartícules que contenien bPEI van resultar transfectives en quasi tots els cassos assajats. Aquestes partícules contenien diferents ratios entre PLGA:bPEI:DNA. En la Figura 10 es mostren imatges representatives obtingudes al microscopi de fluorescència. Com a ADN model i per a una fàcil visualització, es va encapsular un ADN que codifica una proteïna fluorescent (GFP).
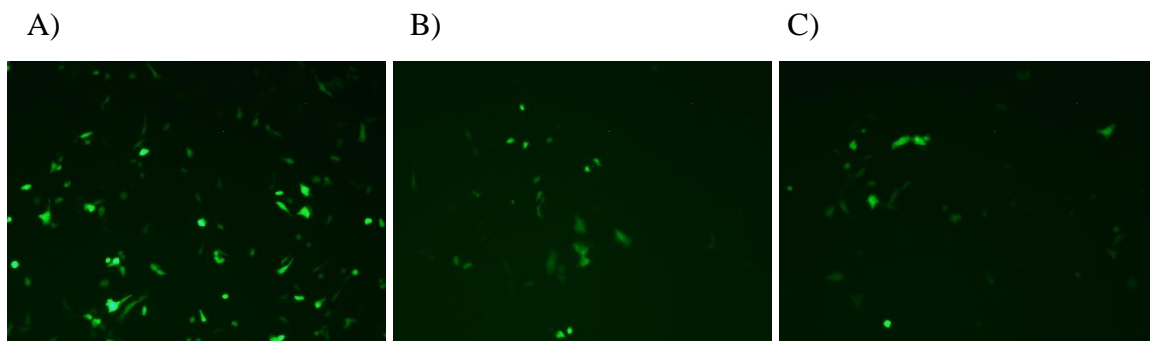
A) B) C)

Figura 10. Imatges obtingudes per microscòpia de fluorescència (excitació en el rang del verd). La incubació va ser de 2-3h en cèl·lules HeLa. Les partícules de PLGA-pèptid:bPEI:ADN van ser: A) PLGA-r₈:bPEI:ADN (60:3:1), B) PLGA-GTHRre:bPEI:ADN (60:3:1), C) PLGA-r₈/PLGA-GTHRre:bPEI:ADN (30/30:3:1).

Un cop aconseguida una alta transfecció, les nanopartícules es van assajar en línies cel·lulars derivades del cervell. En aquest cas, el ADN utilitzat va ser el que codificava la frataxina per tal d'apropar-nos a la versió final de la nostra formulació. Per tant, aquestes partícules que contenien PLGA:bPEI:ADN van ser assajades amb la línia cel·lular de glioblastoma. 24 hores després de la transfecció, les cèl·lules van ser lisades i les proteïnes van ser aplicades a la tècnica de Western Blot per tal de poder observar si

havia hagut un augment en la proteïna de la frataxina. Com es mostra en la Figura 11, la expressió de frataxina va augmentar per a cert tipus de nanopartícules. Com a proteïna control es va utilitzar la tubulina. Curiosament, les partícules que contenien una major quantitat de polímer, i per tant de pèptid, van ser les que van tenir una major transfecció (partícules 1,3 i 5). A excepció de les partícules 4, les quals vam obtenir la major transfecció de totes les partícules assajades. Aquest resultats van ser preliminars i s'han de repetir per tal d'aconseguir una explicació coherent dels fets. Tot i això, els resultats ens indicaven que el camí a seguir era correcte.
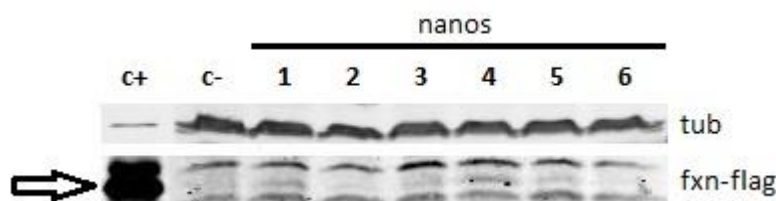

Figura 11. Assaig de transfecció de varies formulacions de PLGA:bPEI:ADN. 1) PLGA-r$_8$:bPEI:DNA a 120:3:1 (w/w/w), 2) PLGA-r$_8$:bPEI:DNA a 30:3:1 (w/w/w), 3) PLGA-GTHRre:bPEI:DNA a 120:3:1 (w/w/w), 4) PLGA-GTHRre:bPEI:DNA a 30:3:1 (w/w/w), 5) PLGA-r$_8$/PLGA-GTHRre:bPEI:DNA a 60/60:3:1 (w/w/w), 6) PLGA-r$_8$/PLGA-GTHRre:bPEI:DNA a 15/15:3:1 (w/w/w). Cèl·lules sense tractar van ser utilitzades com a control negatiu (c-) i cèl·lules transfectades amb Superfect van ser el nostre control positiu (c+).

Finalment, aquestes nanopartícules es van assajar en un model cel·lular de BHE. Les partícules es van adicionar en la part donadora del model i al cap de 2 h, la part acceptora es va analitzar per veure si havien creuat la membrana. Es va fer una extracció del ADN d'aquesta part acceptora i es va analitzar per gel d'agarosa per tal de poder detectar ADN (Figura 12).
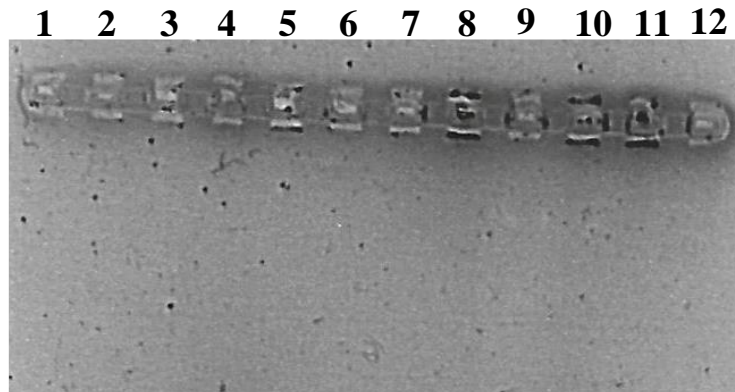
Figura 12. Bandes de ADN detectades amb gel d'agarosa al 0.8%. Cada banda correspon a la extracció del AND de les següents formulacions: 1) PLGA-r$_8$:bPEI:DNA a 60:3:1 (w/w/w), 2) PLGA:bPEI:DNA a 60:3:1 (w/w/w), 3) PLGA-r$_8$/ PLGA-GTHRre:bPEI:DNA a 30/30:3:1 (w/w/w), 4) PLGA-r$_8$:bPEI:DNA a 60:3: (w/w/w), 5) PLGA-GTHRre:bPEI:DNA a 60:3:1 (w/w/w), 6) PLGA-r$_8$/ PLGA-GTHRre:bPEI:DNA a 30/30:3:1 (w/w/w), 7) Doble concentrades PLGA-r$_8$:bPEI:DNA a 60:3:1 (w/w/w), 8) Doble concentrades PLGA-GTHRre:bPEI:DNA a 60:3:1 (w/w/w), 9) Doble concentrades PLGA-r$_8$/ PLGA-GTHRre:bPEI:DNA a 30/30:3:1 (w/w/w), 10) Doble concentrades PLGA-r$_8$:bPEI:DNA a 60:3:1 (w/w/w), 11) Doble concentrades PLGA-GTHRre:bPEI:DNA a 60:3:1 (w/w/w), 12) Doble concentrades PLGA-r$_8$/ PLGA-GTHRre:bPEI:DNA a 30/30:3:1 (w/w/w).

Com es mostra en Figura 12, ADN dels pouets 5, 8, 10 i 11 va poder ser detectat. El que tenen en comú és que el pèptid acoblat a la superfície de les nanopartícules es el THRre, utilitzat com a llançadora de la BHE. Per tant, i com a resultats preliminars, algunes de les formulacions van aconseguir travessar la membrana cel·lular formada com a model. Tot i que els resultats van ser prometedors, encara queda una gran part de caracterització de les nanopartícules, la qual esta planificada com a propers experiments.

Capítol 3. Ús de pèptids com a potenciadors del transport a través de la barrera intestinal

Introducció

Durant les ultimes dècades, l'administració oral de pèptids i proteïnes ha sigut l'objecte d'estudi de molts grups de recerca. No obstant això, degut a la seva baixa estabilitat al

tracte gastro-intestinal i a la seva baixa absorció intestinal, molt poques formulacions han arribat al mercat.[17] Recentment, noves estratègies estan essent utilitzades per tal de superar aquests problemes, tals com l'ús de inhibidors de proteases,[18] l'ús de nanopartícules[19] i/o l'ús de potenciadors del transport intestinal.[20] Centrant-nos amb aquesta última estratègia, l'ús de pèptids com a potenciadors ha atret molta atenció en aquests darrers anys per les seves grans avantatges, tal com una alta especificitat contra altres molècules, una baixa inmunogenicitat i una fàcil escalabilitat.[21]

Els pèptids potenciadors del transport intestinal poden ser classificats en tres grups: potenciadors del transport transcel·lular, potenciadors del transport paracel·lular a través de la modulació de les unions estretes entre intestinals i pèptids directors a cèl·lules especifiques del epiteli intestinal (Figura 13). El primer grup comprèn pèptids capaços de alterar la membrana cel·lular, majoritàriament CPPs, augmentat el transport del medicament desitjat. El segon grup comprèn pèptids que poden modular l'acció de les unions estretes per tal d'obrir-les de manera controlada. L'últim grup inclou pèptids que reconeixen un tipus específic de cèl·lules o teixits augmentant el transport del medicament per aquelles zones.
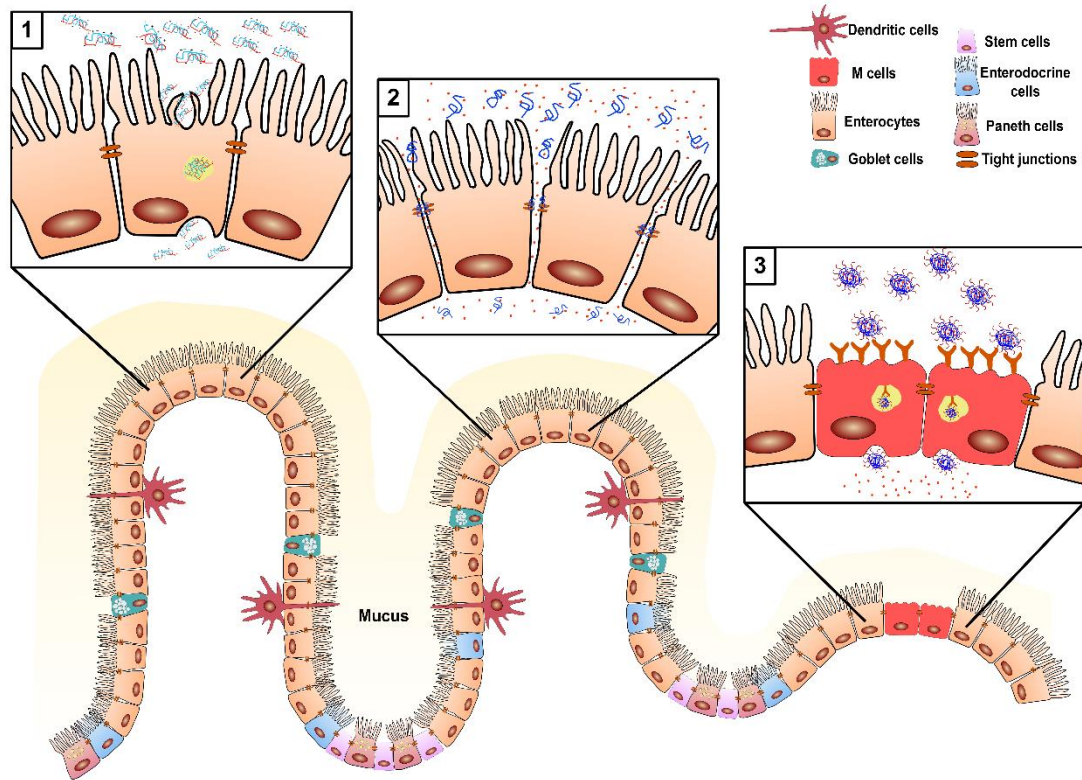
Figura 13. Representació esquemàtica de la membrana intestinal I els seus diferents mecanismes de transport. 1. Pèptids potenciadors del transport transcel·lular, 2. Potenciadors del transport paracel·lular, 3. Pèptids directors a cèl·lules o teixits específics.

Aquest capítol esta centrat en els CPPs per tal de millorar el transport de la insulina per via oral. Seguint com a exemple el treball de la Prof. Morishita,[22,23] el CPP (r_8) va ser utilitzat per complexar la insulina mitjançant unions electrostàtiques. Modificacions d'aquest pèptid pel seu *N*-terminal van portar a la creació de dos lipopeptids: C_{12}-r_8 i Cho-r_8. Un grup àcid gras de mida mitjana estava unit al r_8 en el primer dels casos i un grup colesteril en el segon. La capacitat potenciadora d'aquests pèptids va ser assajada en Caco-2 (model cel·lular estàndard utilitzat com a membrana intestinal, ja que les cèl·lules formen una monocapa amb unions estretes i expressen receptors)[24] i en Ussing Chambers (model pel qual una peça de teixit intestinal és col·locat entre dos cambres simulant condicions reals).[25]

Finalment, 9 compostos derivats dels anterior van ser assajats en Caco-2 per tal de veure si algun dels nous compostos mostrava més activitat transportadora que els seus parents.

Resultats i conclusions

Primerament, l'efecte sobre la TEER (resistència elèctrica del teixit) dels compostos r_8, C_{12}-r_8 i Cho-r_8 va ser assajat en teixit de colon de rata disposat a les Ussing Chambers. Una disminució en els valors de la TEER significa una formació de porus en la membrana o una obertura, la qual si es prolongada pot significar certa toxicitat. Per tant, els nostres compostos van ser assajats durant 2 h per veure l'efecte que tenien sobre el teixit de colon de rata. Com es mostra en la Figura 14, el pèptid r_8 no va modificar la TEER obtenint valors semblants al control negatiu (assaig fet sols amb dissolució tampó). Per contra, els altres dos compostos van fer disminuir la TEER, però de manera diferent. Mentre que el compost C_{12}-r_8 va disminuir la TEER de manera semblant al control positiu (C_{10}), el compost Cho-r_8 va disminuir la TEER i aquesta es va recuperar per, finalment, obtenir valors semblants al control negatiu.
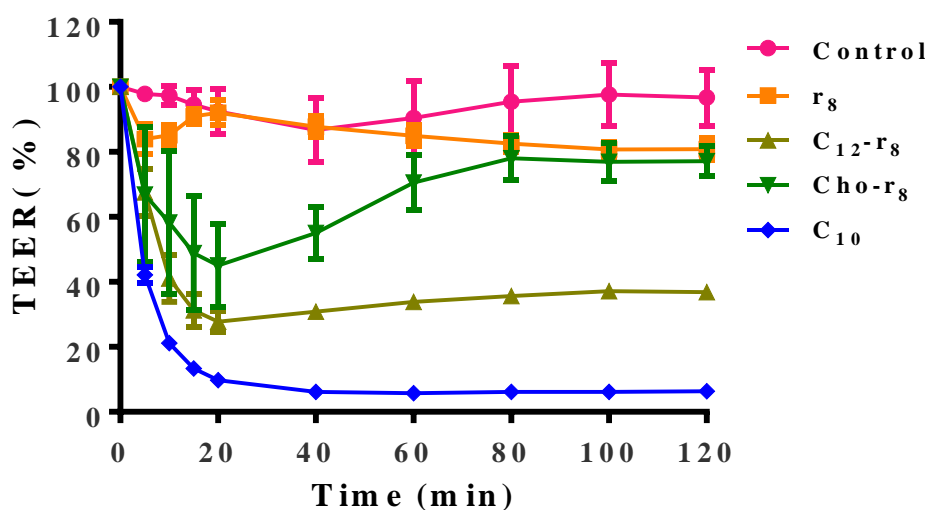

Figura 14. Efecte del r_8 i anàlegs sobre el % de la TEER sobre el teixit de colon de rata muntat en les Ussing chambers. Data representada com a mitjana dels valors $\pm$ SEM (n=3)..

Després d'aquest experiment, una molècula fluorescent de 4 kDa de massa (FD4) va ser afegida al experiment per tal de veure si aquests compostos eren capaços d'augmentar el seu transport. Es va repetir el mateix experiment i els resultats poden ser observats en la Taula 1. La permeabilitat aparent (Papp) del FD4 no va augmentar significativament per als compostos Cho-r_8 i r_8. Pel contrari, el compost C_{12}-r_8 va augmentar significativament la Papp del compost. Ningun dels compostos assajats va obtenir una Papp tan elevada com el control positiu utilitzat (C_{10})

Taula 1. Condicions utilitzades i Papp del FD4 en teixit de colon de rata després de l'adició dels anàlegs del CPP. (n= 3-4). ***P = 0.0001; ****P < 0.0001 (t-test).

Treatment	Concentration (mg/ml)	Concentration (mM)	Papp ($x10^{-6}cm/s$)	Statistical significance
Control	0	0	0.309±0.190	ns
r_8	0.8	0.63	0.265±0.049	ns
Cho-r_8	0.8	0.48	0.478±0.266	ns
C_{12}-r_8	0.8	0.55	1.139±0.230	***
C_{10}	1.94	10	5.667±0.920	****

A la vista dels resultats, el compost C_{12}-r_8 va ser el que més potencial tenia com a transportador a través de la membrana intestinal. Els experiments es van repetir però amb la prèvia formació de complexes entre la insulina i els pèptids. Quan aquests complexos van ser afegits a les cambres, va aparèixer un precipitat que era observable a simple vista. Aquest precipitat es quedava adherit al mucus que segregava el teixit, per tant vam proposar la hipòtesi de que un sistema més simple i que no segregués mucus podria ser l'ideal per tal d'assajar i optimitzar els nostres compostos.

Els compostos doncs, van ser assajats en el model cel·lular de Caco-2 (Figura 15). En aquest cas, la TEER sols va ser mesurada després de les 2 h que durava l'assaig i a les 24 h, per tal d'observar si aquests valors havien augmentat,, indicant que la integritat de la membrana seguia estant intacta.
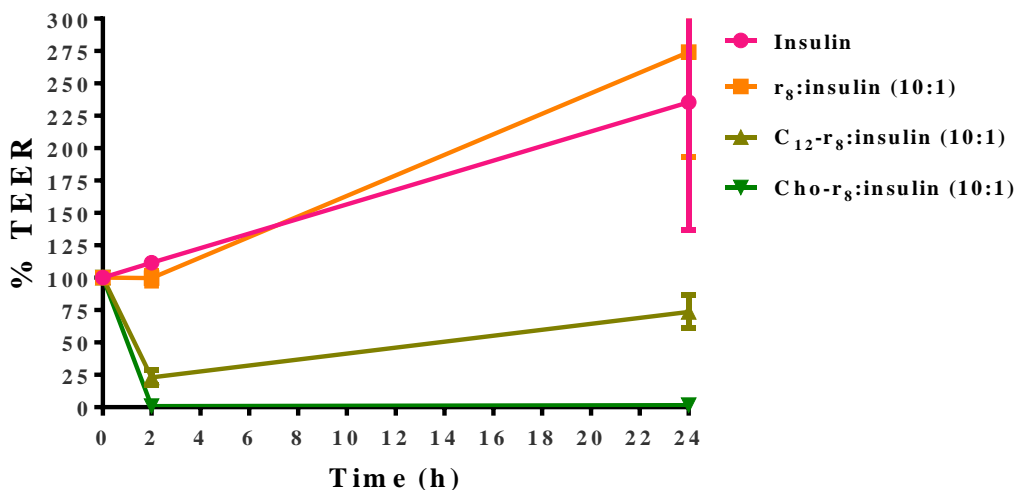
Figura 15. Efecte dels compostos (insulina:CPPs) sobre el % de la TEER en el model cel·lular de Caco-2. Data representada com a mitjana dels valors ± SEM (n=3).

Com podem observar en l'anterior figura i al igual que en les Ussing Chambers, els valors de la TEER per al r_8 no varien respecte al control negatiu. Pel contrari i variant respecte a les Ussing Chambers, el compost Cho-r_8 va disminuir la TEER i no va recuperar els valors afectant a la integritat de la membrana i possiblement destruint la monocapa de cèl·lules formada. Pel que fa al compost C_{12}-r_8 va disminuir la TEER però va recuperar-la fins un 75% després de 24 h. Tot i que aquests resultats semblaven prometedors, el problema de formació d'agregats trobat en les Ussing Chambers, també el vam poder observar en aquest assaig.

Com a resultats preliminars, els diferents anàlegs dels anteriors compostos, també van ser assajats en Caco-2. Diferents perfils de TEER van ser mesurats indicant les següents tendències: i) els compostos amb colesterol fan disminuir la TEER i aquests valors no es recuperen a les 24 h indicant destrucció de la membrana; ii) al augmentar la cadena carbonatada unida al r_8 la TEER disminueix fins que a partir de d'un cert nombre de carbonis, la TEER no es recupera a 24 h; iii) al augmentar el nombre de residus del CPP segueix la mateixa tendència que en el cas anterior.
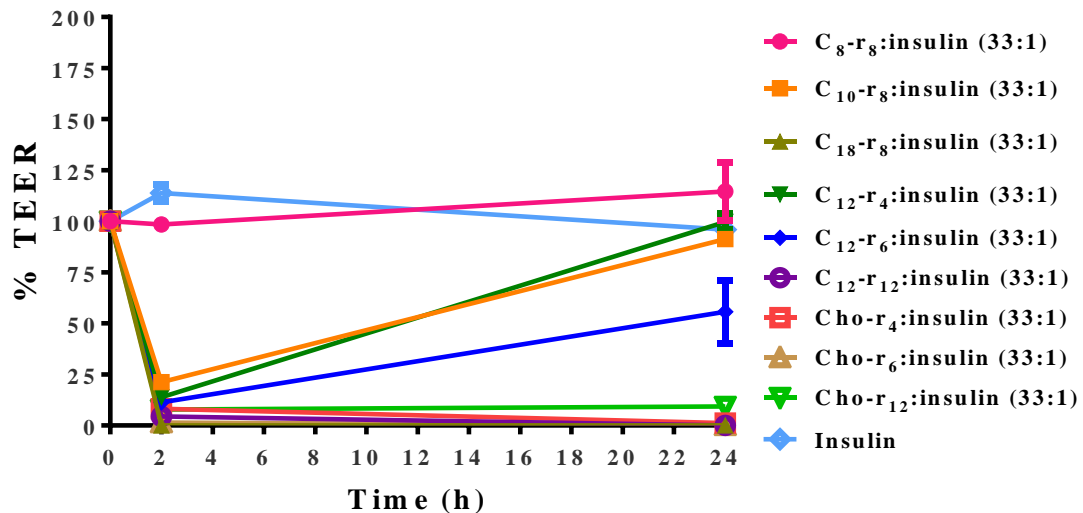
Figura 16. Efecte dels 9 compostos derivats formant complexos amb la insulina sobre el % de la TEER en el model cel·lular de Caco-2. Data representada com a mitjana dels valors ± SEM (n=3).

Tot i tenir considerar alguns compostos com a prometedors, els agregats també van aparèixer en quasi tots els casos assajats. Com a futurs experiments, la estabilitat d'aquests compostos ha de ser un estudi fonamental per tal de poder mesurar el transport de cada complex.

Referencies

1. Harper, T. Global funding of nanotechnologies & its impact. **2011**, (http://cientifica.com/wp-content/uploads/downloads/2011/07/Global-Nanotechnology-Funding-Report-2011.pdf)

2. Chen, H., Roco, M.C., Son, J., Jiang, S., Larson, C.A. & Gao, Q. Global nanotechnology development from 1991 to 2012: Patents, scientific publications, and effect of nsf funding. *Journal of nanoparticle research*, **2013**, (15) 1-21.

3. Statnano. (**last accessed 01/03/2016)**, (http://statnano.com/)

4. Oberdorster, G., Oberdorster, E. & Oberdorster, J. Nanotoxicology: An emerging discipline evolving from studies of ultrafine particles. *Environmental health perspectives*, **2005**, (113) 823-839.

5. Henderson, T.A. & Morries, L.D. Near-infrared photonic energy penetration: Can infrared phototherapy effectively reach the human brain? *Neuropsychiatric disease and treatment*, **2015**, (11) 2191-2208.

6. Alkilany, A.M., Nagaria, P.K., Hexel, C.R., Shaw, T.J., Murphy, C.J. & Wyatt, M.D. Cellular uptake and cytotoxicity of gold nanorods: Molecular origin of cytotoxicity and surface effects. *Small*, **2009**, (5) 701-708.

7. Futaki, S., Suzuki, T., Ohashi, W., Yagami, T., Tanaka, S., Ueda, K. & Sugiura, Y. Arginine-rich peptides. An abundant source of membrane-permeable peptides having potential as carriers for intracellular protein delivery. *The Journal of biological chemistry*, **2001**, (276)5836-5840.

8. Busbee, B.D., Obare, S.O. & Murphy, C.J. An improved synthesis of high-aspect-ratio gold nanorods. *Advanced Materials*, **2003**, (15) 414-416.

9. Nikoobakht, B. & El-Sayed, M.A. Preparation and growth mechanism of gold nanorods (nrs) using seed-mediated growth method. *Chemistry of Materials*, **2003**, (15) 1957-1962.

10. Vigderman, L. & Zubarev, E.R. High-yield synthesis of gold nanorods with longitudinal spr peak greater than 1200 nm using hydroquinone as a reducing agent. *Chemistry of Materials*, **2013**, (25) 1450-1457.

11. Morral, J.A., Davis, A.N., Qian, J., Gelman, B.B. & Koeppen, A.H. Pathology and pathogenesis of sensory neuropathy in Friedreich's ataxia. *Acta neuropathologica*, **2010**, (120) 97-108.

12. Lazaropoulos, M., Dong, Y., Clark, E., Greeley, N.R., Seyer, L.A., Brigatti, K.W., Christie, C., Perlman, S.L., Wilmot, G.R., Gomez, C.M., Mathews, K.D., Yoon, G., Zesiewicz, T., Hoyle, C., Subramony, S.H., Brocht, A.F., Farmer, J.M., Wilson, R.B., Deutsch, E.C. & Lynch, D.R. Frataxin levels in peripheral tissue in Friedreich ataxia. *Annals of Clinical and Translational Neurology*, **2015**, (2) 831-842.

13. Vert, M., Mauduit, J. & Li, S. Biodegradation of PLA/GA polymers: increasing complexity. *Biomaterials*, **1994**, (15) 1209-1213.

14. Prades, R., Oller-Salvia, B., Schwarzmaier, S.M., Selva, J., Moros, M., Balbi, M., Grazú, V., de La Fuente, J.M., Egea, G., Plesnila, N., Teixidó, M. & Giralt, E. Applying the retro-enantio approach to obtain a peptide capable of overcoming the blood–brain barrier. *Angewandte Chemie International Edition*, **2015**, (54) 3967-3972.

15. Cecchelli, R., Aday, S., Sevin, E., Almeida, C., Culot, M., Dehouck, L., Coisne, C., Engelhardt, B., Dehouck, M.-P. & Ferreira, L. A stable and reproducible human blood-brain barrier model derived from hematopoietic stem cells. *PloS one*, **2014**, (9) e99733.

16. Niu, X., Zou, W., Liu, C., Zhang, N. & Fu, C. Modified nanoprecipitation method to fabricate DNA-loaded PLGA nanoparticles. *Drug development and industrial pharmacy*, **2009**, (35) 1375-1383.

17. Fosgerau, K. & Hoffmann, T. Peptide therapeutics: Current status and future directions. *Drug discovery today*, **2015**, (20)122-128

18. Copeland, R.A. in *Evaluation of enzyme inhibitors in drug discovery* (John Wiley & Sons, Inc., **2013**).

19. Yin, L., Ding, J., He, C., Cui, L., Tang, C. & Yin, C. Drug permeability and mucoadhesion properties of thiolated trimethyl chitosan nanoparticles in oral insulin delivery. *Biomaterials*, **2009**, (30)5691-5700.

20. Aungst, B.J. Absorption enhancers: Applications and advances. *The AAPS journal*, **2012**, (14)10-18.

21. Sánchez-Navarro, M., Garcia, J., Giralt, E. & Teixidó, M. Using peptides to increase transport across the intestinal barrier. *Advanced drug delivery reviews*, **(submitted)**

22. Kamei, N., Morishita, M., Ehara, J. & Takayama, K. Permeation characteristics of oligoarginine through intestinal epithelium and its usefulness for intestinal peptide drug delivery. *Journal of controlled release*, **2008**, (131)94-99.

23. Kamei, N., Morishita, M. & Takayama, K. Importance of intermolecular interaction on the improvement of intestinal therapeutic peptide/protein absorption using cell-penetrating peptides. *Journal of controlled release*, **2009**, (136)179-186.

24. Sambuy, Y., De Angelis, I., Ranaldi, G., Scarino, M.L., Stammati, A. & Zucco, F. The Caco-2 cell line as a model of the intestinal barrier: Influence of cell and culture-related factors on Caco-2 cell functional characteristics. *Cell biology and toxicology*, **2005**, (21)1-26.

25. Clarke, L.L. A guide to ussing chamber studies of mouse intestine. *American Journal of Physiology - Gastrointestinal and Liver Physiology*, **2009**, (296)G1151-G1166.